NASA TECHNICAL NOTE

NASA TN D-4812

NASA TN D-4812

AERODYNAMIC CHARACTERISTICS OF A FIVE-JET VTOL CONFIGURATION IN THE TRANSITION SPEED RANGE

by Richard J. Margason and Garl L. Gentry, Jr.

Langley Research Center
Langley Station, Hampton, Va.

NATIONAL AERONAUTICS AND SPACE ADMINISTRATION • WASHINGTON, D. C. • OCTOBER 1968

AERODYNAMIC CHARACTERISTICS OF A FIVE-JET VTOL CONFIGURATION IN THE TRANSITION SPEED RANGE

By Richard J. Margason and Garl L. Gentry, Jr.

Langley Research Center
Langley Station, Hampton, Va.

NATIONAL AERONAUTICS AND SPACE ADMINISTRATION

For sale by the Clearinghouse for Federal Scientific and Technical Information
Springfield, Virginia 22151 – CFSTI price $3.00

AERODYNAMIC CHARACTERISTICS OF A FIVE-JET VTOL CONFIGURATION IN THE TRANSITION SPEED RANGE

By Richard J. Margason and Garl L. Gentry, Jr.
Langley Research Center

SUMMARY

A wind-tunnel investigation of a powered model of a VTOL fighter airplane configuration having three lift engines in the forward fuselage and two deflected lift-cruise engines in the aft fuselage has been conducted to determine the aerodynamic characteristics of the model in the transition speed range. The jet-induced interference showed that the expected increase in lift loss and nose-up pitching moment with increasing forward speed was rather small because of the counteracting effects of the front and rear jets. A substantial part of the nose-up interference pitching moment was found to be due to the engine inlet mass flow for this engine arrangement. These results showed that increasing angle of attack had very little effect on interference lift and drag but that significant increases in interference pitching moment can occur if the horizontal tail is on or below the wing-chord plane. Further investigation of tail height showed that the jet-induced downwash was highest for the low tail position but that the jet-induced longitudinal instability was mild for the three tail positions used in the tests. The effects of ground proximity were found to be relatively small for this configuration.

INTRODUCTION

Research is being conducted by industry and the National Aeronautics and Space Administration toward the development of vertical take-off and landing (VTOL) airplanes that combine the utility of the helicopter with the higher speed and longer range capabilities of conventional airplanes. Jet-supported VTOL configurations are of interest for missions requiring high-subsonic or supersonic cruise performance. Investigations of the aerodynamic characteristics of jet VTOL aircraft in the transition speed range have been restricted largely to studies of the jet-induced effects of the exiting jets on the longitudinal aerodynamic characteristics (refs. 1 to 7). These studies have shown jet-induced lift losses, nose-up trim changes, and reduction in longitudinal stability.

The purpose of the present investigation is to extend the scope of the previous work to determine the effect of inlet mass flow along with the jet-induced effects of the exiting jets on the longitudinal aerodynamic characteristics of one type of jet VTOL fighter

airplane. In addition, tests were performed to determine the jet interference effects on the lateral-directional aerodynamic characteristics. The model tested represented a VTOL fighter configuration with three lift engines in the forward fuselage and two deflected lift-cruise engines in the aft fuselage. The model was tested with three wing configurations and up to three horizontal tail heights.

The investigation was performed in the Langley 300-MPH 7- by 10-foot tunnel. The majority of the tests were performed in the 17-foot (5.18-meter) test section. The model was tested through a range of angle of attack or of sideslip at several thrust coefficients. These tests show the effects of power on the aerodynamic stability and control of the airplane model. The basic data were analyzed to determine changes in jet interference effects caused by changes in wing configuration, by change in angle of attack, by the engine simulator inlet mass flow, by each group of engines, and by variation in the height of the horizontal tail. In addition, downwash effects at the horizontal tail are presented. Also included is an investigation in ground effect at simulated speeds from hover through transition for angles of attack of approximately 0^{o} and 10^{o}.

SYMBOLS

The longitudinal aerodynamic data (lift, drag, and pitching-moment coefficients) in this report are referred to the stability-axis system. The lateral-directional aerodynamic data (rolling-moment, yawing-moment, and side-force coefficients) are referred to the body-axis system. The thrust coefficient is based on the gross thrust produced by the model and is not related to an axis system. All the data are referred to a moment center located on the fuselage reference line at the quarter-chord point of the mean aerodynamic chord of the plain wing (see fig. 1(a)). The forces and moments were nondimensionalized by using the geometry of the plain wing.

The units used for the physical quantities defined in this paper are given both in the U.S. Customary Units and in the International System of Units (SI). Factors relating these two systems of units are presented in reference 8. The symbols used are defined as follows:

A_j sum of areas of operating nozzles, 0.109 foot^2 (0.010 meter^2) when all five nozzles are operating

b wing span, 4.00 feet (1.22 meters)

C_D drag coefficient, $\frac{\text{Drag}}{q_\infty S}$

C_L lift coefficient, $\frac{\text{Lift}}{q_\infty S}$

C_l rolling-moment coefficient, $\frac{\text{Rolling moment}}{q_\infty Sb}$

C_{l_β} effective dihedral parameter, $\frac{\partial C_l}{\partial \beta}$

C_m pitching-moment coefficient, $\frac{\text{Pitching moment}}{q_\infty S\bar{c}}$

C_n yawing-moment coefficient, $\frac{\text{Yawing moment}}{q_\infty Sb}$

C_{n_β} directional stability parameter, $\frac{\partial C_n}{\partial \beta}$

C_T thrust coefficient, $\frac{\text{Thrust}}{q_\infty S}$

C_Y side-force coefficient, $\frac{\text{Side force}}{q_\infty S}$

C_{Y_β} side-force parameter, $\frac{\partial C_Y}{\partial \beta}$

c wing chord, feet (meters)

$\bar{c}$ mean aerodynamic chord of plain wing, 8.04 inches (20.42 centimeters)

$\bar{c}_t$ mean aerodynamic chord of horizontal tail, inches (centimeters)

D drag force, pounds (newtons)

ΔD increment in drag force due to jet interference (see eq. (4)), pounds (newtons)

D_e effective diameter; diameter of circle having same area as sum of all operating nozzles, 4.47 inches (11.35 centimeters) when all five nozzles are operating

h	height of lower surface of model fuselage from ground, feet (meters)
h_t	height of horizontal tail from wing-chord plane, feet (meters)
i_t	tail incidence, degrees
L	measured lift, pounds (newtons)
L_A	lift due to aerodynamic forces, pounds (newtons)
L_T	lift due to thrust, pounds (newtons)
ΔL	increment of lift due to jet interference (see eq. (3)), pounds (newtons)
l_t	tail length measured horizontally from quarter-chord point of wing mean aerodynamic chord to quarter-chord point of tail mean aerodynamic chord, feet (meters)
M	pitching moment, foot-pounds (meter-newtons)
ΔM	increment of pitching moment due to jet interference (see eq. (5)), foot-pounds (meter-newtons)
$\dot{m}$	mass flow, pounds per second (kilograms per second)
q	dynamic pressure, pounds per foot^2 (newtons per meter^2)
S	wing area (based on plain wing), 2.5 feet^2 (0.23 meter^2)
S_t	tail area, 1.02 feet^2 (0.10 meter^2)
T	thrust, pounds (newtons)
$\overline{V}$	nondimensional horizontal-tail volume, $\frac{S_t}{S}\frac{l_t}{\bar{c}}$
V	velocity, feet per second (meters per second)
x	distance along airfoil chord line from leading edge, feet (meters)

y_l distance measured perpendicular from airfoil chord line to the airfoil lower surface, feet (meters)

y_u distance measured perpendicular from airfoil chord line to the airfoil upper surface, feet (meters)

α angle of attack, degrees

β angle of sideslip, degrees

δ deflection of movable surface (with subscript to denote surface deflected), degrees

ϵ effective downwash angle, degrees

ρ density, slugs per foot^3 (kilograms per meter^3)

Subscripts:

F lift engine simulators in forward fuselage

f flap (see fig. 1(c))

H hover

i inlet

j jet

n nozzle

R lift-cruise engine simulators in rear portion of fuselage

s slat (see fig. 1(c))

t horizontal tail

∞ free stream

MODEL AND APPARATUS

The model represents a VTOL fighter airplane with a high wing, body-mounted nacelles for the lift-cruise engines, lift engines mounted inside the forward portion of the fuselage, and empennage mounted at the rear of the fuselage. The model drawings in figure 1 and the photographs in figure 2 show the general arrangement of the model along with the different wing configurations which were tested. The three wing configurations tested are described as follows: A, the plain wing with high-lift flaps, a stall-control device, and a fixed forewing; B, the plain wing with high-lift flaps; and C, the plain wing. The details of the wing geometry are presented in figure 1(a) and the details of the high-lift flaps and stall-control device (slat) are presented in figure 1(c). The flap had a constant chord and extended along the trailing edge from the wing tip to the wing-nacelle juncture. The leading-edge slat had a varying chord equal to 15 percent of the wing chord and extended from the wing tip to the intersection of the leading edges of the forewing and of the basic wing. Provisions were made so that the horizontal tail could be located $1.06\bar{c}$ above the wing-chord plane (high position), on the wing-chord plane (mid position), or $0.62\bar{c}$ below the wing-chord plane (low position). The tail length for the mid and low tail was slightly shorter than that for the high tail, with a resulting decrease in tail volume $\overline{V}$ (from 1.43 to 1.34).

The thrust was provided by five ejector-type jet-engine simulators (ref. 9), three forward of the moment center to represent lift engines and two aft of the moment center to represent lift-cruise engines. The jet exhaust from all the ejectors was directed downward normal to the fuselage-reference plane. The ejectors were powered by cold, dry compressed air which was brought onboard the model with thin-wall metal tubing bent to follow the sting support and to form a limber spring across the strain-gage balance so that it did not change the balance sensitivity. A sheet-metal fairing which can be seen in figure 2(b) was used to shield these air lines from the airstream.

The model was mounted in the 17-foot (5.18-meter) test section of the Langley 300-MPH 7- by 10-foot tunnel on a sting-supported six-component strain-gage balance for measurement of the total forces and moments. This test section is equipped with an endless-belt moving ground plane, described in detail in reference 10.

TEST PROCEDURE AND ACCURACY

In order to cover a range of both angle of attack and effective velocity ratio from hover to conventional flight, tests of the model were made in the 17-foot (5.18-meter) test section of the Langley 300-MPH 7- by 10-foot tunnel at the following conditions:

α, deg	β, deg	q_∞		T		C_T	$\sqrt{\frac{\rho_\infty V_\infty^2}{\rho_j V_j^2}}$
		psf	N/m^2	lb	N		
-6 to 26	0	11.0	527	0	0	0	∞
		11.0	527	93	414	3.3	0.16
		6.9	329	139	618	7.9	.10
0, 11, or 21	-26 to 6	11.0	527	0	0	0	∞
		11.0	527	93	414	3.3	.16
		6.9	329	139	618	7.9	.10
0 or 10	0	0 to 11.0	0 to 527	139 to 30	618 to 133	∞ to 1.0	0 to 0.30

The Reynolds number based on free-stream velocity and mean aerodynamic chord ranged as high as 0.4×10^6.

Three configurations of this model were tested. Configuration A ($\delta_f = 30^o$, $\delta_s = 35^o$, fixed forewing) was tested with the horizontal tail off, in the high position, in the mid position, and in the low position. It was also tested through the range of sideslip angles at angles of attack of 0^o, 11^o, and 21^o with the complete empennage, with only the vertical tail, and without either the vertical or horizontal tail. Configuration A was also tested at a range of ground heights from 1 effective diameter to 11 effective diameters at angles of attack of 0^o and 10^o. The ground-effect tests at heights of 6 effective diameters or less were made with the endless-belt ground plane moving at free-stream velocity. Configurations B ($\delta_f = 30^o$) and C ($\delta_f = 0^o$) were tested with the horizontal tail off, in the mid position, and in the low position. In addition, the model with the wing off was tested with the horizontal tail off and with the tail on at all three tail positions.

Some data were obtained with configuration B installed in the 7- by 10-foot (2.13- by 3.05-meter) test section. The purpose of these tests was to determine whether a powered model of this size could be tested in the smaller test section without significant wall effects. For these tests the thrust was held constant at approximately 139 lb (618 N), the free-stream dynamic pressure varied from 0 to 58 psf (0 to 2777 N/m^2), and the Reynolds number based on free-stream velocity and mean aerodynamic chord ranged as high as 0.93×10^6.

No corrections have been made to the data for blockage or tunnel wall effects. Some of the data show considerable scatter for test conditions where the flow around the model is dominated by the turbulent exhaust from the ejectors.

Thrust was determined from total and static pressures measured in the jet exits by using a calibration of gross thrust as a function of the difference between these pressures. A description of the calibration method is presented in reference 9. Thrust coefficient and effective velocity ratio were then determined (using the total of the individually measured thrusts) from the following equations:

$$C_T = \frac{T}{q_\infty S} \tag{1}$$

$$\sqrt{\frac{\rho_\infty V_\infty^2}{\rho_j V_j^2}} \approx \sqrt{\frac{q_\infty}{\left(\frac{T}{2A_j}\right)}} \tag{2}$$

A plot showing the relation between thrust coefficient and effective velocity ratio for this model is presented in figure 3. This figure shows that the thrust coefficient varies more in magnitude than the effective velocity ratio, especially at low free-stream velocities. Therefore, although small differences in the values of thrust coefficient may exist among the figures, the values of effective velocity ratio are essentially constant. All the thrust data presented in this report were obtained with the jets directed downward to provide a force perpendicular to the fuselage reference line (fig. 1(a)). The Reynolds number of the ejector jet-exit flow in both test sections, based on the exit velocity and the 2-inch (5.08-cm) diameter of one ejector exit, ranged up to 0.8×10^6.

PRESENTATION OF RESULTS

The results of a wind-tunnel investigation of aerodynamic stability and control characteristics of a model of a jet-powered VTOL fighter airplane are presented in the following figures:

DISCUSSION OF RESULTS

Basic Longitudinal Aerodynamic Data

The basic longitudinal aerodynamic data are presented in figures 4 to 9; these data were obtained for the tail-off configuration. Figures 4, 6, and 8 present the variation of lift, pitching-moment, and thrust coefficients with angle of attack and the variation of lift coefficient with drag coefficient. Also presented (figs. 5, 7, and 9) are the variations of lift divided by thrust, drag divided by thrust, and pitching moment divided by thrust times the effective jet-exit diameter as a function of effective velocity ratio.

Since configuration A ($\delta_f = 30^o$, $\delta_s = 35^o$, and fixed forewing) has the leading-edge slats along with the flaps, it provides the highest values of maximum lift coefficient and stalls at a higher angle of attack (fig. 4(a)) than configuration B ($\delta_f = 30^o$) (fig. 6(a)). The pitching-moment data for all three configurations (A, B, and C) with the horizontal

tail off show that power increases the instability found without thrust. The thrust-coefficient data (figs. 4(d), 6(d), and 8(d)) show that thrust is essentially constant with increasing angle of attack.

Longitudinal Stability and Control

The longitudinal tail-effectiveness data are presented in figures 10 to 44 for low, mid, and high positions of the horizontal tail at several tail incidences for configuration A and for low and mid positions for configurations B and C.

For configuration A with the horizontal tail in the high position (figs. 10 to 12) the pitching-moment data indicate that the tail provides a contribution to stability for angles of attack up to approximately 10° to 12°. The contribution of the tail to stability reversed, in general, above these angles of attack. For the power-off configuration the tail-on configuration again becomes stable above an angle of attack of 20°. This variation is typical of the deep-stall problem of T-tails as shown by the data presented in reference 11 for the high-tail transport configuration. Although the data for the power-on configurations do not demonstrate this second stable region, these same trends would be expected at higher angles of attack than those presented in this report.

The data for the mid and low tail positions (figs. 15 to 17 and 20 to 22) show a positive tail contribution to stability throughout the angle-of-attack range. These data also show that the lower horizontal-tail positions bring the tail down into a flow region where the power effects on trim levels are more pronounced. These effects are discussed in the section on interference effects at the horizontal tail. The stability levels of configuration A were not significantly changed as a result of power at any of the three tail positions. This mild jet-induced longitudinal instability is in sharp contrast to that found on the configuration described in reference 7. A detailed comparison of the results of the present investigation with those in reference 7 was presented in reference 12.

The data for configuration B ($\delta_f = 30^{\circ}$) are presented for the mid and low tail positions. The data at the mid position (figs. 25 to 27) for angles of attack above 6° to 8° show a region where the horizontal tail does not provide a contribution to stability. The data at the low position (figs. 30 to 32) show that the horizontal tail provides a contribution to stability throughout the test range of angle of attack and at all thrust conditions except at the highest thrust coefficient.

The data for configuration C ($\delta_f = 0^{\circ}$) presented in figures 35 to 37 and 40 to 42 for the mid and low tail positions show a contribution to stability throughout the test range of angle of attack. The tail-on pitching-moment-coefficient data at both tail positions are relatively linear with increasing angle of attack, and with the power off it has a

stable slope. As the power is increased to the highest thrust coefficient the stability is reduced until it is essentially neutral.

Longitudinal Interference Effects

The jet-induced increments of lift and pitching moments presented in this section were determined in a manner similar to that in references 3 to 7. The direct thrust effects and the aerodynamic forces calculated from the power-off data were subtracted from the measured power-on data to leave only the jet-induced interference increments including inlet effects. All the power-on data in this report are for a jet deflected 90° from the fuselage reference line. The equations for the jet interference increments are given in terms of effective velocity ratio as follows:

$$\frac{\Delta L}{T} = \frac{L}{T} - \left[\cos \alpha + C_L \frac{S}{2A_j} \frac{\rho_\infty V_\infty^2}{\rho_j V_j^2}\right] \tag{3}$$

$$\frac{\Delta D}{T} = \frac{D}{T} - \left[\sin \alpha + C_D \frac{S}{2A_j} \frac{\rho_\infty V_\infty^2}{\rho_j V_j^2}\right] \tag{4}$$

$$\frac{\Delta M}{TD_e} = \frac{M}{TD_e} - \left[\left(\frac{M}{TD_e}\right)_H + C_m \frac{S}{2A_j} \frac{\bar{c}}{D_e} \frac{\rho_\infty V_\infty^2}{\rho_j V_j^2}\right] \tag{5}$$

$$\frac{L}{L_T + L_A} = \frac{L/T}{\left[\cos \alpha + C_L \frac{S}{2A_j} \frac{\rho_\infty V_\infty^2}{\rho_j V_j^2}\right]} \tag{6}$$

The values of C_L, C_D, and C_m in these equations are the coefficients obtained for the power-off condition.

Since both power-on and power-off data are used to compute these interference effects, they are subject to experimental scatter which may be magnified in the computation of these increments. This scatter tends to increase with an increase in the effective velocity ratio. Because of these factors, the interference effects are presented as faired curves to indicate trends rather than precise numbers. The interference lift (eq. (3)) and interference drag (eq. (4)) presented have a maximum scatter of ±0.10 times the effective velocity ratio; the interference pitching moment (eq. (5)) has a maximum scatter of ±0.15 times the effective velocity ratio; and the effective lift ratio (the ratio of

measured lift to direct lift force, eq. (6)) has a maximum scatter of ±0.08 times the effective velocity ratio. The general trend of interference effects is increasing lift loss, increasing drag increment, and increasing nose-up pitching moment as the effective velocity ratio increases.

The photographs in figure 45 illustrate through flow-visualization techniques the wakes from the five jet-engine simulators used to power this model (configuration B ($\delta_f = 30^o$) with the tail off); water vapor was used to make the wakes visible. For these photographs the model was installed in the 7- by 10-foot (2.13- by 3.05-meter) test section of the Langley 300-MPH 7- by 10-foot tunnel. These photographs are useful in obtaining a qualitative understanding of the cause of the basic interference effects. The first three photographs illustrate the jets with a deflection of 60^o from the free stream for effective velocity ratios of 0, 0.16, and 0.23. In hover, the wakes are straight, being deflected only when they strike the wind-tunnel floor. As the free-stream velocity increases, the jets are deflected aft above the tunnel floor as a result of the interaction between the jet and free-stream velocity so that at the highest effective velocity ratio the wakes are closest to the model. These are also the conditions for which the interference effects are the largest. The fourth photograph shows the model with a jet deflection of 90^o and an effective velocity ratio of 0.23. The deflections of the three jets in the forward portion of the fuselage are especially interesting. This photograph shows that the most forward jet deflects closest to the model; the second and third jets from the front are partially shielded from the free stream and each deflects farther from the model than the jet immediately ahead. Quantitative results of interferences of the jets on the forces and moments are presented in the following sections of this report from data obtained in the 17-foot (5.18-meter) test section.

Effect of wing configuration.- Presented in figure 46 are the basic interference data for the fuselage alone and for each of the three model configurations (tail off) tested at angles of attack of 0.6^o and 10.8^o. (See fig. 1 for sketches.) All these configurations show approximately a 2-percent lift loss in hover. The largest interference effects (lift loss and nose-up pitching moment) at a forward velocity occur with the fuselage alone. The jet interference effects decrease progressively with the addition of the wing, flaps, and leading-edge slats. These results are different from those of references 1 and 7 which show opposite trends. These differences are probably due to the locations of the engine exits. In both references the exits are located under the wing ahead of the trailing edge. On this model the rear jets are behind the wing trailing edge where they provide favorable interference effects which are discussed in more detail in the section on the effect of engine location.

Effect of angle of attack.- The effect of angle of attack on the longitudinal interference is presented in figure 47 for configuration A, in figure 48 for configuration B, and

in figure 49 for configuration C. These data show, in general, that the interference drag and the interference-lift loss decrease slightly and that the effective lift ratio increases slightly with increasing angle of attack. The interference pitching moment tends to increase with increasing angle of attack. This effect was noted in reference 7. When there are inlets at a considerable distance ahead of the center of gravity, such as the cruise-engine inlets of the present model, an increase in angle of attack results in the inlet momentum drag being applied higher with respect to the center of gravity and thus contributes a nose-up pitching moment. This inlet effect is one factor in this trend. In addition, the height of the horizontal tail affects the magnitude of the interference pitching moment and its rate of increase with angle of attack. This part of the increment is the result of reduced pressures on the surface area behind the jets as indicated in reference 2. The largest values of interference pitching moment on this model occur when the horizontal tail is on or below the wing-chord plane where it is closest to the jet wake.

Effect of inlet mass flow.- The effect of the inlet mass flow is presented in figure 50 for configuration A ($\delta_f = 30^o$, $\delta_s = 35^o$, and fixed forewing) and in figure 51 for configuration B ($\delta_f = 30^o$). The horizontal tail is off for both configurations. The solid curves represent the condition with the engine-simulator inlets open and are the same as those presented in figure 46. The inlet mass flow causes the inlet momentum drag force; unfortunately, the inlet mass flow was not measured, so direct computation of this drag force is not possible. However, the calibration data in reference 9 provide information from which the ratio of inlet mass flow to exit mass flow may be estimated. These data were used in the following equation to predict the inlet drag increment

$$\frac{\Delta D}{T} = \frac{\dot{m}_i V_\infty}{\dot{m}_j V_j} \tag{7}$$

The results of these calculations checked the experimental values shown in figures 50 and 51 for the model with the inlets closed. The data for an angle of attack of 0.6^o show an interference-pitching-moment increment (nose-up) that is caused by the inlet drag increment due to flow which is turned from the free stream into the lift-engine-simulator inlets.

At an angle of attack of 10.8^o the situation is a little different. For configuration A (fig. 50(b)) the interference-drag increment is greater than at an angle of attack of 0.6^o so that its contribution to the interference pitching moment is increased; however, the total interference pitching moment is nearly the same. This indicates that there is a redistribution of lift on the model which does not change the total lift but does reduce the contribution of lift to the interference pitching moment. In contrast, for configuration B (fig. 51(b)) the interference-drag increment at an angle of attack of 10.8^o is similar to the value at an angle of attack of 0.6^o but the interference pitching moment is greater. In

this case the contribution of drag is unchanged but a redistribution of lift causes an increase in nose-up pitching moment. These data show that the engine inlet mass flow contributes a nose-up interference pitching-moment increment, a positive interference-drag increment, and little change in interference lift.

Effect of operating lift engines alone or lift-cruise engines alone.- A series of tests were performed on configuration A ($\delta_f = 30^o$, $\delta_s = 35^o$, and fixed forewing) with the horizontal tail off to determine some of the effects related to engine location. For these tests, the three lift engine simulators in the forward portion of the fuselage were operated alone (lift-cruise engines off) and the two lift-cruise engine simulators were operated alone (lift engines off). These two groups are compared with the basic condition where all five engine simulators are operating. In figure 52, the data for pitching moment as a function of angle of attack are presented for comparison with the data with all engines operating at a thrust coefficient of 8.0. The data in figure 52 show that even though the direct thrust contribution changes the level of the pitching moments, their variation with angle of attack is essentially the same.

To determine whether any mutual interference effects exist with all the engines operating which do not exist with just the lift engines or just the lift-cruise engines operating, these two groups of engines were run separately. The curves given in figure 53 by the symbols present the measured data. It is noted that the measured pitching-moment data for the case with all the jet engines operating contain the following increments of pitching moment: direct thrust contribution of each engine group, aerodynamic pitching moment, interference due to the lift engines, interference due to the lift-cruise engines, and possible interference due to the mutual interaction of the flow from the two groups of engines.

Next it is noted that each of the other two curves has a thrust contribution, the aerodynamic pitching moment, and only the interference effect due to that particular group of engines. When these two quantities are combined directly, the mutual interference effect is missing as desired, but the aerodynamic pitching moment is included twice since it was measured with both sets of data. The following equation was used to subtract one increment of aerodynamic pitching moment and nondimensionalize the data by the total thrust and the effective diameter of all five engine simulators:

$$\frac{M}{TD_e} = \left(\frac{M_F}{T_F D_{e,F}}\right)\frac{T_F D_{e,F}}{TD_e} + \left(\frac{M_R}{T_R D_{e,R}}\right)\frac{T_R D_{e,R}}{TD_e} - C_m \frac{S}{2A_j}\frac{\bar{c}}{D_e}\frac{\rho_\infty V_\infty^2}{\rho_j V_j^2} \qquad (8)$$

The resulting curve is shown as a dash line in figure 53 and is within experimental accuracy of checking the measured data. It is then inferred that the mutual interference effect described here is either very small or does not exist in this case.

Finally, the interference effects were computed directly. The data in figure 54(a) for all five engines operating show the same lift loss and nose-up pitching-moment interference effects as does the curve for configuration A ($\delta_f = 30^o$, $\delta_s = 35^o$, and fixed forewing) presented in figure 46. When the lift engines were operating alone, the largest lift loss was measured; small interference pitching moments were measured which varied from slightly nose-up at low effective velocity ratios to nose-down at higher effective velocity ratios. The lift-cruise engines operating alone result in a small lift augmentation and a large nose-up pitching moment. These results imply high suction pressure on the lower surface behind the engine nozzle. They also imply that favorable lift is induced when a lifting surface is ahead of the jets. Similar interference effects are presented in figure 54(b) for configuration B ($\delta_f = 30^o$) and in figure 54(c) for configuration C ($\delta_f = 0^o$). These results show that the locations of the engines produce significant changes in the interference effects.

Effect of horizontal-tail height.- The longitudinal stability and control data presented in figures 10 to 44 have been analyzed to determine the effect of the horizontal tail on the longitudinal interference for each of the three model configurations tested. These interference effects are presented in figure 55 for configuration A ($\delta_f = 30^o$, $\delta_s = 35^o$, and fixed forewing), in figure 56 for configuration B ($\delta_f = 30^o$), and in figure 57 for configuration C ($\delta_f = 0^o$). Part (a) of each of these figures shows the data for an angle of attack of 0.6^o and part (b) shows the data for an angle of attack of 10.8^o. These data show the smallest nose-up pitching moment for the tail off and increasing nose-up increments as the tail is put in the high position (fig. 55 only) and then lowered to the mid position and the low position; the largest increments are incurred at the low position. These tail-on data are consistent with each of the tail incidences used in the investigation; therefore, these pitching-moment interference increments must be due to a jet-induced downwash at the horizontal tail. A similar trend is noticed with the lift loss; the smallest loss occurs with the tail off and increases with tail on as the tail is brought closer to the jet wake of the model. The interference drag, however, shows very little effect of the horizontal-tail position. In general, this indicates that a high tail position is desirable to minimize the effects of jet-induced downwash in transition flight.

The longitudinal stability and control data for all the configurations tested were analyzed to determine the effective downwash angle and the effective dynamic pressure at the horizontal tail. The results are presented in figures 58, 59, and 60 for configurations A, B, and C, respectively. The variation of dynamic pressure at the tail for configuration B with mid tail position was omitted because data were not obtained at enough tail incidences to determine it accurately. The data for configuration A with the high tail position (fig. 58(a)) show very little effect of thrust on the downwash at the tail. The data for all configurations for the other two tail positions, mid and low, show the following trends. At angles of attack less than approximately 15^o the power produces an increase

of 4^{o} to 8^{o} in downwash angle and about the same $\partial\epsilon/\partial\alpha$ as for the power-off data. The downwash angles for $C_T \approx 3.3$ tend to be up to 2^{o} higher than those for $C_T \approx 8.0$. At angles of attack above 15^{o} the downwash angles from the power-off data started to decrease whereas the downwash angles from the power-on data continued to increase through the highest test angle of attack.

Ground Effect

A series of tests were performed with configuration A ($\delta_f = 30^{o}$, $\delta_s = 35^{o}$, and fixed forewing) to determine the effect of height above the ground on the longitudinal aerodynamic characteristics through the transition speed range. The data are presented in figures 61 to 64 for angles of attack of 0.6^{o} and 10.8^{o} for the horizontal tail off and for the three tail positions ($i_t = 0^{o}$). The height of the model above the ground h was measured perpendicular from the ground to a point on the lower surface of the model fuselage below the moment center. The data at an angle of attack of 10.8^{o} could only be obtained down to a ground height of 2 effective diameters. Below this height the model support system touched the moving-belt ground board. At an angle of attack of 0.6^{o}, as the ground is approached in hover, the lift loss does not increase much until heights below 2 effective diameters are reached. At forward speeds this change in lift shifts from a loss to a gain somewhere above an effective velocity ratio or 0.10 for this particular model. Data in reference 13 show that this result depends on the configuration details. The pitching moment for tail-off hover is not affected by reduced ground height until heights below 4 effective diameters are reached; however, as the effective velocity ratio increases the change in pitching moment occurs farther from the ground. The largest decrease in pitching moment occurs with the tail-on configuration at the highest effective velocity ratio at heights below 4 effective diameters. As the hover condition was reached for the tail-on configurations, virtually no change in pitching moment was measured. If this airplane uses a landing-gear height equal to at least 1 effective diameter, the lift loss due to ground effect would be less than 2 percent of the thrust; and, if the last portion of the vertical landings were made in the hovering mode, there would be no static pitching-moment change due to ground effect.

Wall Effects on Longitudinal Aerodynamic Data

One of the most difficult facets of testing powered wind-tunnel models in transition from hover to forward flight is determining when wind-tunnel wall effects become significant enough to modify the results. The model described in this report was tested in both test sections of the Langley 300-MPH 7- by 10-foot tunnel in an effort to evaluate these effects. The model was mounted on its side in the smaller test section to provide more distance for the jet wake between the model and the wind-tunnel wall. With this installation, the test-section height was 10 feet (3.05 meters) and the width was 7 feet

(2.13 meters). In the larger test section the height was 15.8 feet (4.82 meters) and the width was 17 feet (5.18 meters). The comparisons of data are presented for configuration B ($\delta_f = 30^o$) with the tail off and with the tail in the mid position at an incidence of 5.2^o.

The wall effects when the jets are operating are presented in figures 65 and 66. The nondimensionalized lift data (fig. 65) from the smaller test section show that less lift is developed at the lower effective velocity ratios and more lift is developed at the higher effective velocity ratios than was measured in the larger test section. The reason for the loss in total lift at the lower speeds is the limiting lower speed at which potential flow can be obtained in a closed-test-section wind tunnel. This limit occurs much sooner in the smaller test section. Below this limiting speed lateral recirculation occurs in the vicinity of the model. Since the flow conditions generated by this problem are so complex, development of analytical techniques which could correct the data is considered unlikely. However, methods for estimating when these conditions might be present are discussed in references 10 and 14. At forward-speed conditions greater than an effective velocity ratio of about 0.12 for this model, potential flow conditions were obtained. The increased lift measured in the smaller test section is caused by larger wall-induced upwash angles at the wing and along the fuselage. Additional test data would be required to provide enough information for proper verification of the wall correction techniques described in reference 14.

A comparison of longitudinal interference effects caused by the two test sections is presented in figure 66. This comparison indicates that generally the data from the smaller test section show reduced interference effects. The most significant difference is the interference pitching moment; the data obtained in the smaller test section are a third to a half of those obtained in the larger test section. These results show that the wall effects can change the magnitudes of the interference effects and that the model should be relatively small compared with the test-section size in order to reduce the magnitudes of the limiting lower speed and of the wall-induced flow angularities. Although the 15.8- by 17-foot (4.82- by 5.18-meter) test section is considered to be large enough for this model, verification of this fact and determination of the limiting lower speed would require tests in a still larger test section. In any event, these results clearly show that the 10- by 7-foot (3.05- by 2.13-meter) test section is too small for tests on the powered model described in this report.

Lateral-Directional Aerodynamic Data

Figures 67 to 75 show the effect of sideslip angle β on the aerodynamic characteristics for configuration A ($\delta_f = 30^o$, $\delta_s = 35^o$, and fixed forewing). The data are presented for the complete model with horizontal and vertical tail on, the complete model minus the horizontal tail, and the complete model minus horizontal and vertical

tails. The data are presented at three angles of attack (0.6°, 11°, and 21°) for three thrust coefficients (0, ≈3.4, and ≈8.0).

The positive dihedral effect $-C_{l_\beta}$ increased with power on all three configurations at angles of attack of 0.6° and 11°; whereas, the directional stability C_{n_β} for the complete model and the complete model minus the horizontal tail reduced with power but did not become unstable. When the vertical tail was removed, the model was directionally unstable at all thrust coefficients as would be expected. The side-force slope at these test conditions also increased with increasing power as expected, due to the inlet effect.

At an angle of attack of 21°, the rolling moment indicates positive dihedral effect with power off for angles of sideslip from -25° to 0°, where it breaks neutral. However, negative dihedral effect is exhibited at small negative sideslip angles (-5° to 0°) with power on. At small positive angles of sideslip (0° to 5°), positive dihedral effect is exhibited with the power on. Also at an angle of attack of 21°, the model was directionally unstable with power off but was neutrally stable or only slightly unstable with power on.

The sideslip derivatives are summarized for small sideslip angles in figure 76. These data show that at angles of attack of 0.6° and 11° configuration A ($\delta_f = 30°$, $\delta_s = 35°$, and fixed forewing) has positive dihedral effect and is directionally stable. At an angle of attack of 21°, these lateral-directional characteristics demonstrate some instabilities.

CONCLUDING REMARKS

An investigation of the jet-induced interference on a VTOL fighter airplane configuration having three lift engines in the forward fuselage and two deflected lift-cruise engines in the aft fuselage has been conducted in the Langley 300-MPH 7- by 10-foot tunnel, primarily in the 17-foot (5.18-meter) test section. Results of the investigation showed the expected losses in lift and nose-up moments in the transition speed range to be rather small as a result of the counteracting effects of front and rear jets. Comparison of the fuselage-alone and fuselage-plus-wing data indicates that the wing and flap reduced the jet interference effects slightly.

An investigation of horizontal tail height showed that the jet-induced downwash was highest for the low tail position but that the jet-induced longitudinal instability was relatively mild.

The results showed that increasing angle of attack had very little effect on interference lift and drag but that significant increases in interference pitching moment can occur if the horizontal tail is on or below the wing-chord plane. A substantial part of

the nose-up trim change was found to be due to the inlet mass flow for this engine arrangement. Mutual interaction between the lift-engine and lift-cruise-engine exit flows was found to be negligible.

A large positive dihedral effect was induced by the power. The lateral-directional aerodynamic data at angles of attack of 0.6^{o} and 11^{o} showed a positive dihedral effect and directional stability. At an angle of attack of 21^{o} these characteristics showed some instabilities.

A few additional tests which were performed in the 7- by 10-foot (2.13- by 3.05-meter) test section showed that it was too small for tests on this model. The effects of ground proximity were found to be relatively small for this configuration.

Langley Research Center,
National Aeronautics and Space Administration,
Langley Station, Hampton, Va., May 20, 1968,
721-01-00-18-23.

REFERENCES

1. Williams, John; and Wood, Maurice N.: Aerodynamic Interference Effects With Jet-Lift V/Stol Aircraft Under Static and Forward-Speed Conditions. Tech. Rep. No. 66403, Brit. R.A.E., Dec. 1966.

2. Vogler, Raymond D.: Surface Pressure Distributions Induced on a Flat Plate By a Cold Air Jet Issuing Perpendicularly From the Plate and Normal to a Low-Speed Free-Stream Flow. NASA TN D-1629, 1963.

3. Vogler, Raymond D.: Interference Effects of Single and Multiple Round or Slotted Jets on a VTOL Model in Transition. NASA TN D-2380, 1964.

4. Spreemann, Kenneth P.: Investigation of Interference of a Deflected Jet With Free Stream and Ground on Aerodynamic Characteristics of a Semispan Delta-Wing VTOL Model. NASA TN D-915, 1961.

5. Otis, James H., Jr.: Induced Interference Effects on a Four-Jet VTOL Configuration With Various Wing Planforms in the Transition Speed Range, NASA TN D-1400, 1962.

6. Gentry, Garl L.; and Margason, Richard J.: Jet-Induced Lift Losses on VTOL Configurations Hovering In and Out of Ground Effect. NASA TN D-3166, 1966.

7. Vogler, Raymond D.; and Kuhn, Richard E.: Longitudinal and Lateral Stability Characteristics of Two Four-Jet VTOL Models in the Transition Speed Range. NASA TM X-1092, 1965.

8. Mechtly, E. A.: The International System of Units – Physical Constants and Conversion Factors. NASA SP-7012, 1964.

9. Margason, Richard J.; and Gentry, Garl L.: Static Calibration of an Ejector Unit for Simulation of Jet Engines in Small-Scale Wind-Tunnel Models. NASA TN D-3867, 1967.

10. Turner, Thomas R.: Endless-Belt Technique for Ground Simulation. Conference on V/STOL and STOL Aircraft, NASA SP-116, 1966, pp. 435-446.

11. Ray, Edward J.; and Taylor, Robert T.: Effect of Configuration Variables on the Subsonic Longitudinal Stability Characteristics of a High-Tail Transport Configuration. NASA TM X-1165, 1965.

12. Margason, Richard J.: Jet-Induced Effects in Transition Flight. Conference on V/STOL and STOL Aircraft, NASA SP-116, 1966, pp. 177-189.

13. Vogler, Raymond D.: Ground Effects on Single- and Multiple-Jet VTOL Models at Transition Speeds Over Stationary and Moving Ground Planes. NASA TN D-3213, 1966.

14. Heyson, Harry H.; and Grunwald, Kalman J.: Wind-Tunnel Boundary Interference for V/STOL Testing. Conference on V/STOL and STOL Aircraft, NASA SP-116, 1966, pp. 409-434.

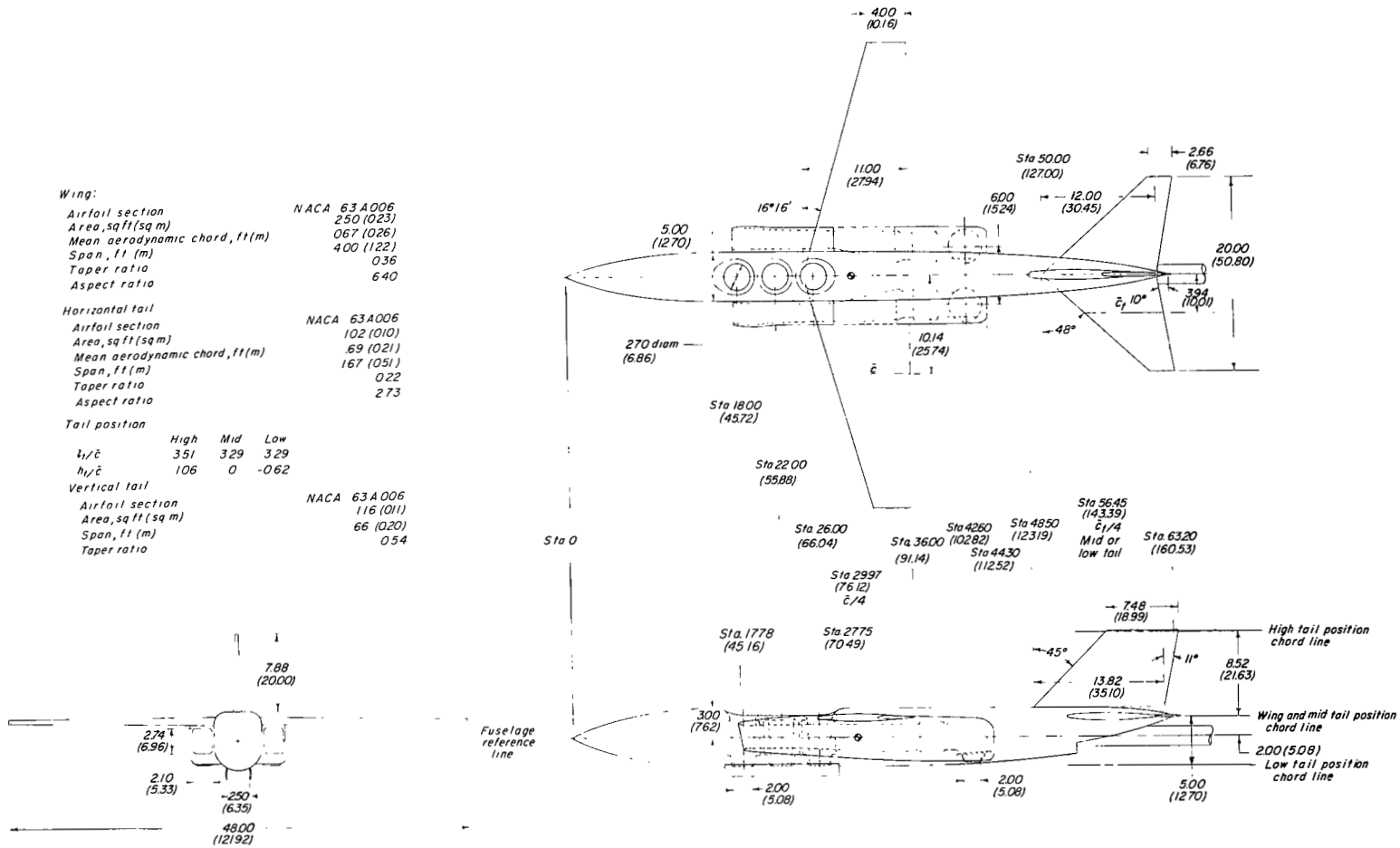

Wing:

Airfoil section	NACA 63A006
Area, sq ft (sq m)	2.50 (.023)
Mean aerodynamic chord, ft (m)	.067 (.026)
Span, ft (m)	4.00 (1.22)
Taper ratio	.036
Aspect ratio	6.40

Horizontal tail

Airfoil section	NACA 63A006
Area, sq ft (sq m)	.102 (.010)
Mean aerodynamic chord, ft (m)	.69 (.021)
Span, ft (m)	1.67 (.051)
Taper ratio	.022
Aspect ratio	2.73

Tail position

	High	Mid	Low
$l_t/\bar{c}$	3.51	3.29	3.29
$h_t/\bar{c}$	1.06	0	-.062

Vertical tail

Airfoil section	NACA 63A006
Area, sq ft (sq m)	.116 (.011)
Span, ft (m)	.66 (.020)
Taper ratio	0.54

(a) Three-view drawing of configuration C ($\delta_f = 0^0$) and table of geometric characteristics.

Figure 1.- Details of models. All dimensions are in inches (centimeters) unless otherwise noted.

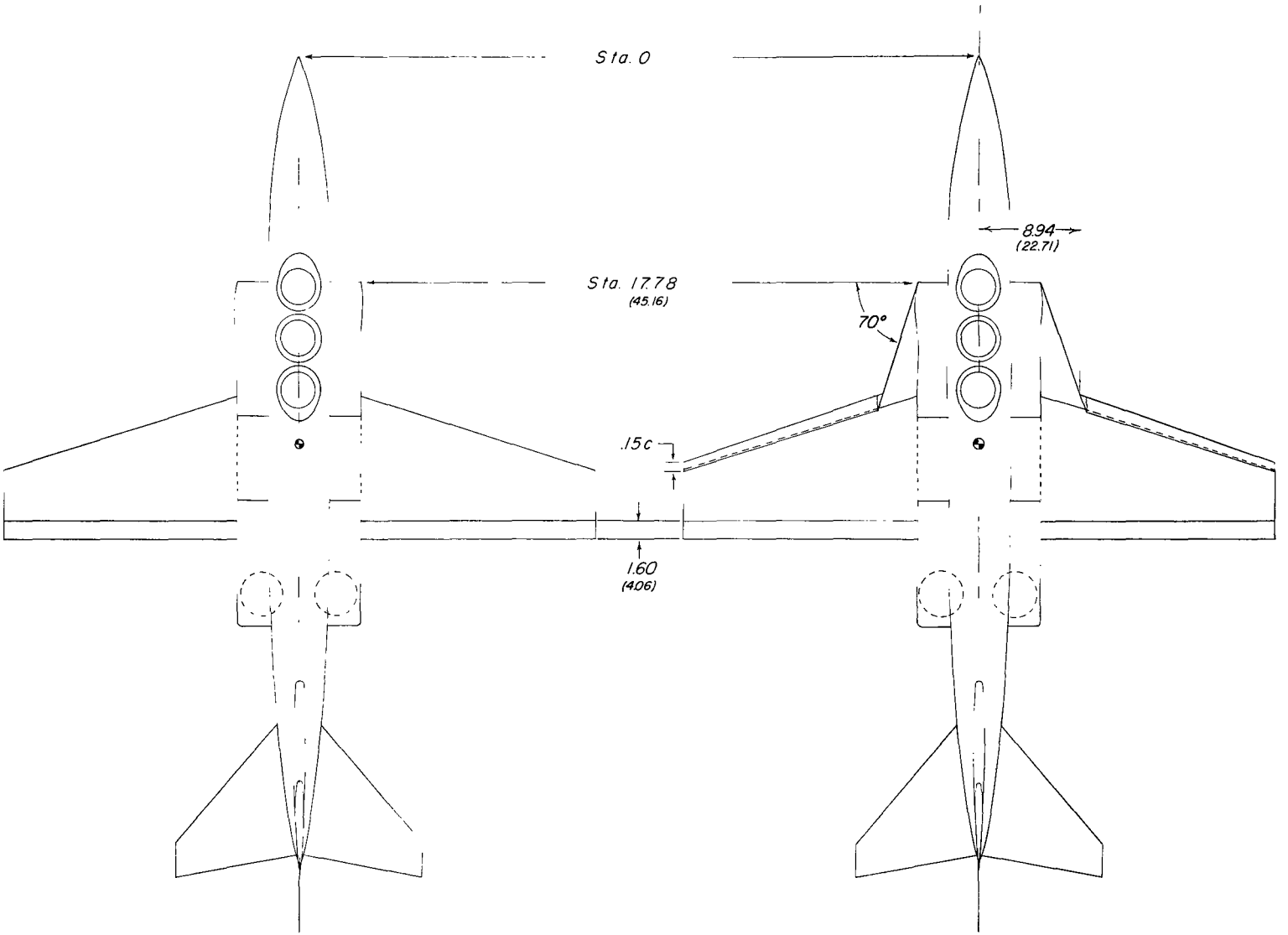

(b) Top view of configuration A ($\delta_f = 30^0$, $\delta_s = 35^0$, fixed forewing) and configuration B ($\delta_f = 30^0$).

Figure 1.- Continued.

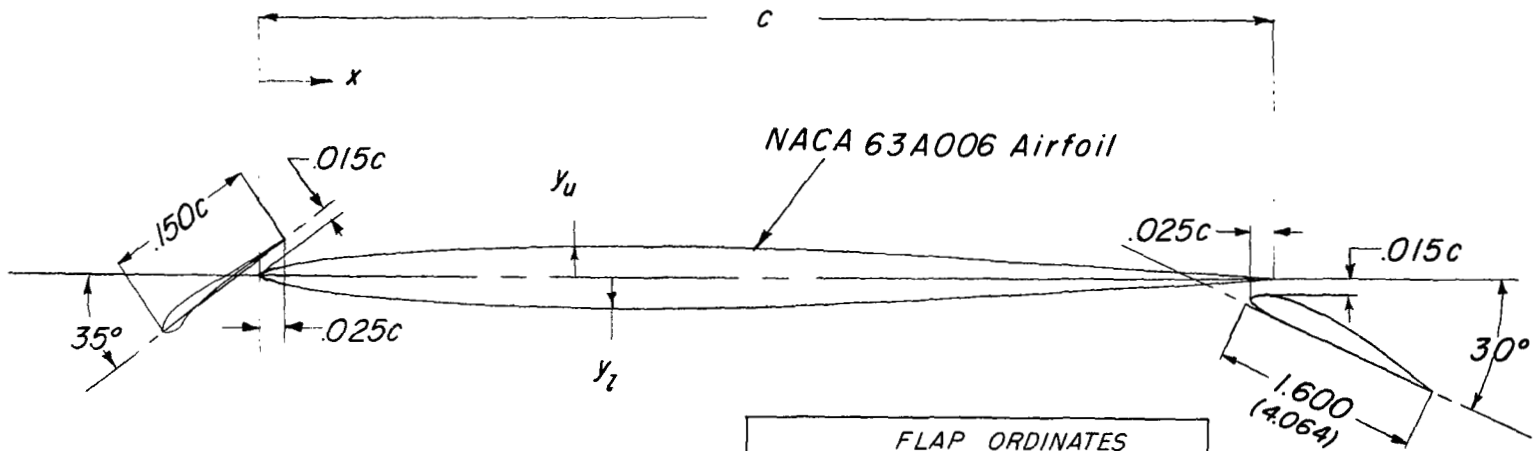

SLAT ORDINATES		
x/c	y_u/c	y_l/c
0	0	0
.0100	.0308	-.0282
.0200	.0410	-.0411
.0500	.0592	-.0538
.0750	.0746	-.0588
.1000	.0815	-.0565
.1500	.0900	-.0410
.2000	.0923	-.0256
.3000	.0923	0
.4000	.0873	.0205
.5000	.0846	.0258
.6000	.0719	.0282
.7000	.0562	.0258
.8000	.0462	.0154
.9000	.0282	.0103
1.0000	.0103	0

FLAP ORDINATES		
x/c	y_u/c	y_l/c
0	.0350	-.0350
.0125	.0544	-.0194
.0250	.0650	-.0150
.0500	.0788	-.0094
.0750	.0888	-.0063
.1000	.0950	-.0013
.1500	.1069	-.0003
.2000	.1138	0
.3000	.1169	0
.4000	.1138	0
.5000	.1050	0
.6000	.0913	0
.7000	.0738	0
.8000	.0525	0
.9000	.0281	0
.9500	.0150	0
1.0000	.0013	0

(c) Section view at mean aerodynamic chord of wing (NACA 63A006 airfoil), slat, and flap for configuration A ($\delta_f = 30^0$, $\delta_s = 35^0$, fixed forewing) and ordinates for slat and flap.

Figure 1.- Concluded.

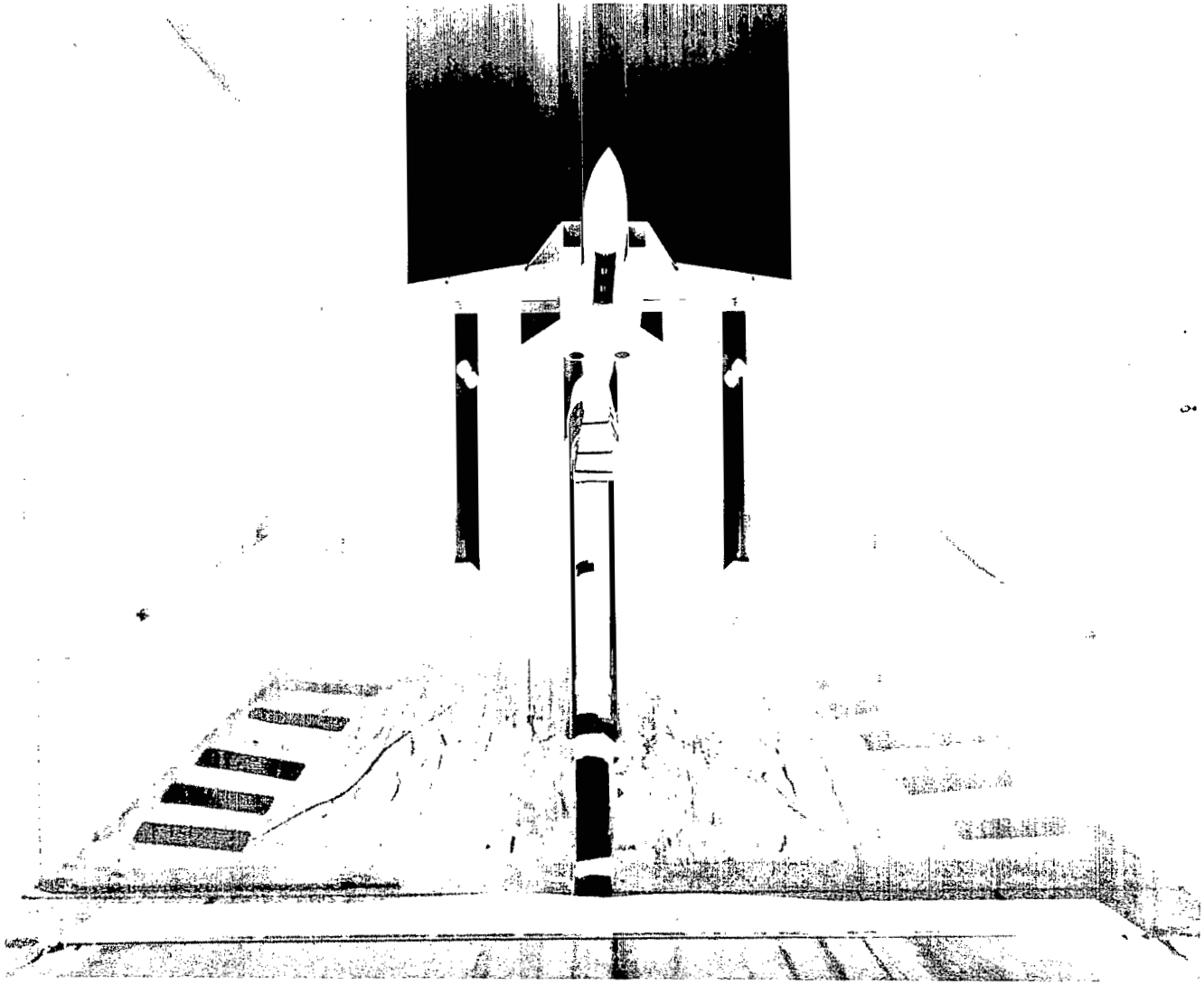

(a) Lower quarter front view of configuration A ($\delta_f = 30^0$, $\delta_s = 35^0$, fixed forewing). L-66-1391

Figure 2.- Photographs of models in 17-foot (5.18-meter) test section of Langley 300-MPH 7- by 10-foot tunnel.

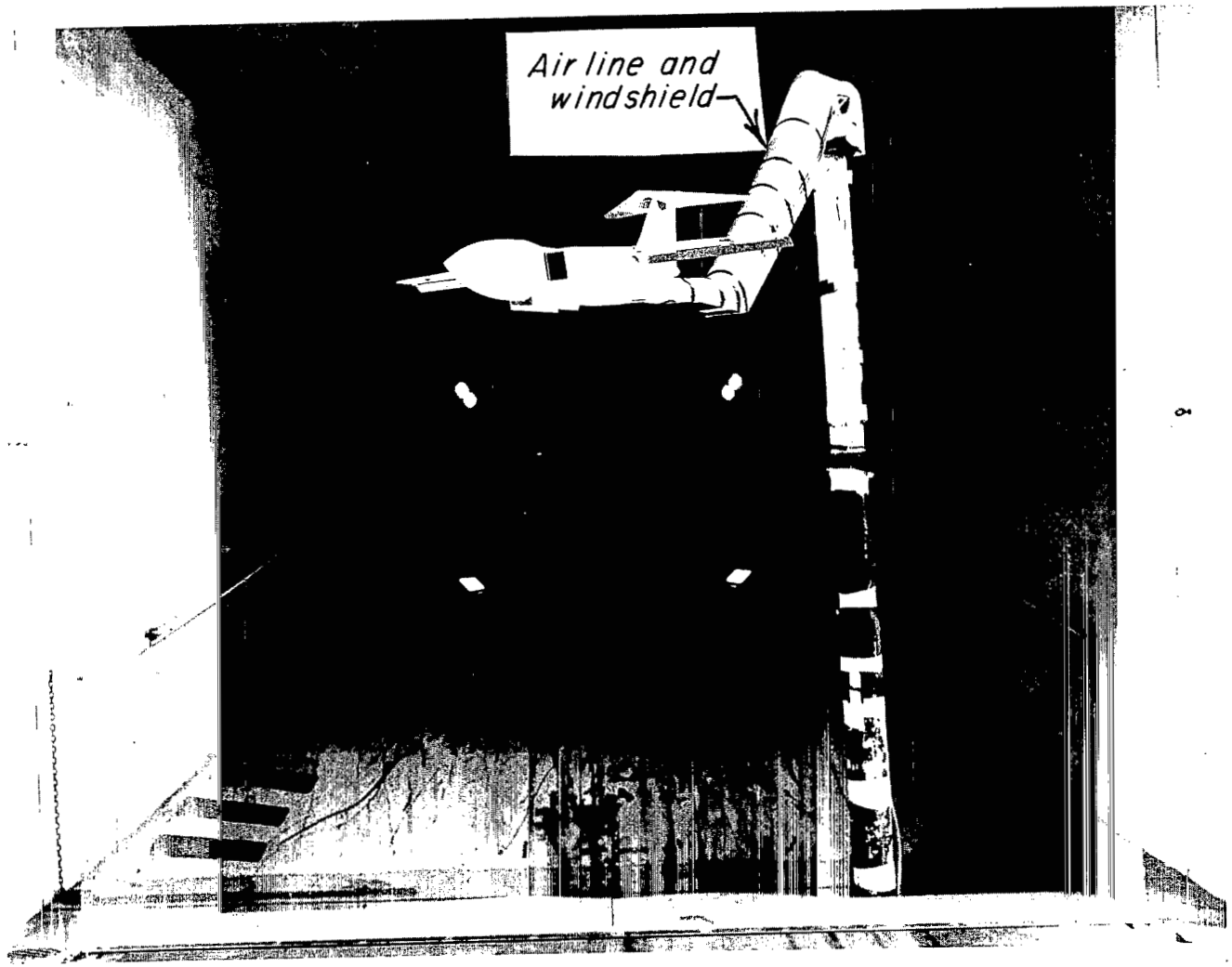

(b) Three-quarter side view of configuration A ($\delta_f = 30^0$, $\delta_s = 35^0$, fixed forewing) with horizontal tail in high position. L-66-1393

Figure 2.- Continued.

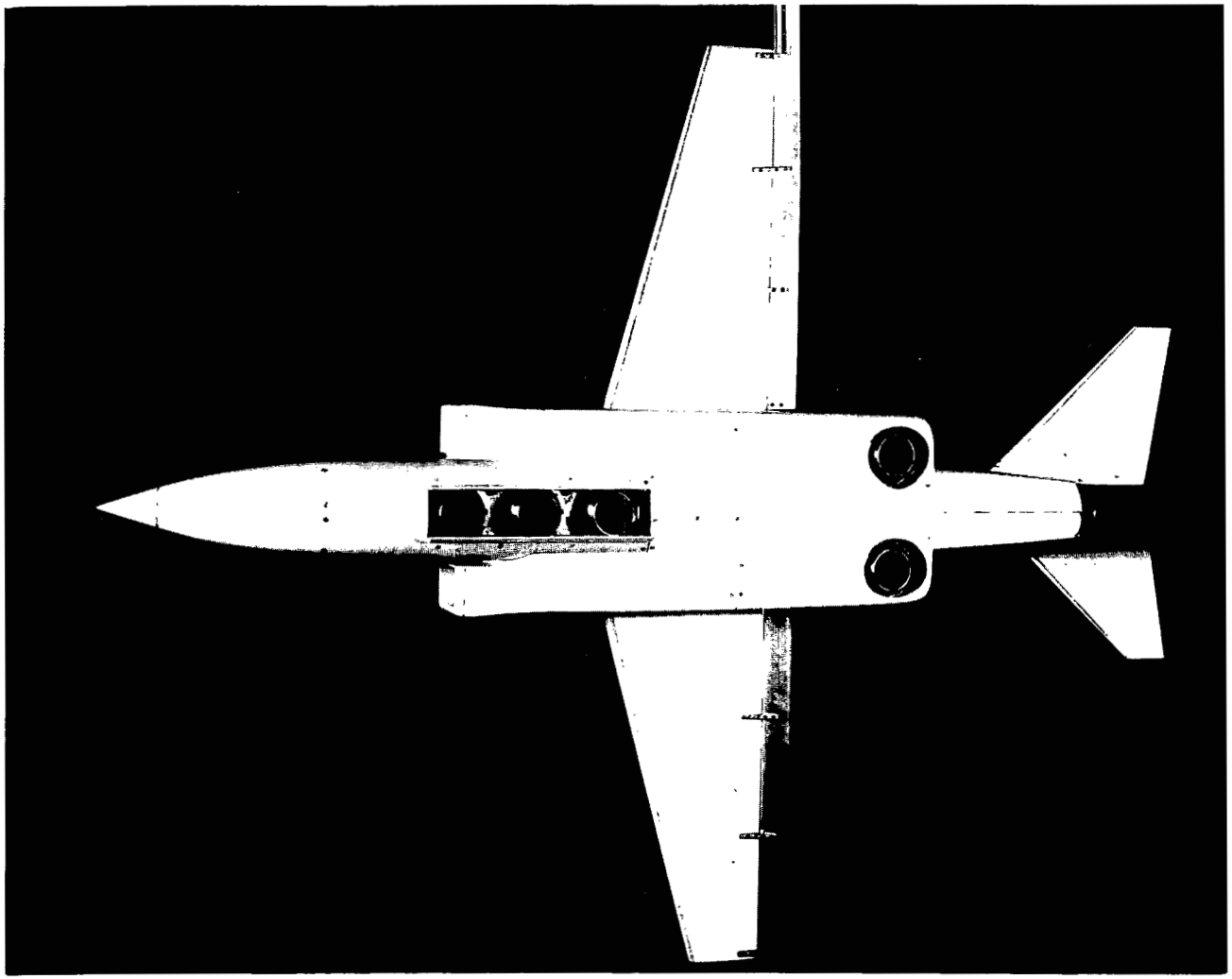

(c) Bottom view of configuration B ($\delta_f = 30^0$) with horizontal tail in mid position. L-65-7360

Figure 2.- Concluded.

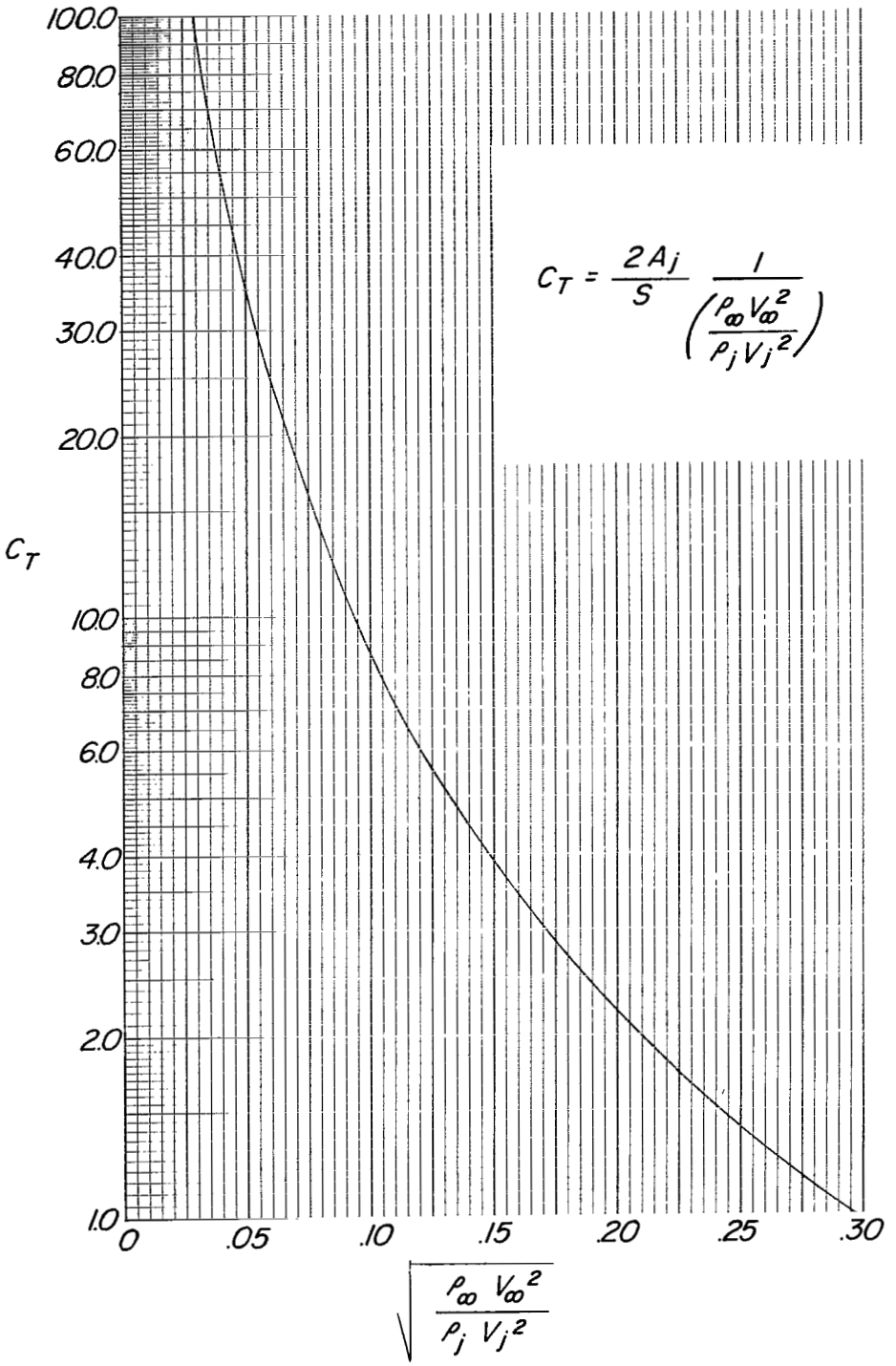

Figure 3.- Thrust coefficient as a function of effective velocity ratio.

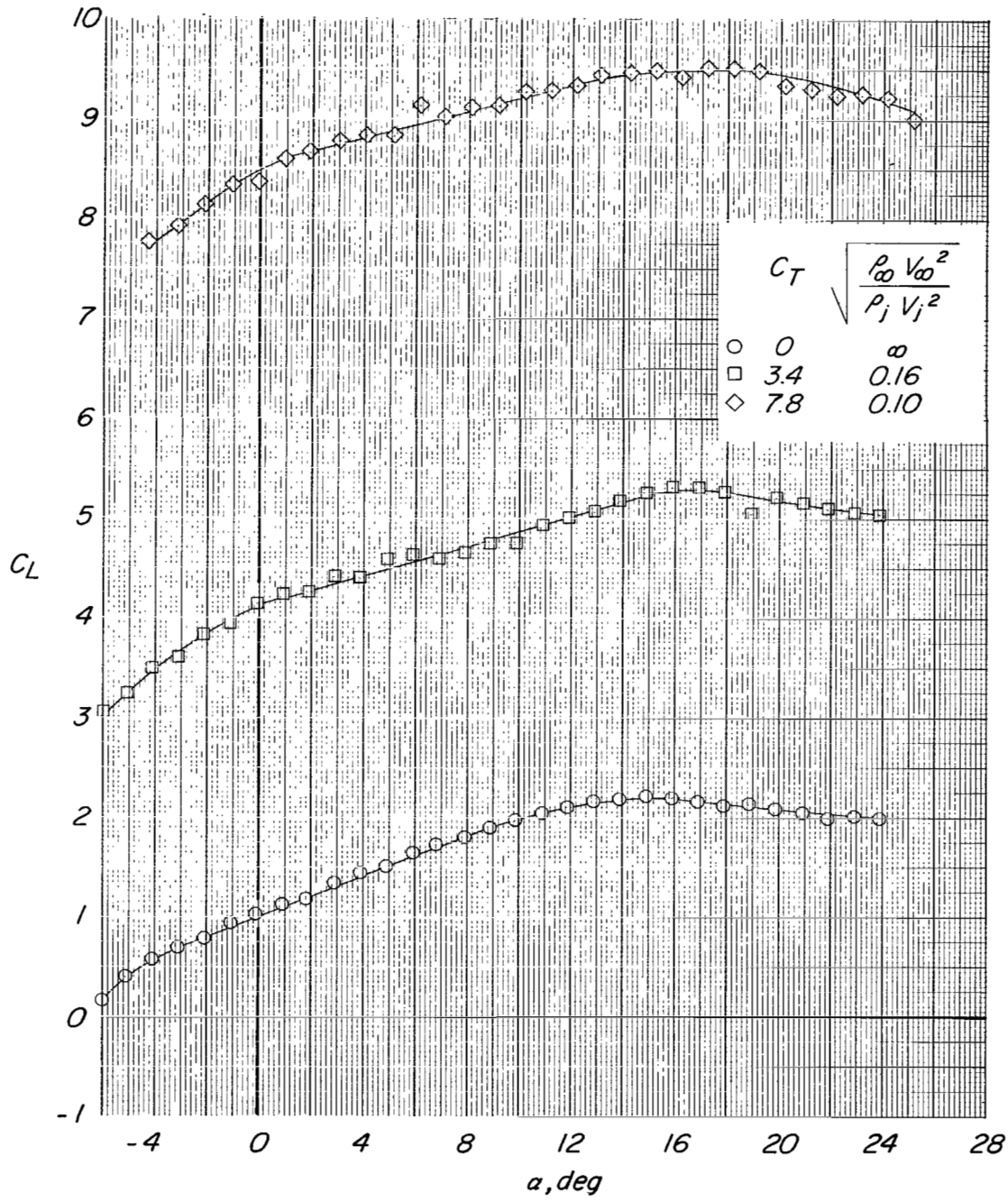

(a) Variation of C_L with α.

Figure 4.- Effect of thrust coefficient on longitudinal aerodynamic characteristics for configuration A ($\delta_f = 30^0$, $\delta_s = 35^0$, fixed forewing) with horizontal tail off.

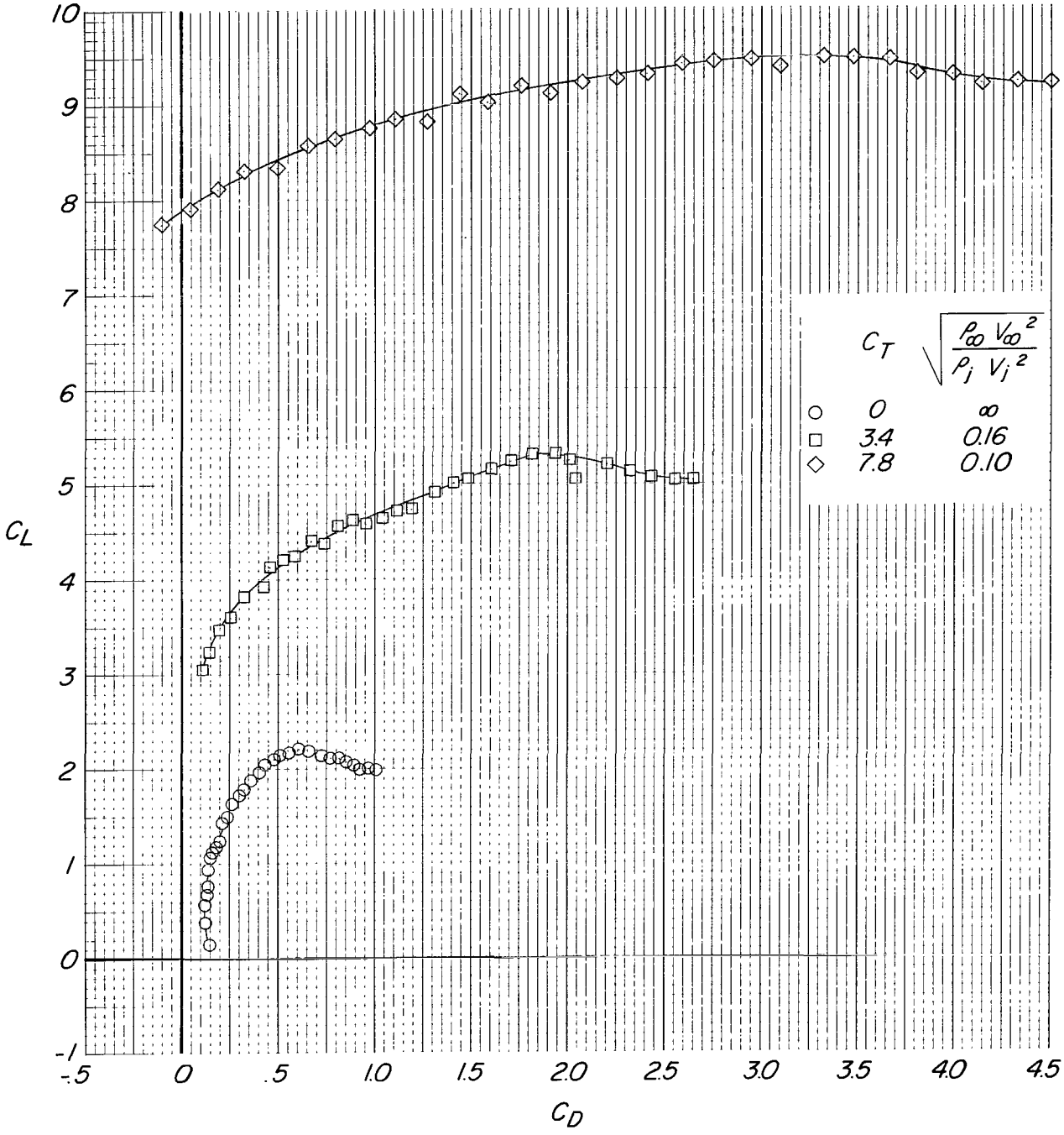

(b) Variation of C_L with C_D.

Figure 4.- Continued.

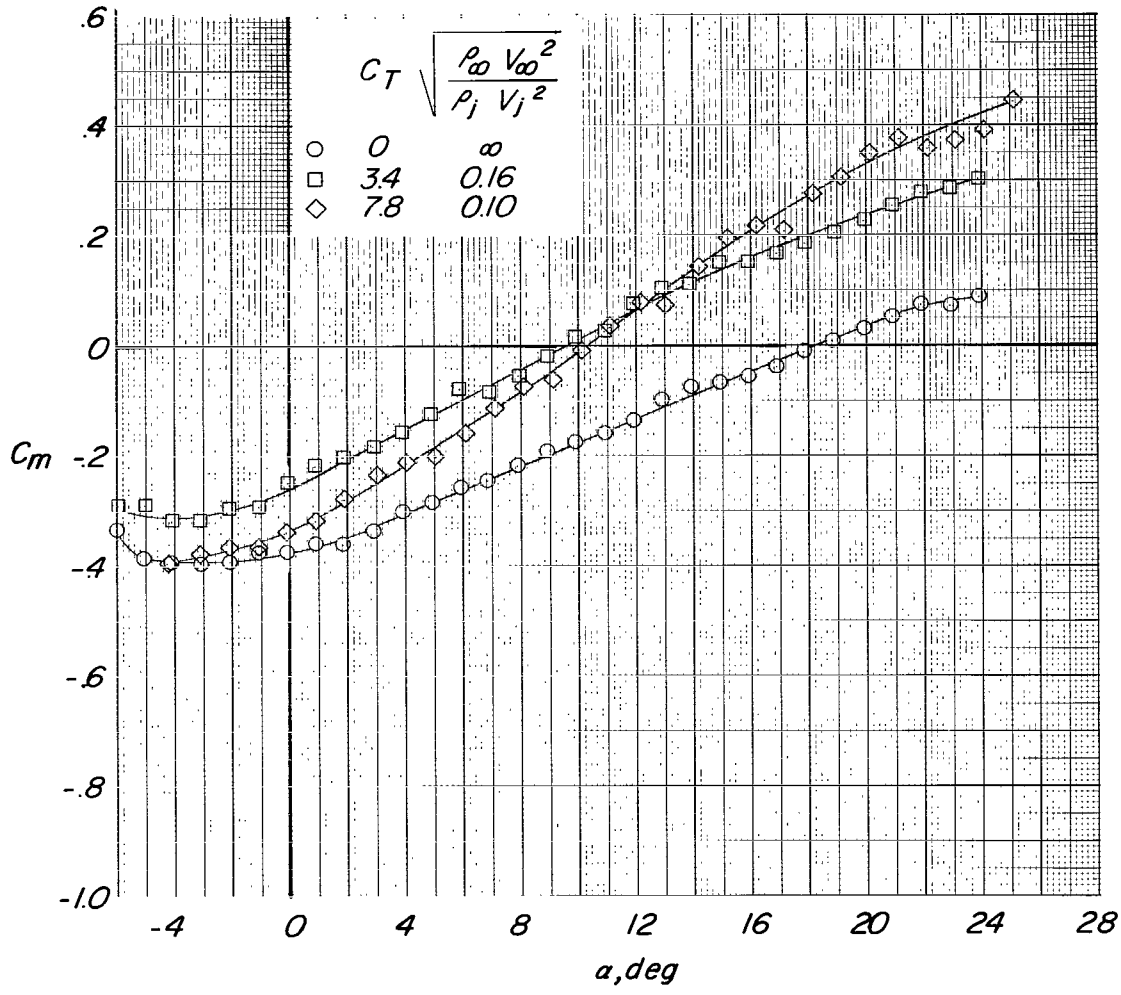

(c) Variation of C_m with α.

Figure 4.- Continued.

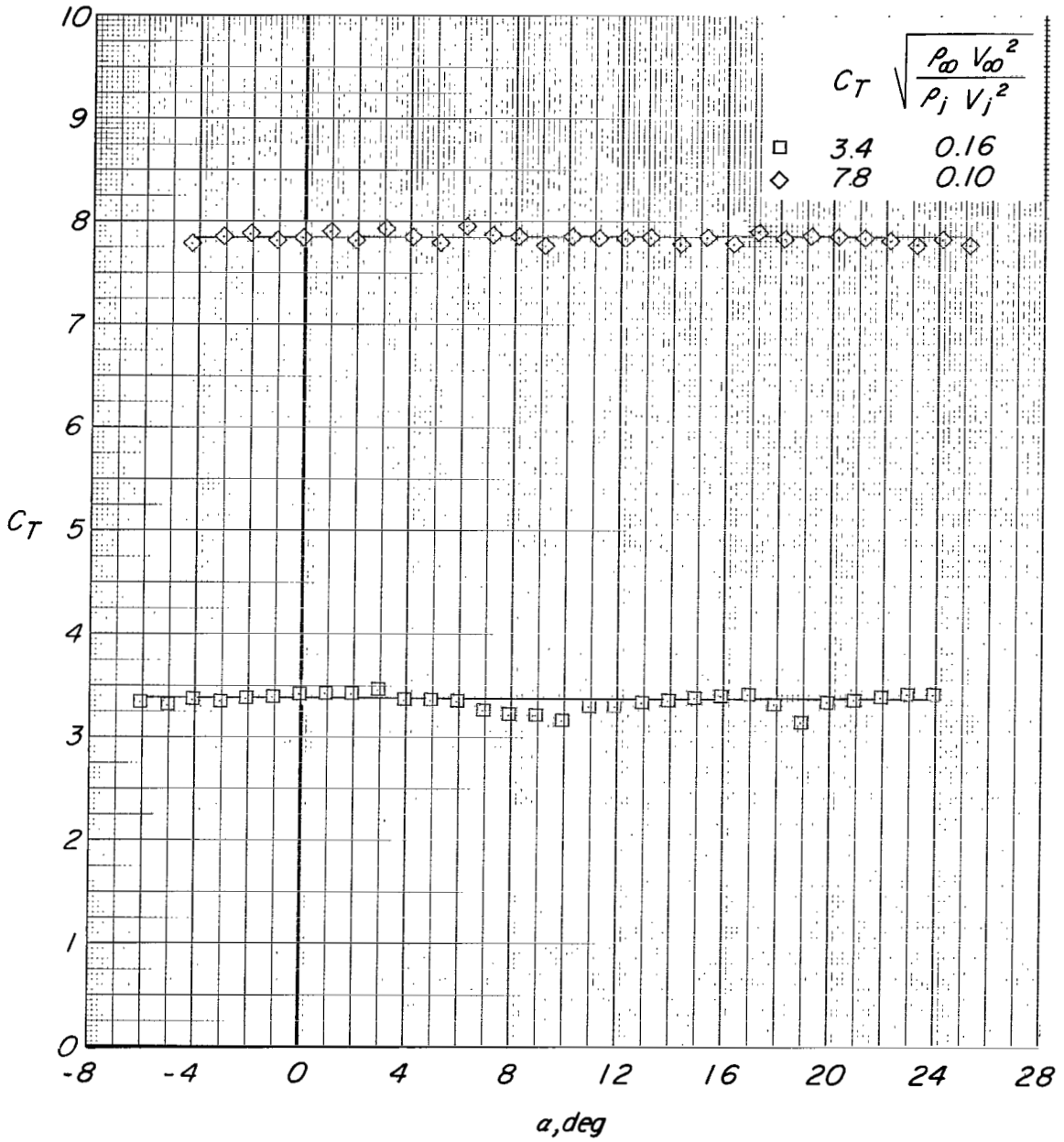

(d) Variation of C_T with α.

Figure 4.- Concluded.

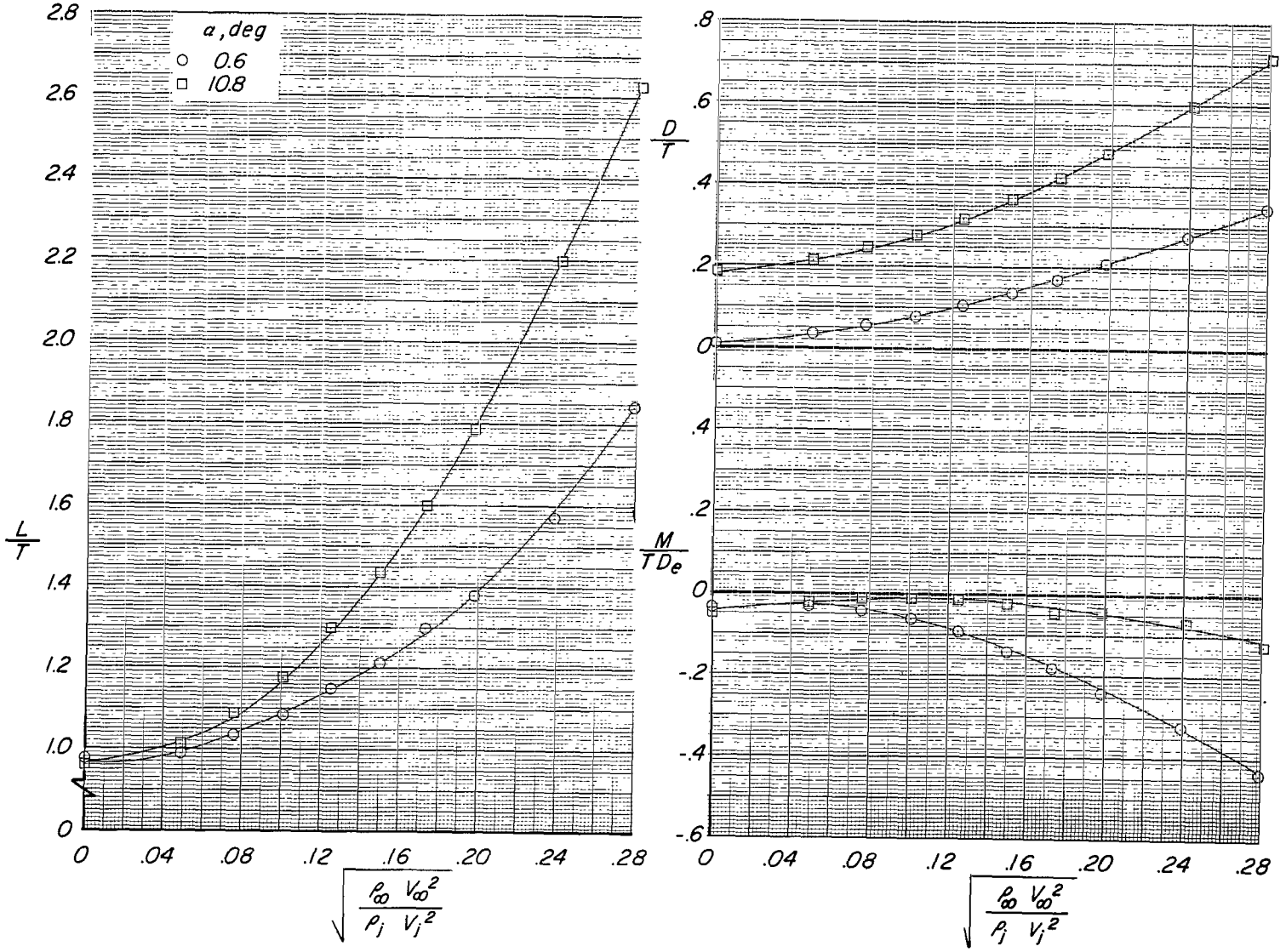

Figure 5.- Effect of variation of effective velocity ratio on longitudinal aerodynamic characteristics for configuration A ($\delta_f = 30^0$, $\delta_s = 35^0$, fixed forewing) with horizontal tail off.

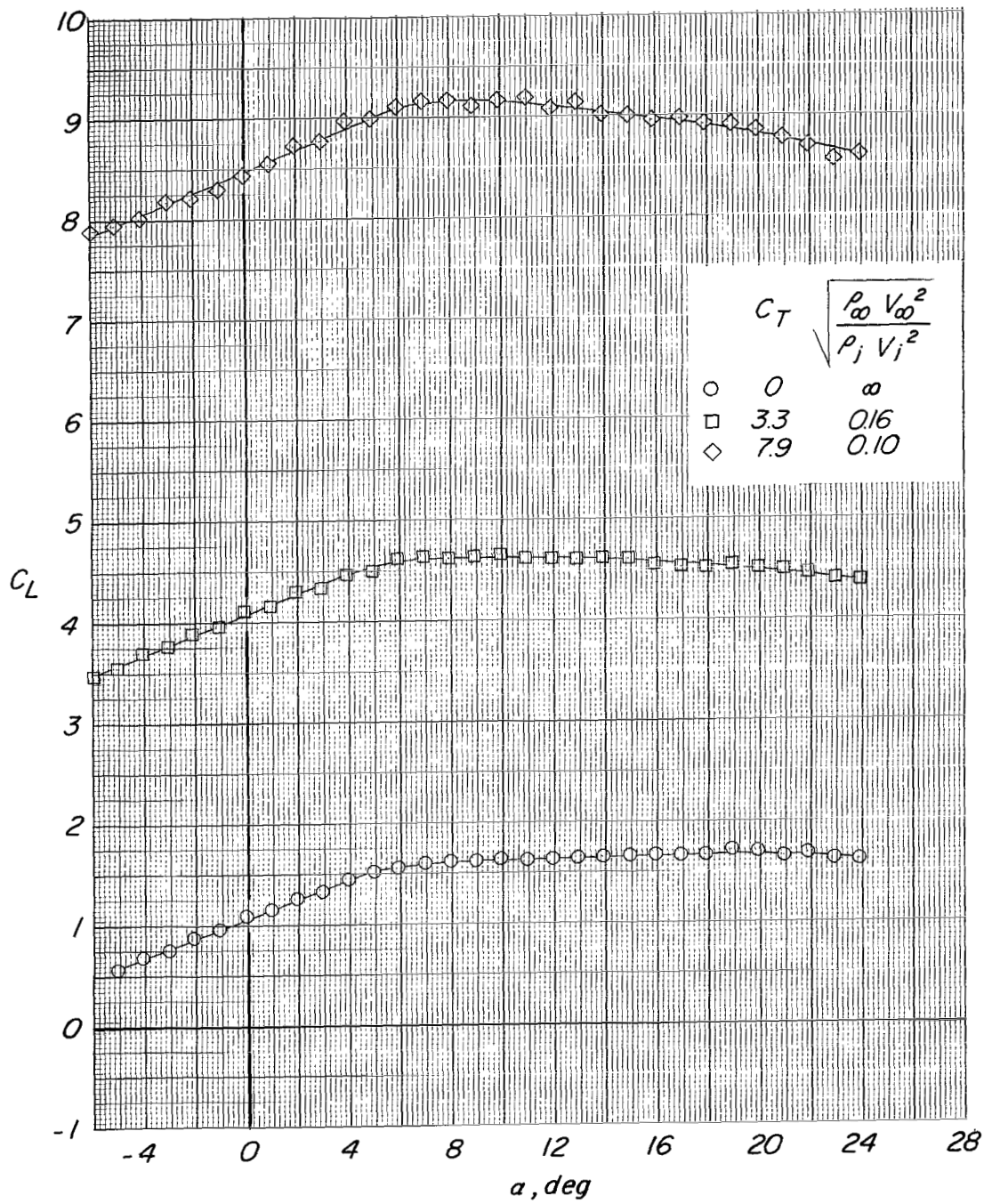

(a) Variation of C_L with α.

Figure 6.- Effect of thrust coefficient on longitudinal aerodynamic characteristics for configuration B ($\delta_f = 30^0$) with horizontal tail off.

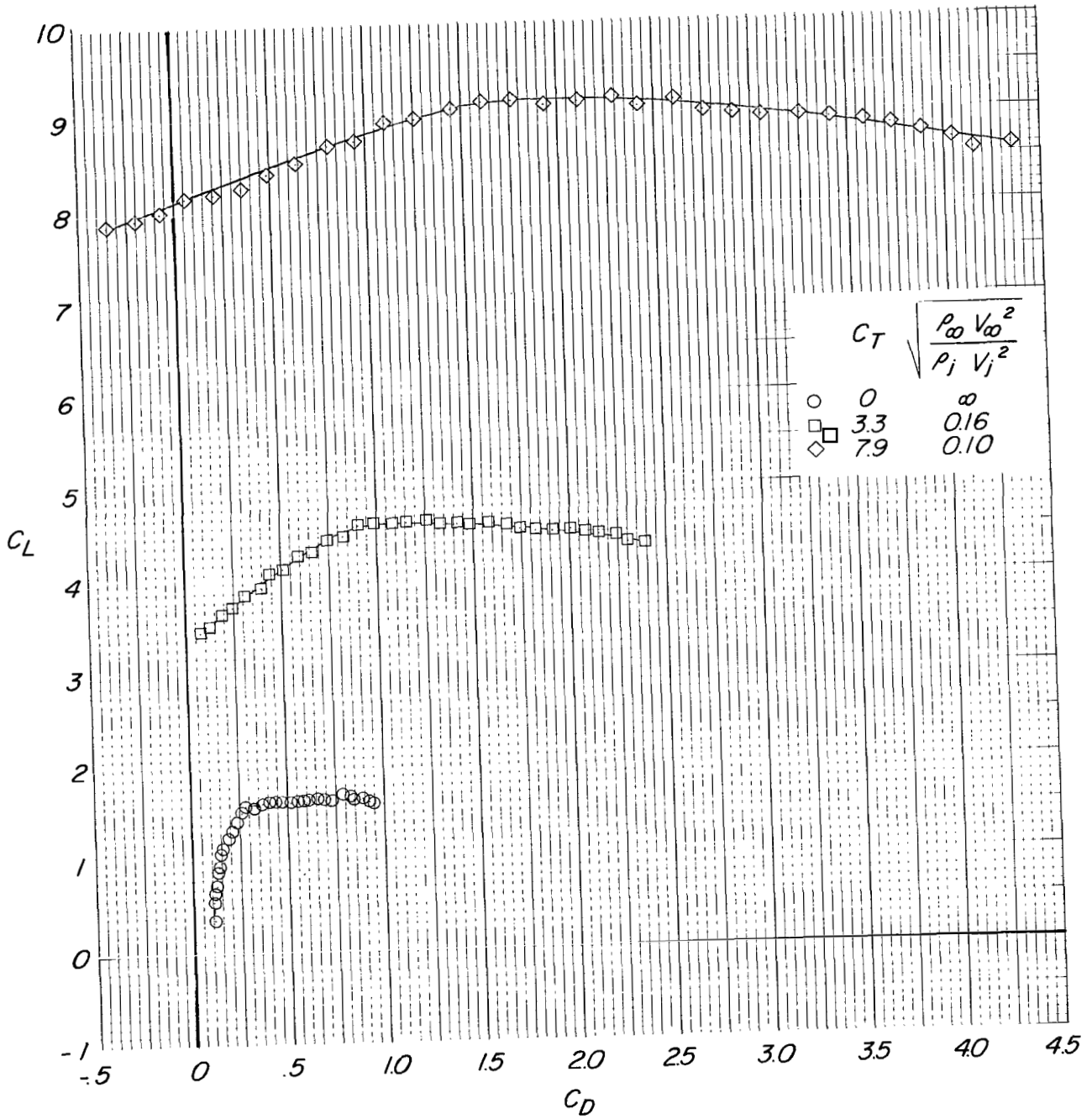

(b) Variation of C_L with C_D.

Figure 6.- Continued.

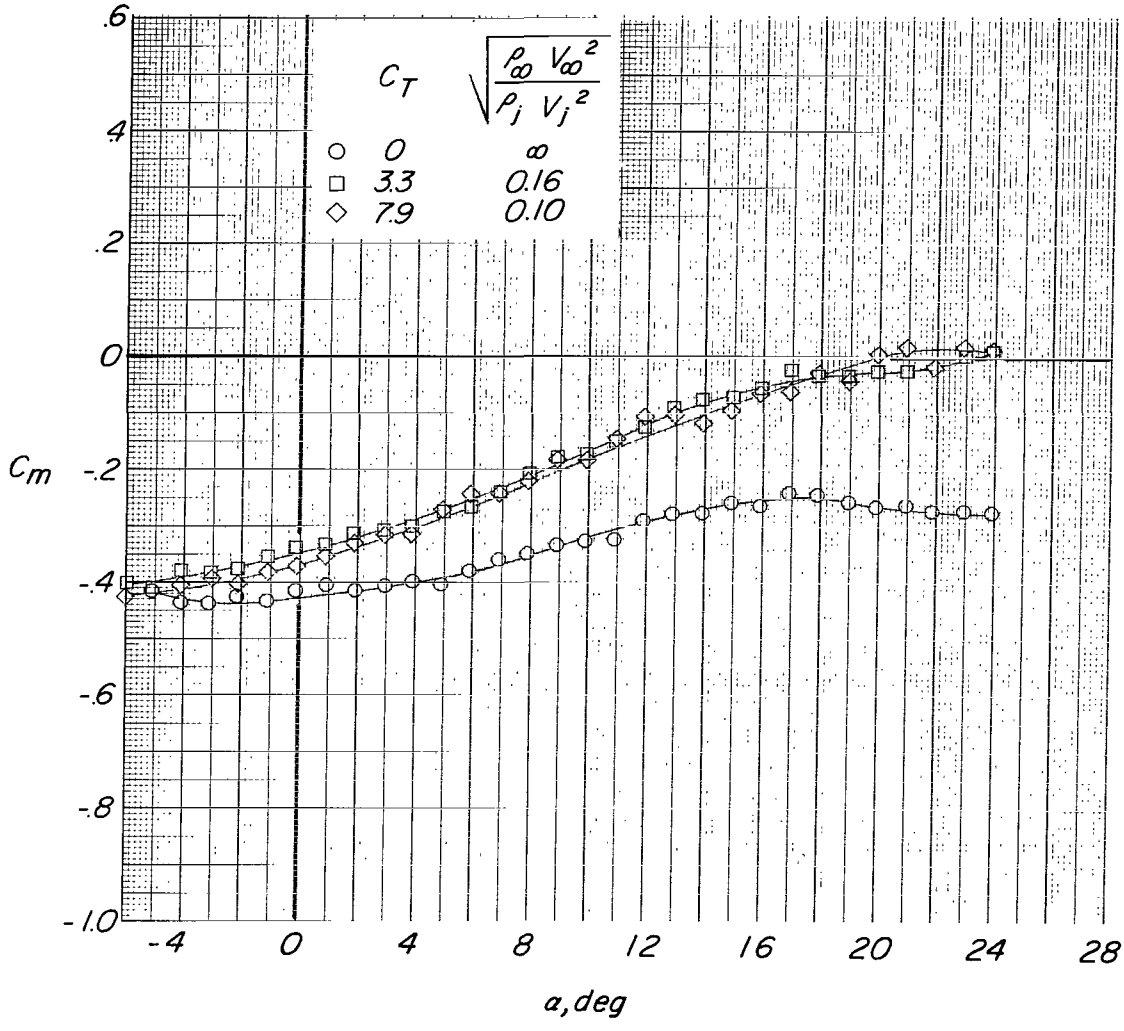

(c) Variation of C_m with α.

Figure 6.- Continued.

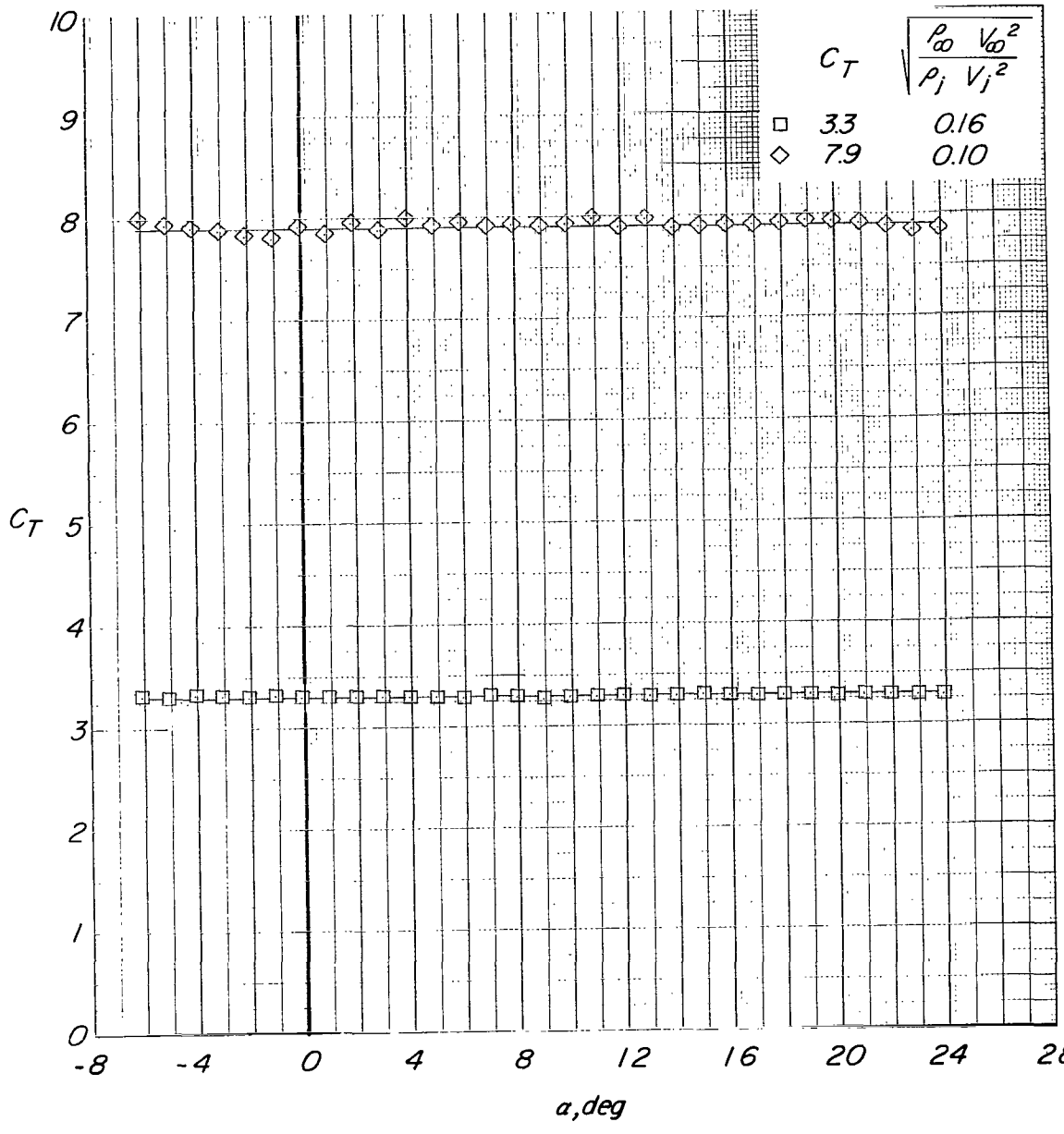

(d) Variation of C_T with α.

Figure 6.- Concluded.

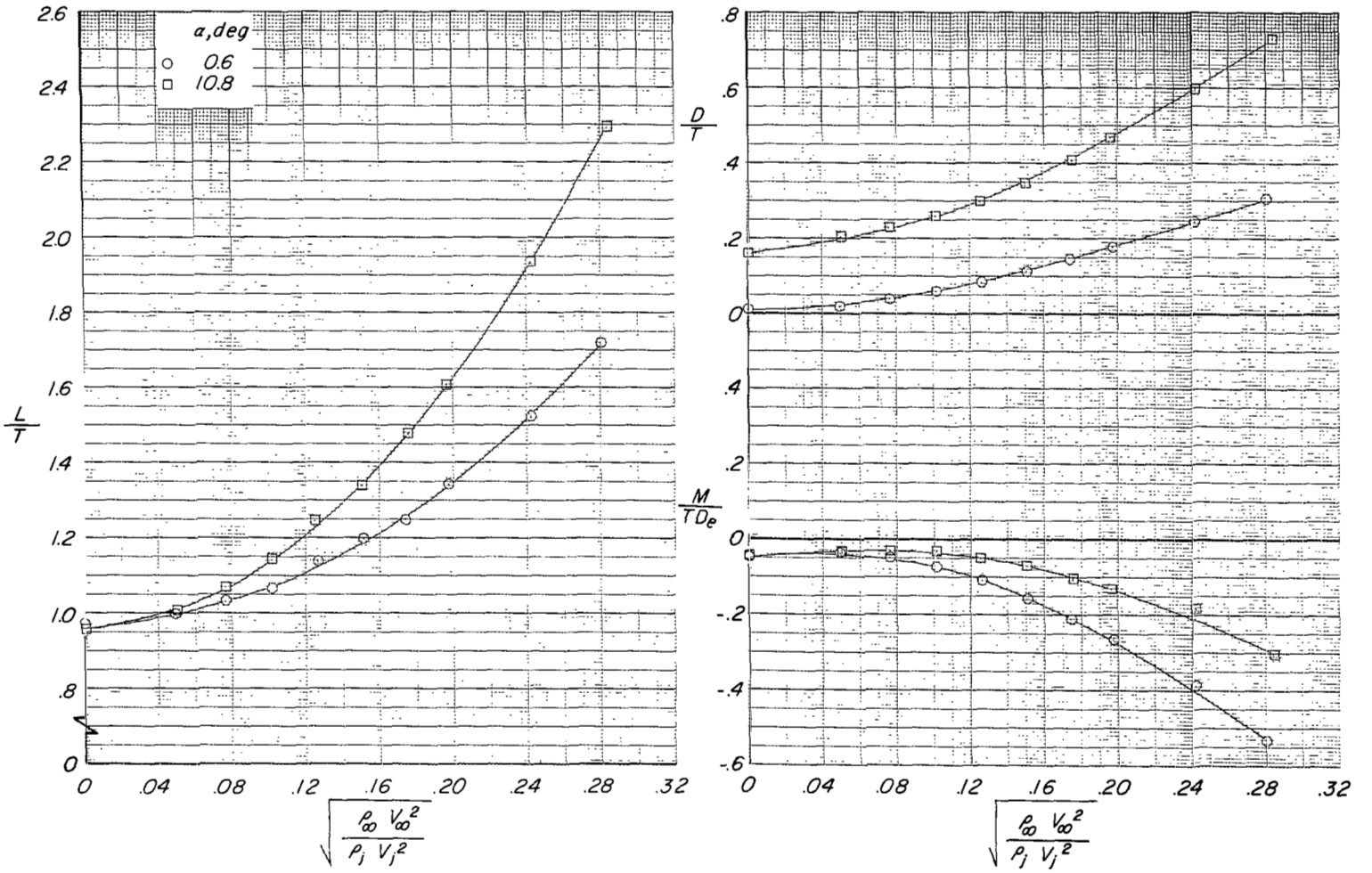

Figure 7.- Effect of variation of effective velocity ratio on longitudinal aerodynamic characteristics for configuration B ($\delta_f = 30^0$) with horizontal tail off.

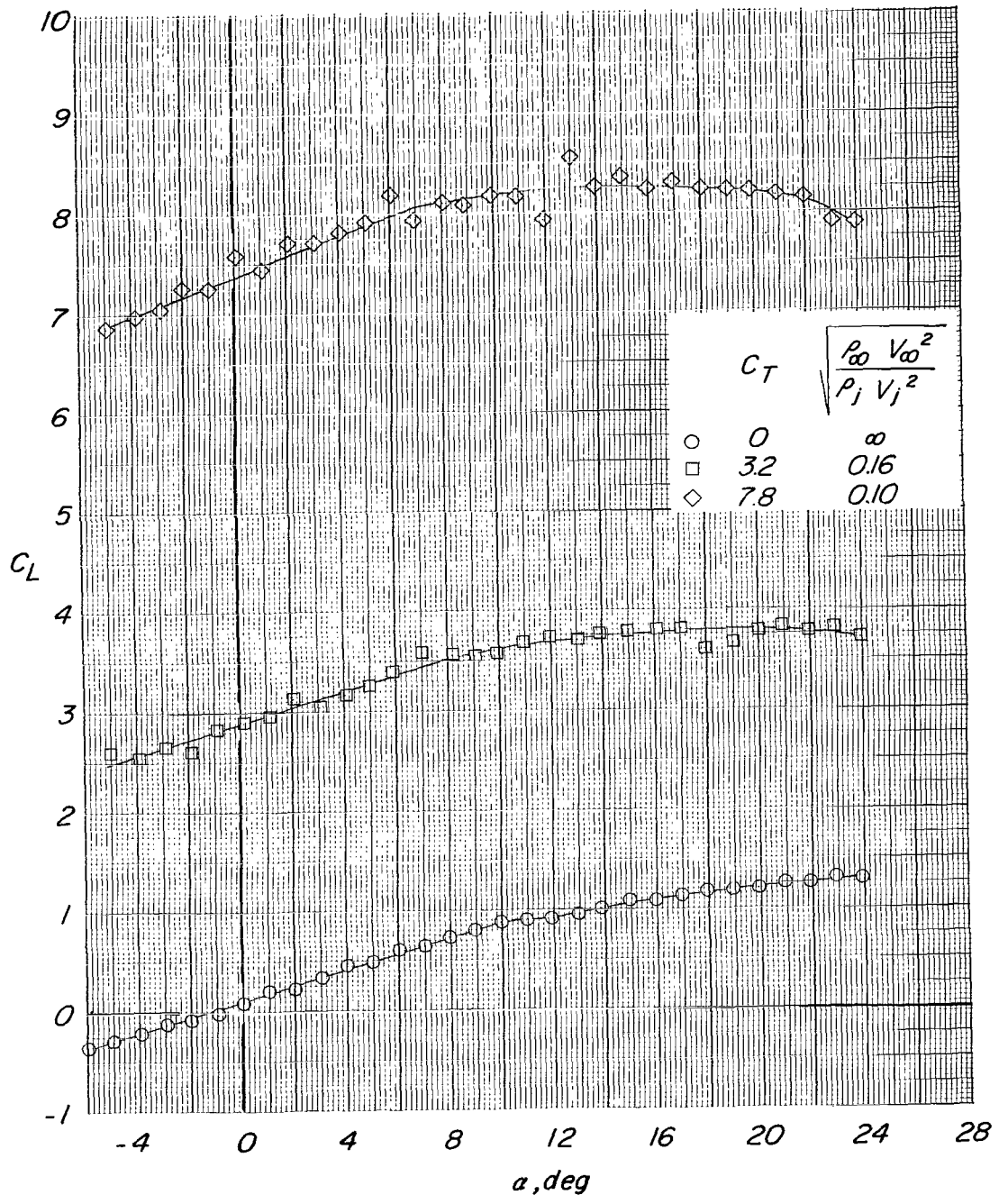

(a) Variation of C_L with α.

Figure 8.- Effect of thrust coefficient on longitudinal aerodynamic characteristics for configuration C ($\delta_f = 0^0$) with horizontal tail off.

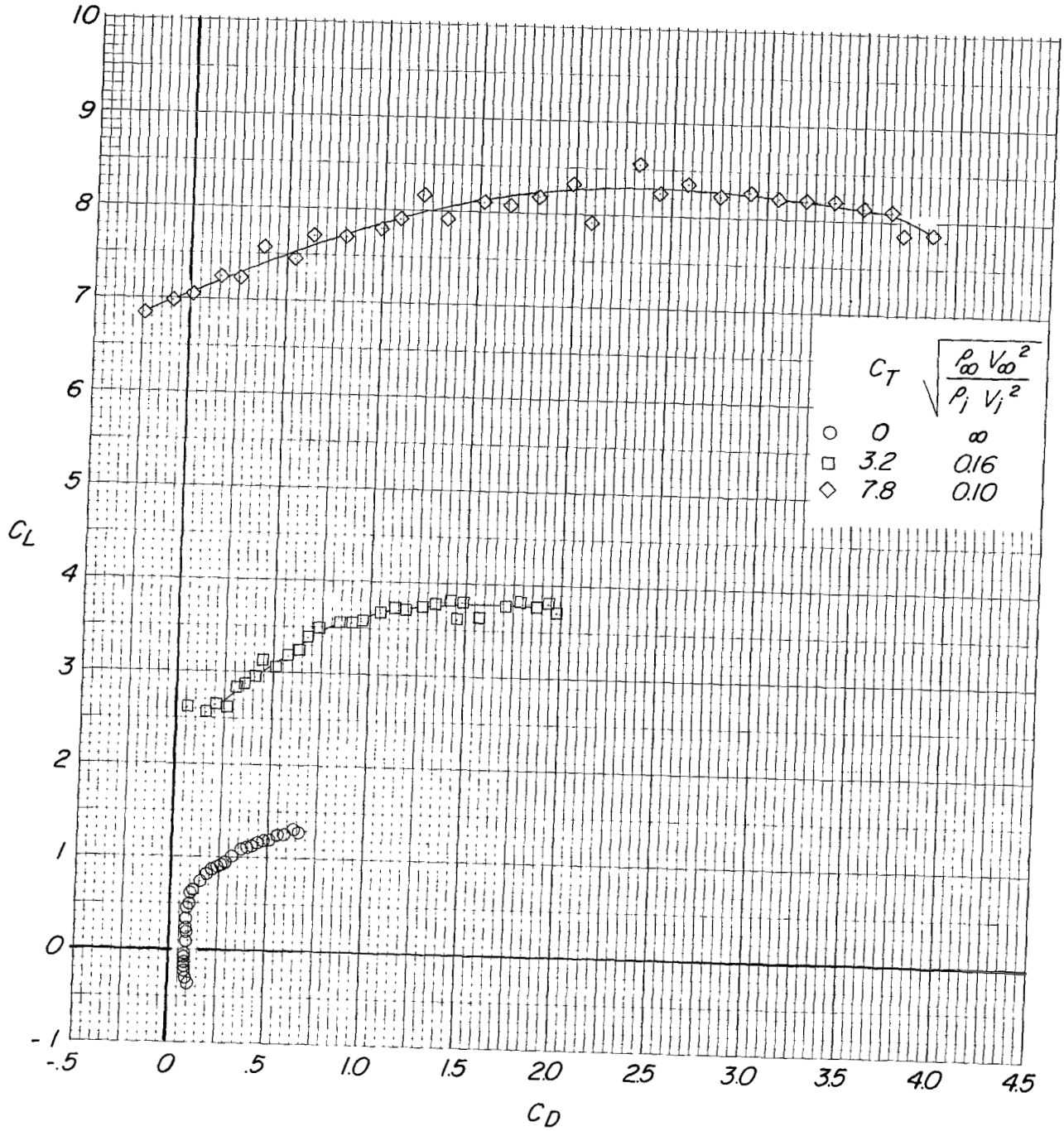

(b) Variation of C_L with C_D.

Figure 8.- Continued.

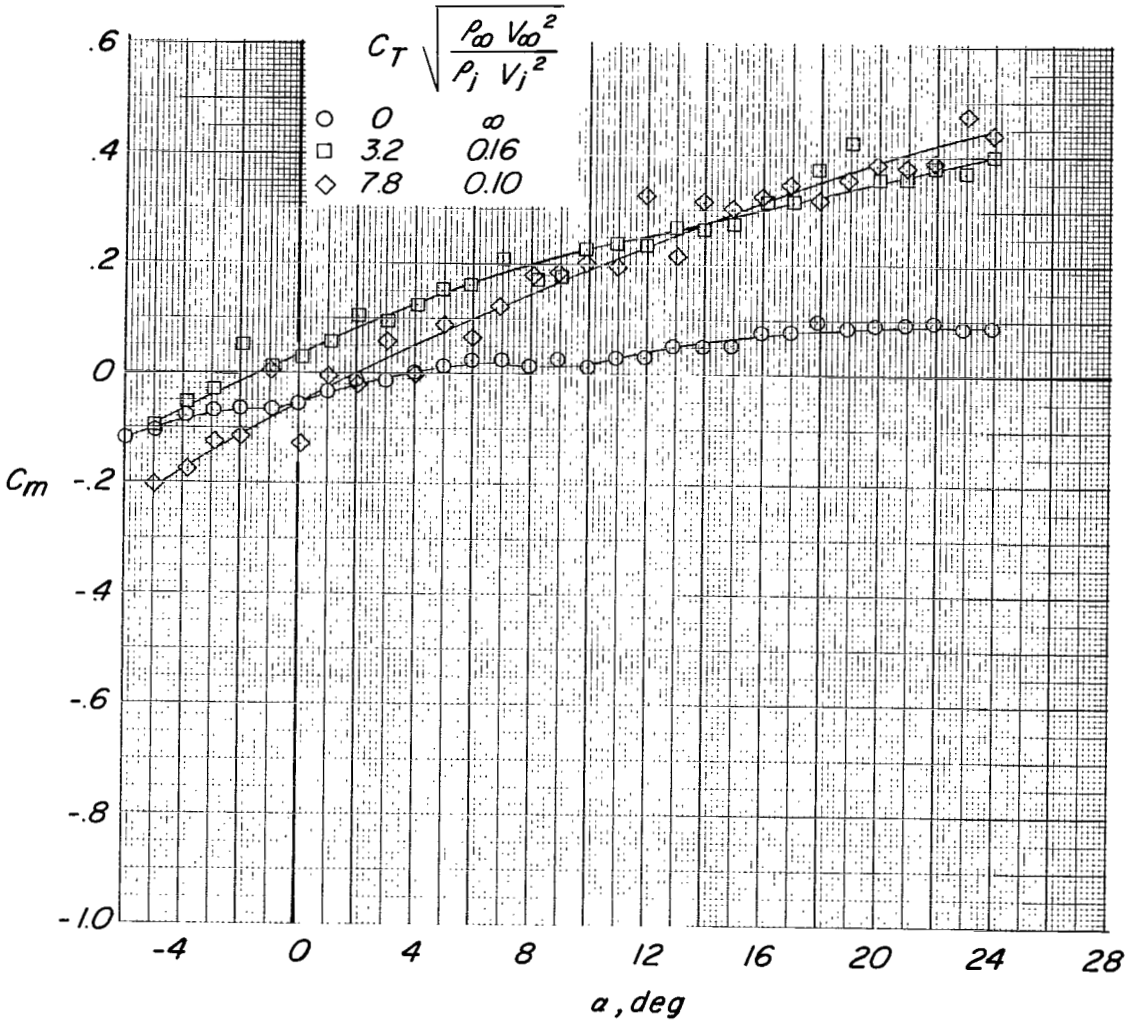

(c) Variation of C_m with α.

Figure 8.- Continued.

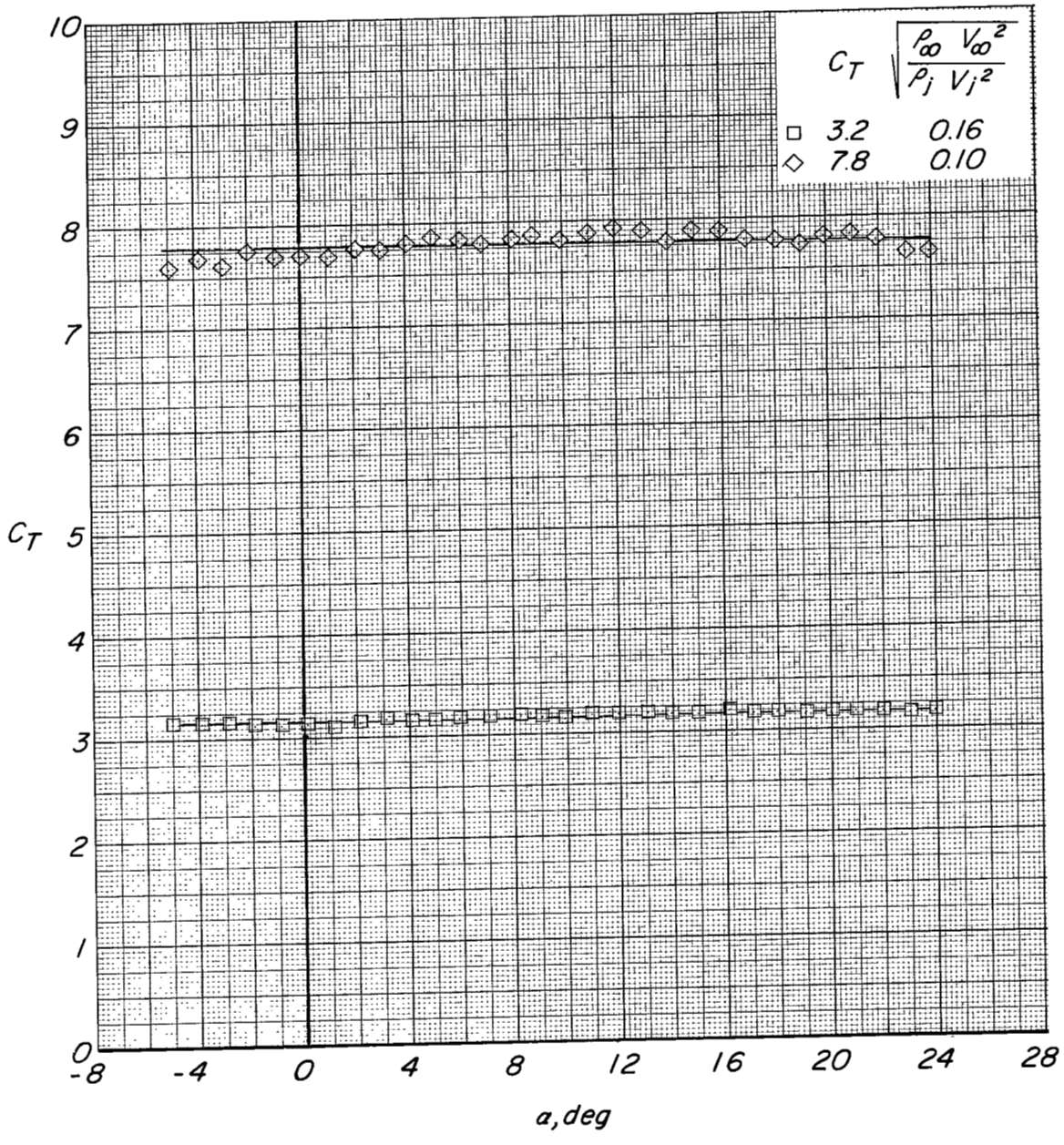

(d) Variation of C_T with α.

Figure 8.- Concluded.

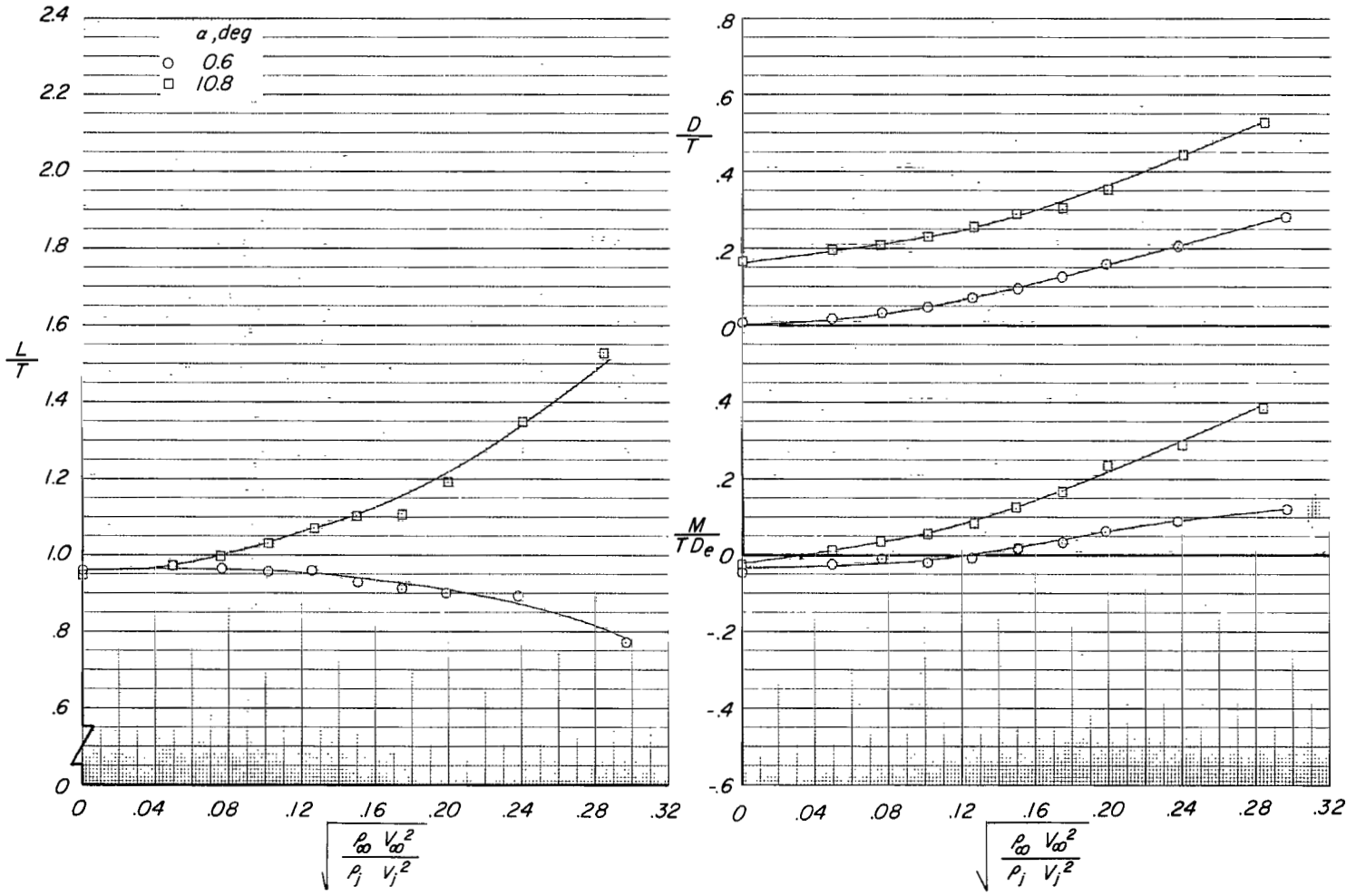

Figure 9.- Effect of variation of effective velocity ratio on longitudinal aerodynamic characteristics for configuration C ($\delta_f = 0^0$) with horizontal tail off.

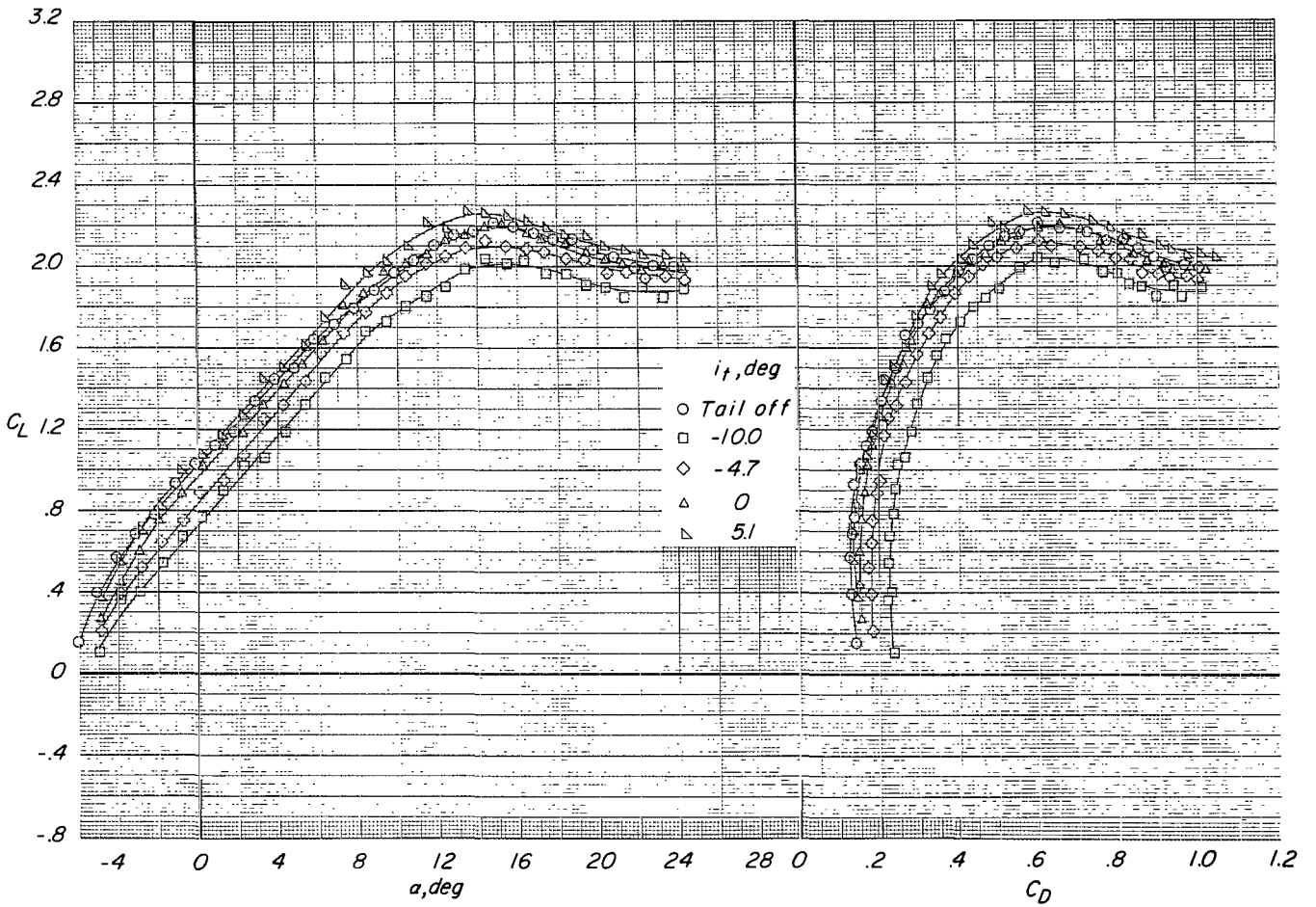

(a) Variation of C_L with α and C_D.

Figure 10.- Effect of tail incidence on longitudinal aerodynamic characteristics for configuration A ($\delta_f = 30^0$, $\delta_s = 35^0$, fixed forewing) with tail in high position. $C_T = 0$.

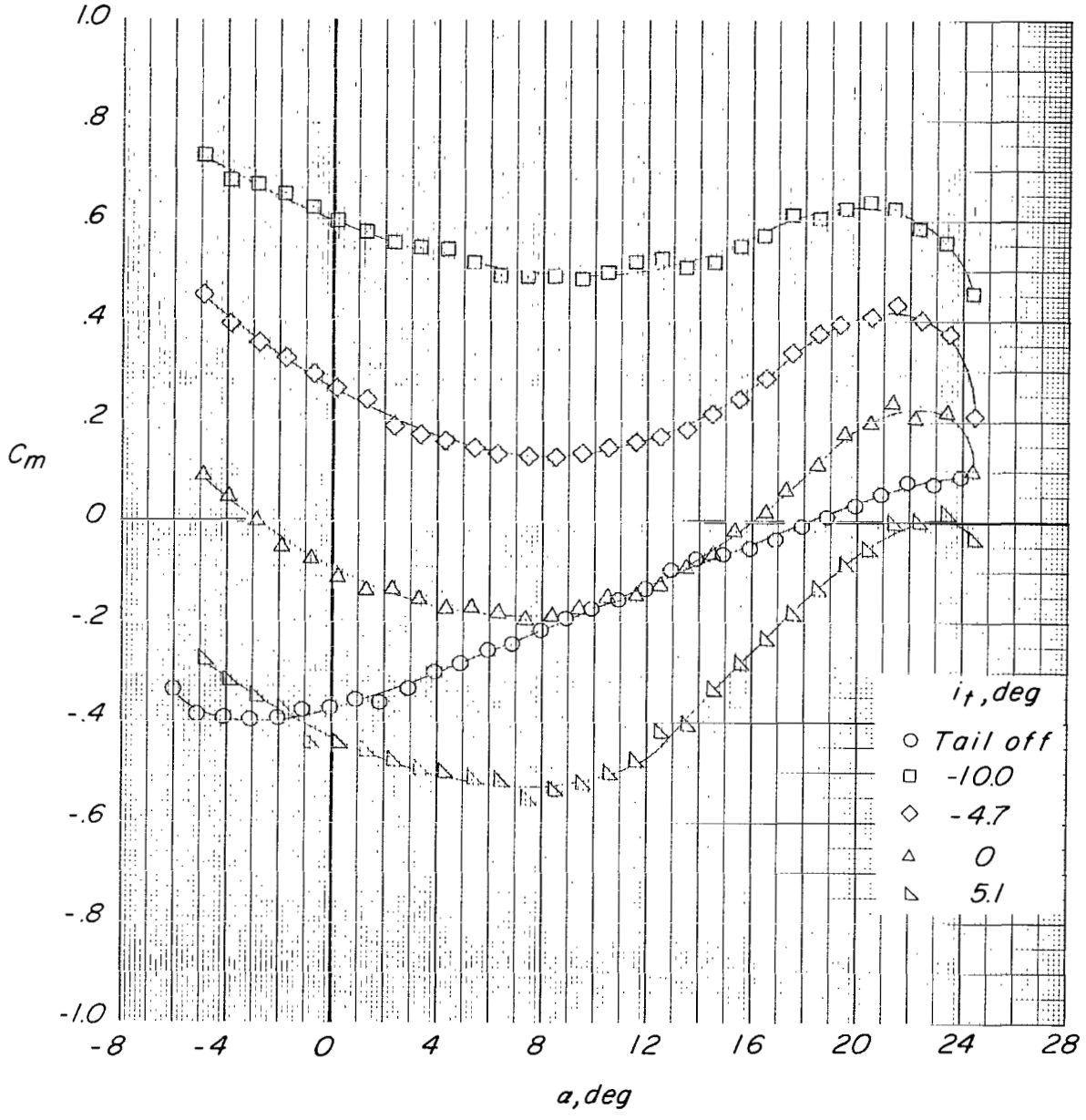

(b) Variation of C_m with α.

Figure 10.- Continued.

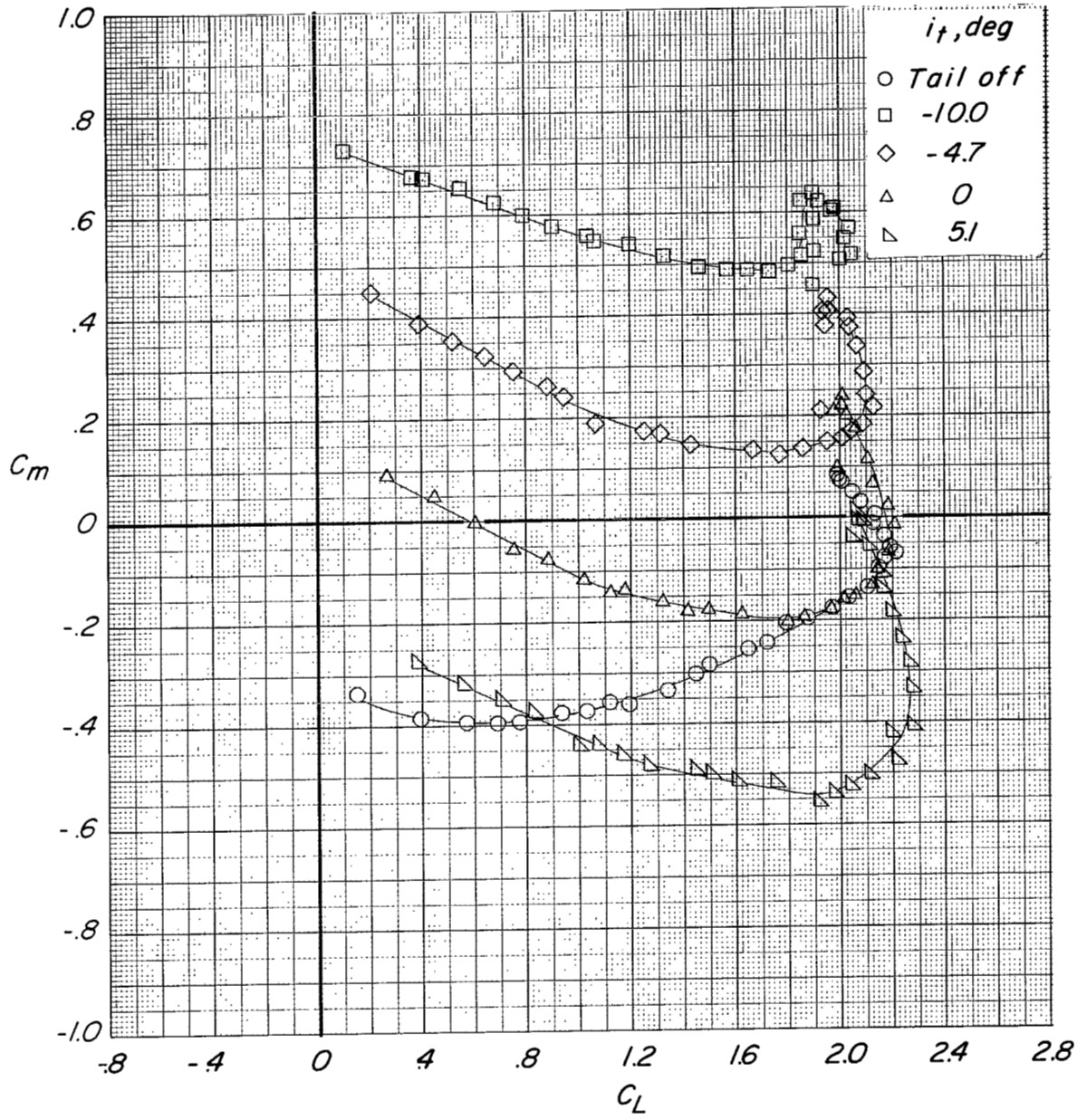

(c) Variation of C_m with C_L.

Figure 10.- Concluded.

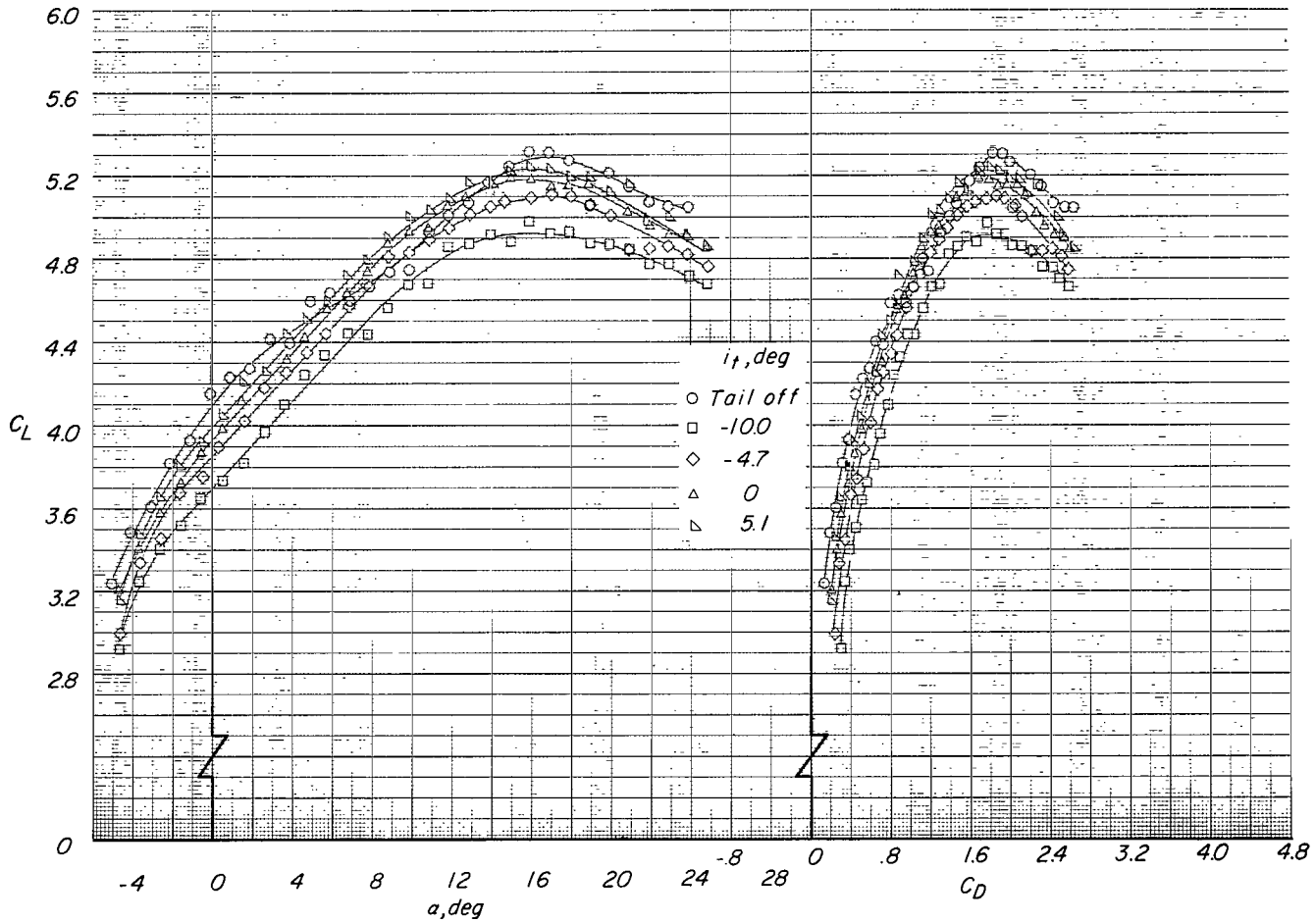

(a) Variation of C_L with α and C_D.

Figure 11.- Effect of tail incidence on longitudinal aerodynamic characteristics for configuration A ($\delta_f = 30^o$, $\delta_s = 35^o$, fixed forewing) with tail in high position. $C_T = 3.3$.

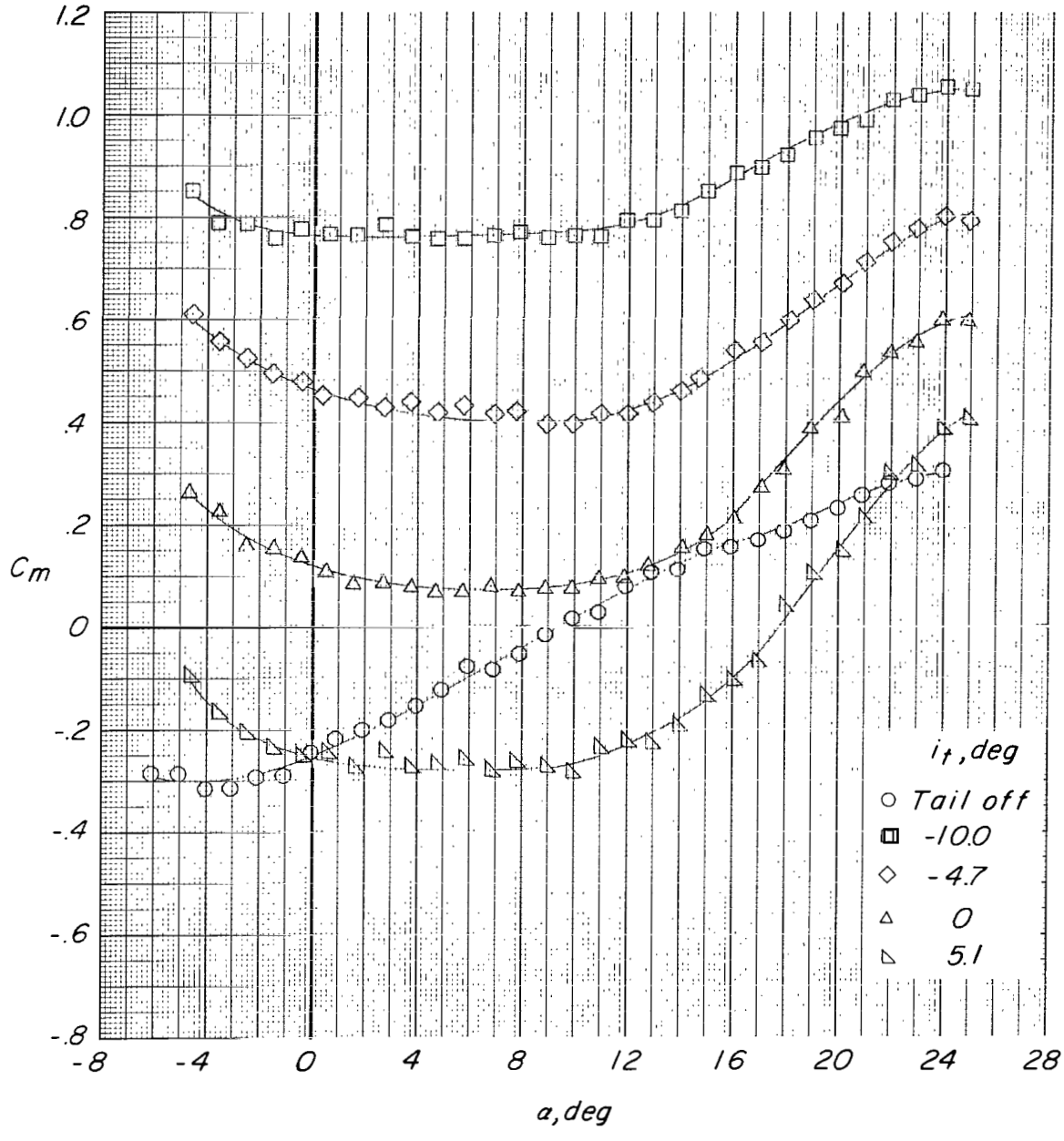

(b) Variation of C_m with α.

Figure 11.- Concluded.

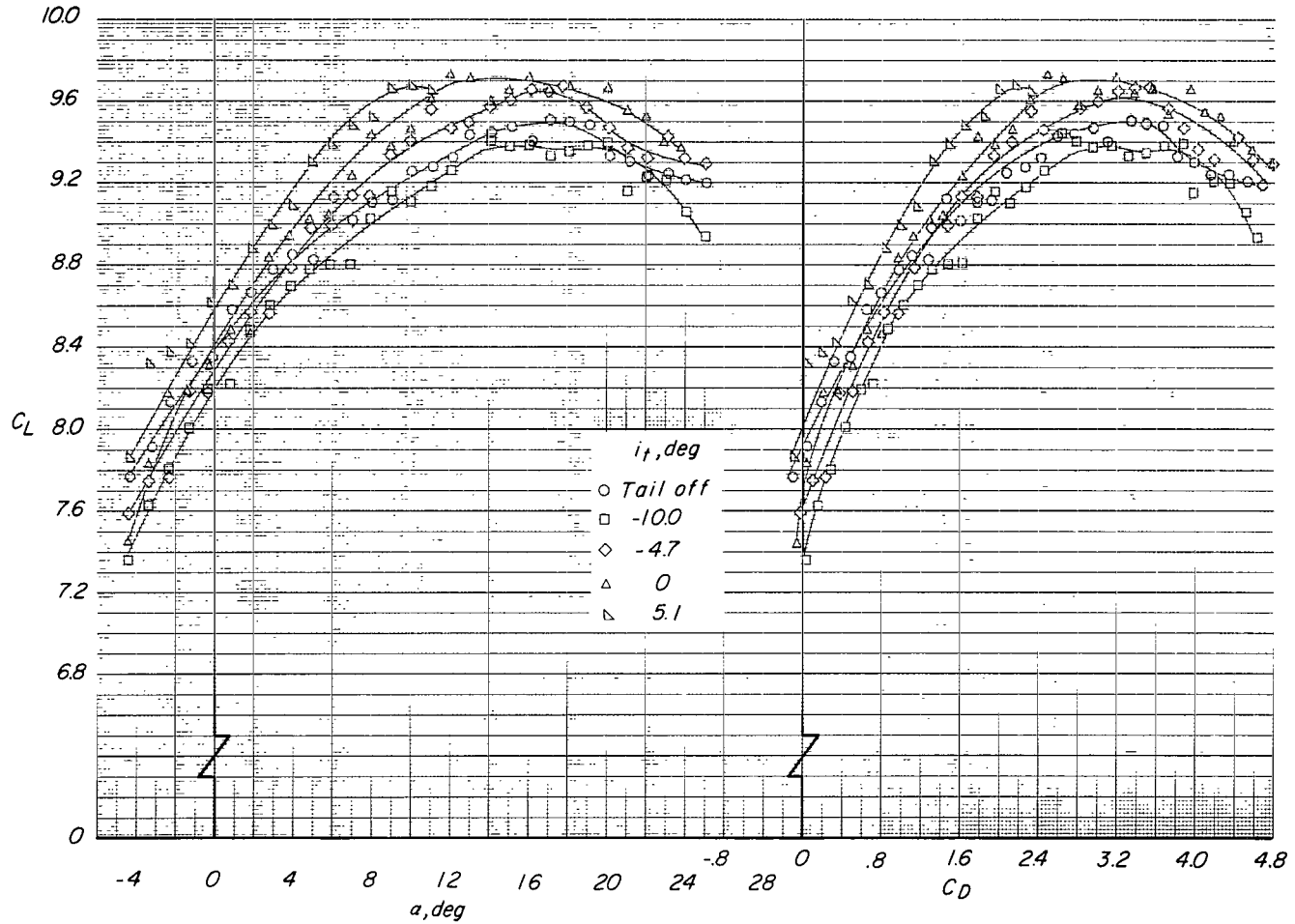

(a) Variation of C_L with α and C_D.

Figure 12.- Effect of tail incidence on longitudinal aerodynamic characteristics for configuration A ($\delta_f = 30^0$, $\delta_s = 35^0$, fixed forewing) with tail in high position. $C_T = 8.0$.

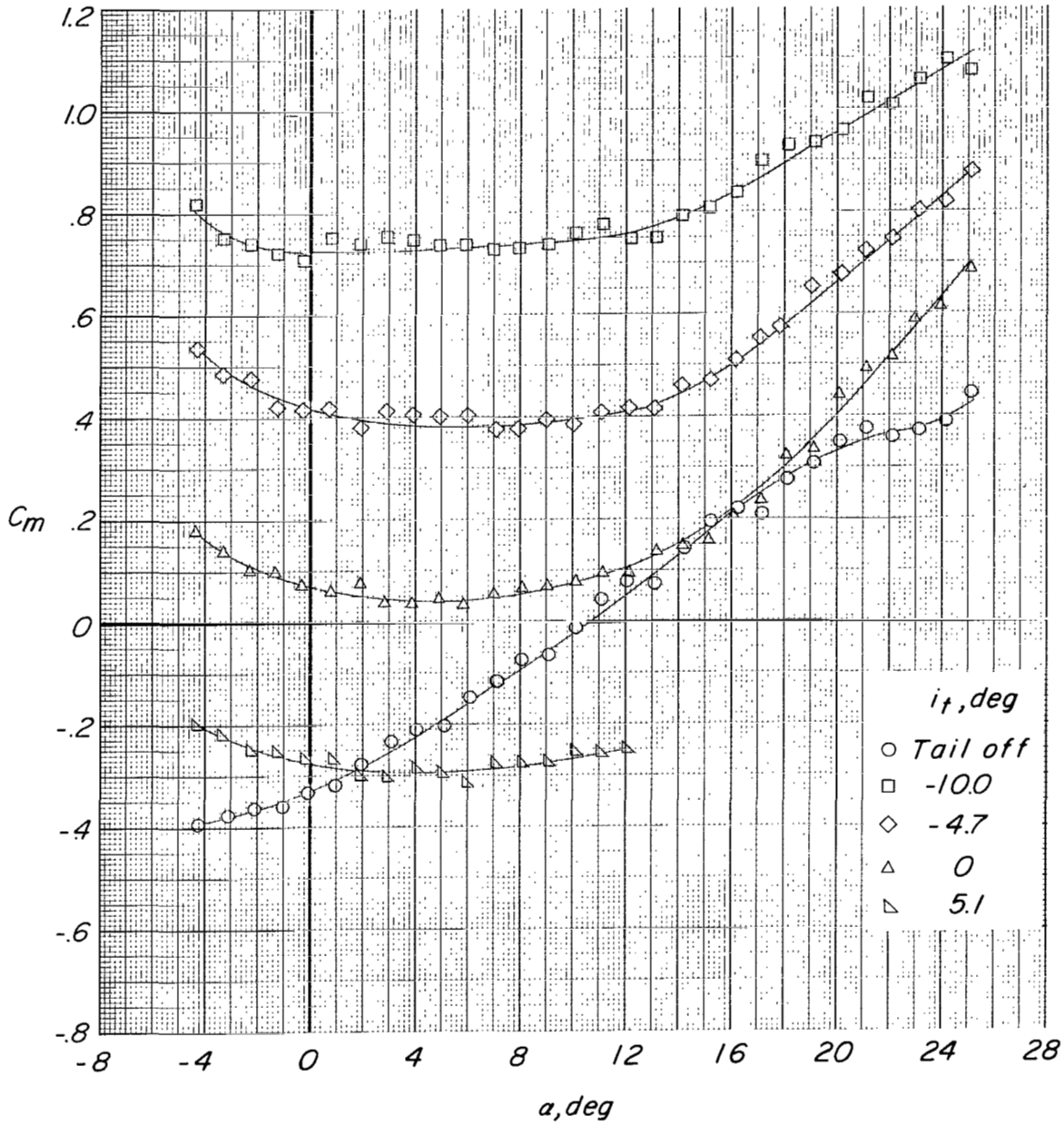

(b) Variation of C_m with α.

Figure 12.- Concluded.

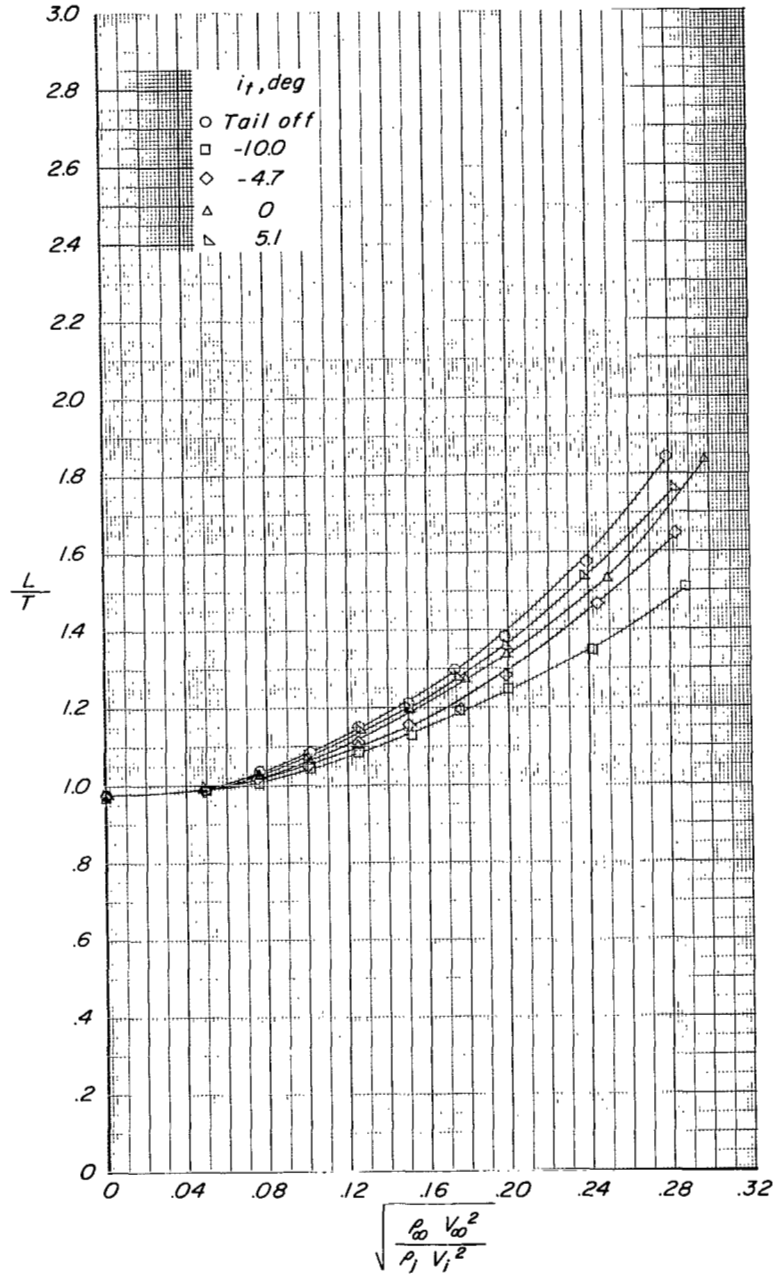

(a) Variation of L/T with effective velocity ratio.

Figure 13.- Effect of tail incidence on longitudinal aerodynamic characteristics for configuration A ($\delta_f = 30^0$, $\delta_s = 35^0$, fixed forewing) with tail in high postition. $\alpha \approx 0.6$.

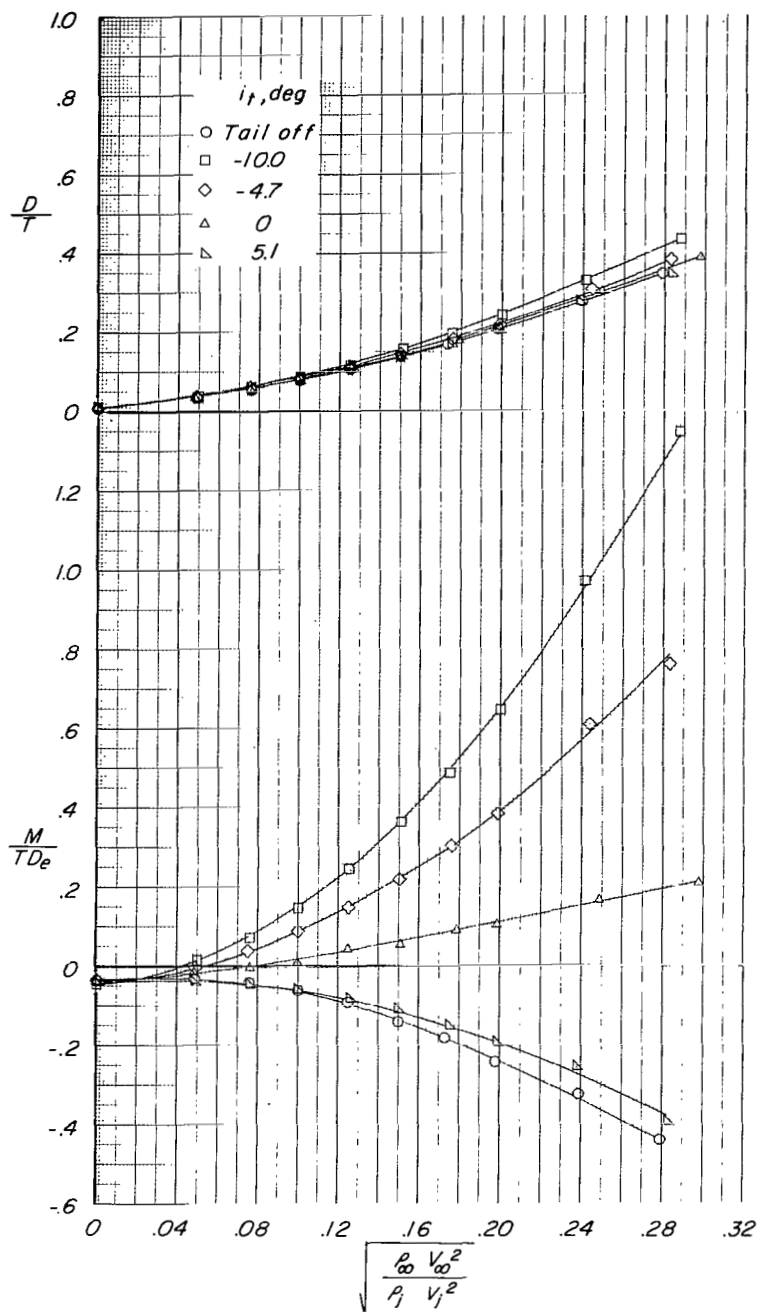

(b) Variation of D/T and M/TD_e with effective velocity ratio.

Figure 13.- Concluded.

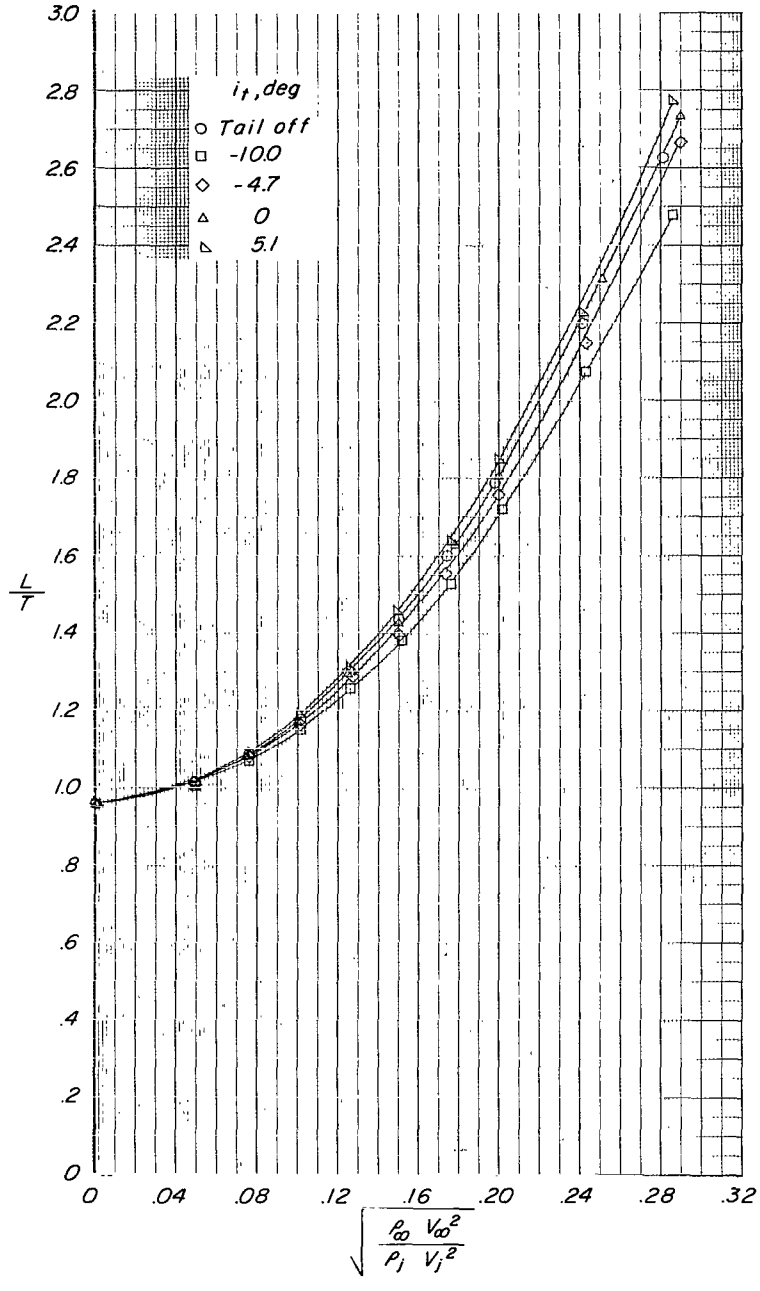

(a) Variation of L/T with effective velocity ratio.

Figure 14.- Effect of tail incidence on longitudinal aerodynamic characteristics for configuration A ($\delta_f = 30^0$, $\delta_s = 35^0$, fixed forewing) with tail in high position. $\alpha \approx 10.8^0$.

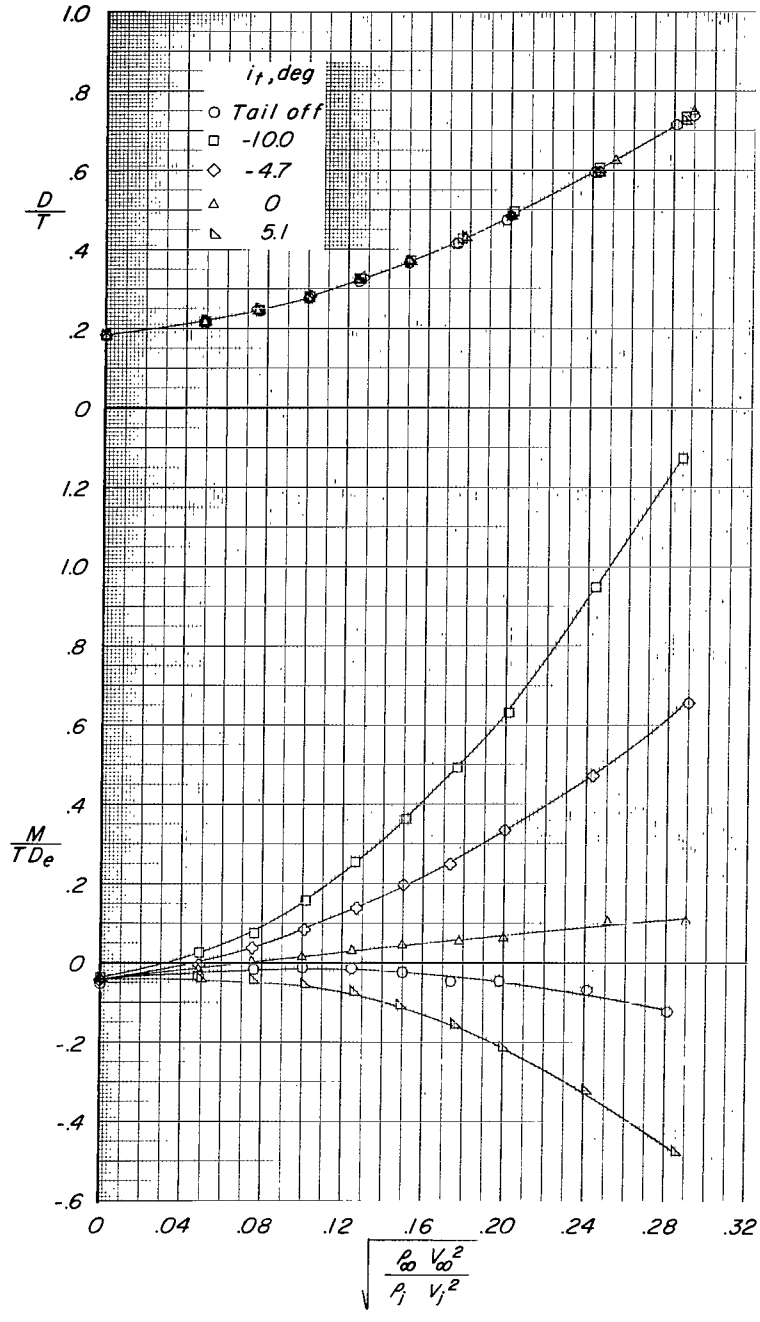

(b) Variation of D/T and M/TD_e with effective velocity ratio.

Figure 14.- Concluded.

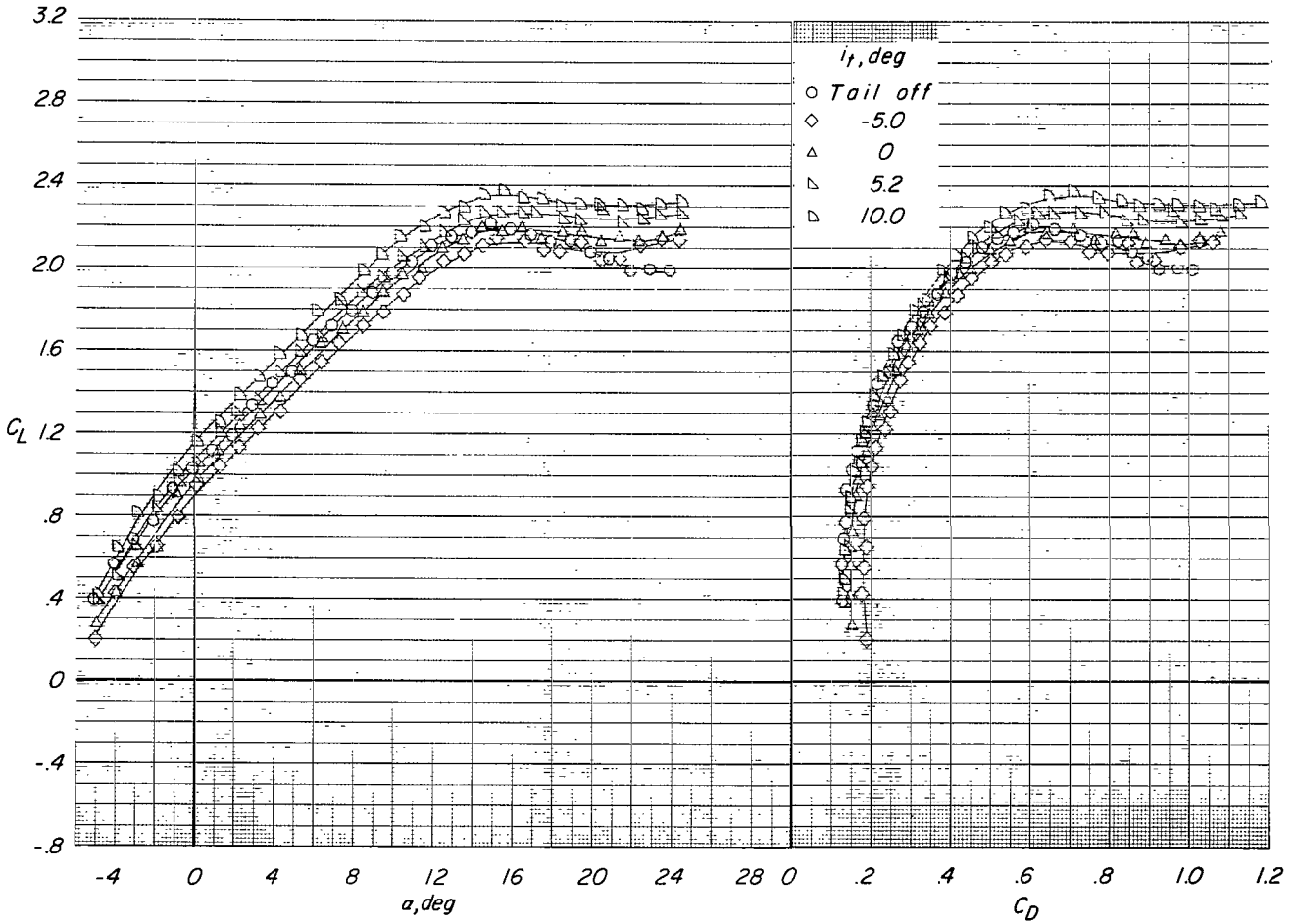

(a) Variation of C_L with α and C_D.

Figure 15.- Effect of tail incidence on longitudinal aerodynamic characteristics for configuration A ($\delta_f = 30^0$, $\delta_s = 35^0$, fixed forewing) with tail in mid position. $C_T = 0$.

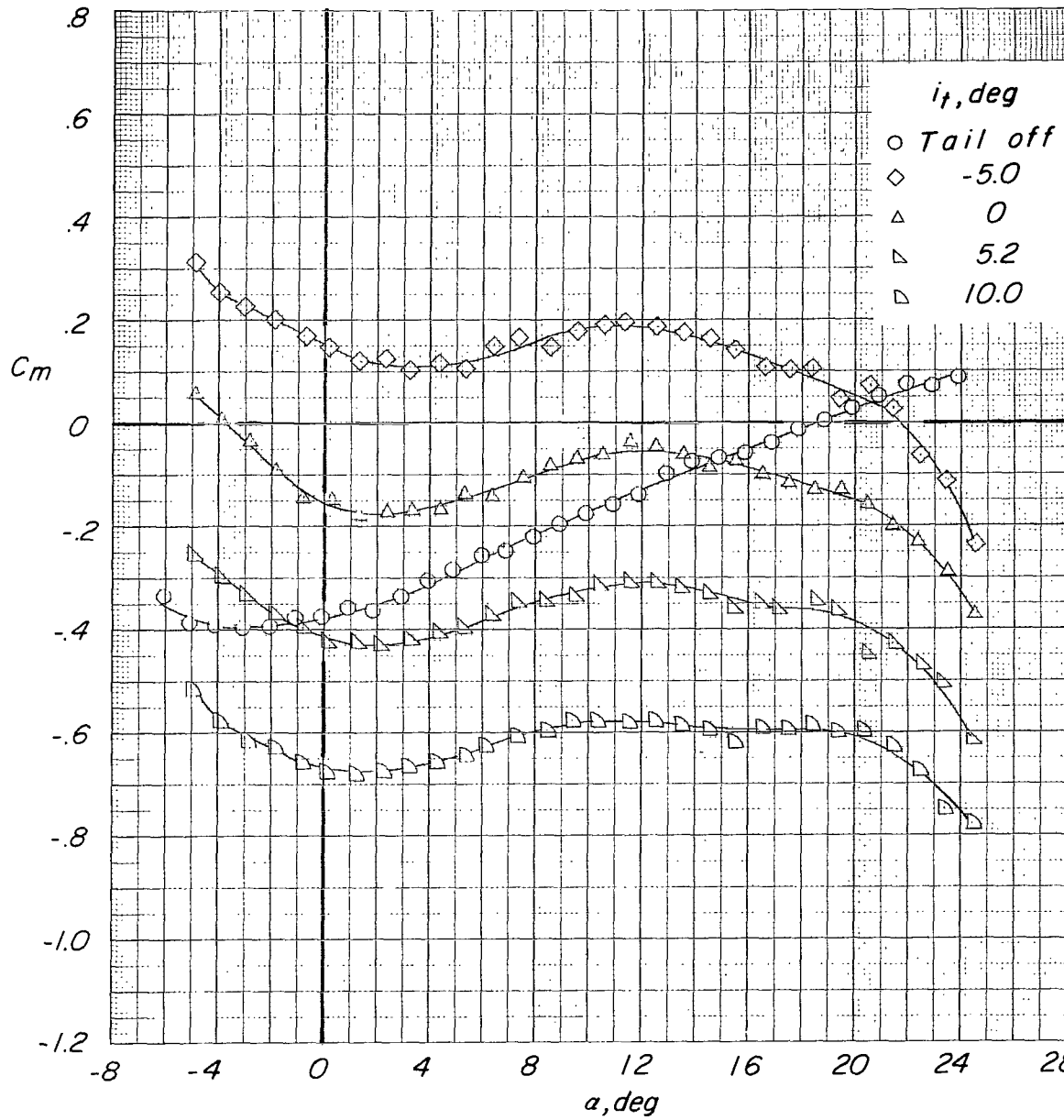

(b) Variation of C_m with α.

Figure 15.- Continued.

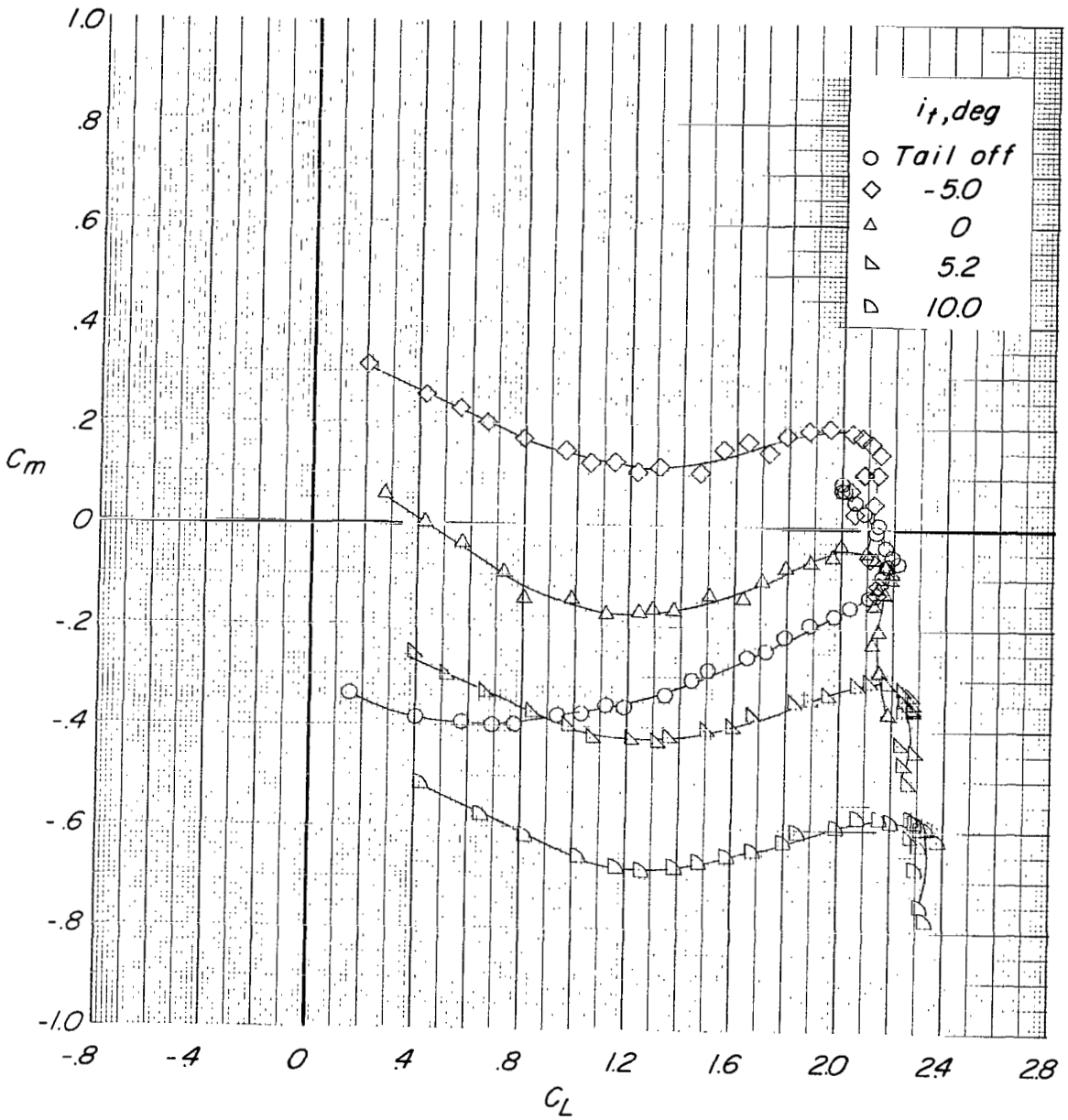

(c) Variation of C_m with C_L.

Figure 15.- Concluded.

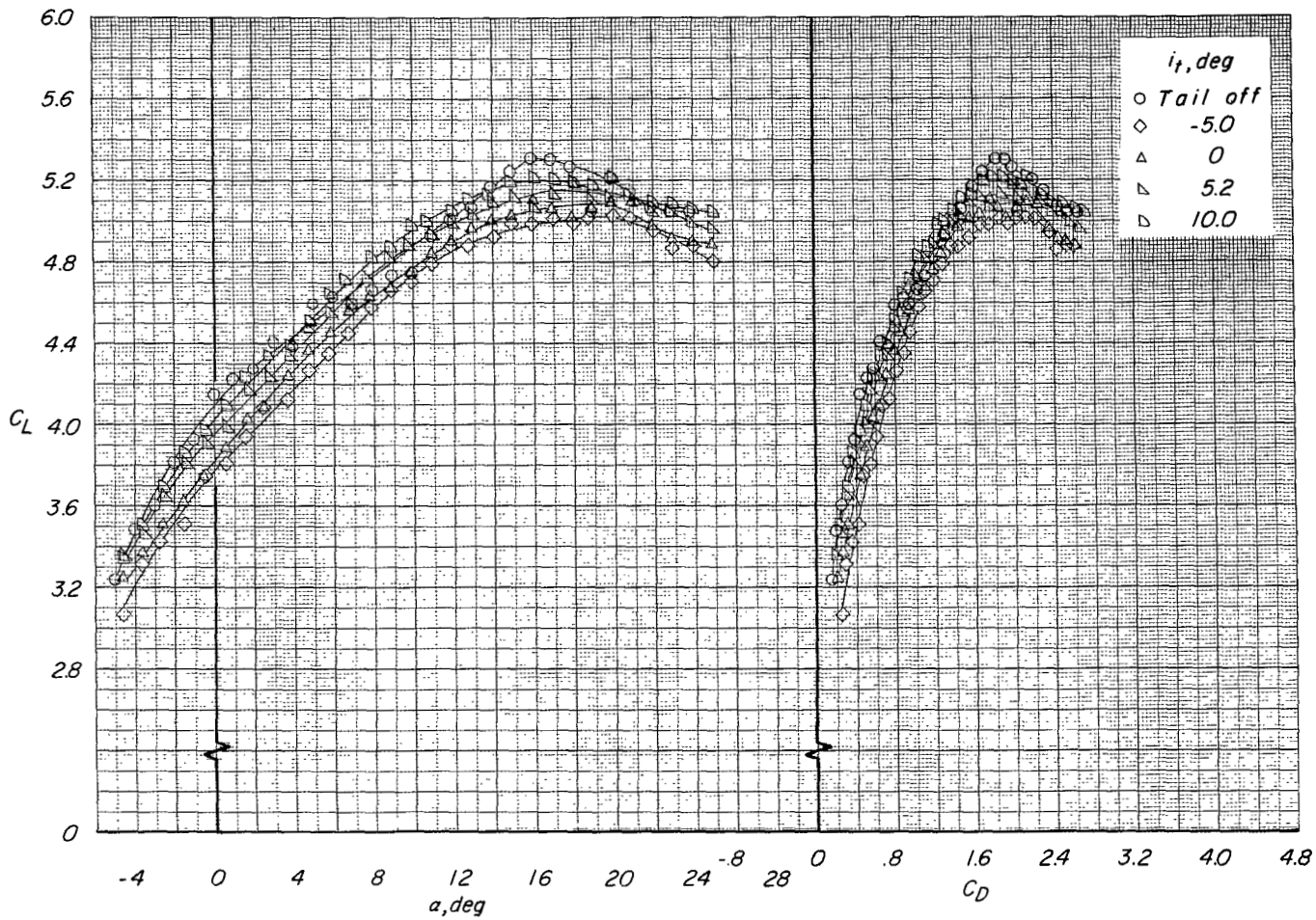

(a) Variation of C_L with α and C_D.

Figure 16.- Effect of tail incidence on longitudinal aerodynamic characteristics for configuration A ($\delta_f = 30^0$, $\delta_s = 35^0$, fixed forewing) with tail in mid position. $C_T = 3.3$.

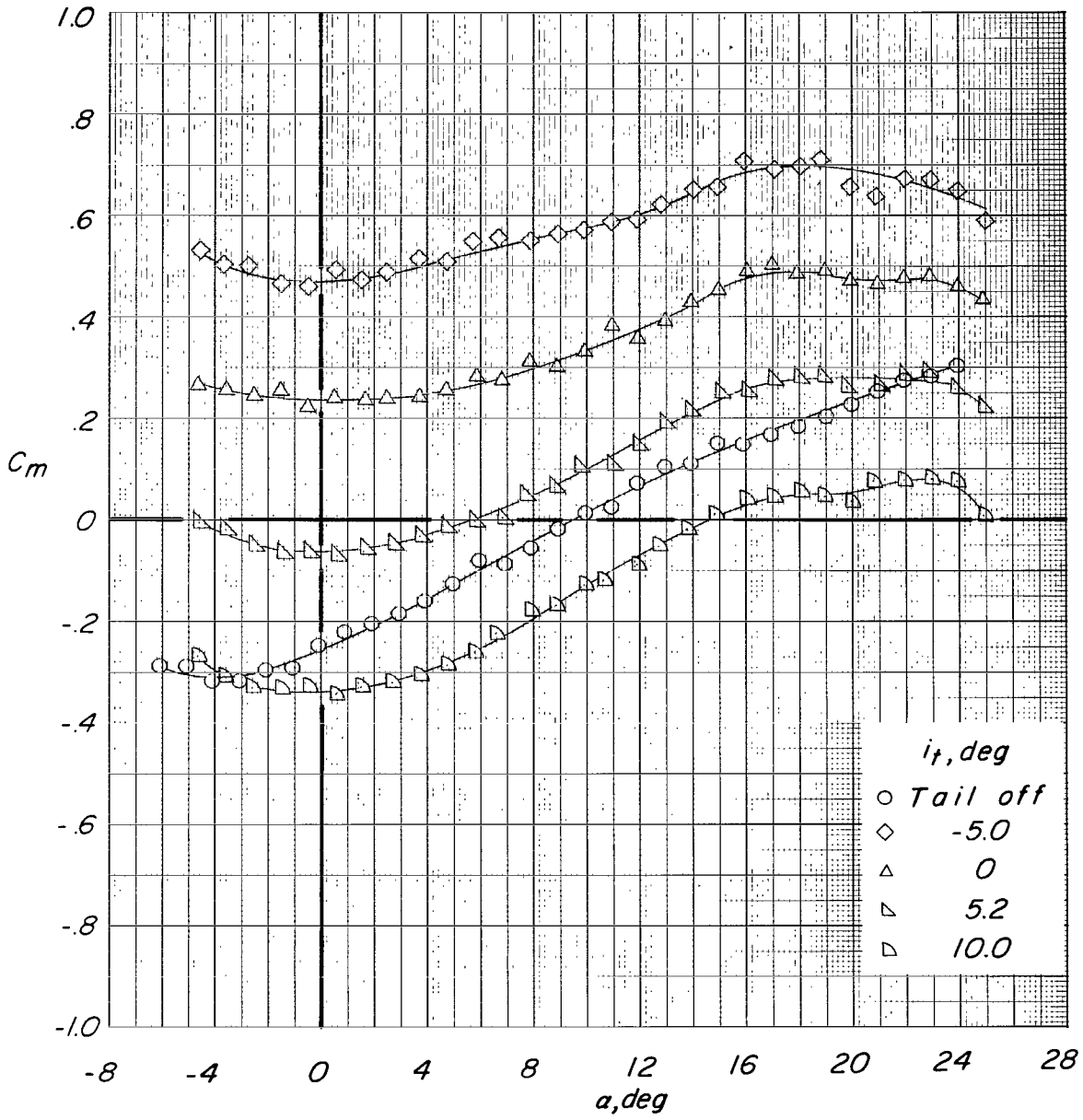

(b) Variation of C_m with α.

Figure 16.- Concluded.

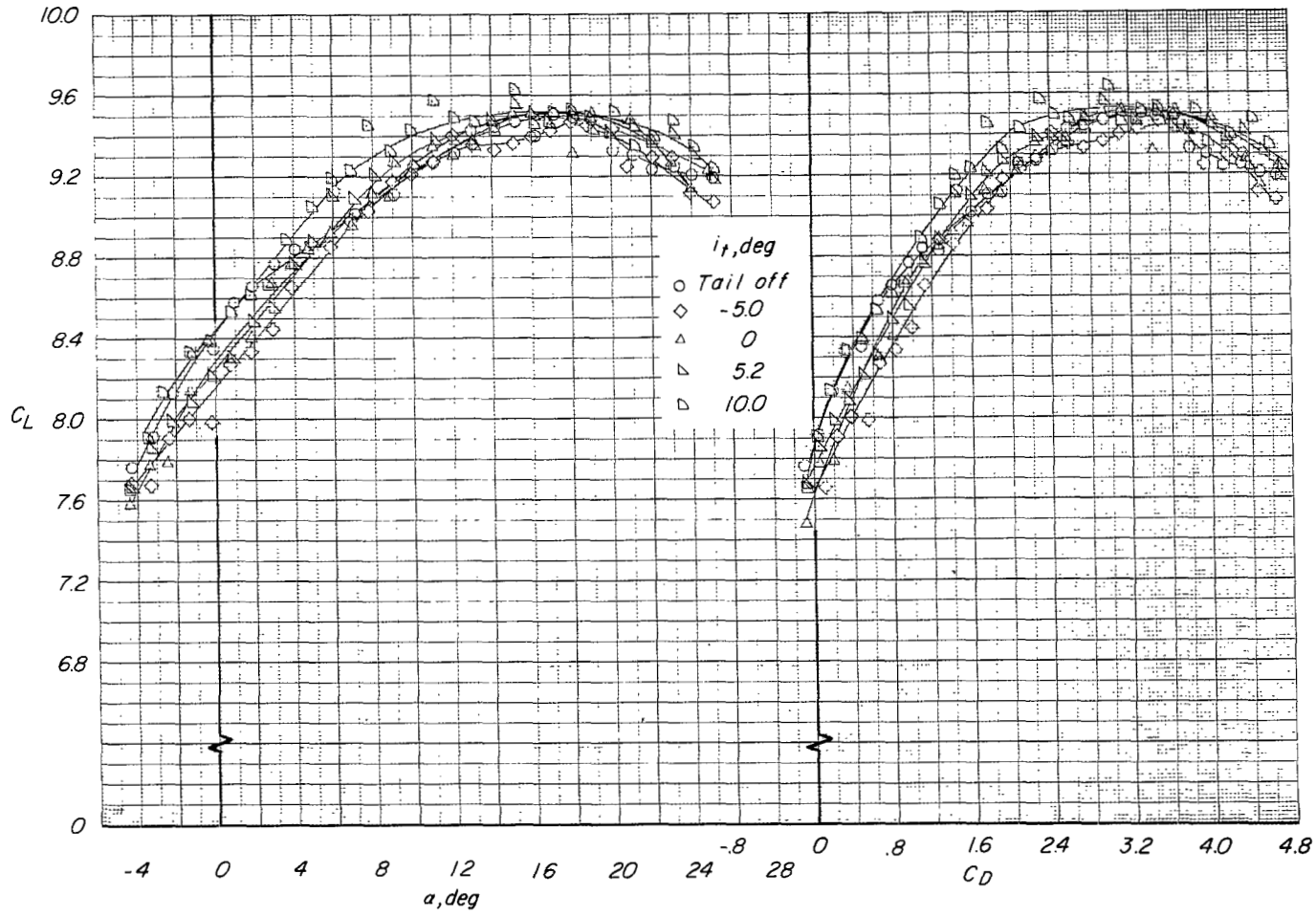

(a) Variation of C_L with α and C_D.

Figure 17.- Effect of tail incidence on longitudinal aerodynamic characteristics for configuration A ($\delta_f = 30^0$, $\delta_s = 35^0$, fixed forewing) with tail in mid position. $C_T = 7.9$.

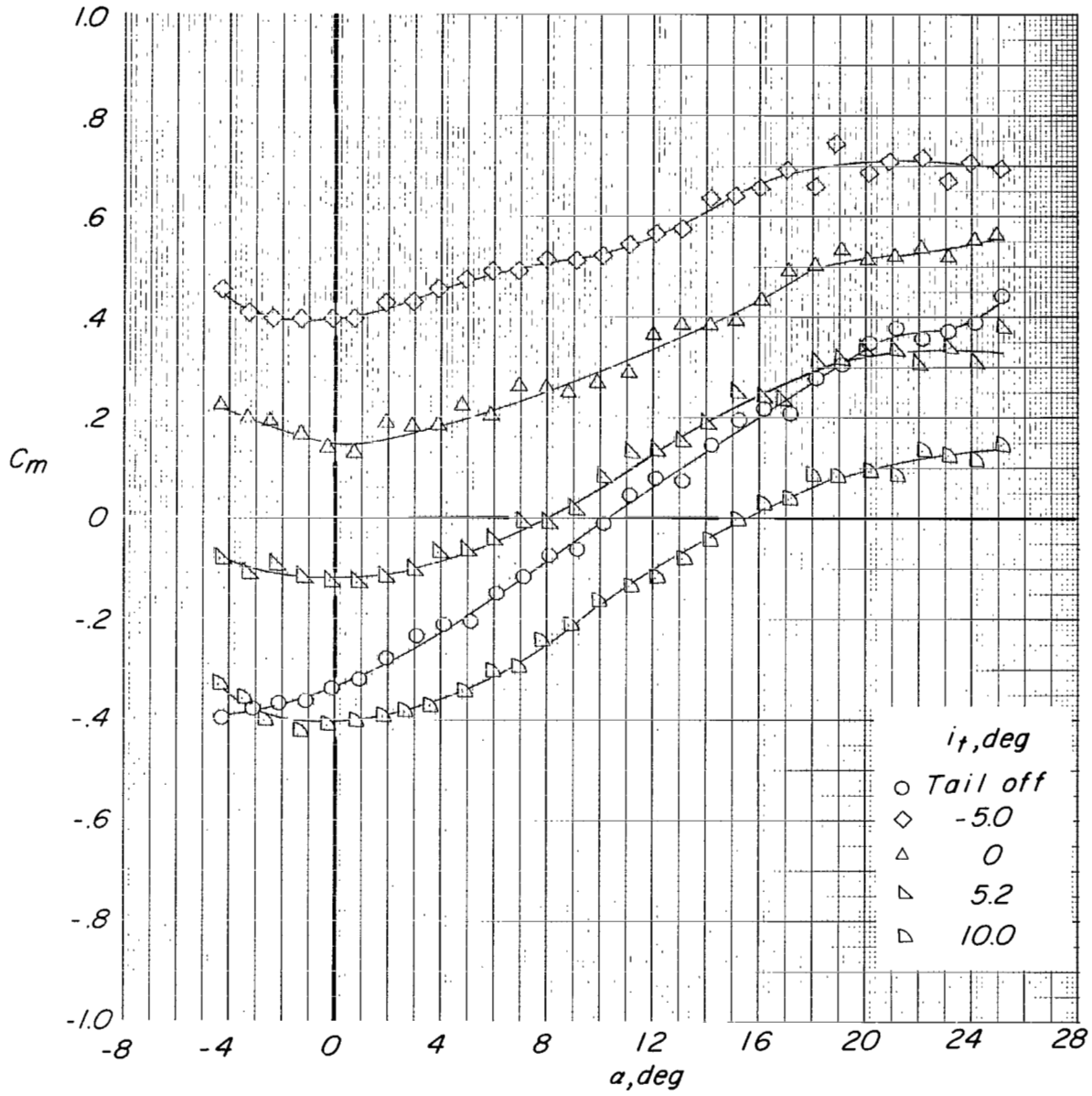

(b) Variation of C_m with α.

Figure 17.- Concluded.

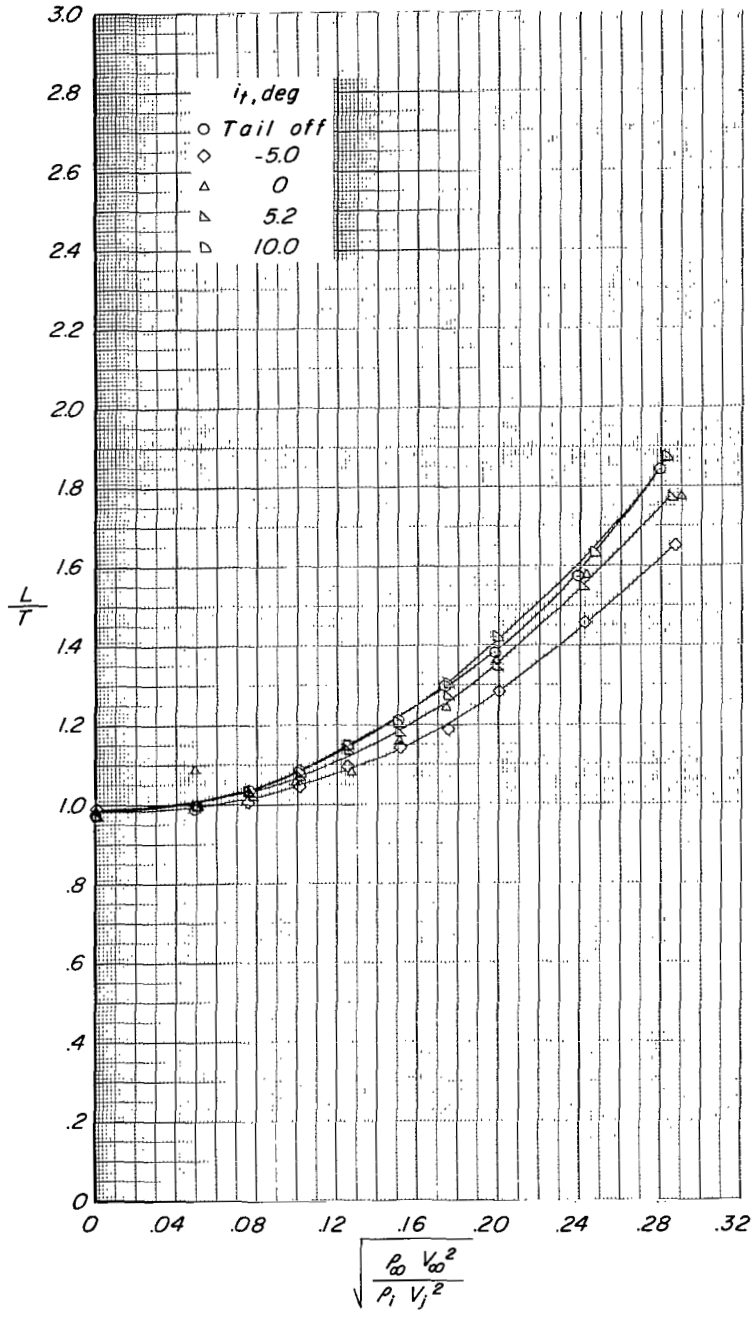

(a) Variation of L/T with effective velocity ratio.

Figure 18.- Effect of tail incidence on longitudinal aerodynamic characteristics for configuration A ($\delta_f = 30^0$, $\delta_s = 35^0$, fixed forewing) with tail in mid position. $\alpha \approx 0.6^0$.

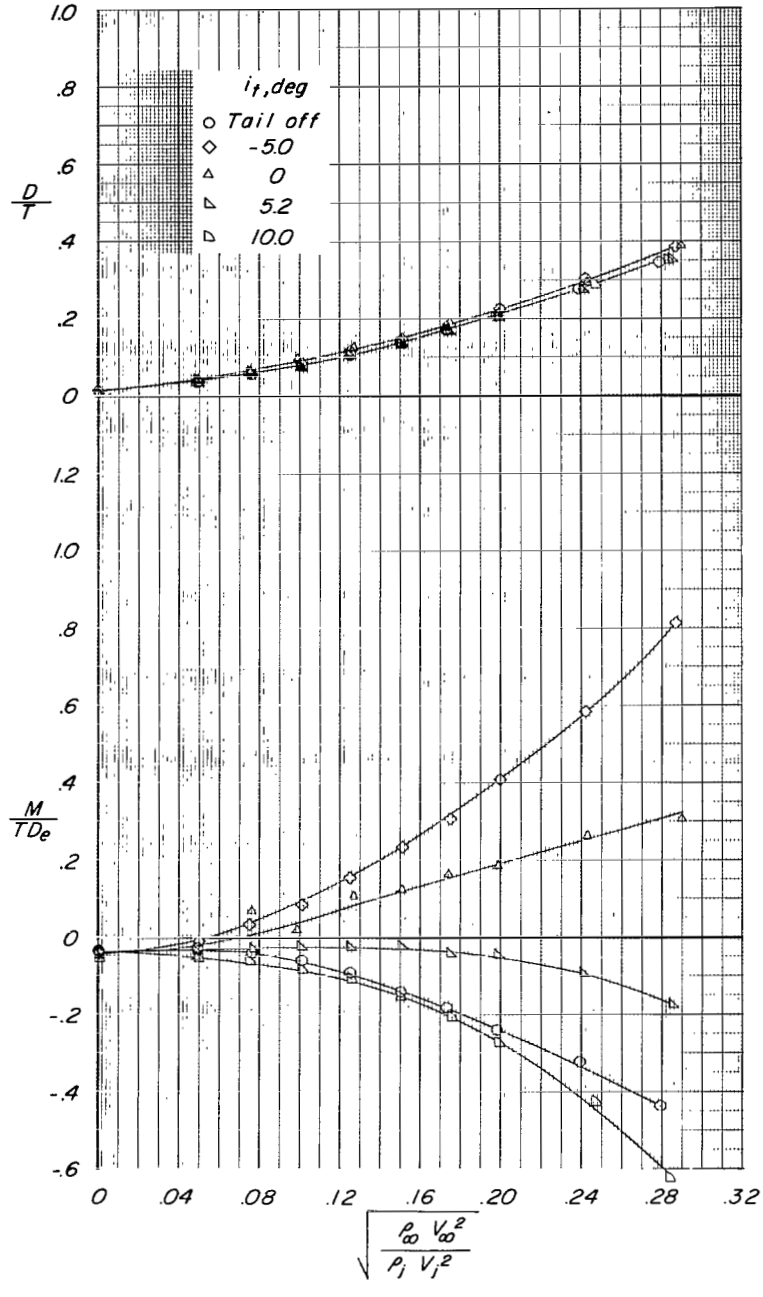

(b) Variation of D/T and M/TD_e with effective velocity ratio.

Figure 18.- Concluded.

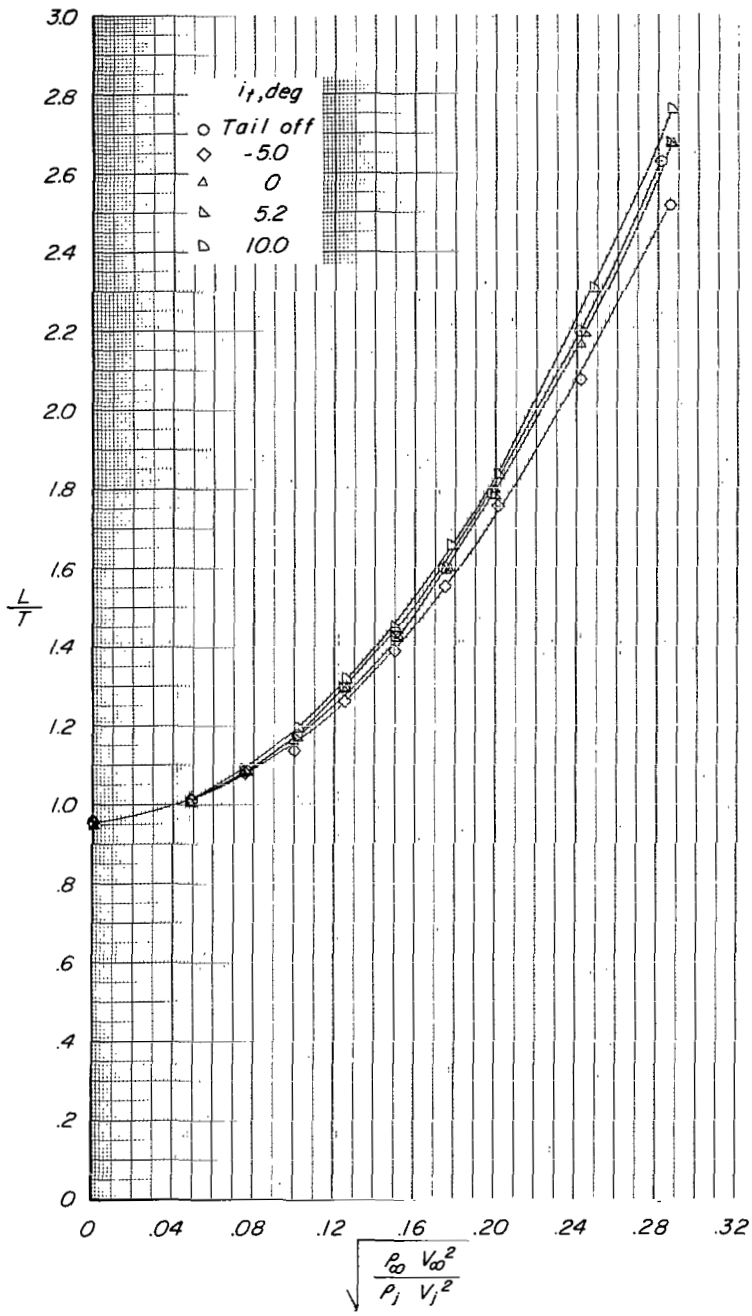

(a) Variation of L/T with effective velocity ratio.

Figure 19.- Effect of tail incidence on longitudinal aerodynamic characteristics for configuration A ($\delta_f = 30^0$, $\delta_s = 35^0$, fixed forewing) with tail in mid position. $\alpha \approx 10.8^0$.

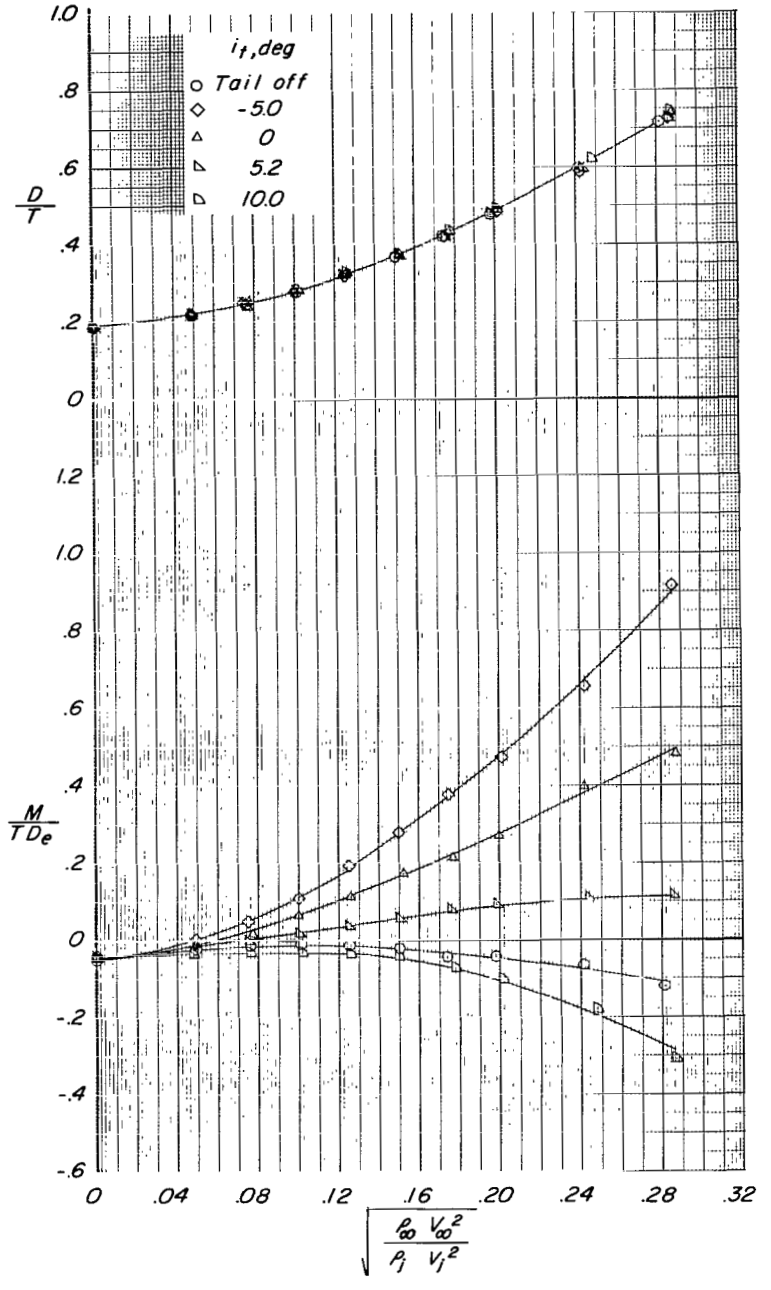

(b) Variation of D/T and M/TD_e with effective velocity ratio.

Figure 19.- Concluded.

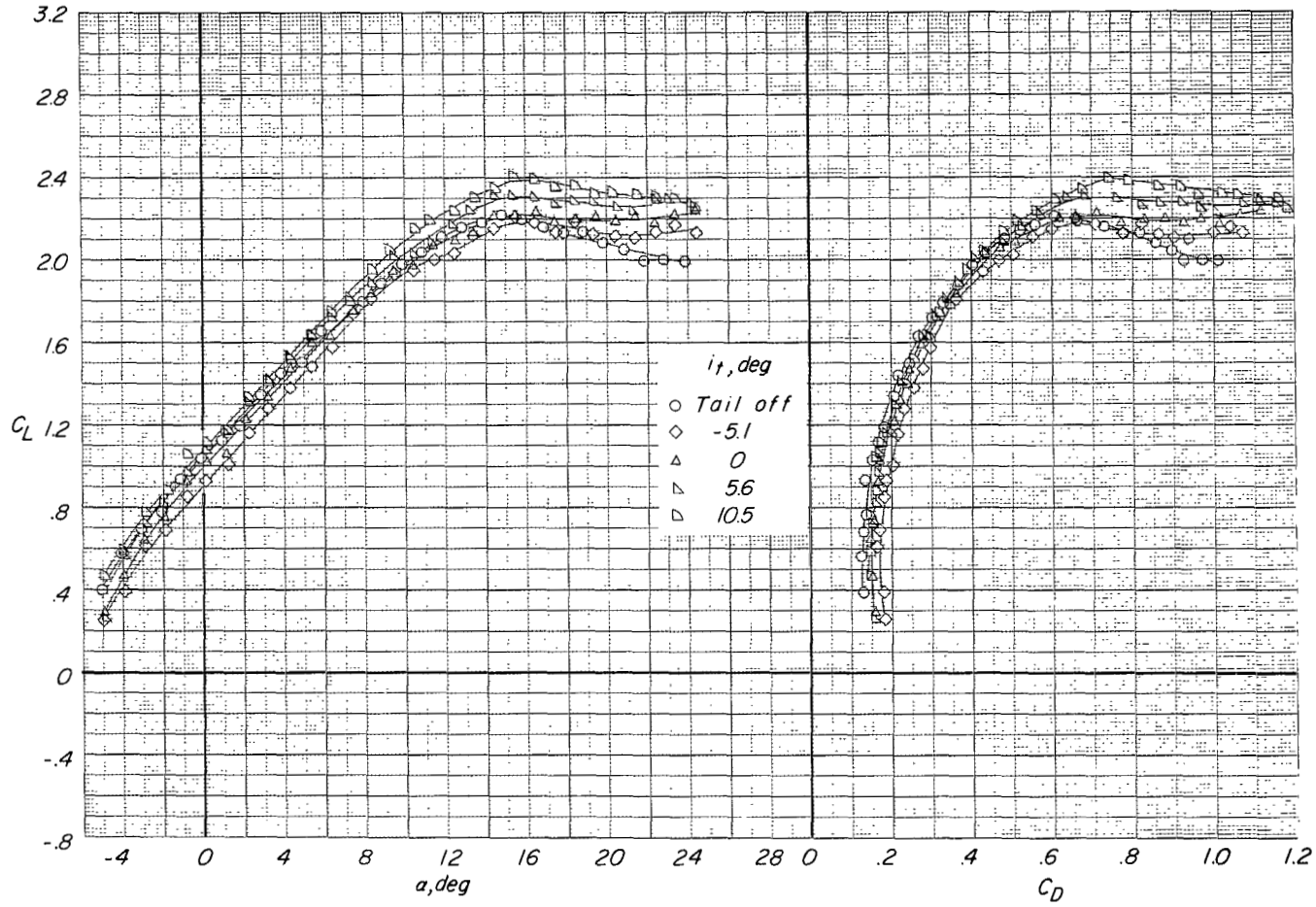

(a) Variation of C_L with α and C_D.

Figure 20.- Effect of tail incidence on longitudinal aerodynamic characteristics for configuration A ($\delta_f = 30^0$, $\delta_s = 35^0$, fixed forewing) with tail in low position. $C_T = 0$.

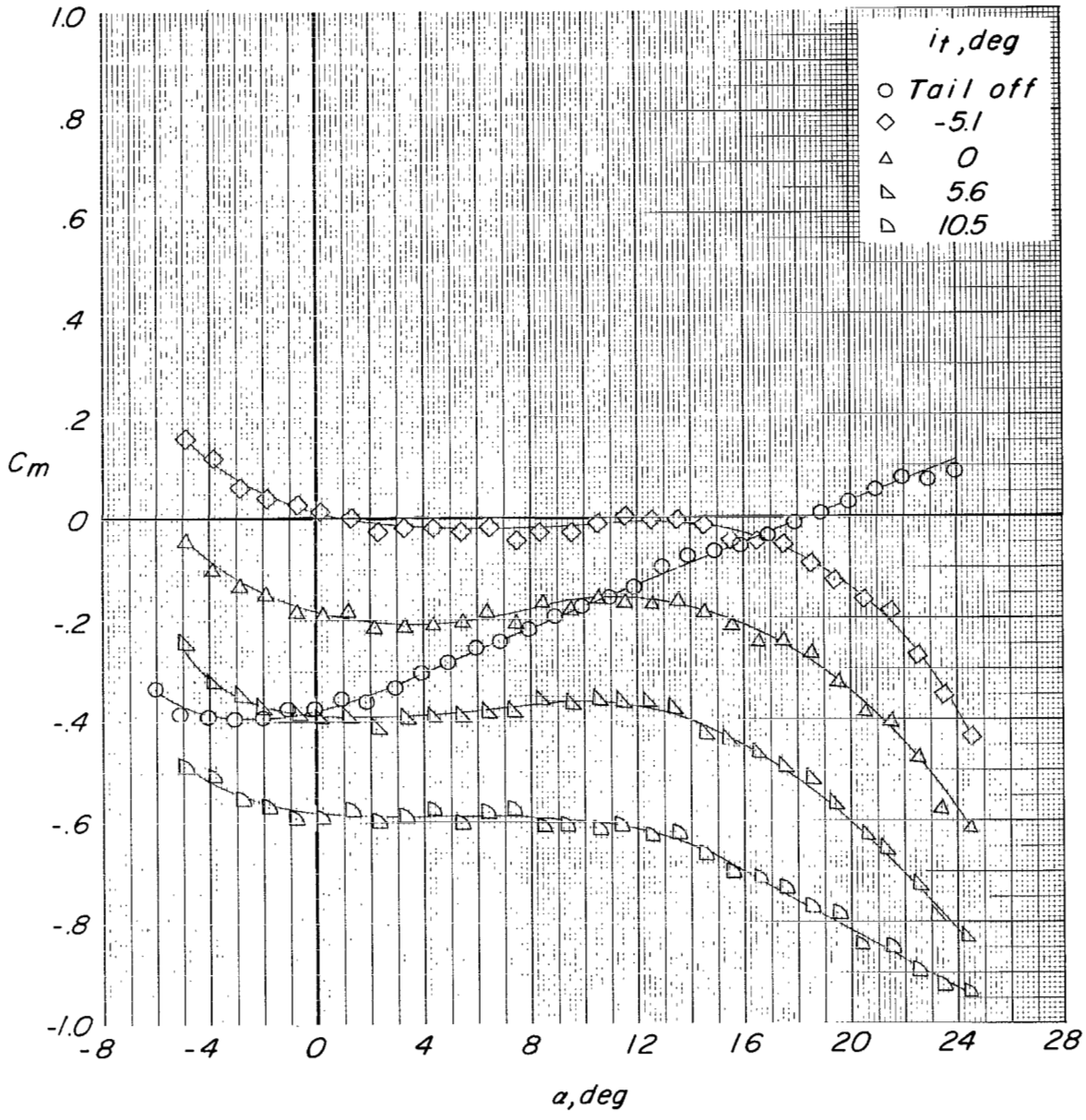

(b) Variation of C_m with α.

Figure 20.- Continued.

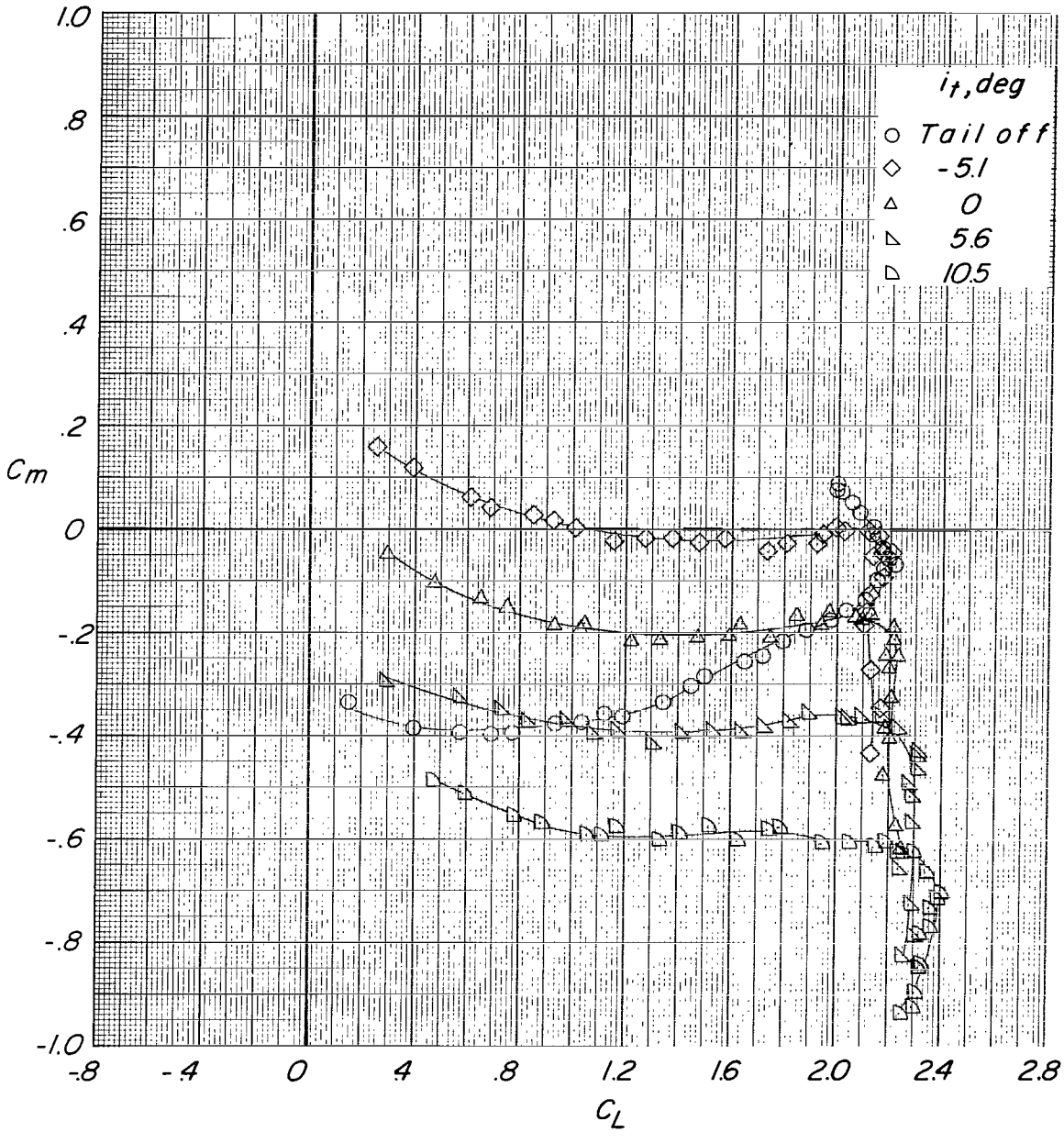

(c) Variation of C_m with C_L.

Figure 20.- Concluded.

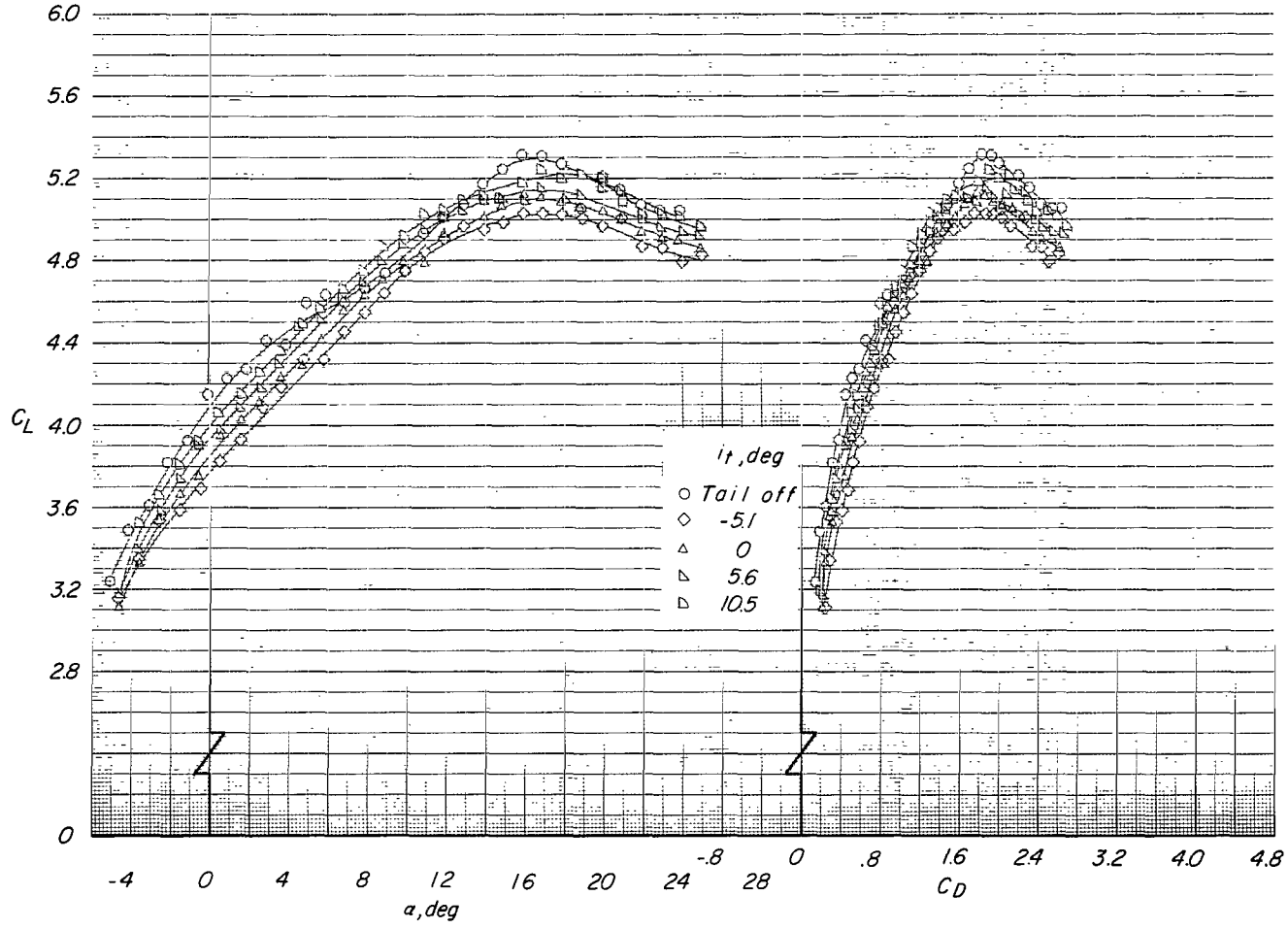

(a) Variation of C_L with α and C_D.

Figure 21.- Effect of tail incidence on longitudinal aerodynamic characteristics for configuration A ($\delta_f = 30^0$, $\delta_s = 35^0$, fixed forewing) with tail in low position. $C_T = 3.3$.

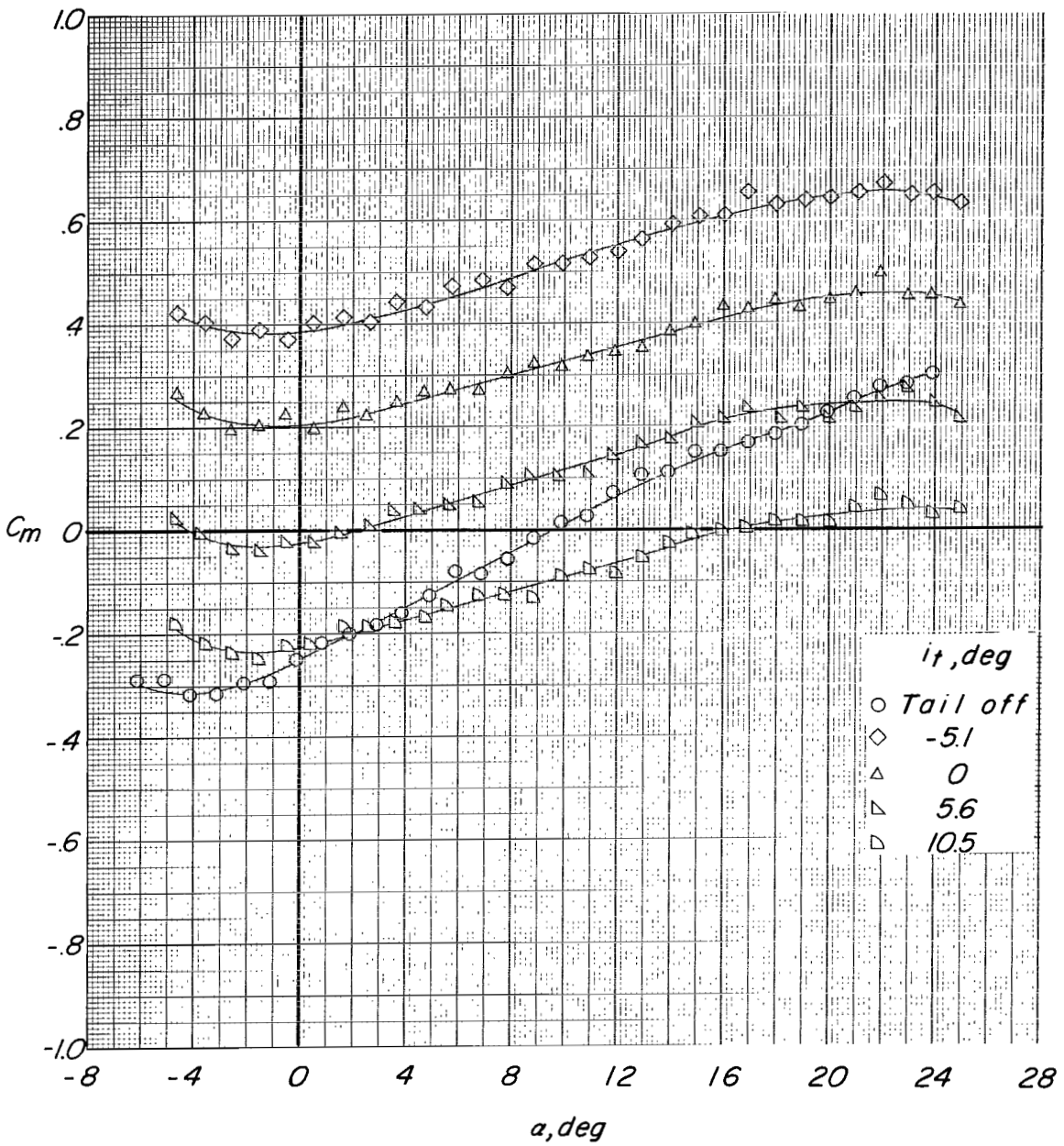

(b) Variation of C_m with α.

Figure 21.- Concluded.

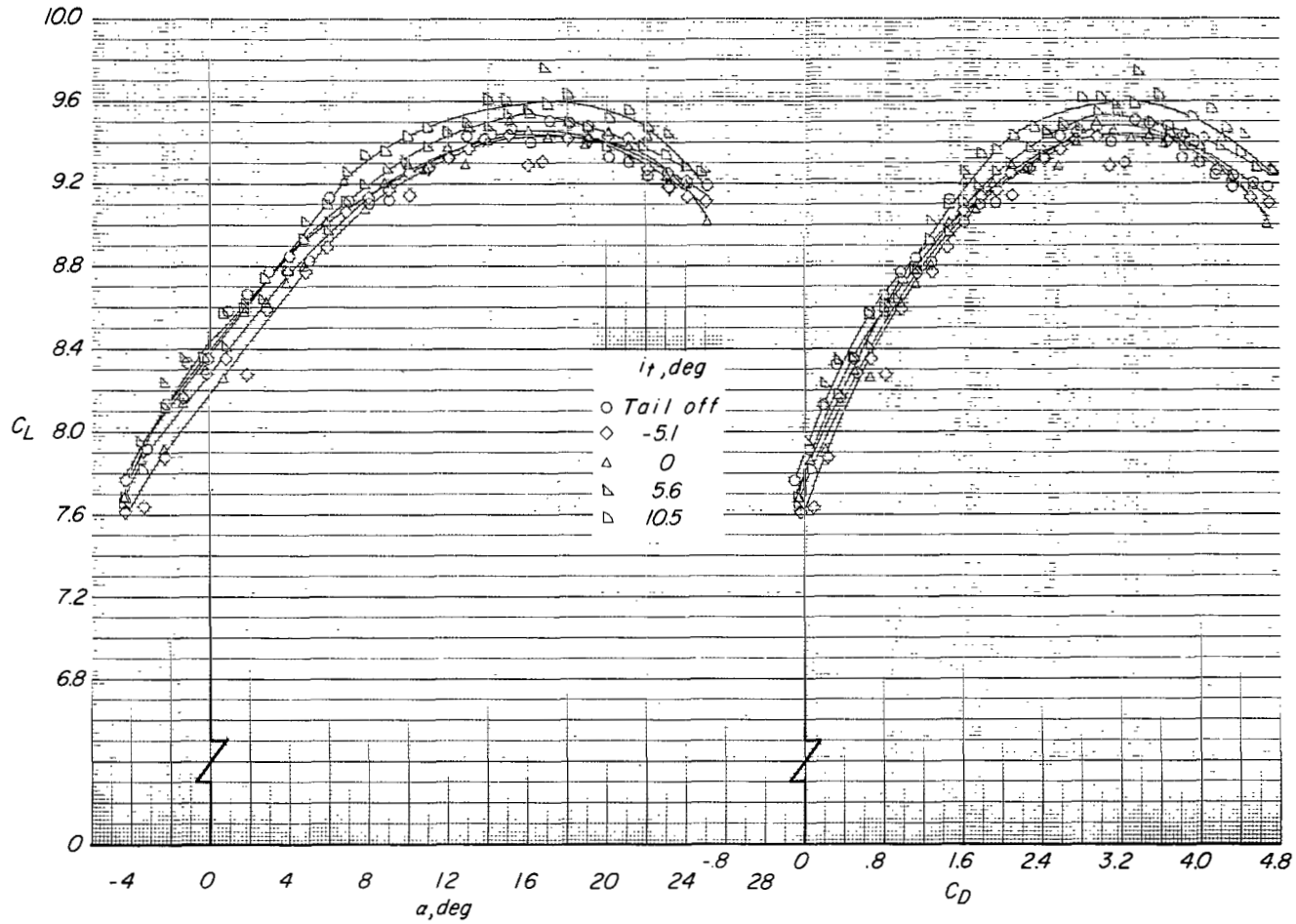

(a) Variation of C_L with α and C_D.

Figure 22.- Effect of tail incidence on longitudinal aerodynamic characteristics for configuration A ($\delta_f = 30^0$, $\delta_s = 35^0$, fixed forewing) with tail in low position. $C_T = 7.9$.

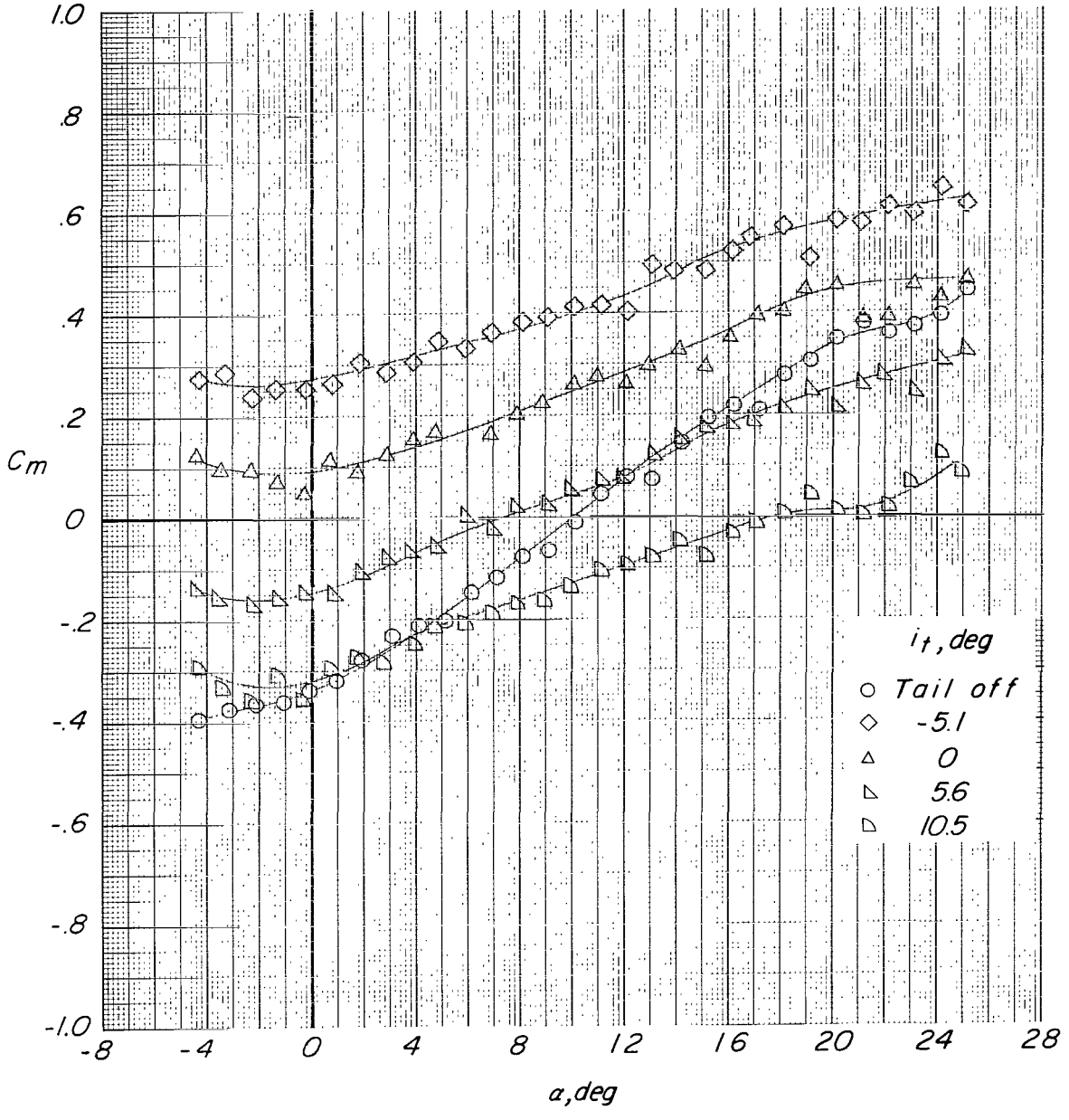

(b) Variation of C_m with α.

Figure 22.- Concluded.

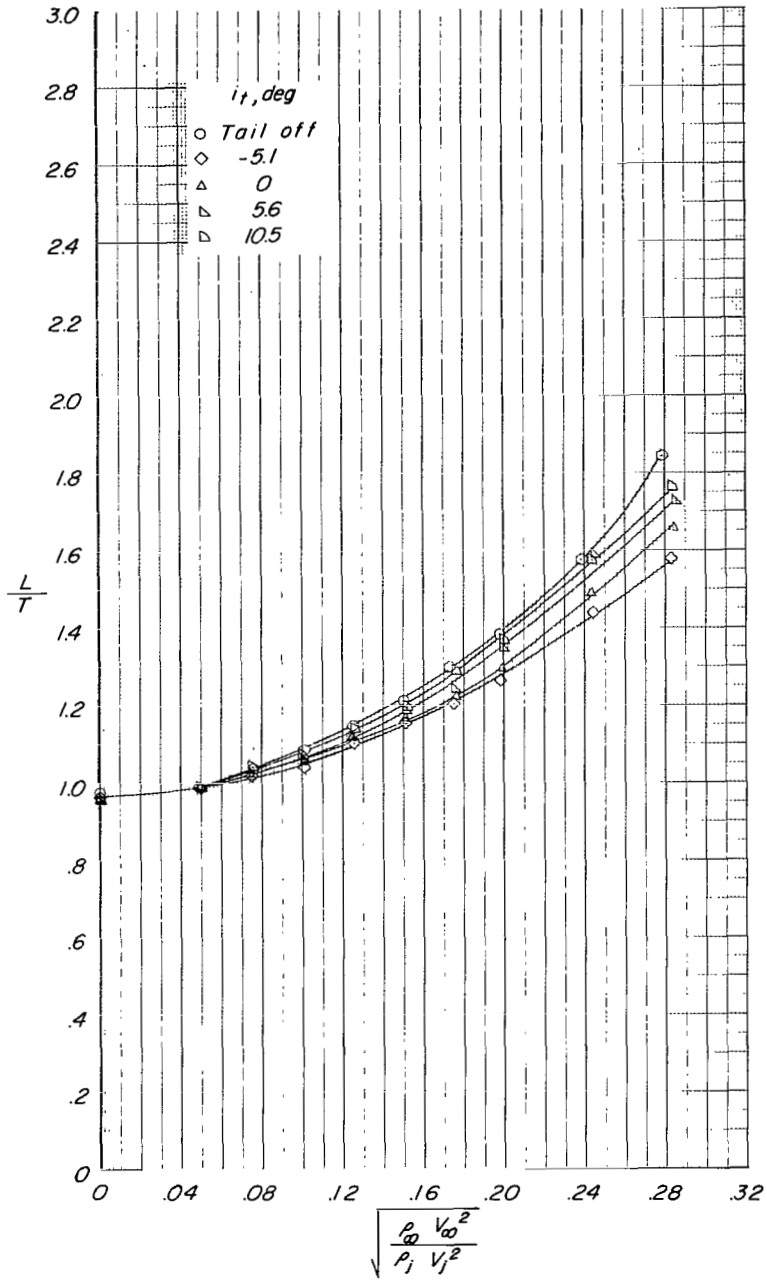

(a) Variation of L/T with effective velocity ratio.

Figure 23.- Effect of tail incidence on longitudinal aerodynamic characteristics for configuration A ($\delta_f = 30^0$, $\delta_s = 35^0$, fixed forewing) with tail in low position. $\alpha \approx 0.6^0$.

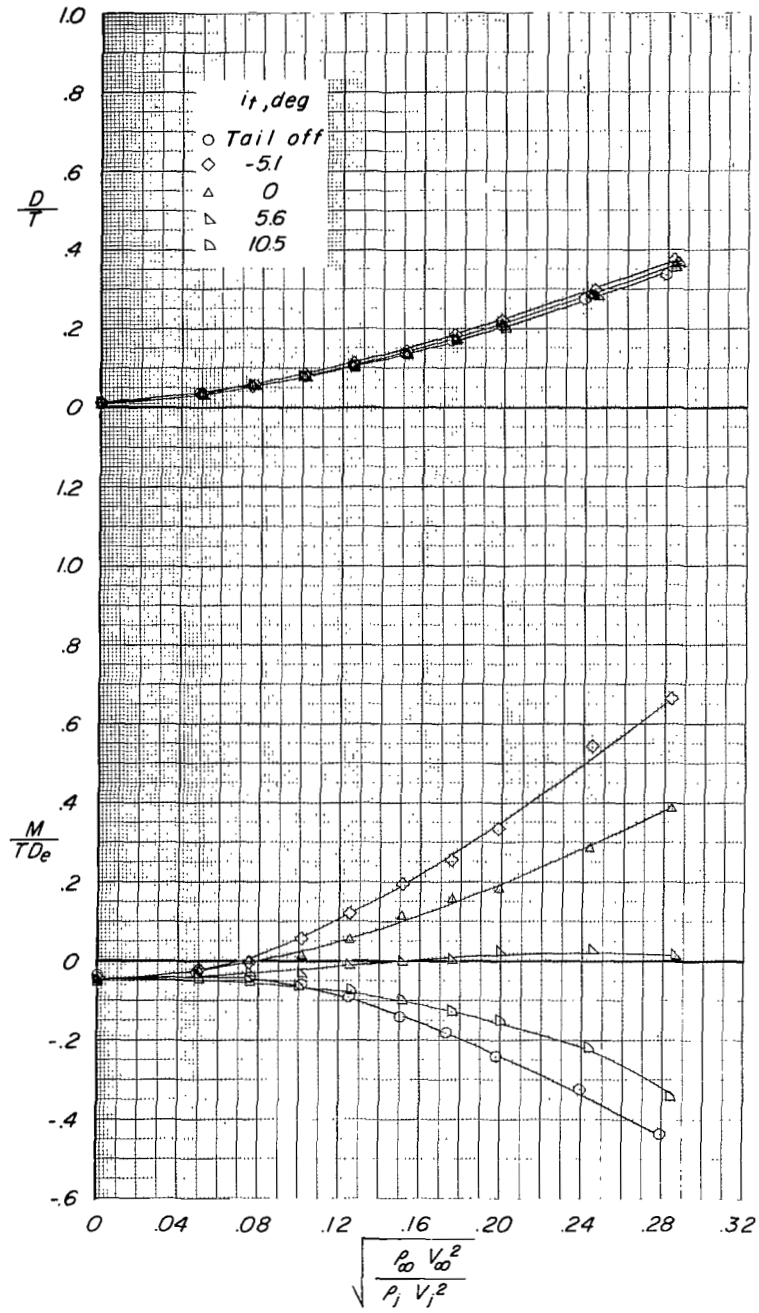

(b) Variation of D/T and M/TD_e with effective velocity ratio.

Figure 23.- Concluded.

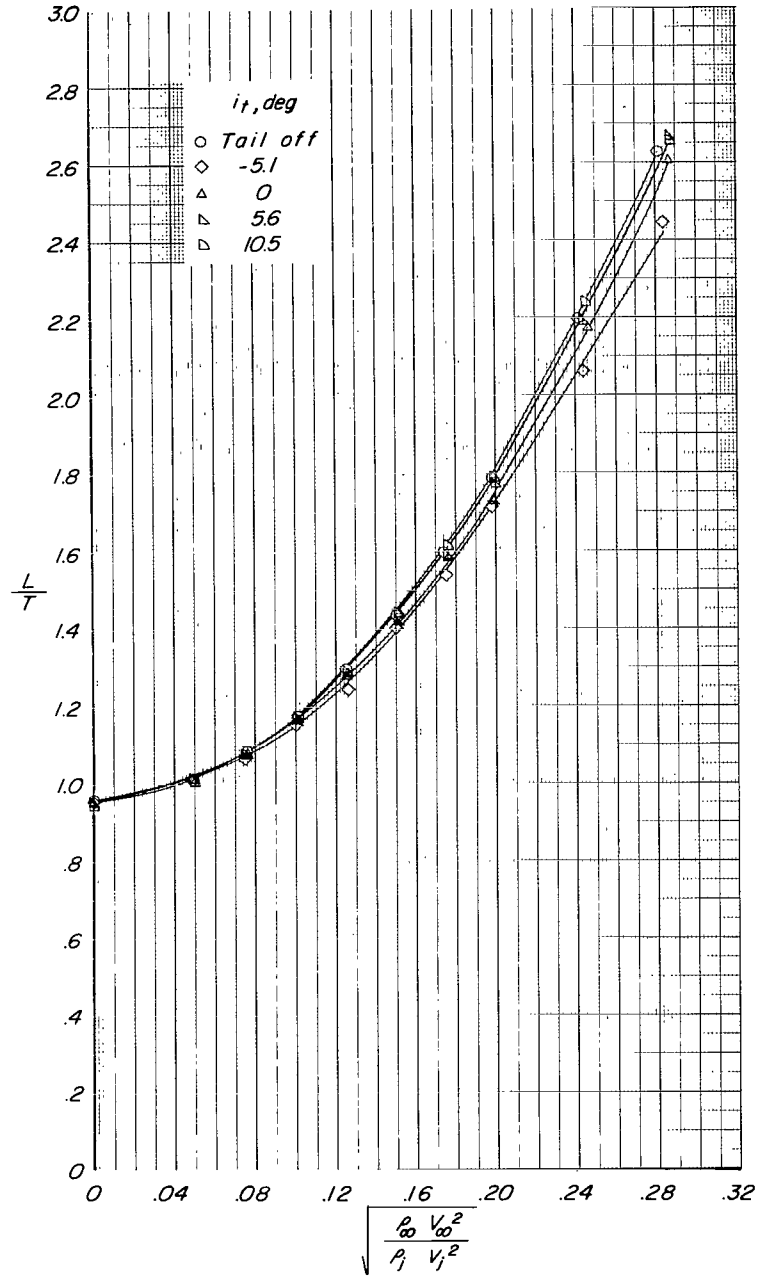

(a) Variation of L/T with effective velocity ratio.

Figure 24.- Effect of tail incidence on longitudinal aerodynamic characteristics for configuration A ($\delta_f = 30^0$, $\delta_s = 35^0$, fixed forewing) with tail in low position. $\alpha \approx 10.8^0$.

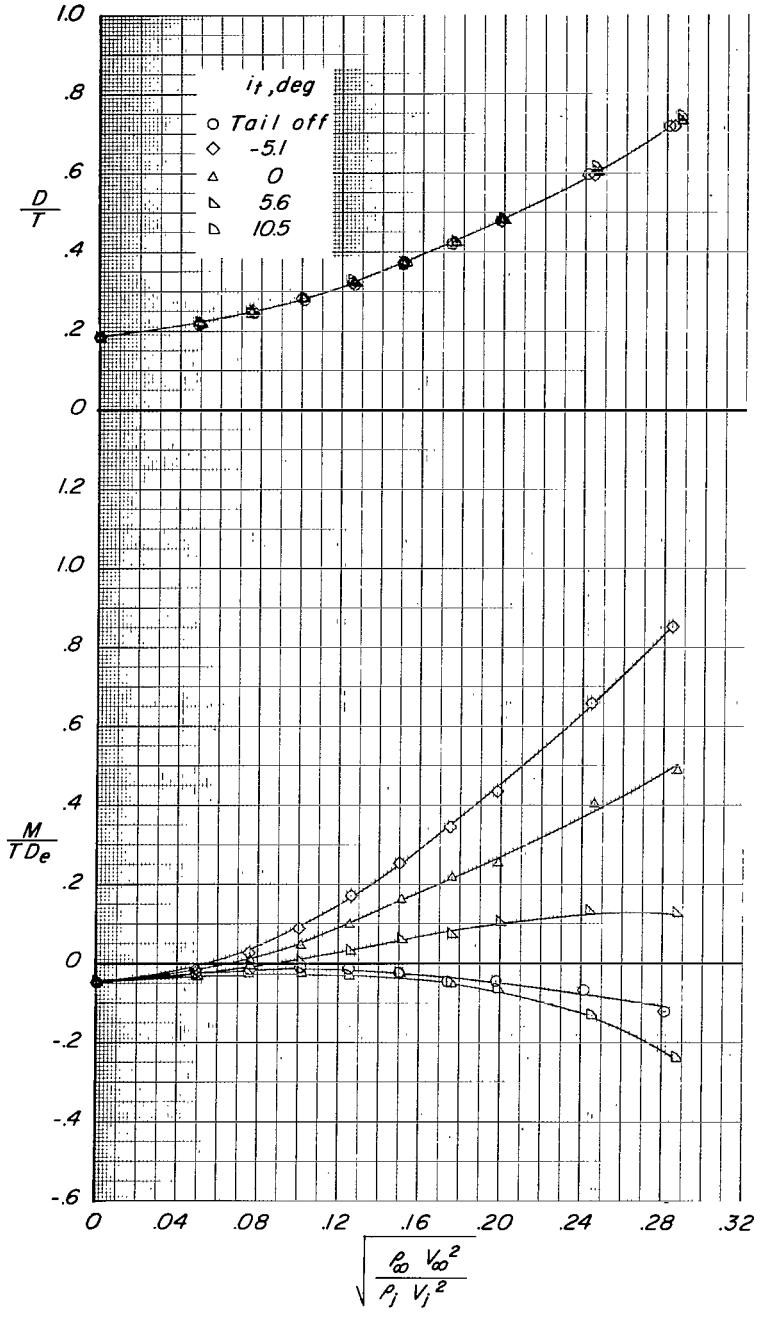

(b) Variation of D/T and M/TD_e with effective velocity ratio.

Figure 24.- Concluded.

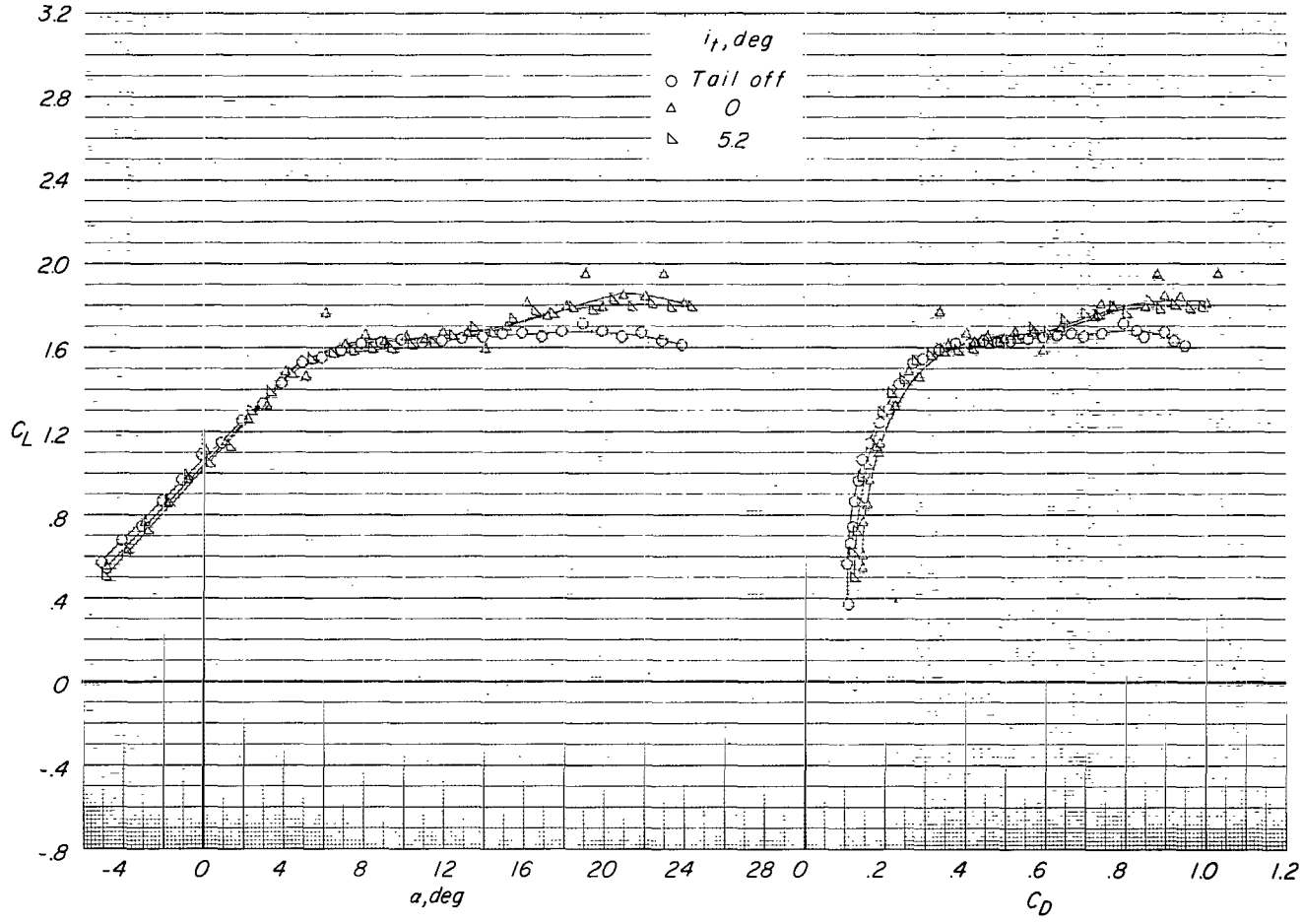

(a) Variation of C_L with α and C_D.

Figure 25.- Effect of tail incidence on longitudinal aerodynamic characteristics for configuration B ($\delta_f = 30^0$) with tail in mid position. $C_T = 0$.

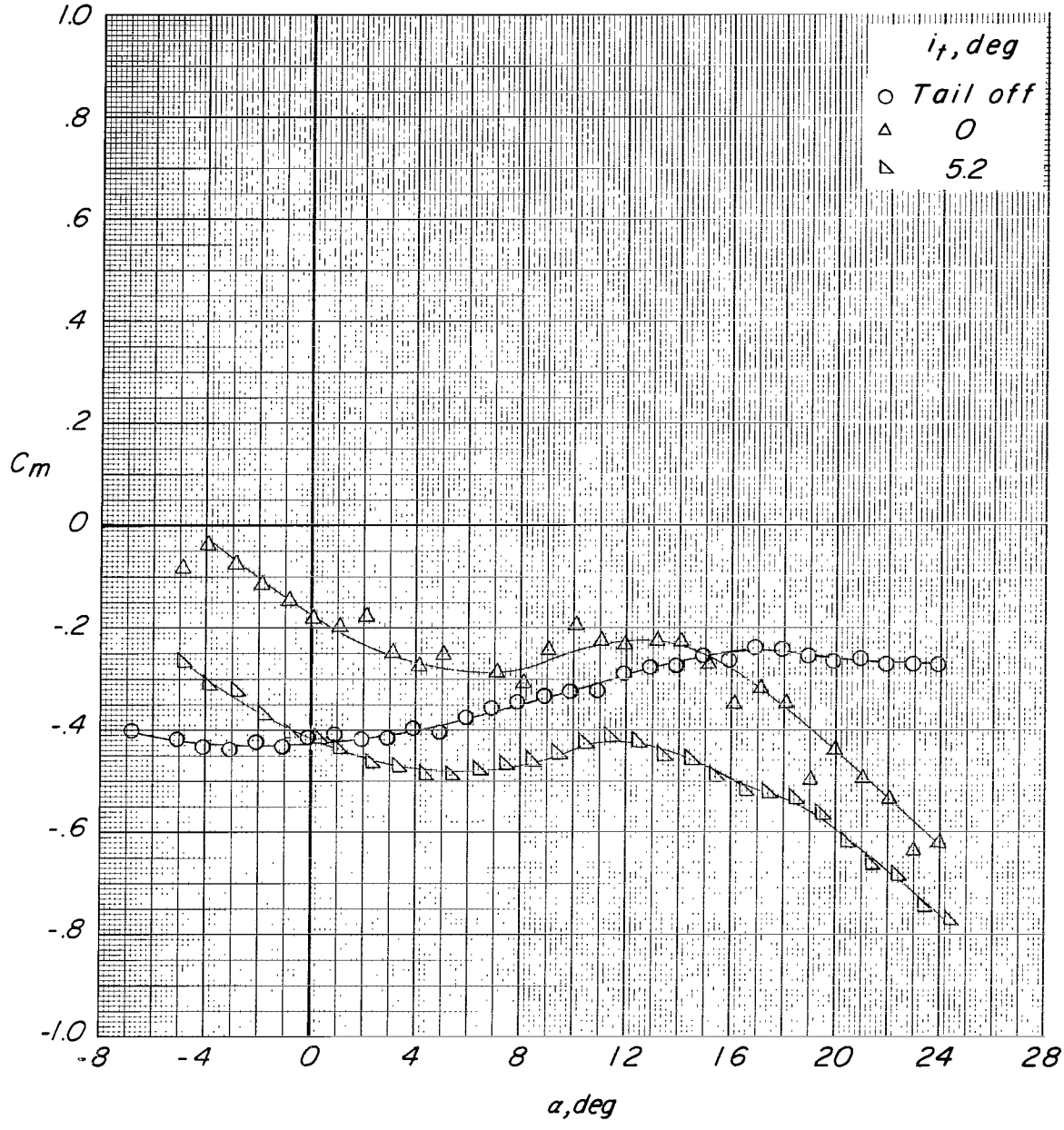

(b) Variation of C_m with α.

Figure 25.- Continued.

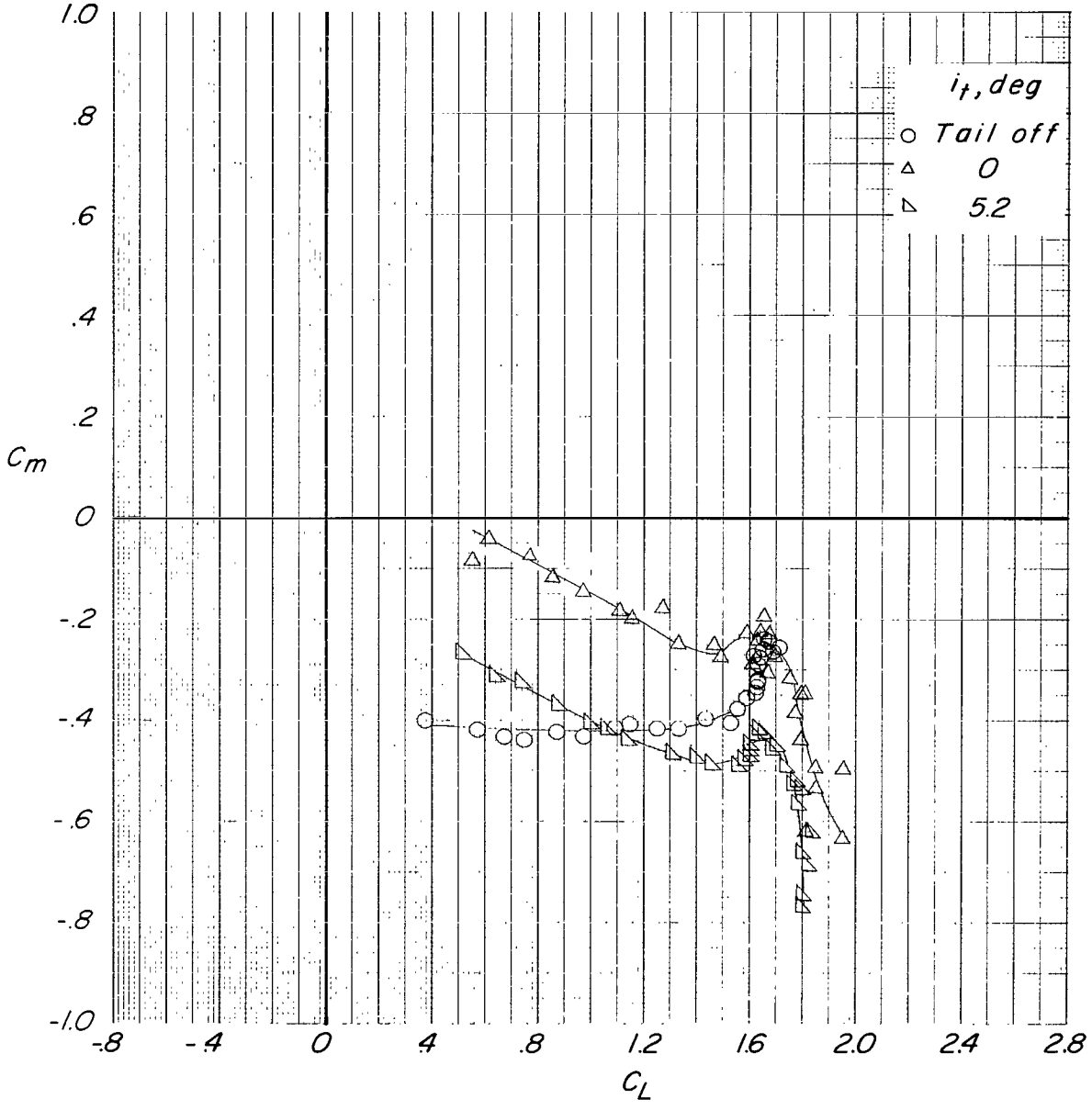

(c) Variation of C_m with C_L.

Figure 25.- Concluded.

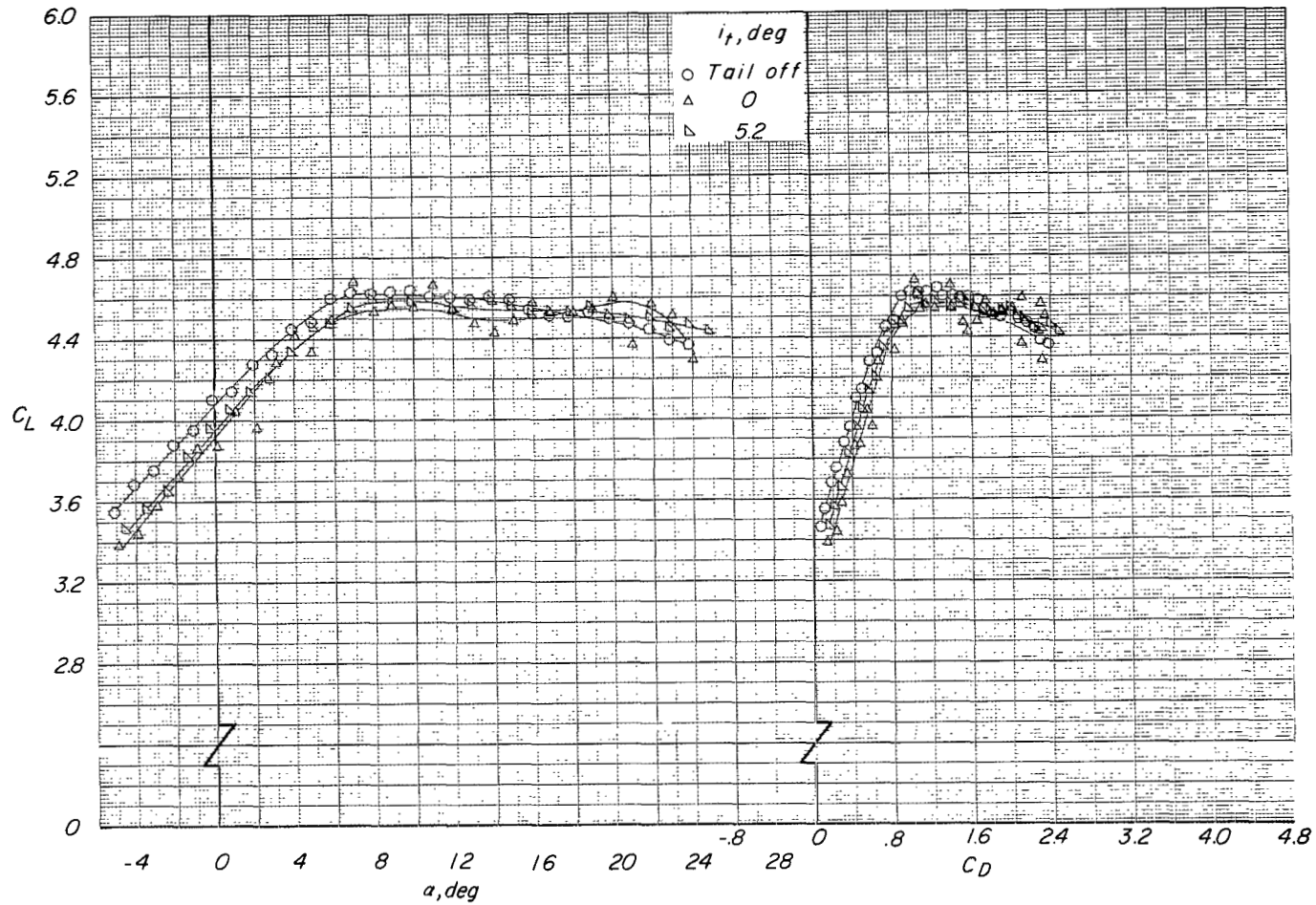

(a) Variation of C_L with α and C_D.

Figure 26.- Effect of tail incidence on longitudinal aerodynamic characteristics for configuration B (δ_f = 30°) with tail in mid position. C_T = 3.3.

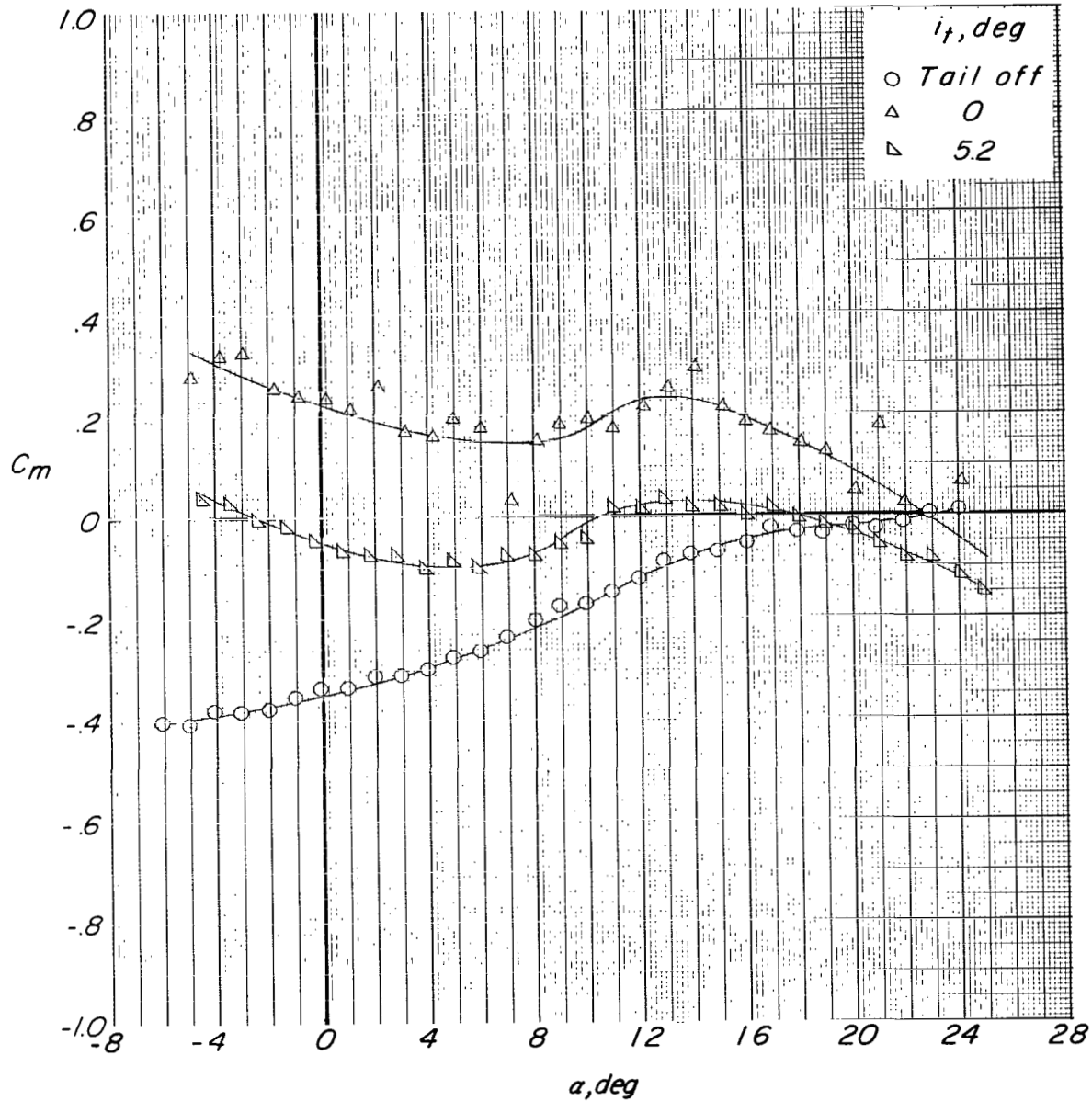

(b) Variation of C_m with α.

Figure 26.- Concluded.

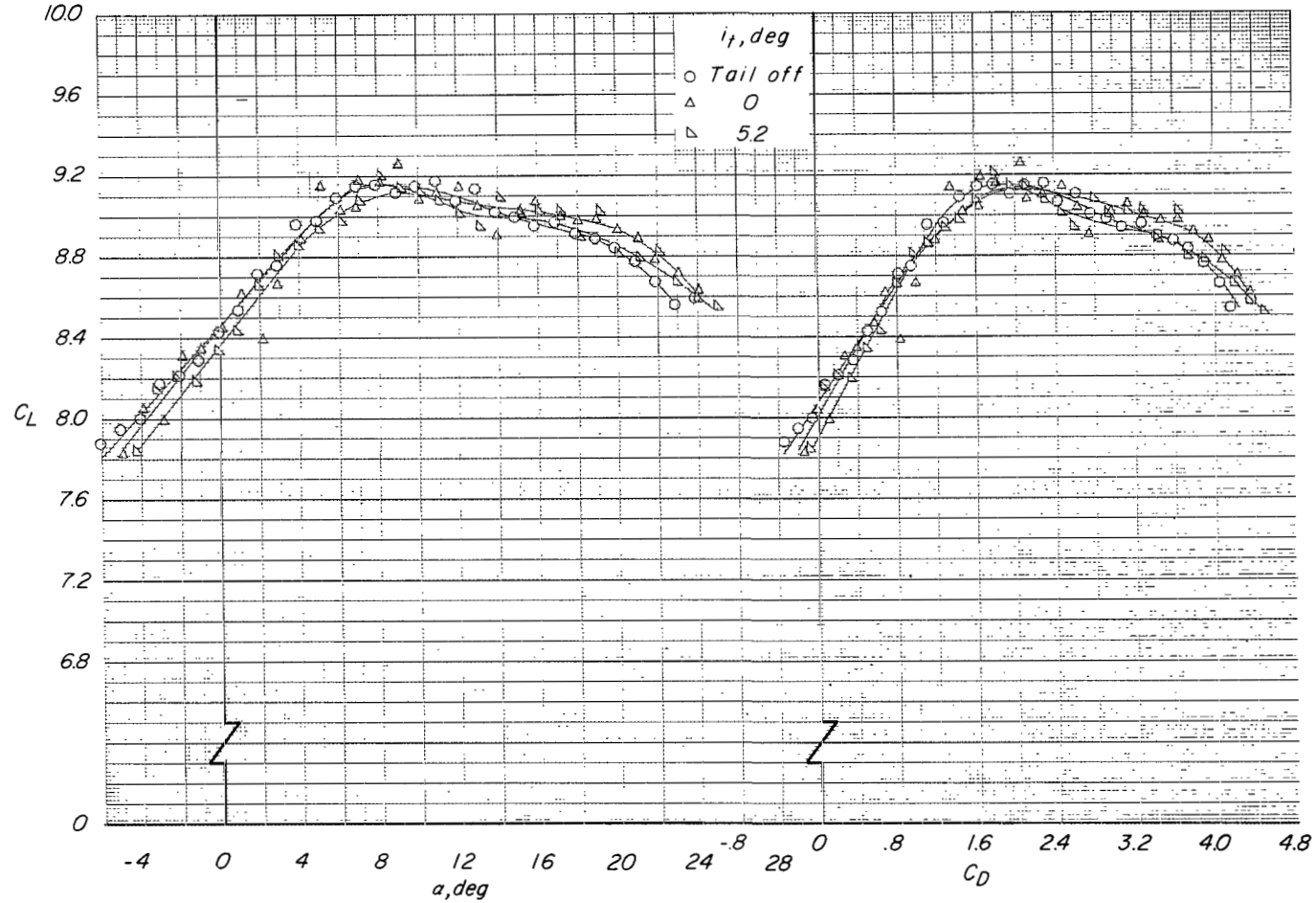

(a) Variation of C_L with α and C_D.

Figure 27.- Effect of tail incidence on longitudinal aerodynamic characteristics for configuration B (δ_f = 30°) with tail in mid position. C_T = 7.9.

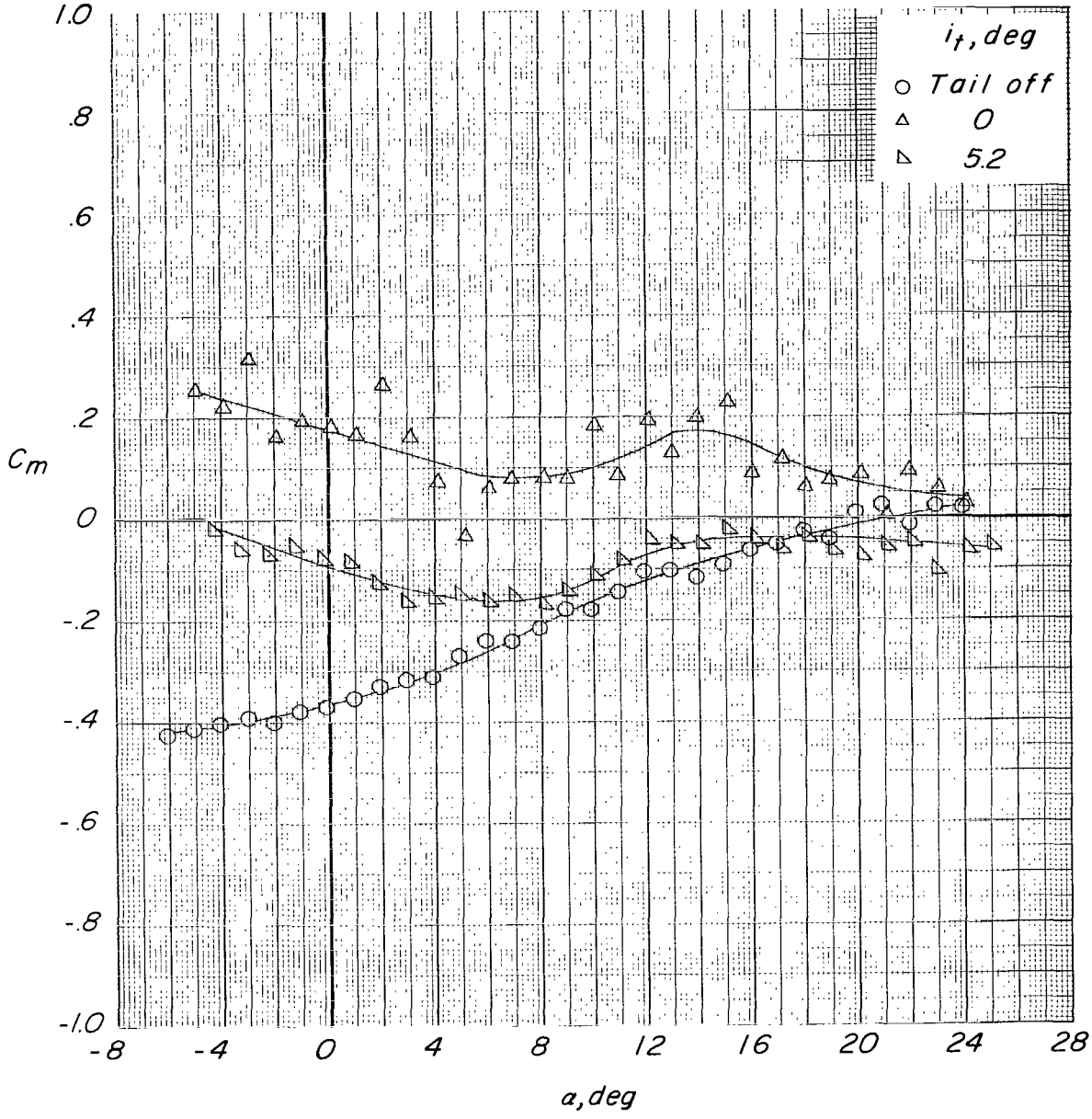

(b) Variation of C_m with α.

Figure 27.- Concluded.

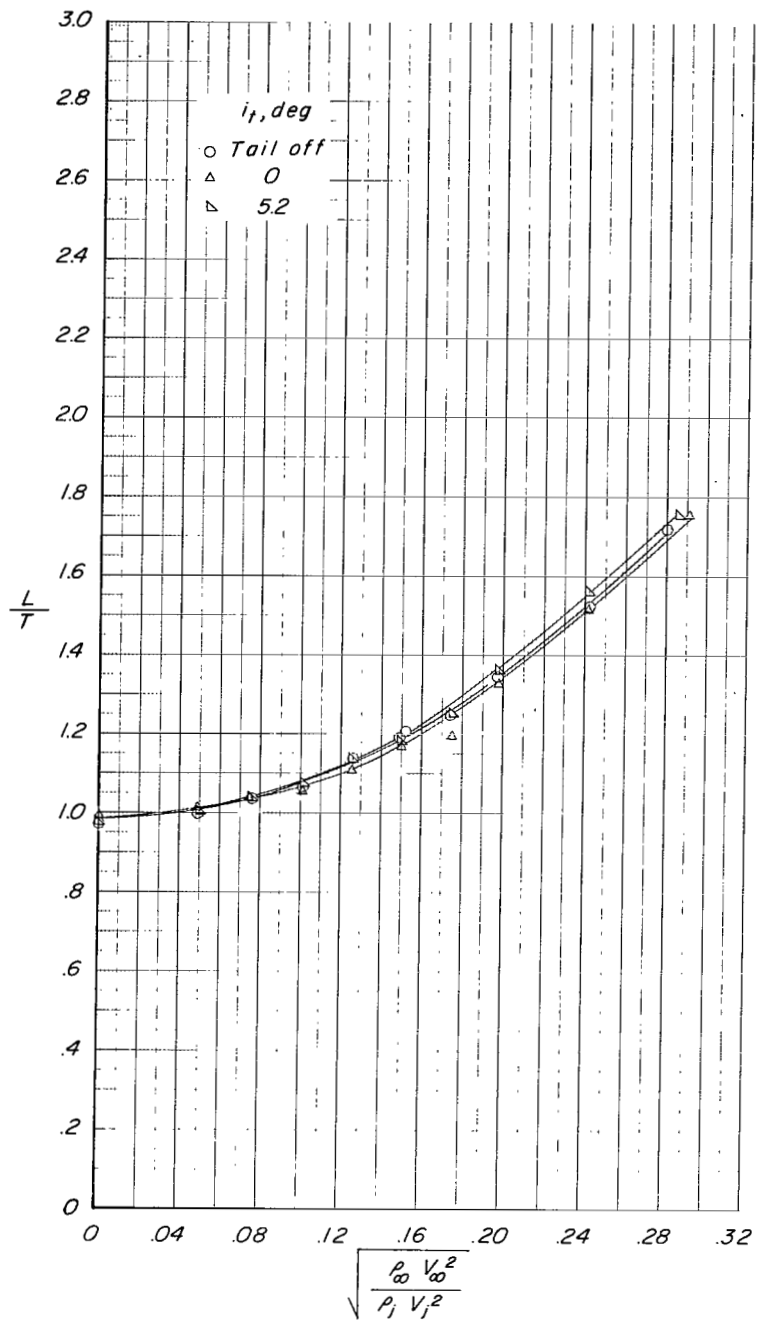

(a) Variation of L/T with effective velocity ratio.

Figure 28.- Effect of tail incidence on longitudinal aerodynamic characteristics for configuration B (δ_f = 30°) with tail in mid position. $\alpha \approx 0.6^0$.

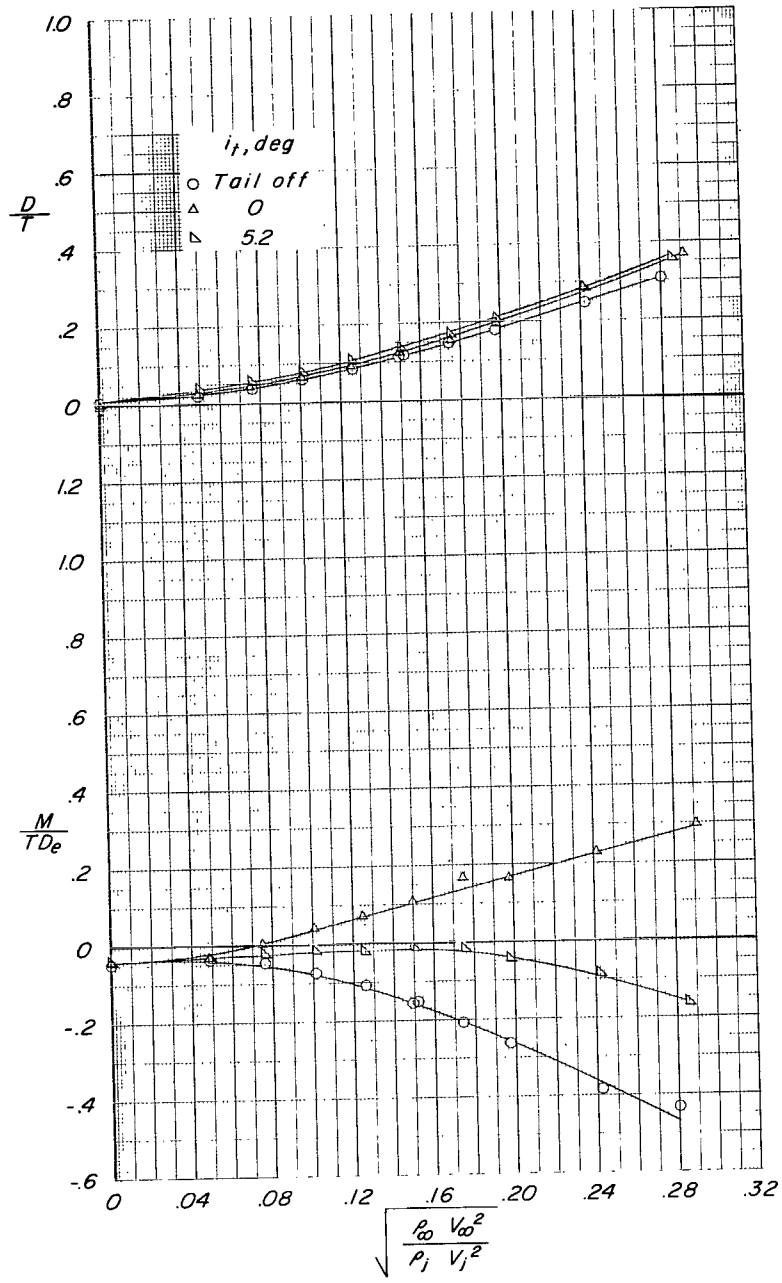

(b) Variation of D/T and M/TD_e with effective velocity ratio.

Figure 28.- Concluded.

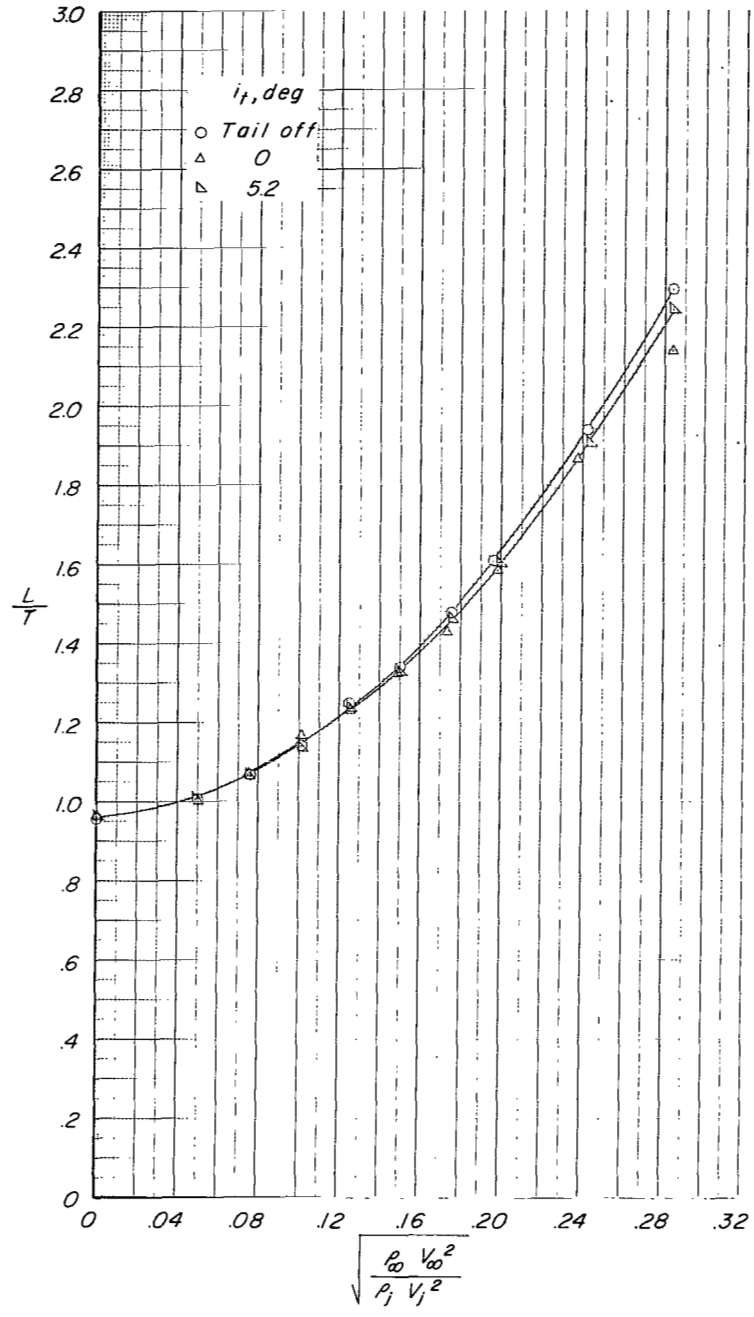

(a) Variation of L/T with effective velocity ratio.

Figure 29.- Effect of tail incidence on longitudinal aerodynamic characteristics for configuration B ($\delta_f = 30^0$) with tail in mid position. $\alpha \approx 10.8^0$.

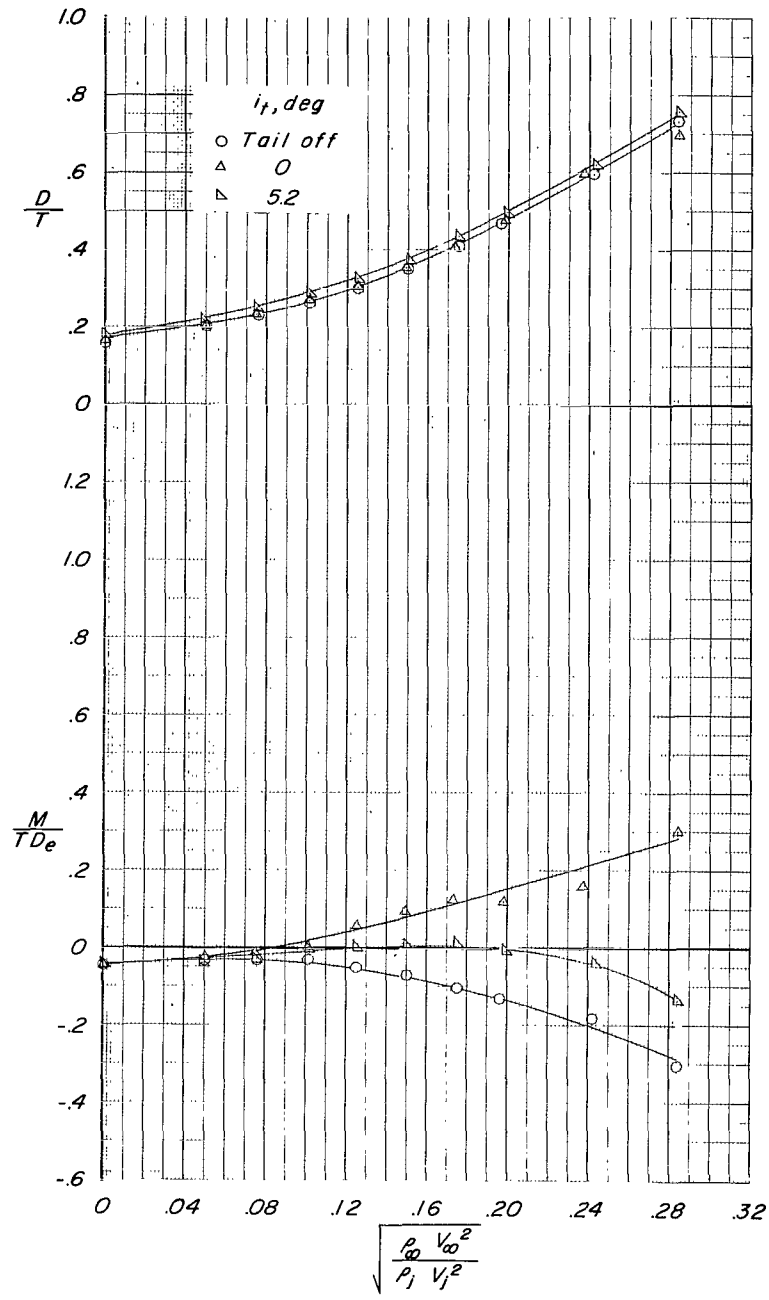

(b) Variation of D/T and M/TD_e with effective velocity ratio.

Figure 29.- Concluded.

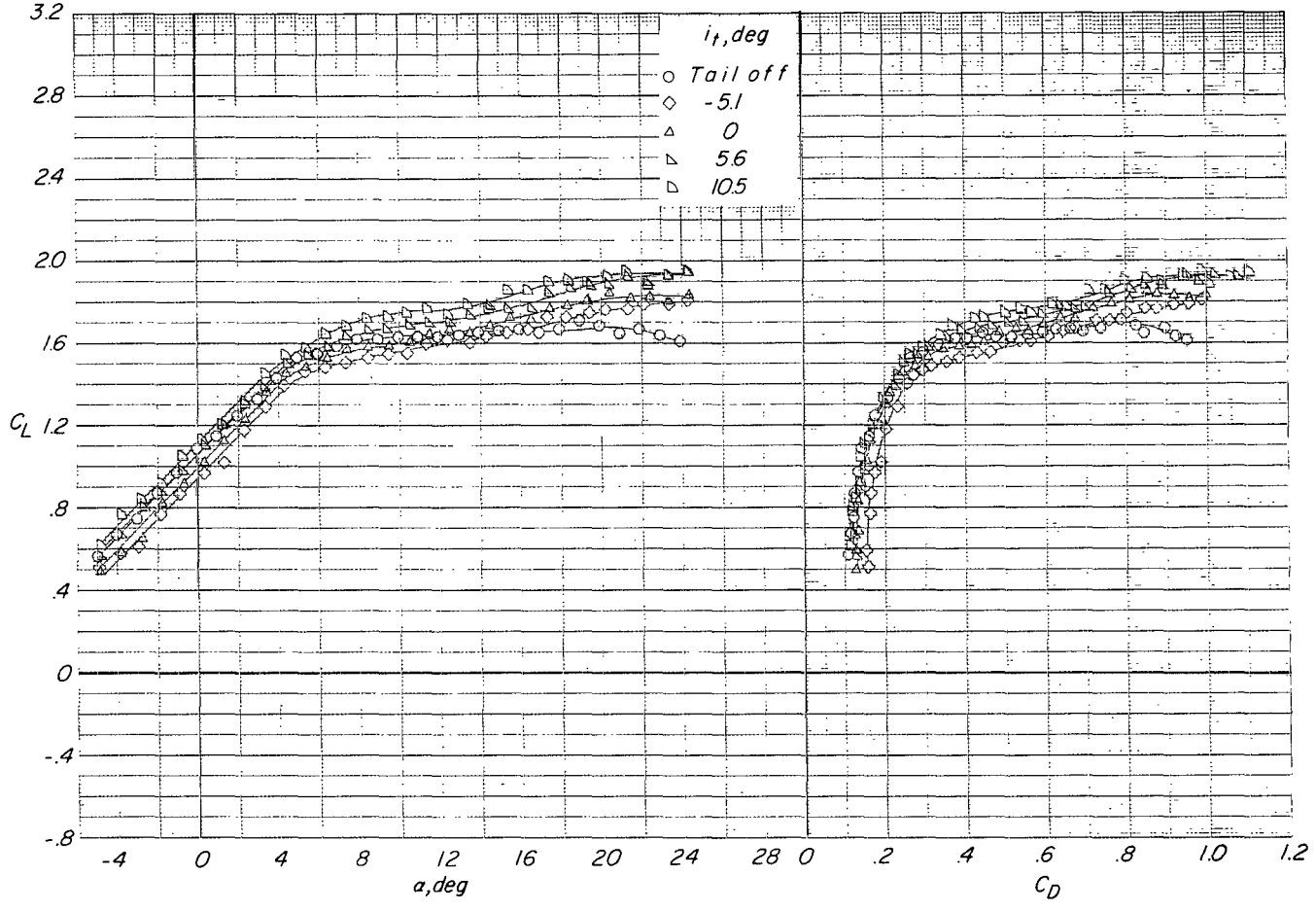

(a) Variation of C_L with α and C_D.

Figure 30.- Effect of tail incidence on longitudinal aerodynamic characteristics for configuration B ($\delta_f = 30^0$) with tail in low position. $C_T = 0$.

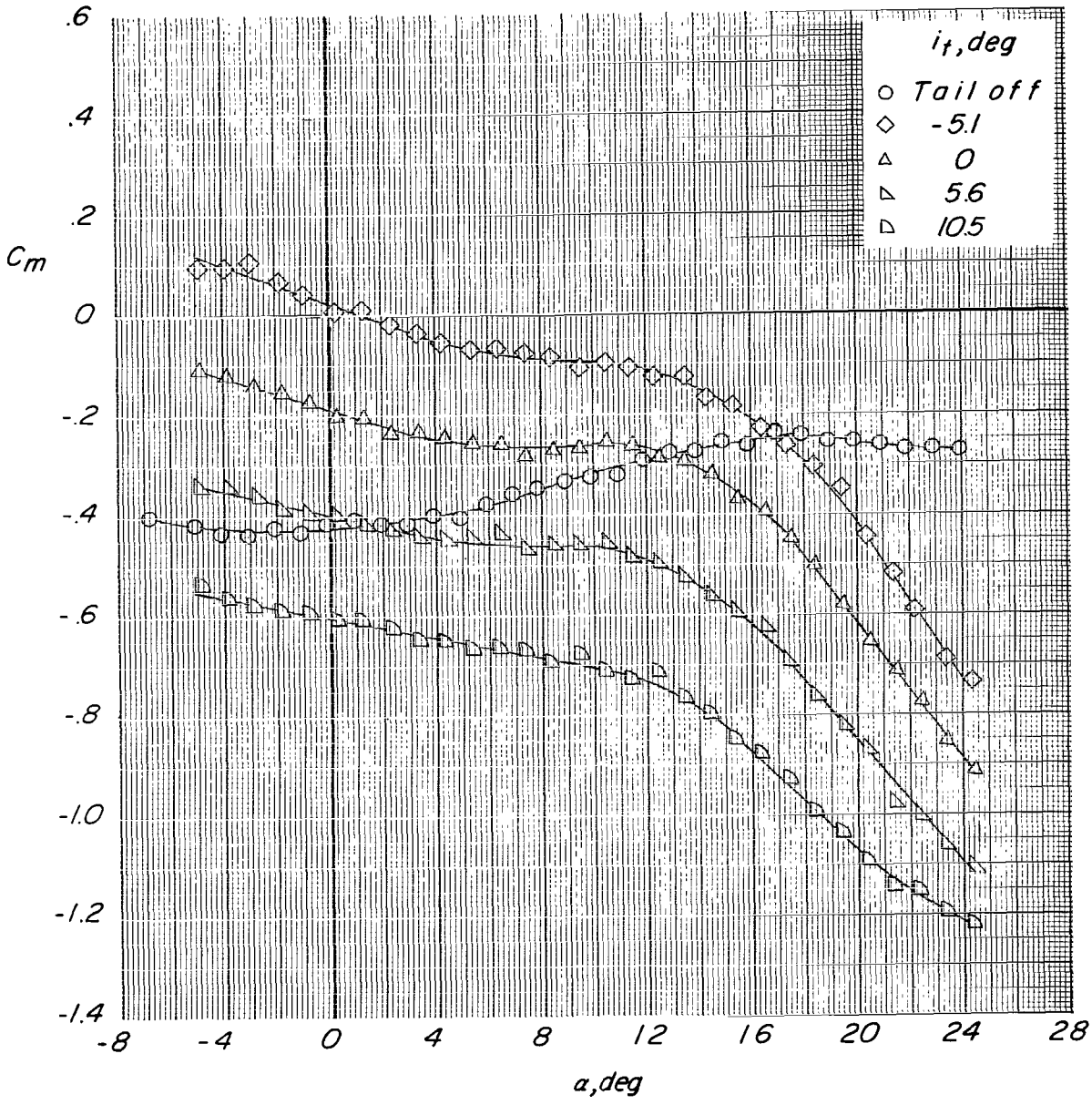

(b) Variation of C_m with α.

Figure 30.- Continued.

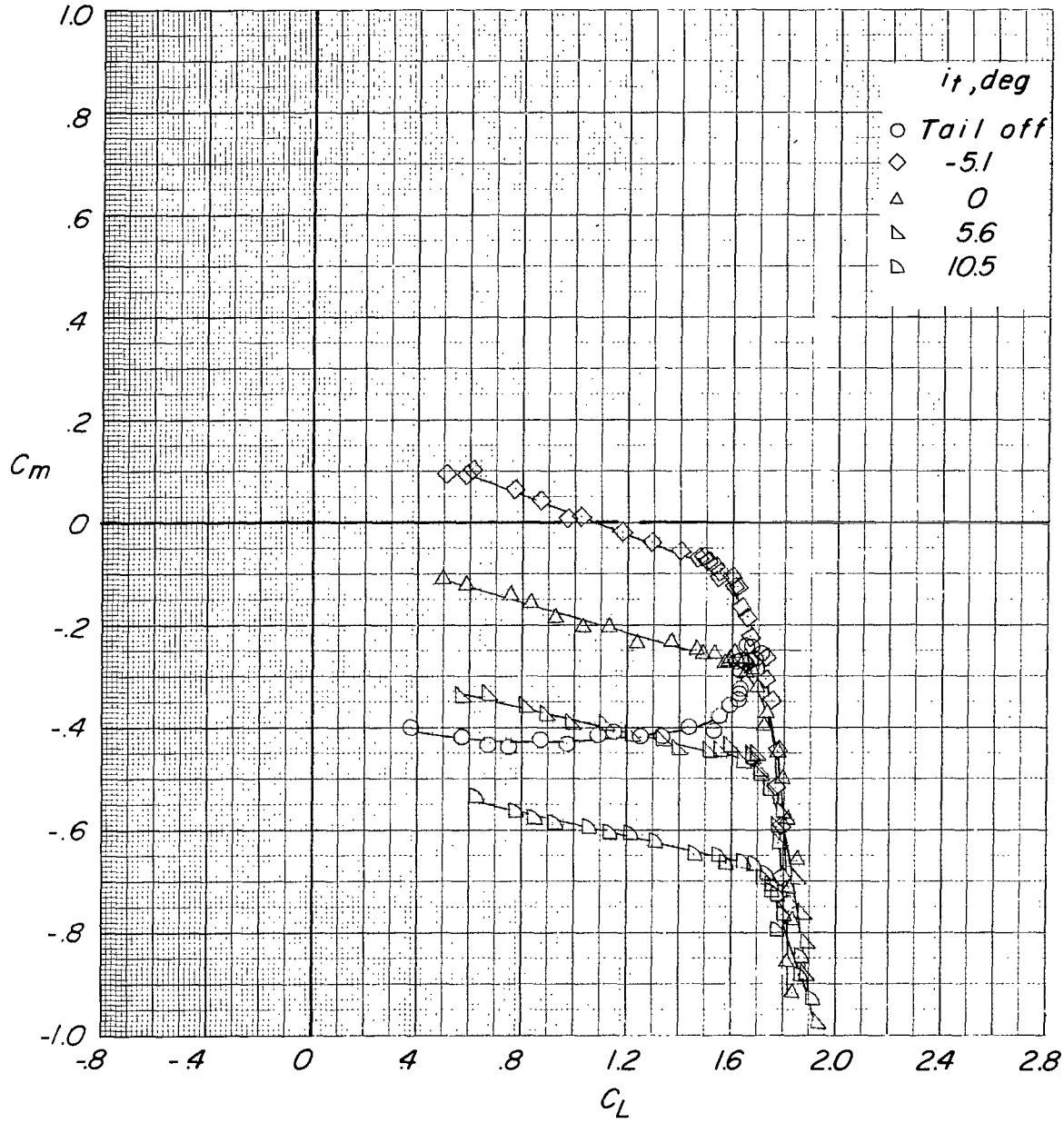

(c) Variation of C_m with C_L.

Figure 30.- Concluded.

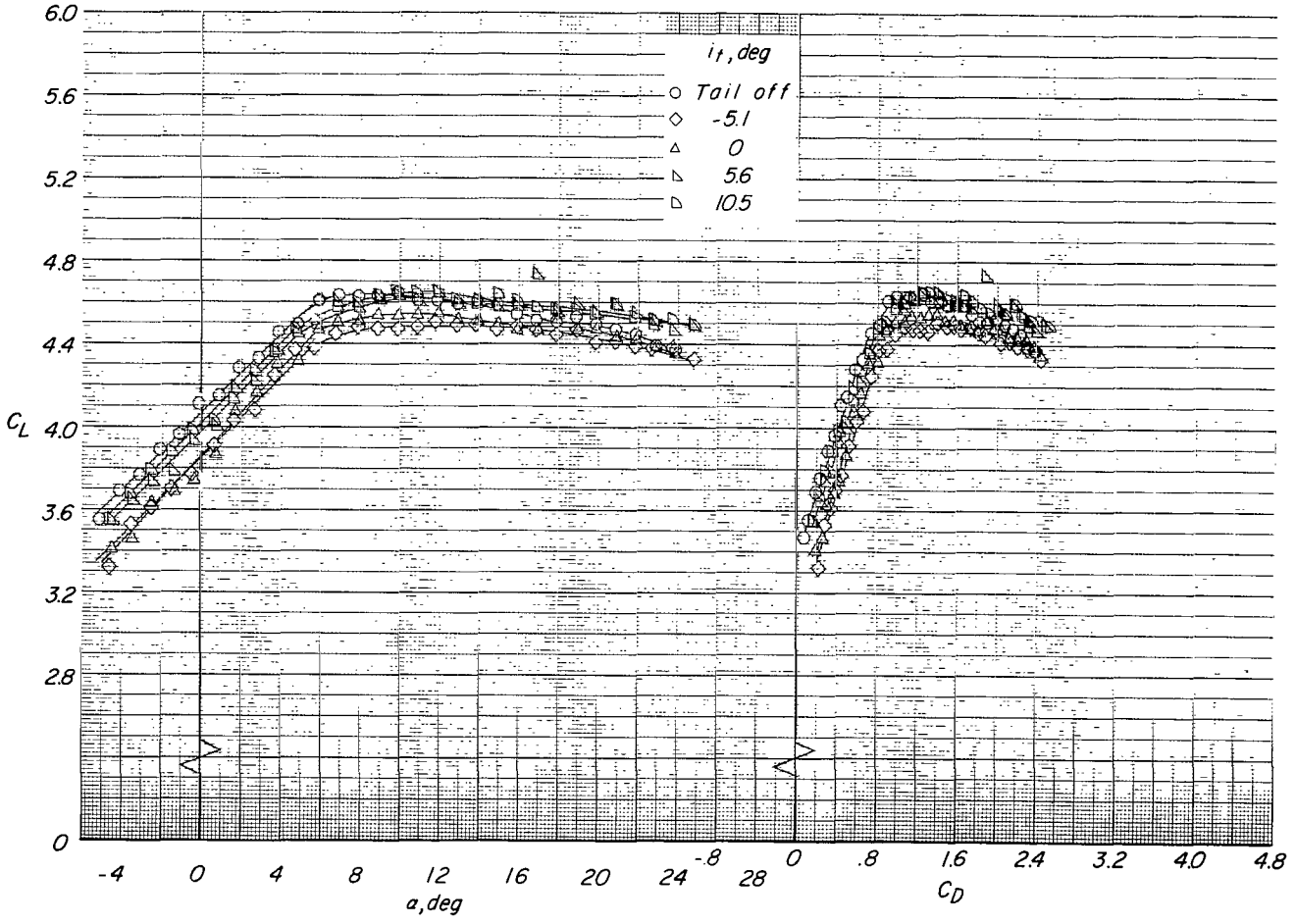

(a) Variation of C_L with α and C_D.

Figure 31.- Effect of tail incidence on longitudinal aerodynamic characteristics for configuration B ($\delta_f = 30^0$) with tail in low position. $C_T = 3.3$.

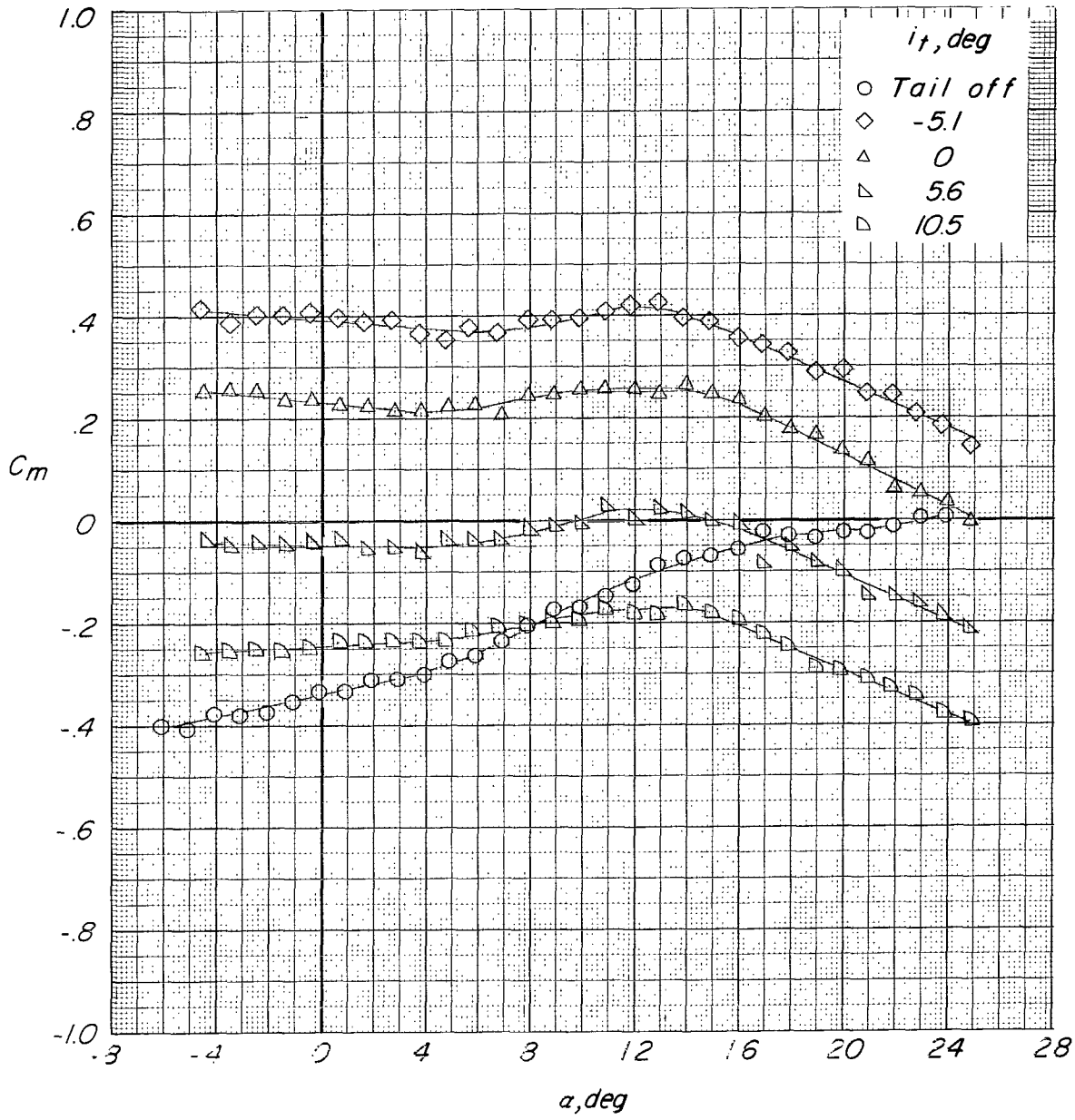

(b) Variation of C_m with α.

Figure 31.- Concluded.

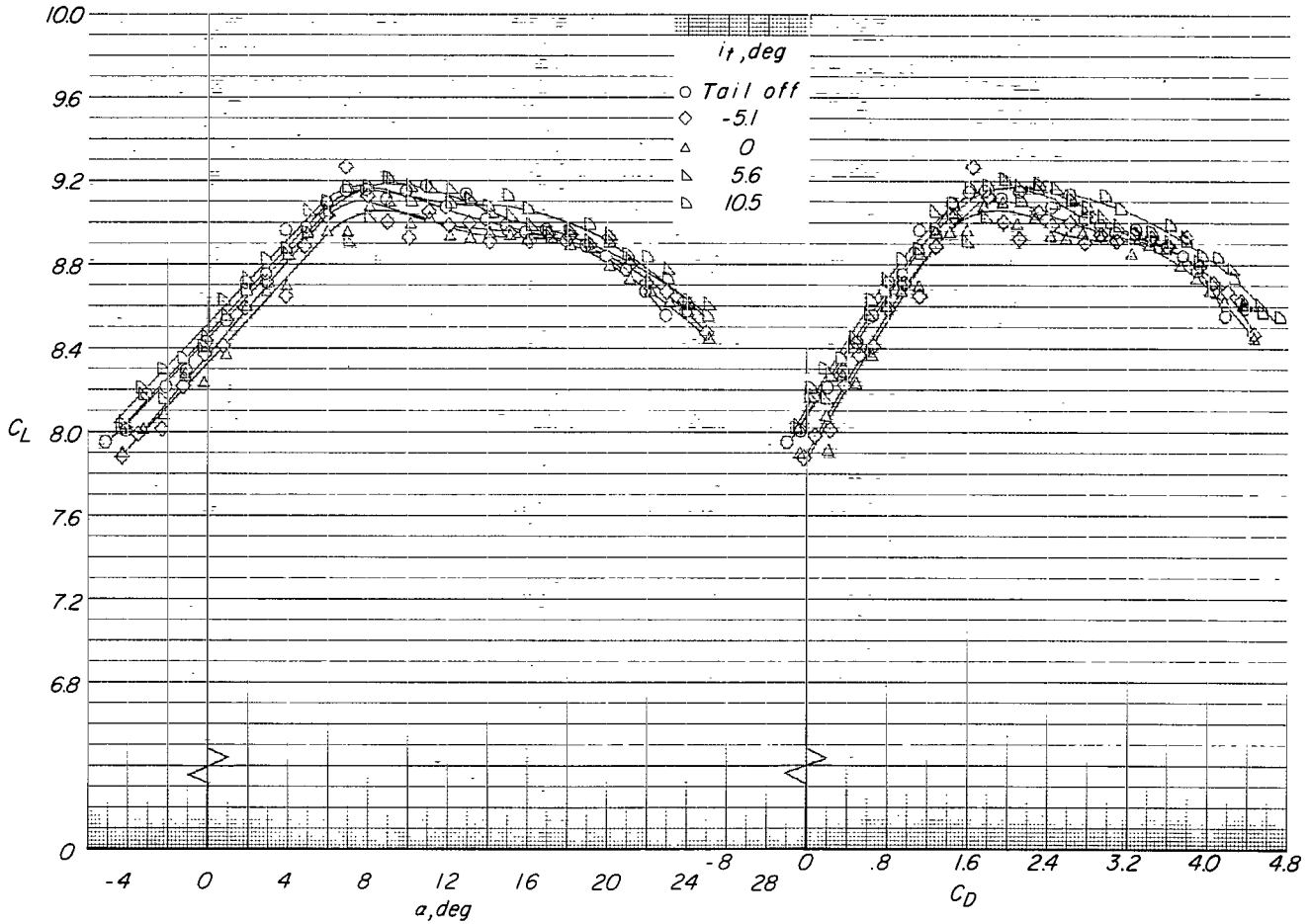

(a) Variation of C_L with α and C_D.

Figure 32.- Effect of tail incidence on longitudinal aerodynamic characteristics for configuration B ($\delta_f = 30^0$) with tail in low position. $C_T = 7.9$.

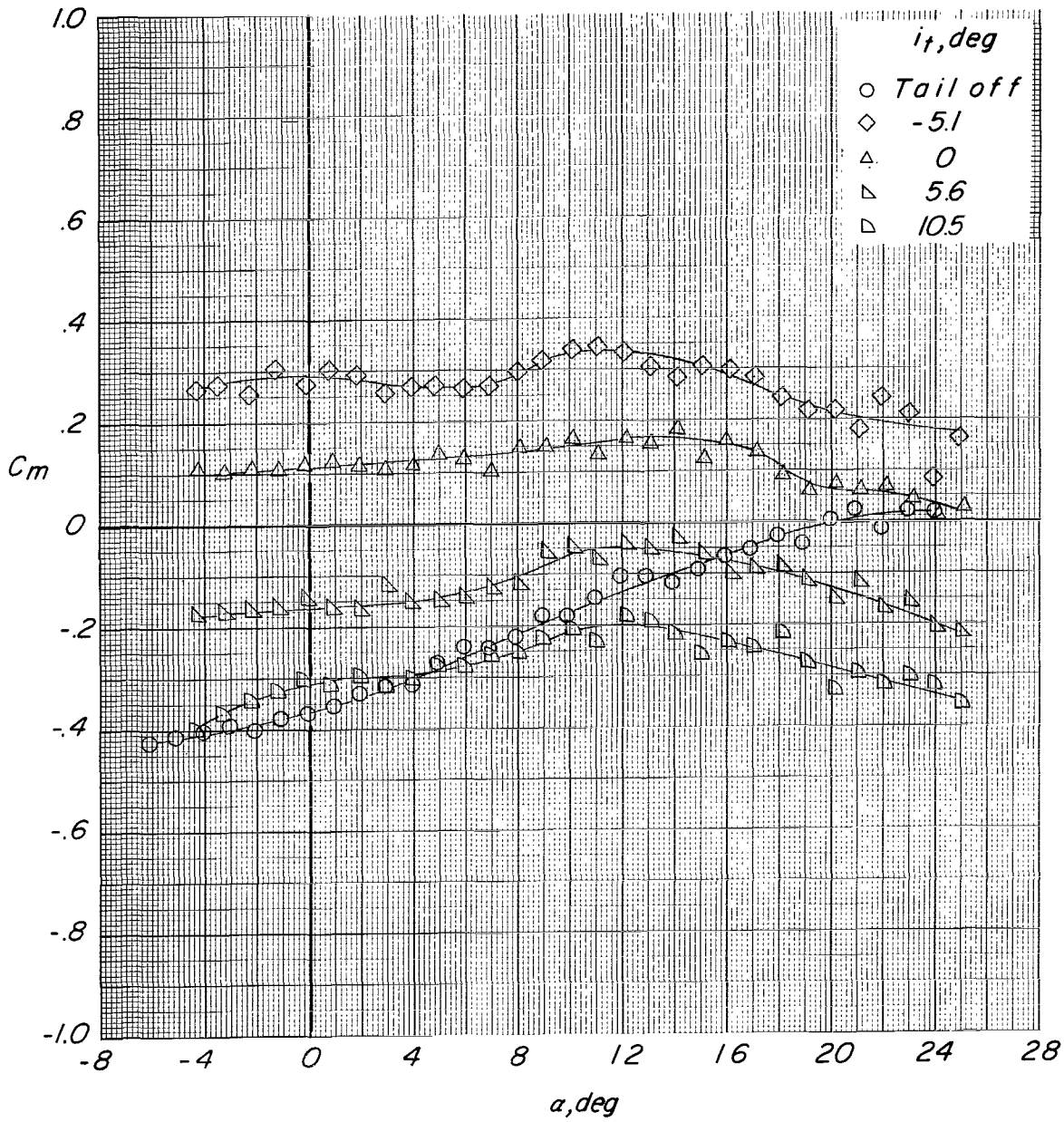

(b) Variation of C_m with α.

Figure 32.- Concluded.

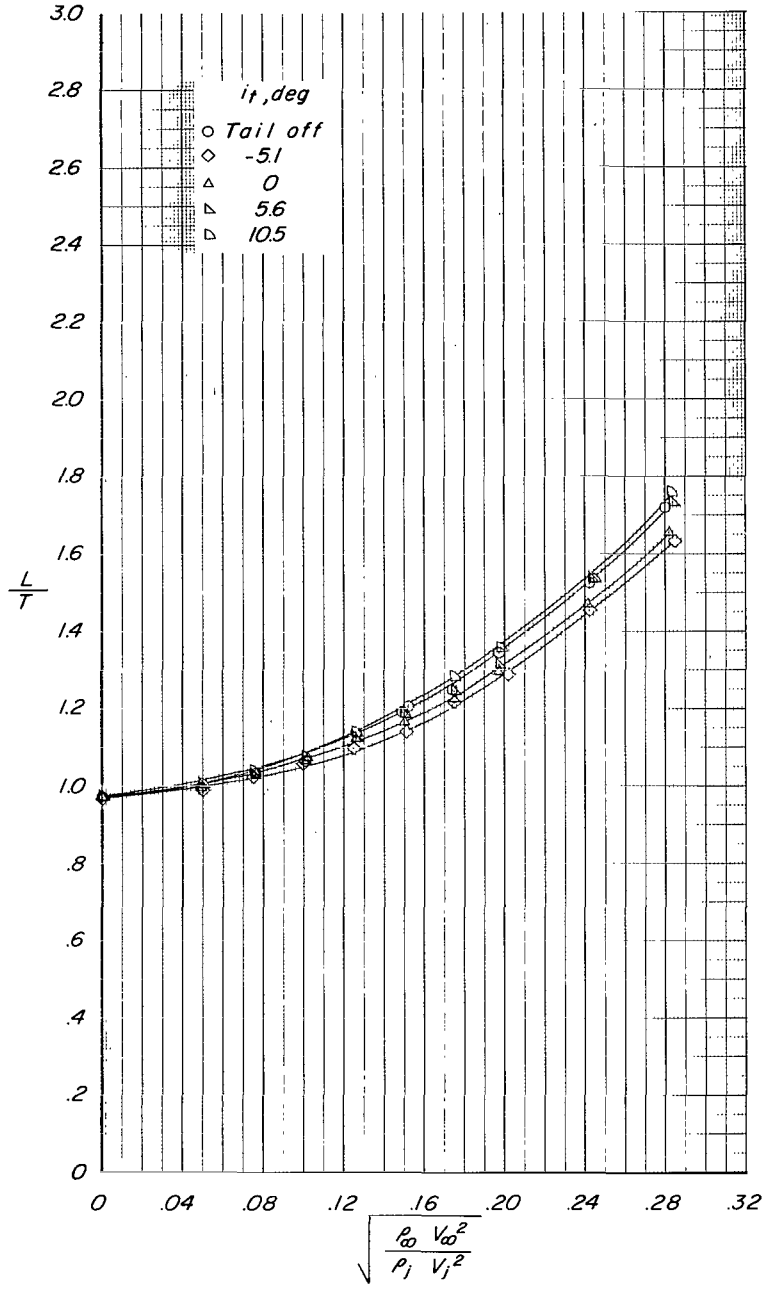

(a) Variation of L/T with effective velocity ratio.

Figure 33.- Effect of tail incidence on longitudinal aerodynamic characteristics for configuration B ($\delta_f = 30^0$) with tail in low position. $\alpha \approx 0.6^0$.

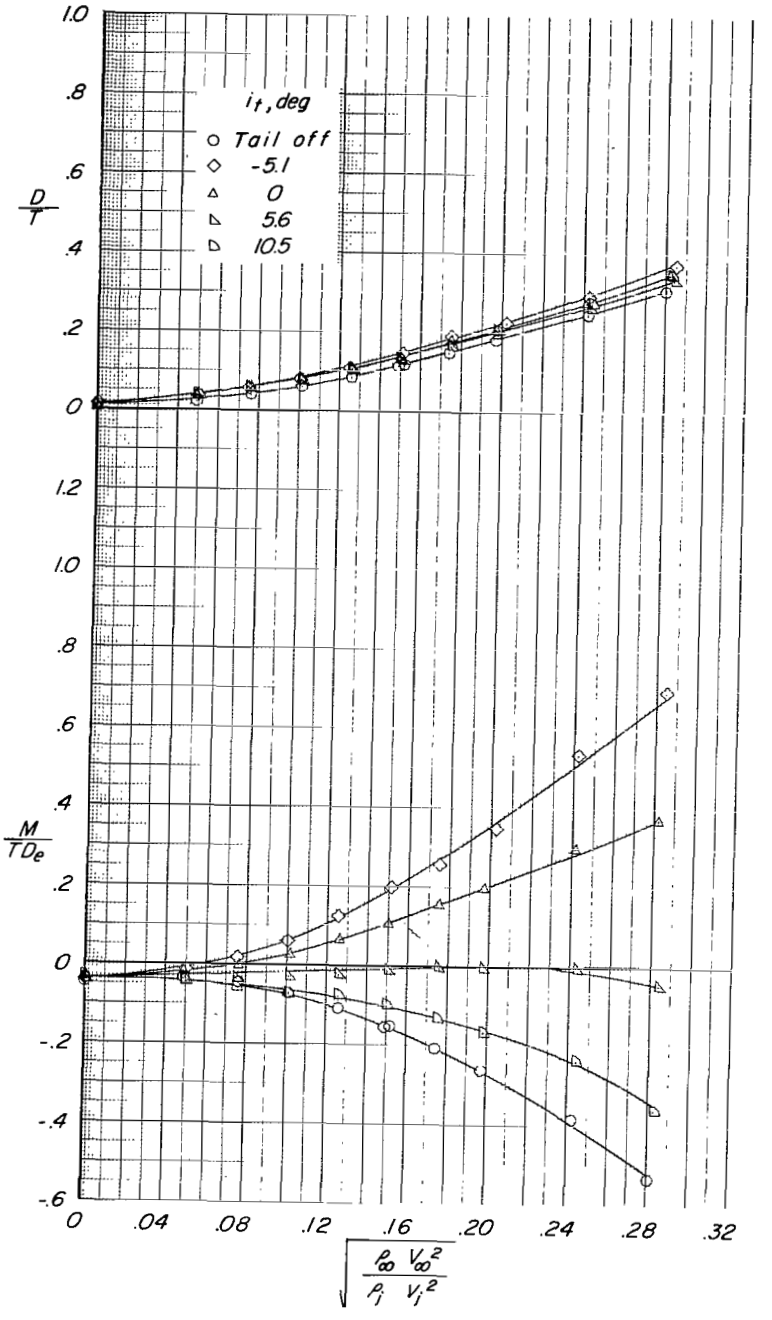

(b) Variation of D/T and M/TD_e with effective velocity ratio.

Figure 33.- Concluded.

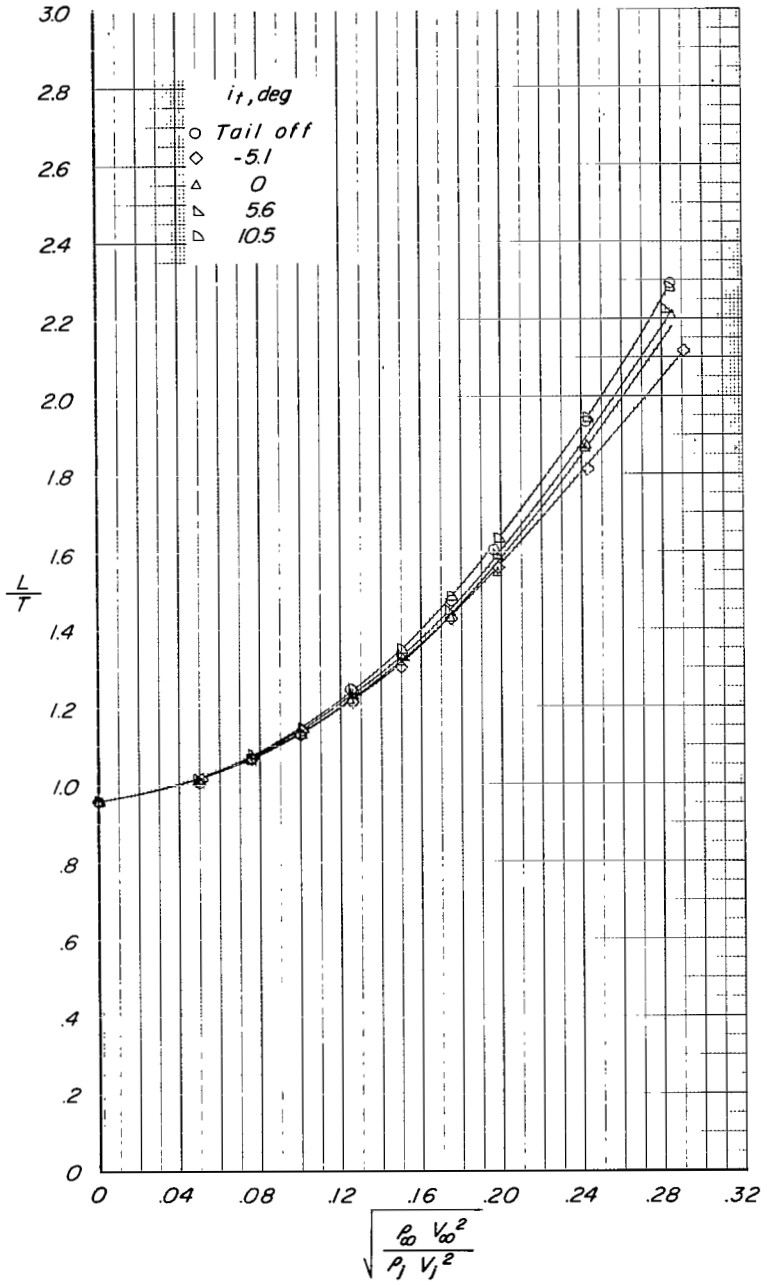

(a) Variation of L/T with effective velocity ratio.

Figure 34.- Effect of tail incidence on longitudinal aerodynamic characteristics for configuration B ($\delta_f = 30^0$) with tail in low position. $\alpha \approx 10.8^0$.

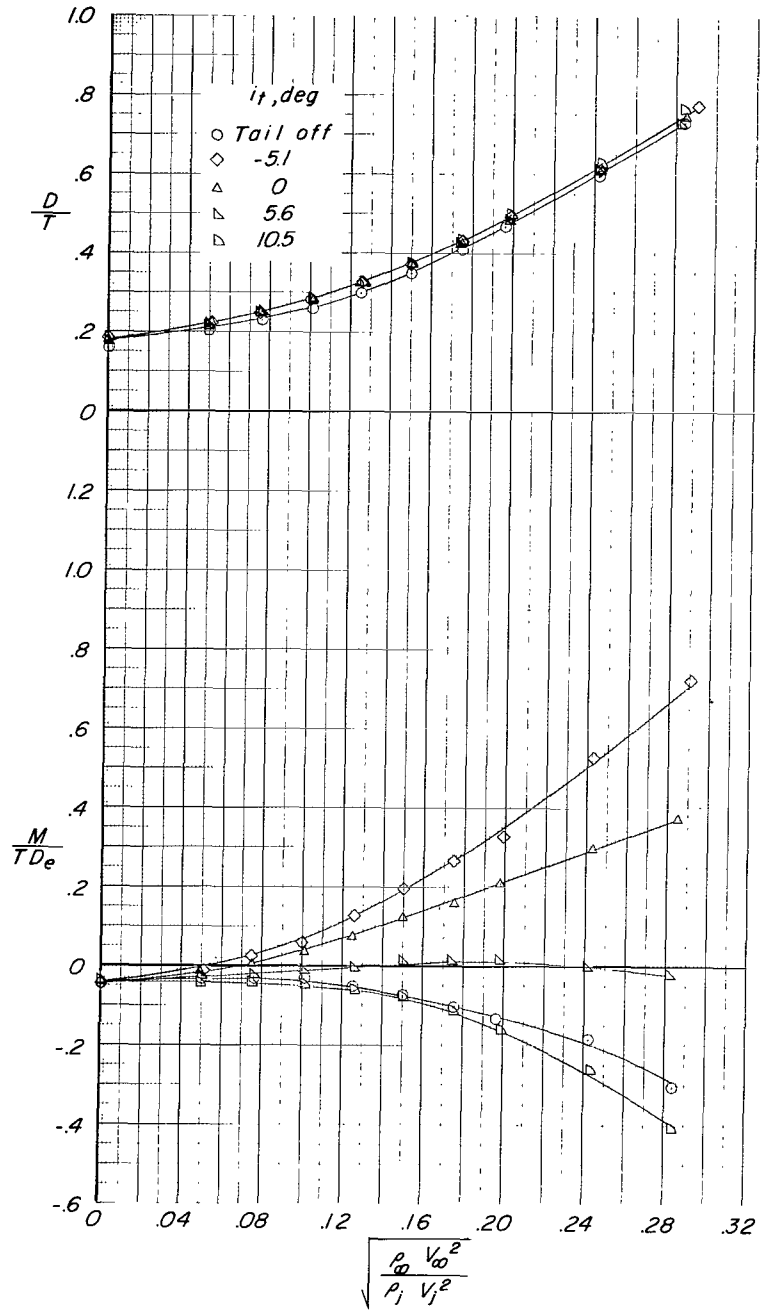

(b) Variation of D/T and M/TD_e with effective velocity ratio.

Figure 34.- Concluded.

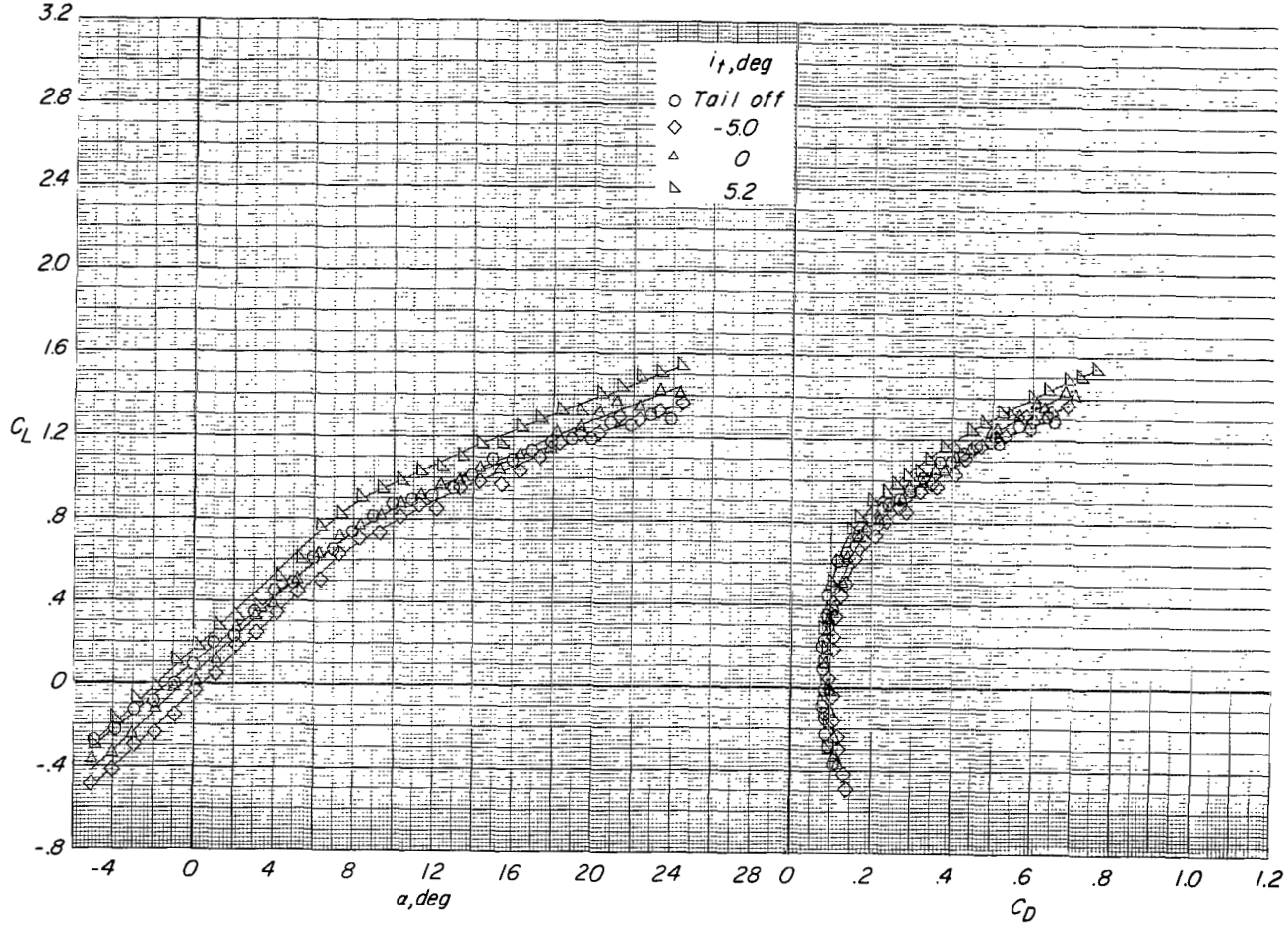

(a) Variation of C_L with α and C_D.

Figure 35.- Effect of tail incidence on longitudinal aerodynamic characteristics for configuration C ($\delta_f = 0^0$) with tail in mid position. $C_T = 0$.

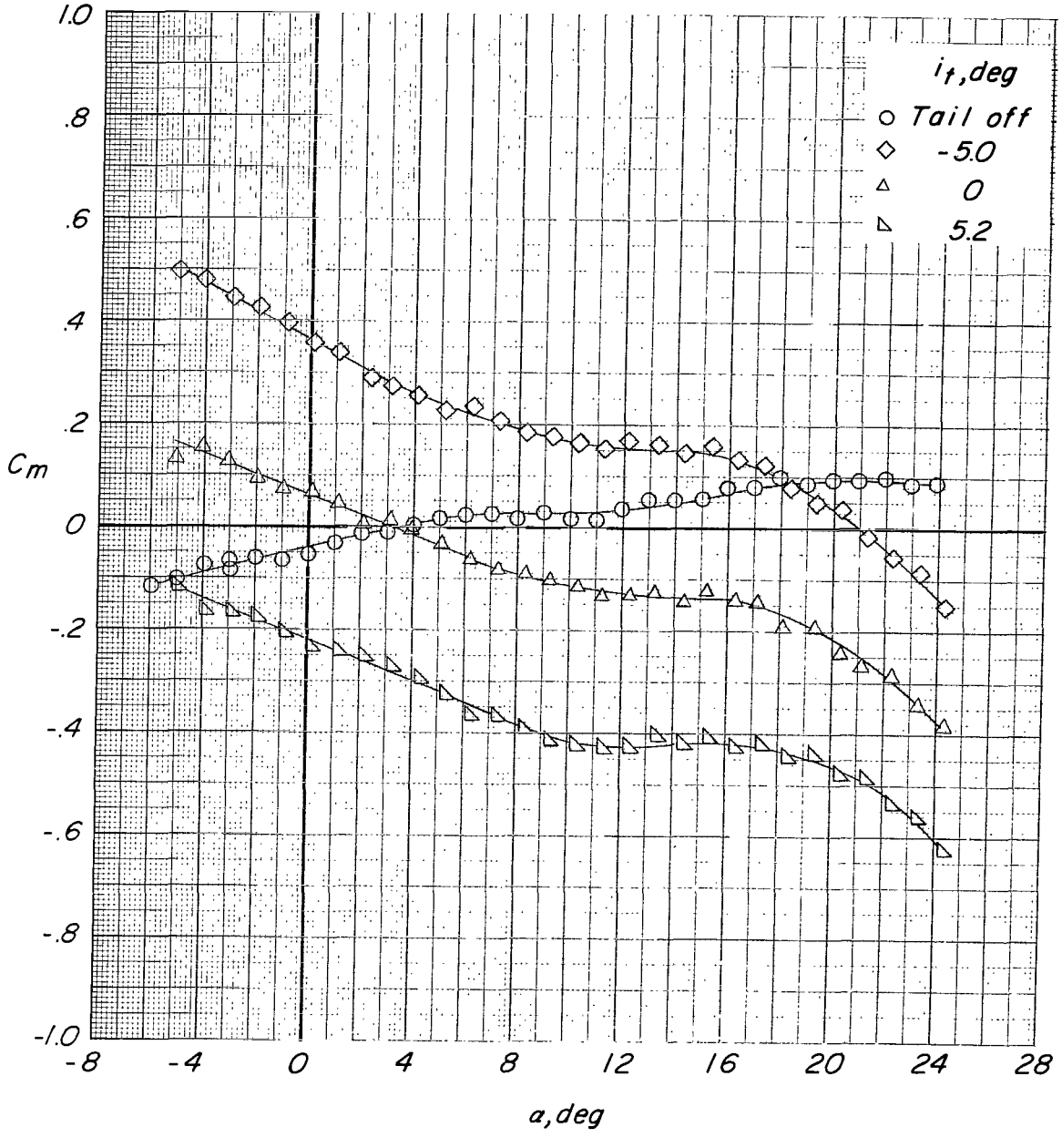

(b) Variation of C_m with α.

Figure 35.- Continued.

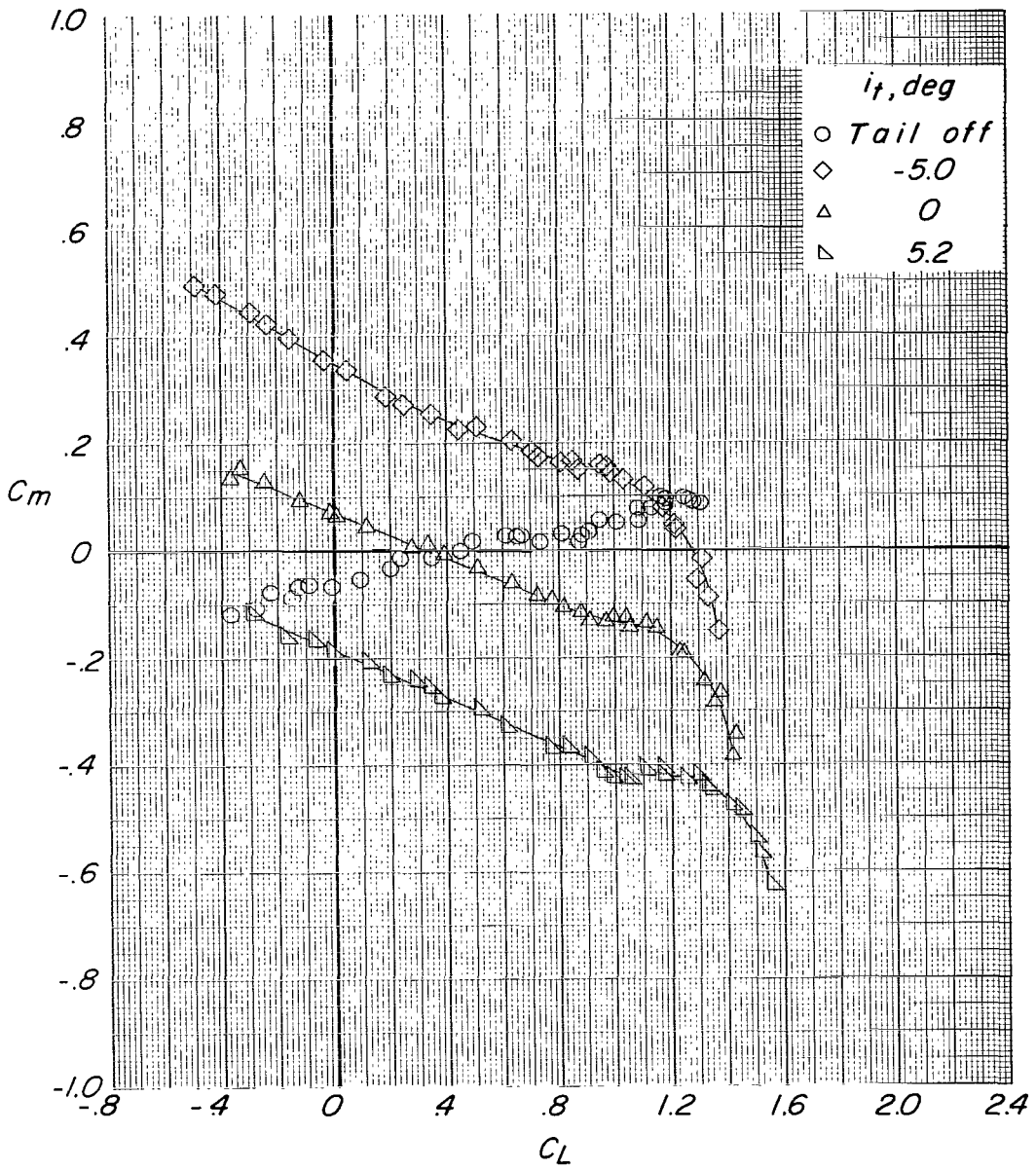

(c) Variation of C_m with C_L.

Figure 35.- Concluded.

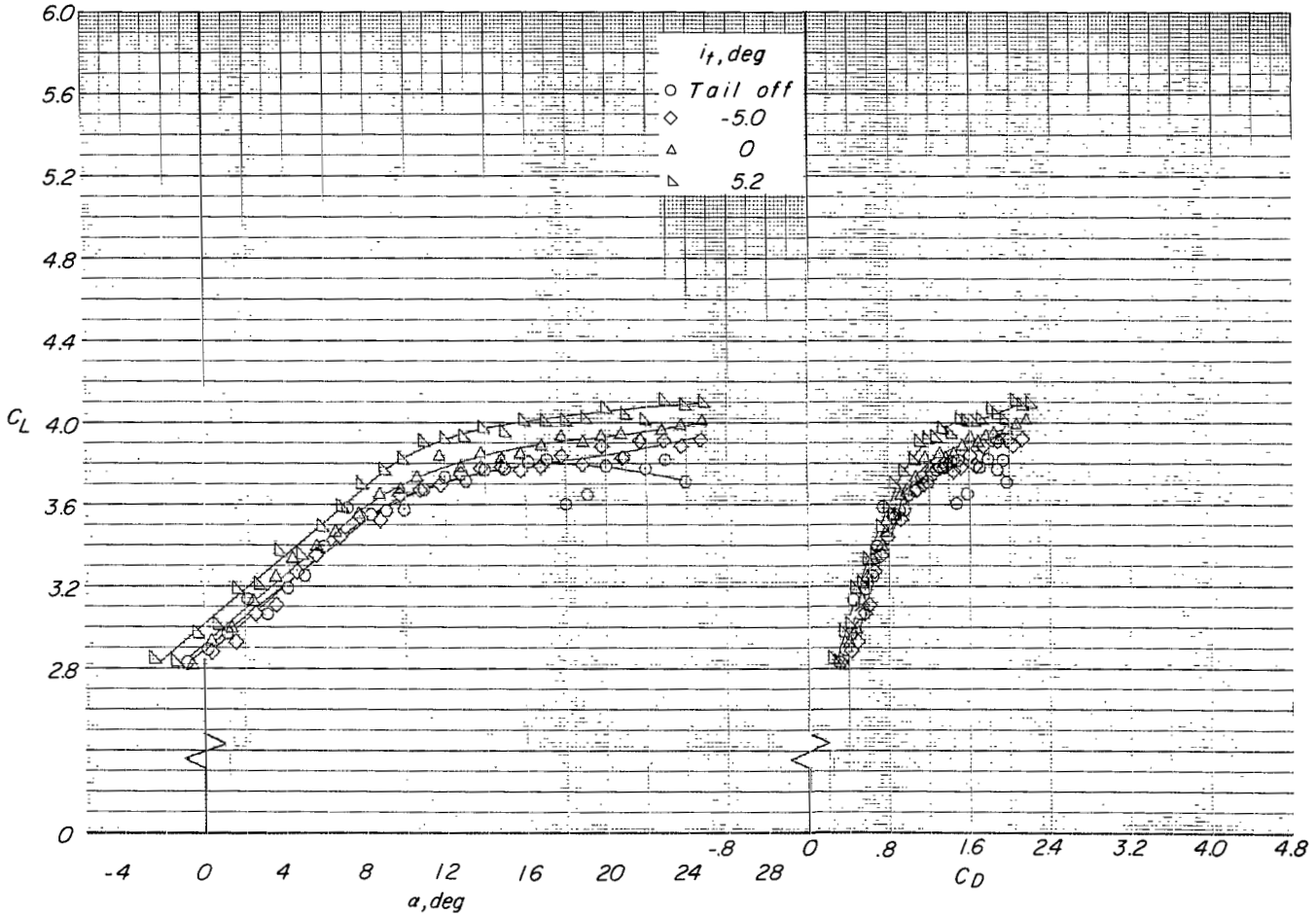

(a) Variation of C_L with α and C_D.

Figure 36.- Effect of tail incidence on longitudinal aerodynamic characteristics for configuration C ($\delta_f = 0^0$) with tail in mid position. $C_T = 3.3$.

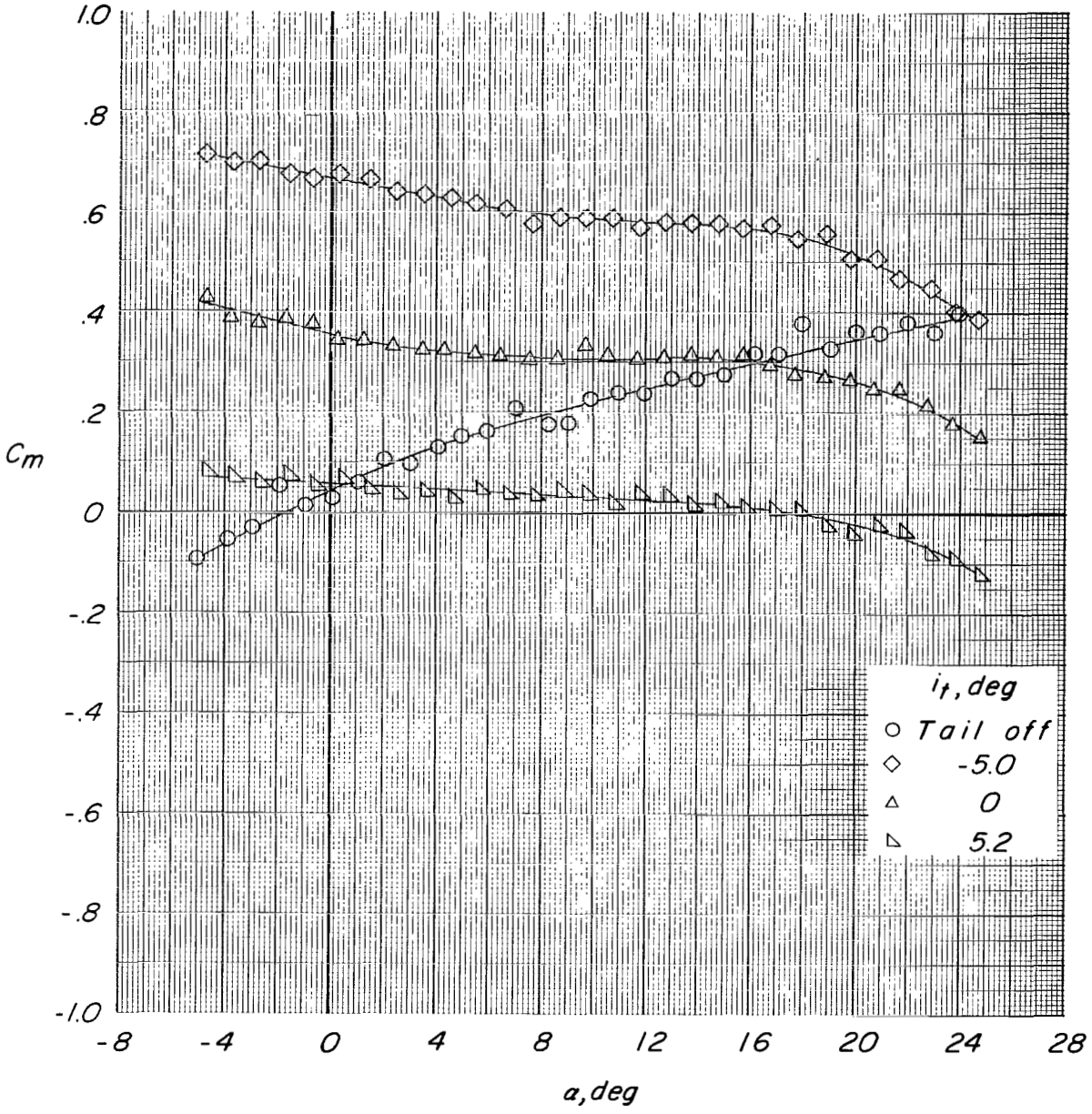

(b) Variation of C_m with α.

Figure 36.- Concluded.

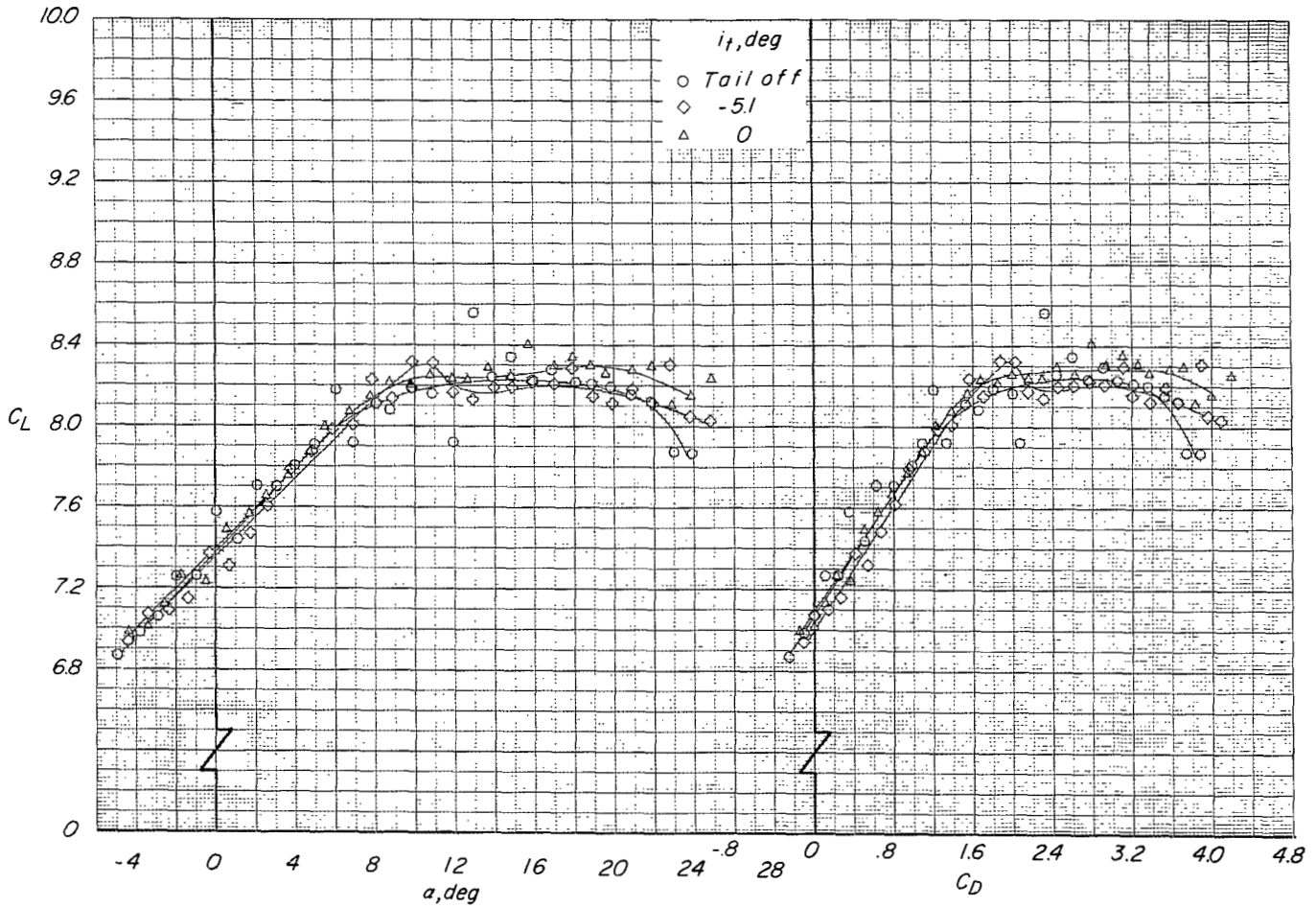

(a) Variation of C_L with α and C_D.

Figure 37.- Effect of tail incidence on longitudinal aerodynamic characteristics for configuration C ($\delta_f = 0^o$) with tail in mid position. $C_T = 7.9$.

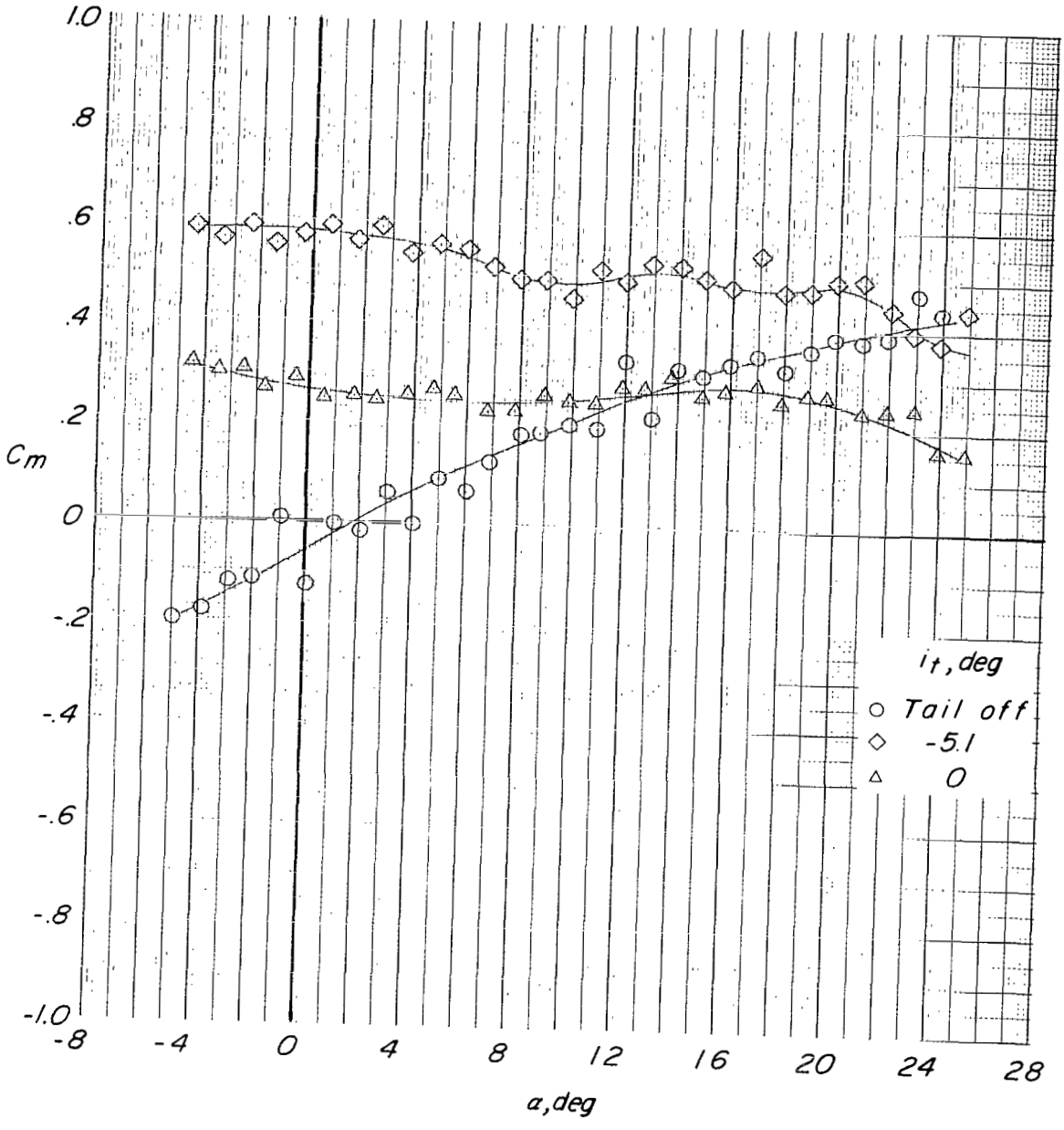

(b) Variation of C_m with α.

Figure 37.- Concluded.

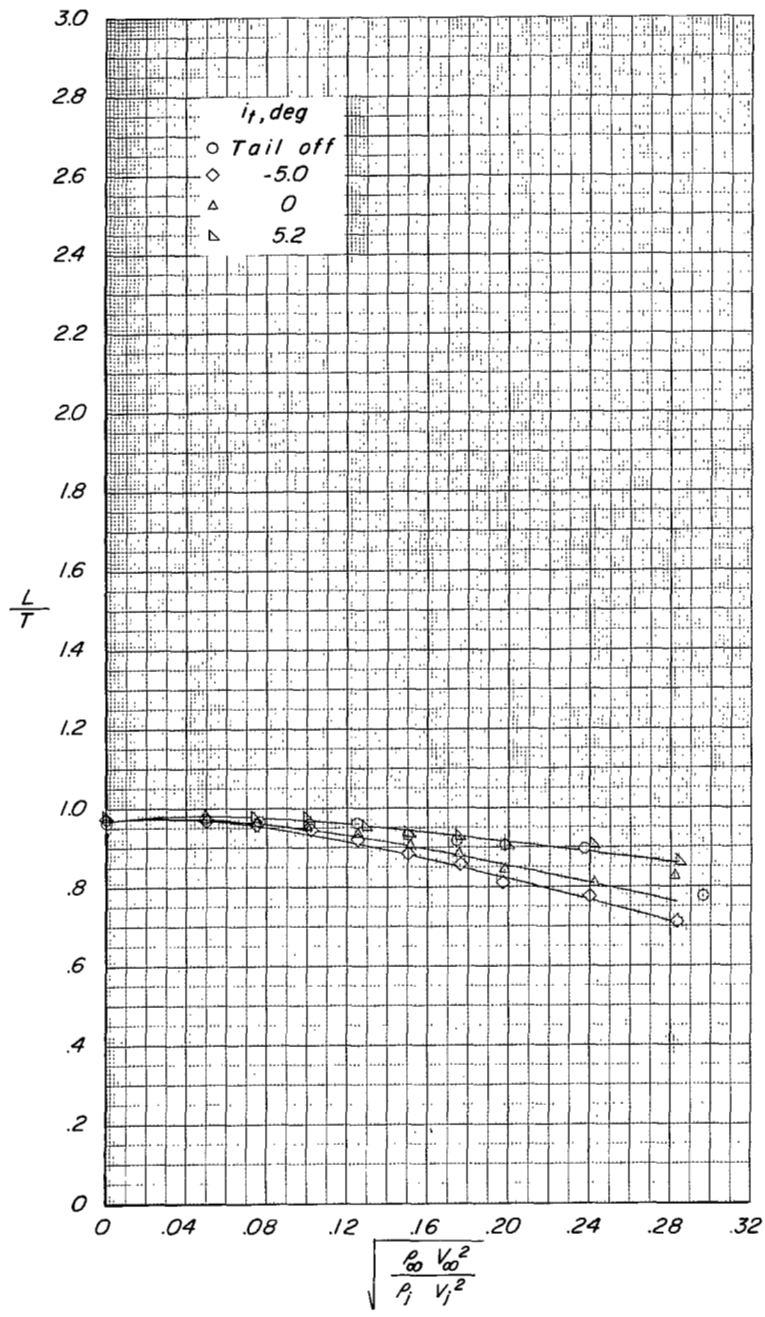

(a) Variation of L/T with effective velocity ratio.

Figure 38.- Effect of tail incidence on longitudinal aerodynamic characteristics for configuration C ($\delta_f = 0^0$) with tail in mid position. $\alpha \approx 0.6^0$.

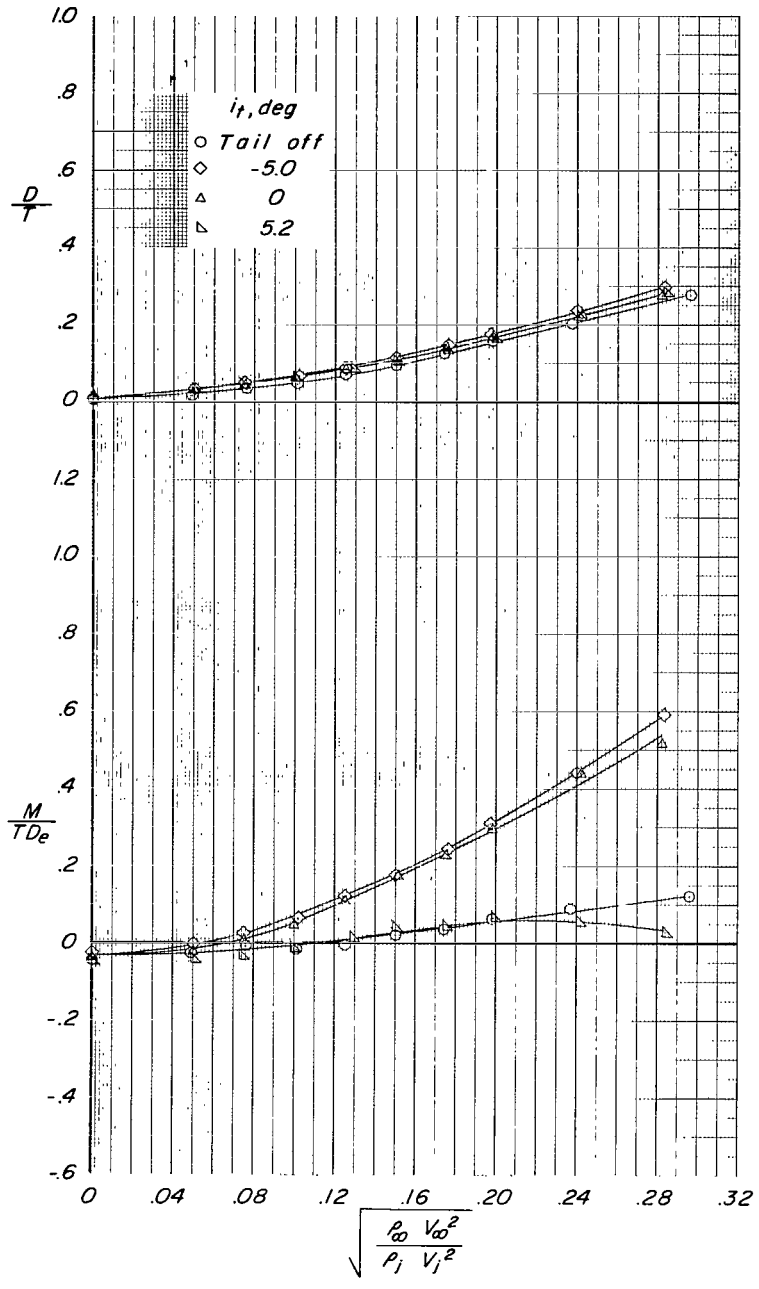

(b) Variation of D/T and M/TD_e with effective velocity ratio.

Figure 38.- Concluded.

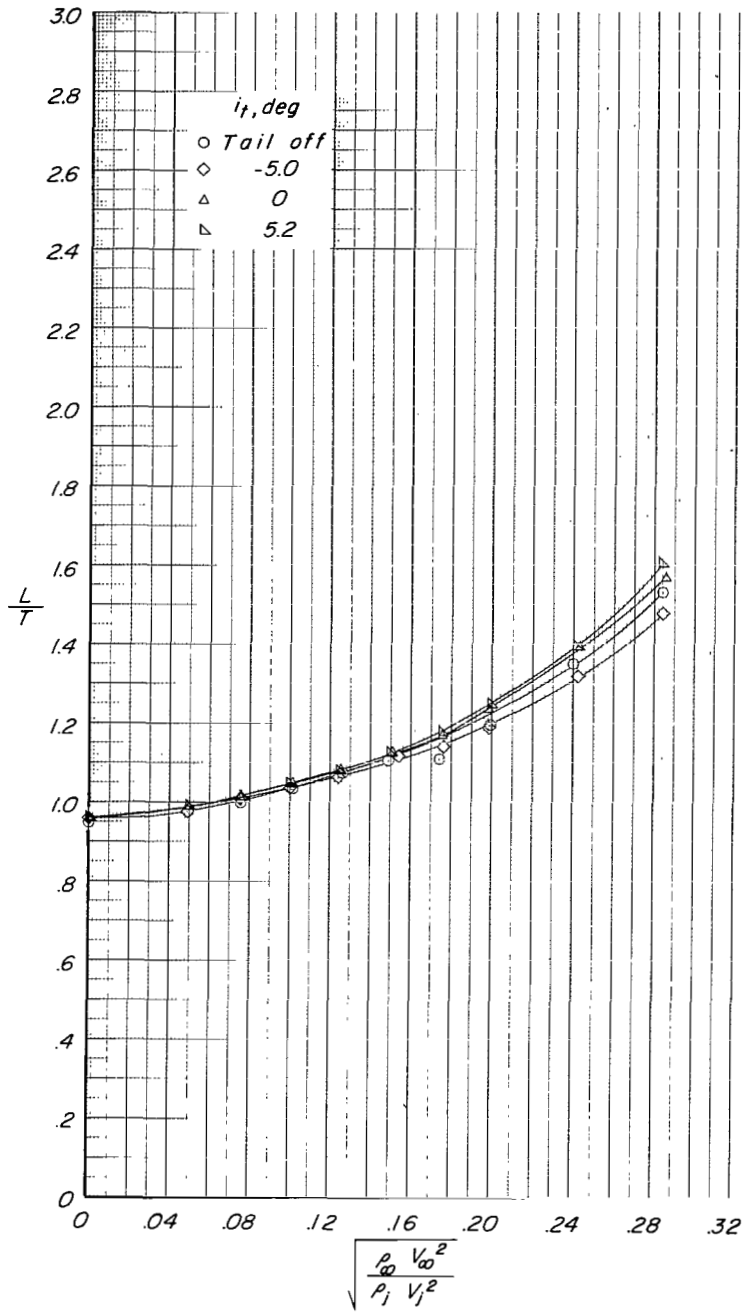

(a) Variation of L/T with effective velocity ratio.

Figure 39.- Effect of tail incidence on longitudinal aerodynamic characteristics for configuration C ($\delta_f = 0^0$) with tail in mid position. $\alpha \approx 10.8^0$.

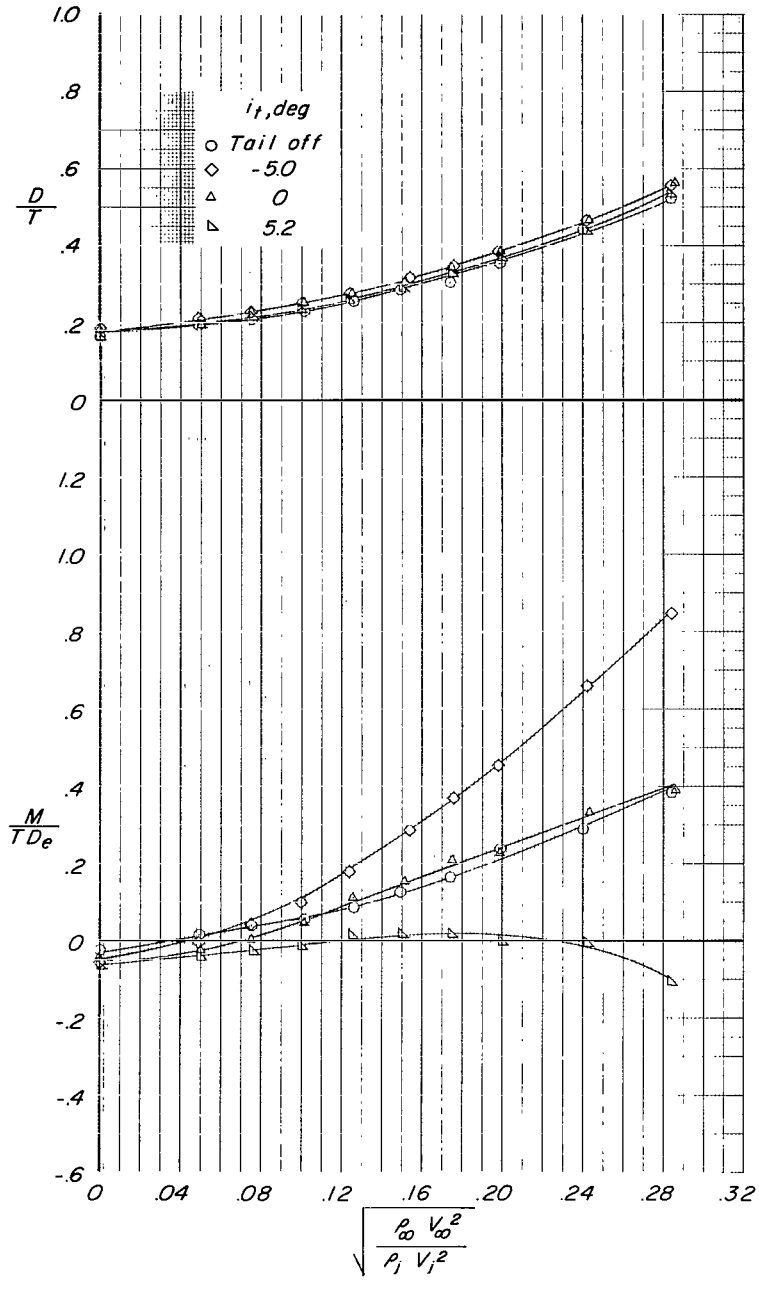

(b) Variation of D/T and M/TD_e with effective velocity ratio.

Figure 39.- Concluded.

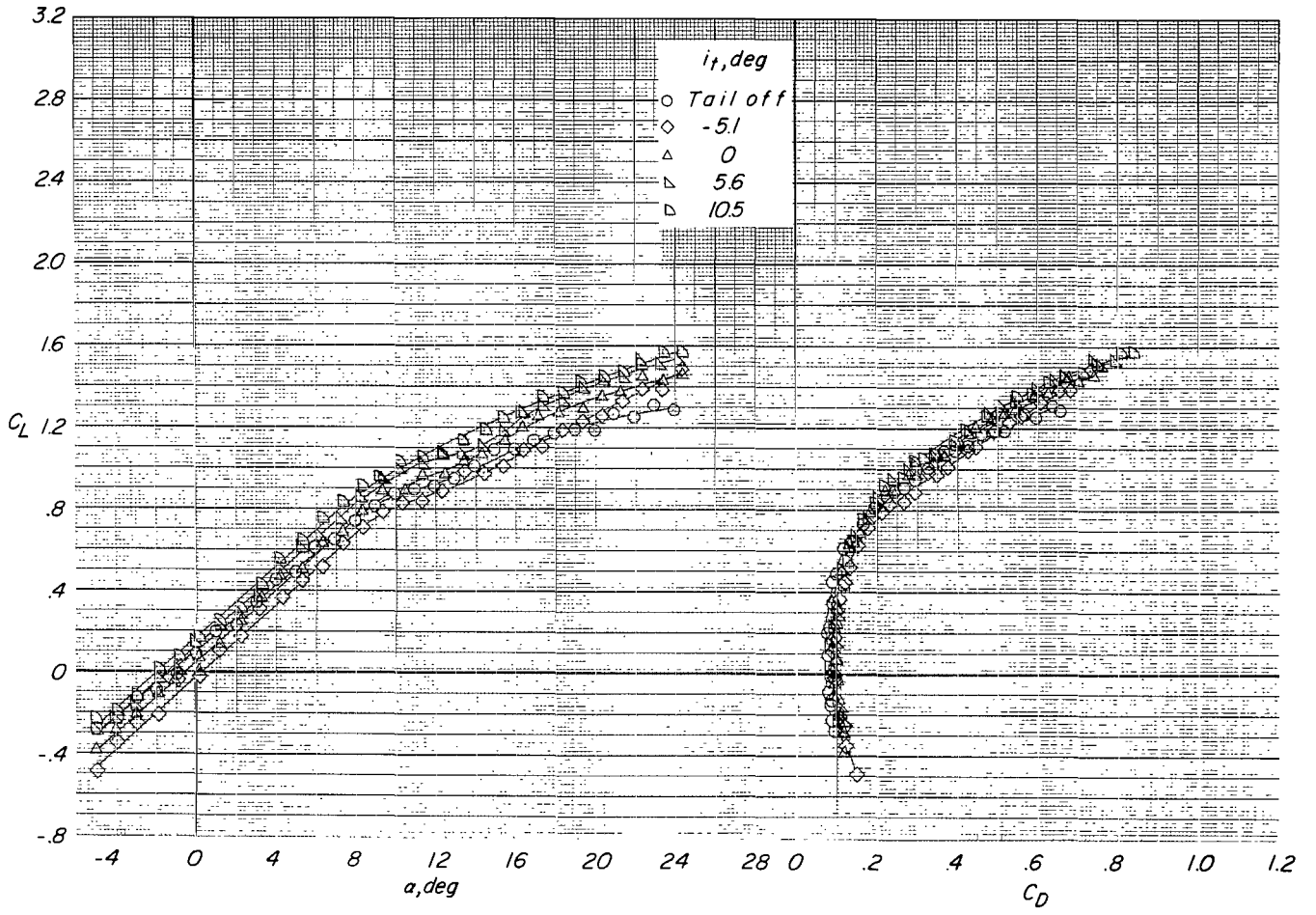

(a) Variation of C_L with α and C_D.

Figure 40.- Effect of tail incidence on longitudinal aerodynamic characteristics for configuration C ($\delta_f = 0^0$) with tail in low position. $C_T = 0$.

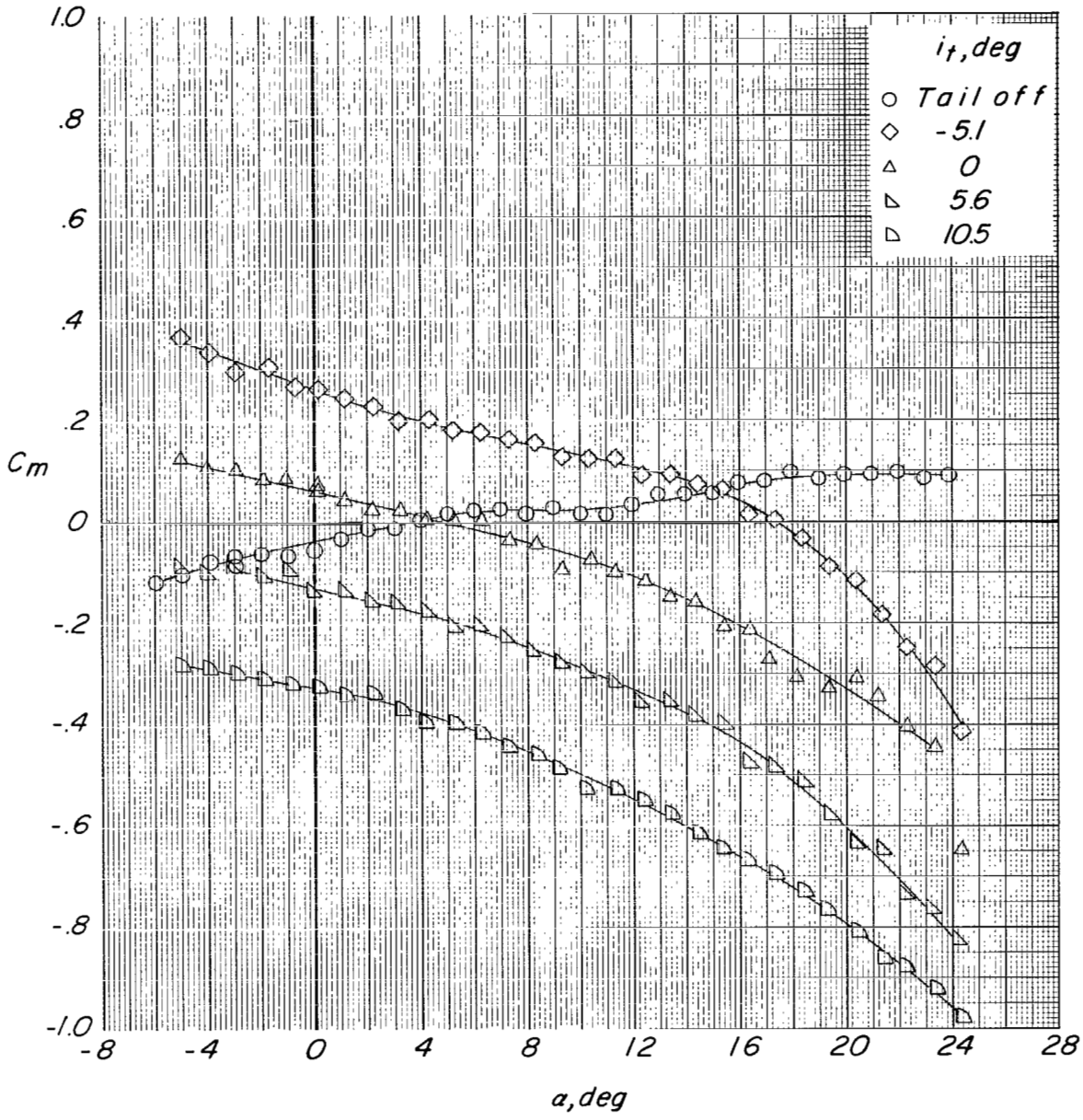

(b) Variation of C_m with α.

Figure 40.- Continued.

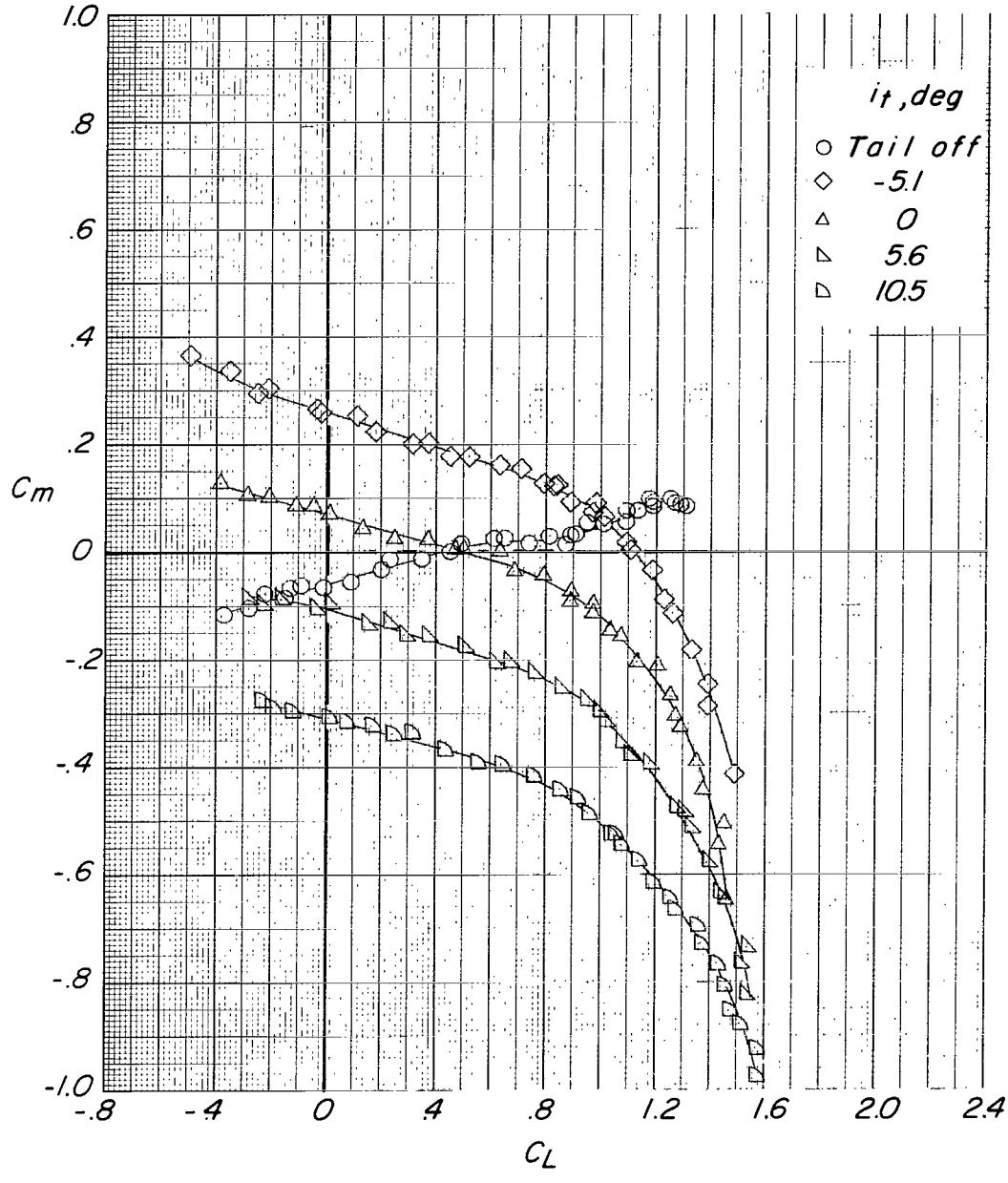

(c) Variation of C_m with C_L.

Figure 40.- Concluded.

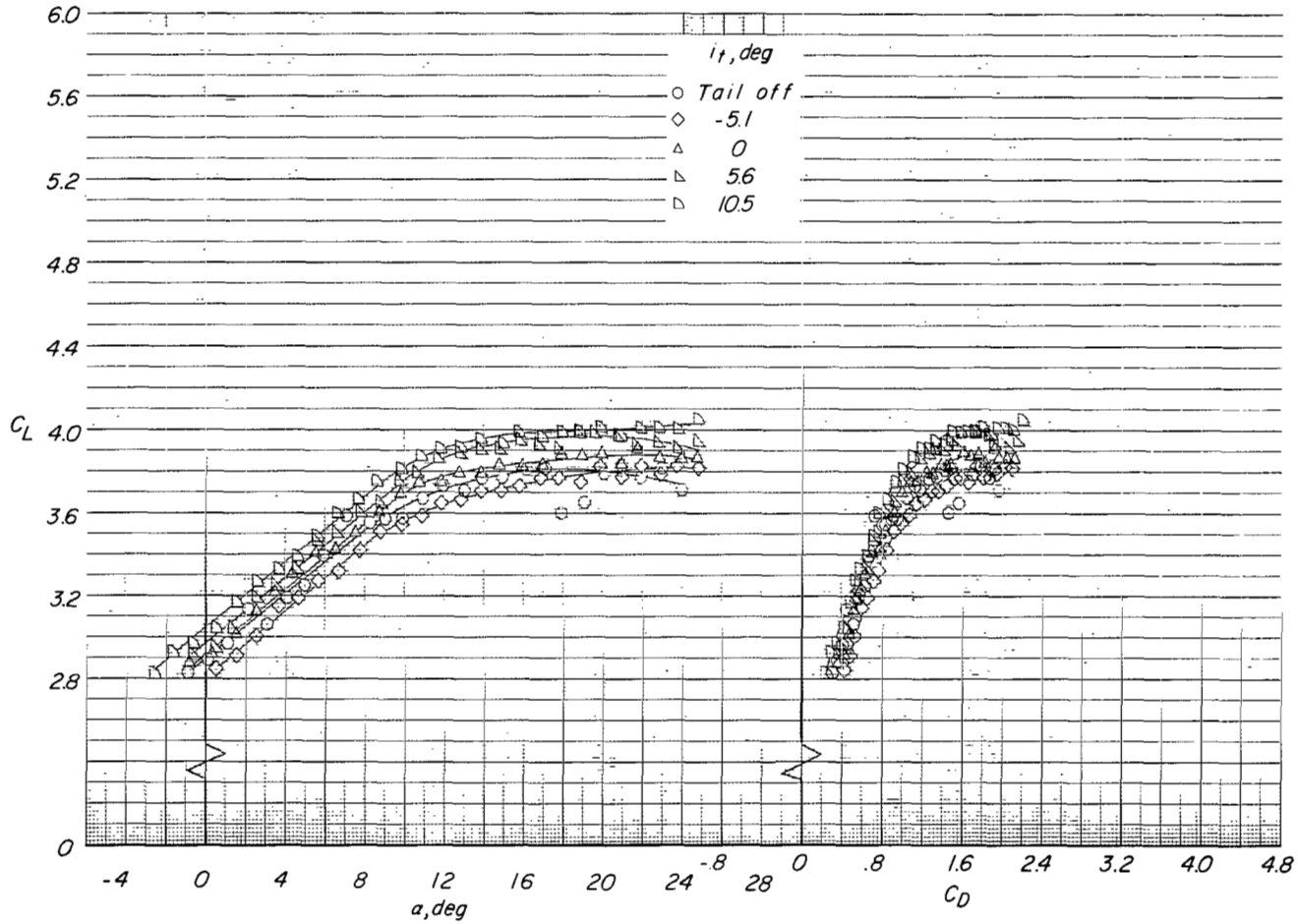

(a) Variation of C_L with α and C_D.

Figure 41.- Effect of tail incidence on longitudinal aerodynamic characteristics for configuration C ($\delta_f = 0^0$) with tail in low position. $C_T = 3.4$.

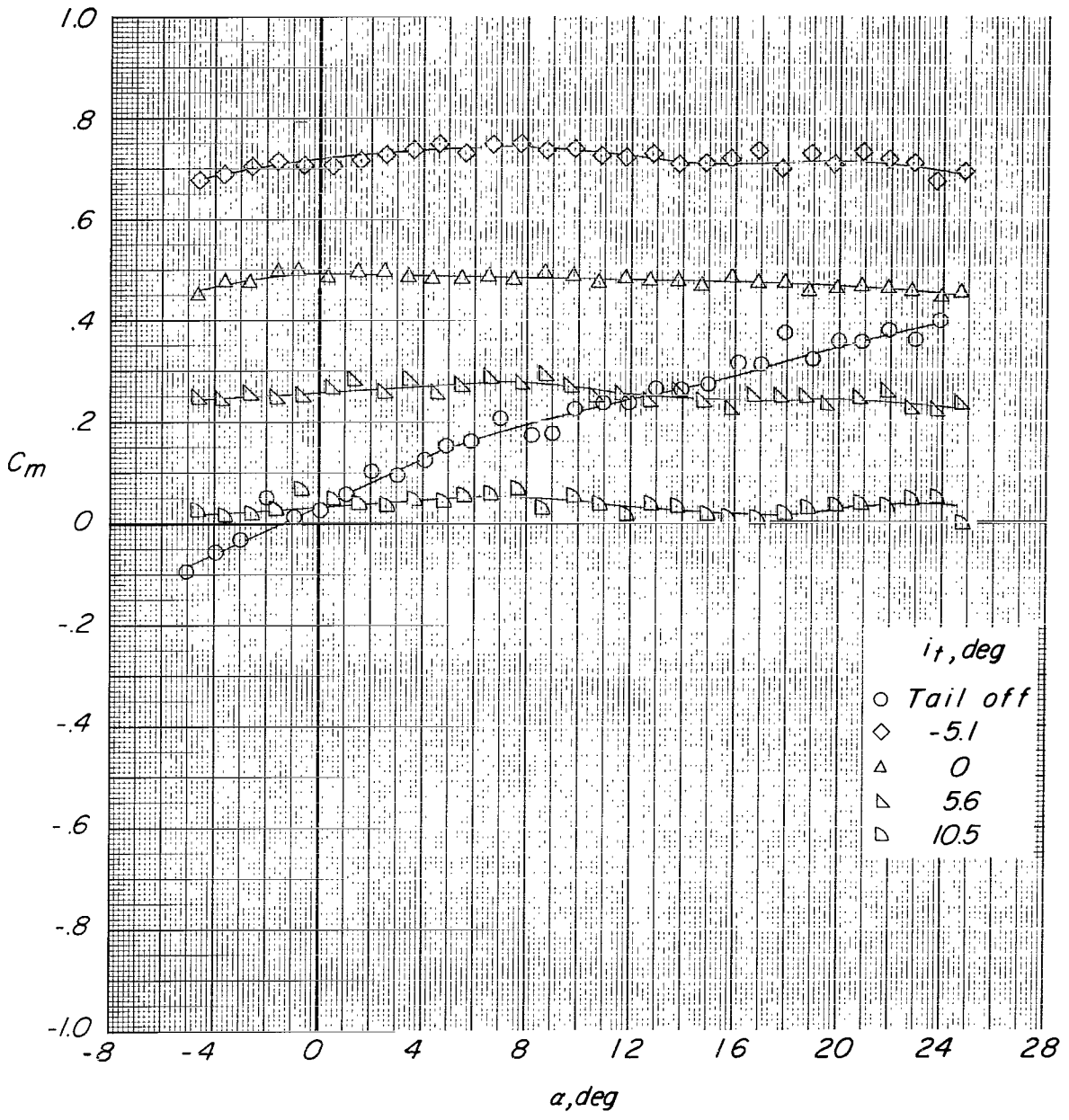

(b) Variation of C_m with α.

Figure 41.- Concluded.

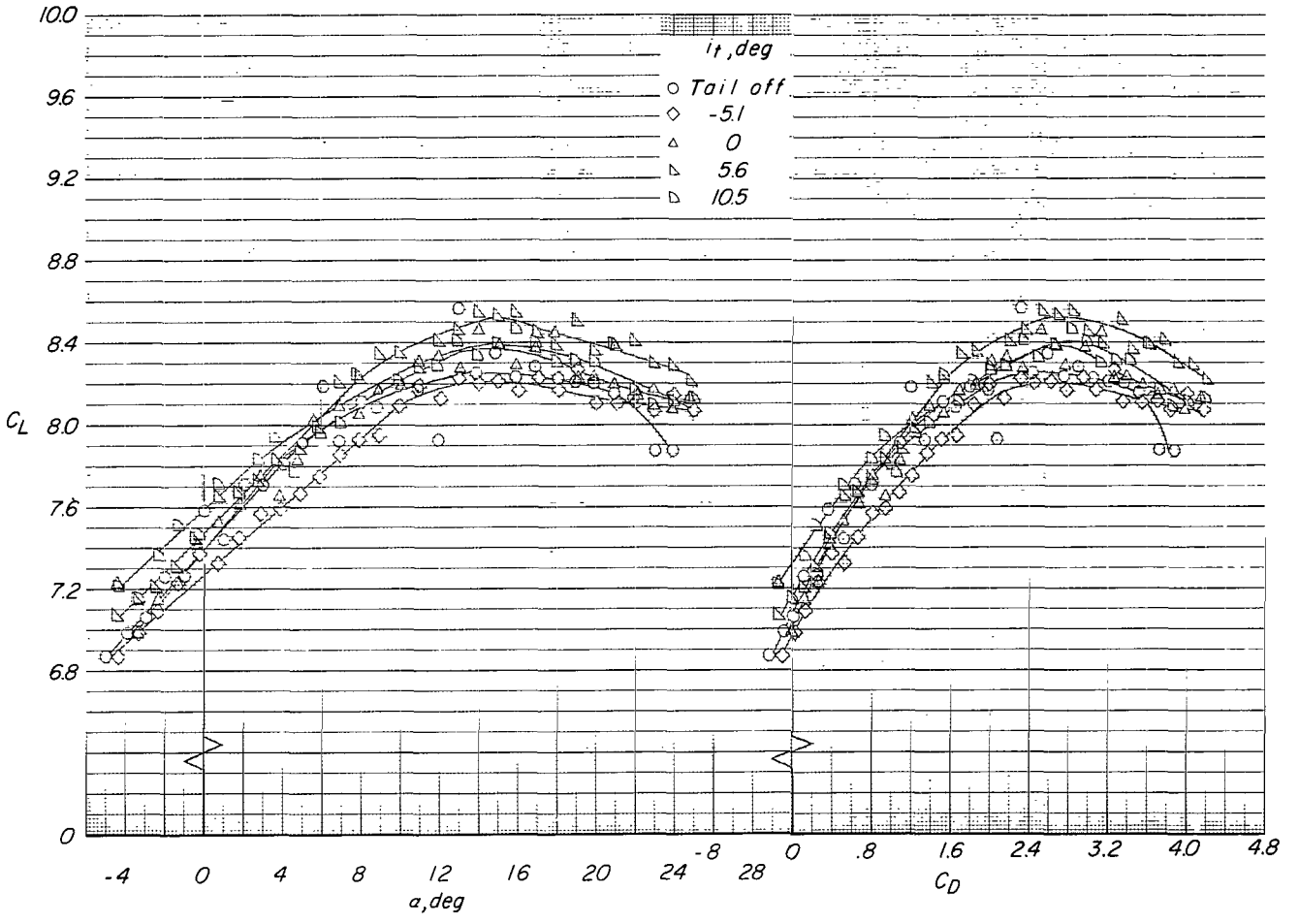

(a) Variation of C_L with α and C_D.

Figure 42.- Effect of tail incidence on longitudinal aerodynamic characteristics for configuration C ($\delta_f = 0^0$) with tail in low position. $C_T = 7.9$.

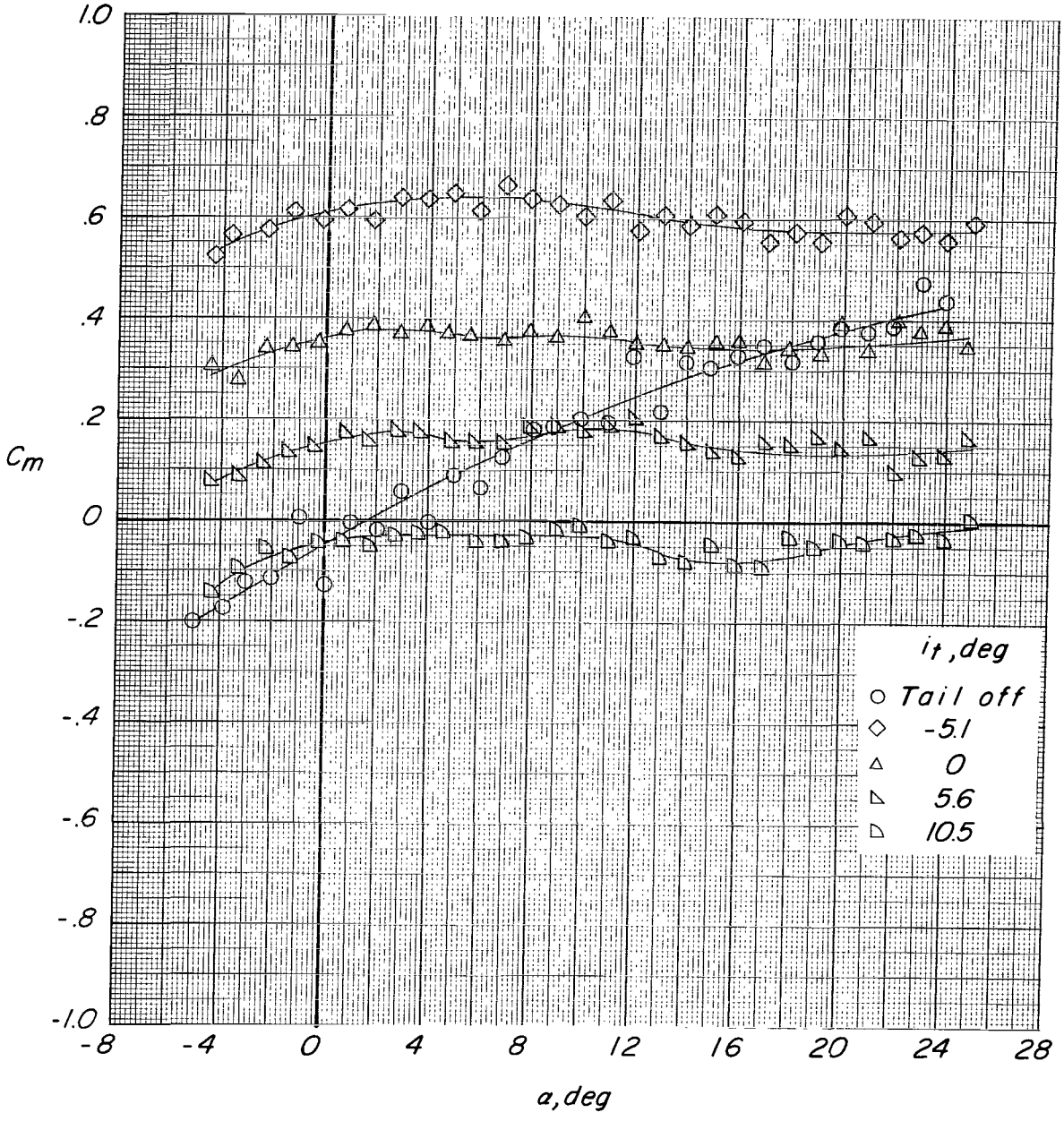

(b) Variation of C_m with α.

Figure 42.- Concluded.

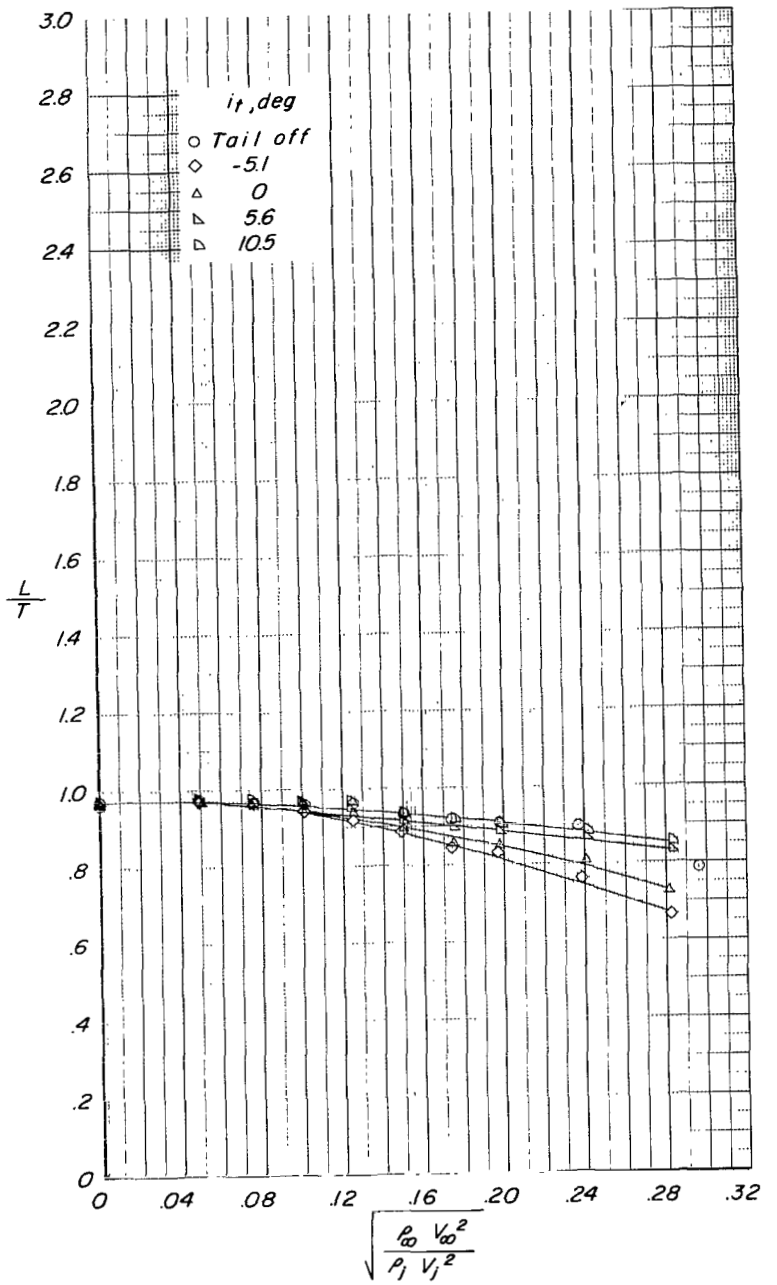

(a) Variation of L/T with effective velocity ratio.

Figure 43.- Effect of tail incidence on longitudinal aerodynamic characteristics for configuration C ($\delta_f = 0^0$) with tail in low position. $\alpha \approx 0.6^0$.

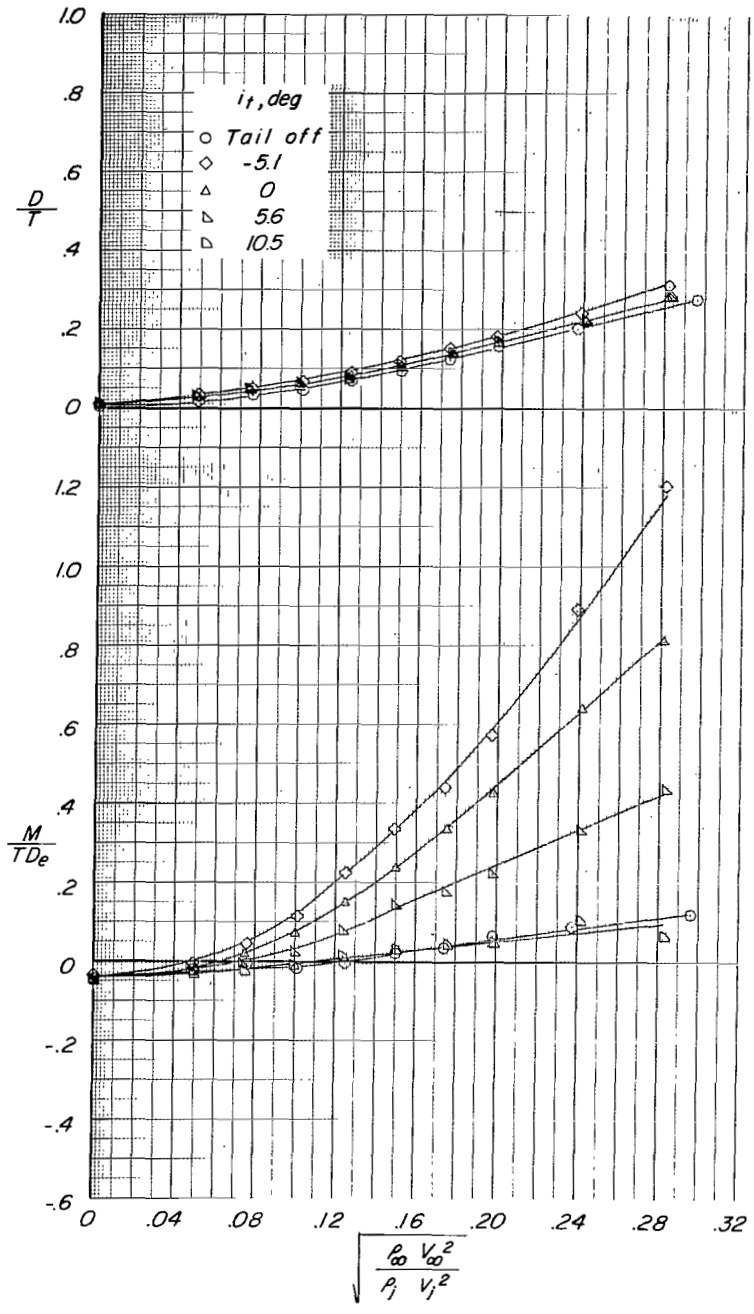

(b) Variation of D/T and M/TD_e with effective velocity ratio.

Figure 43.- Concluded.

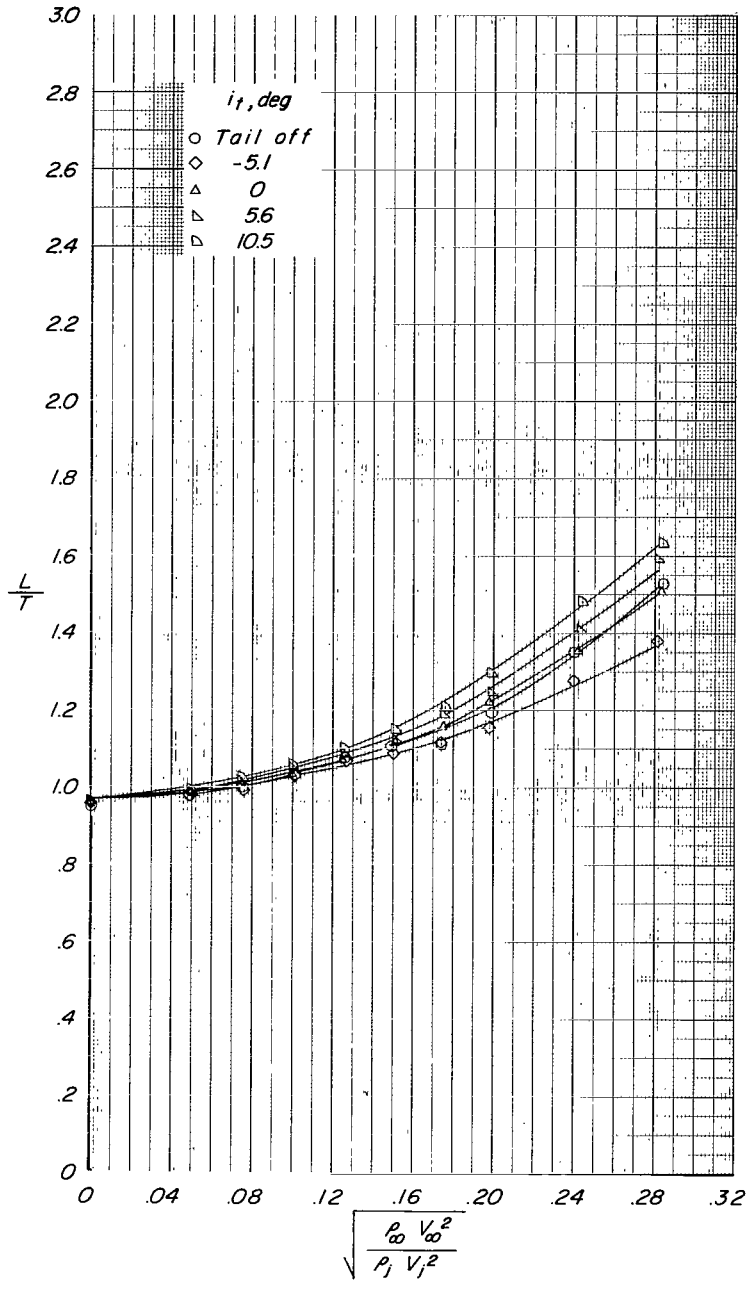

(a) Variation of L/T with effective velocity ratio.

Figure 44.- Effect of tail incidence on longitudinal aerodynamic characteristics for configuration C ($\delta_f = 0^0$) with tail in low position. $\alpha \approx 10.8^0$.

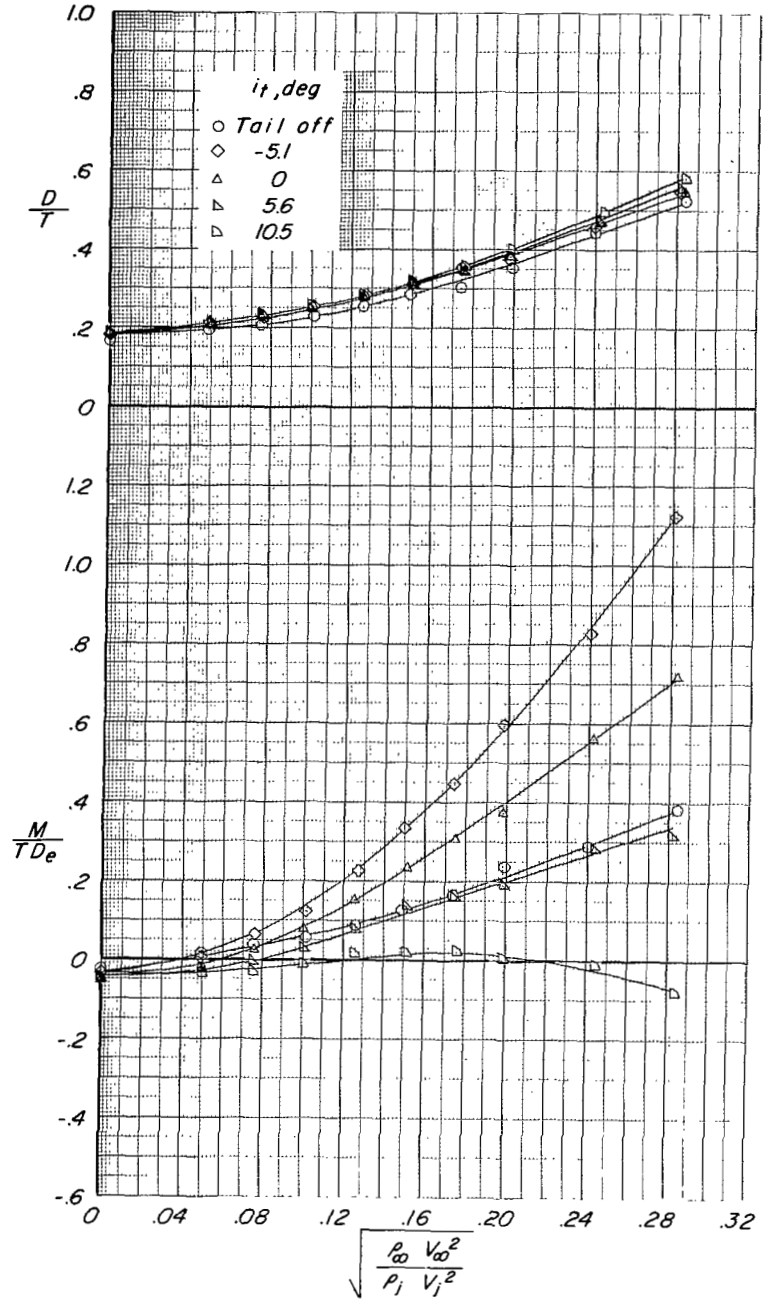

(b) Variation of D/T and M/TD_e with effective velocity ratio.

Figure 44.- Concluded.

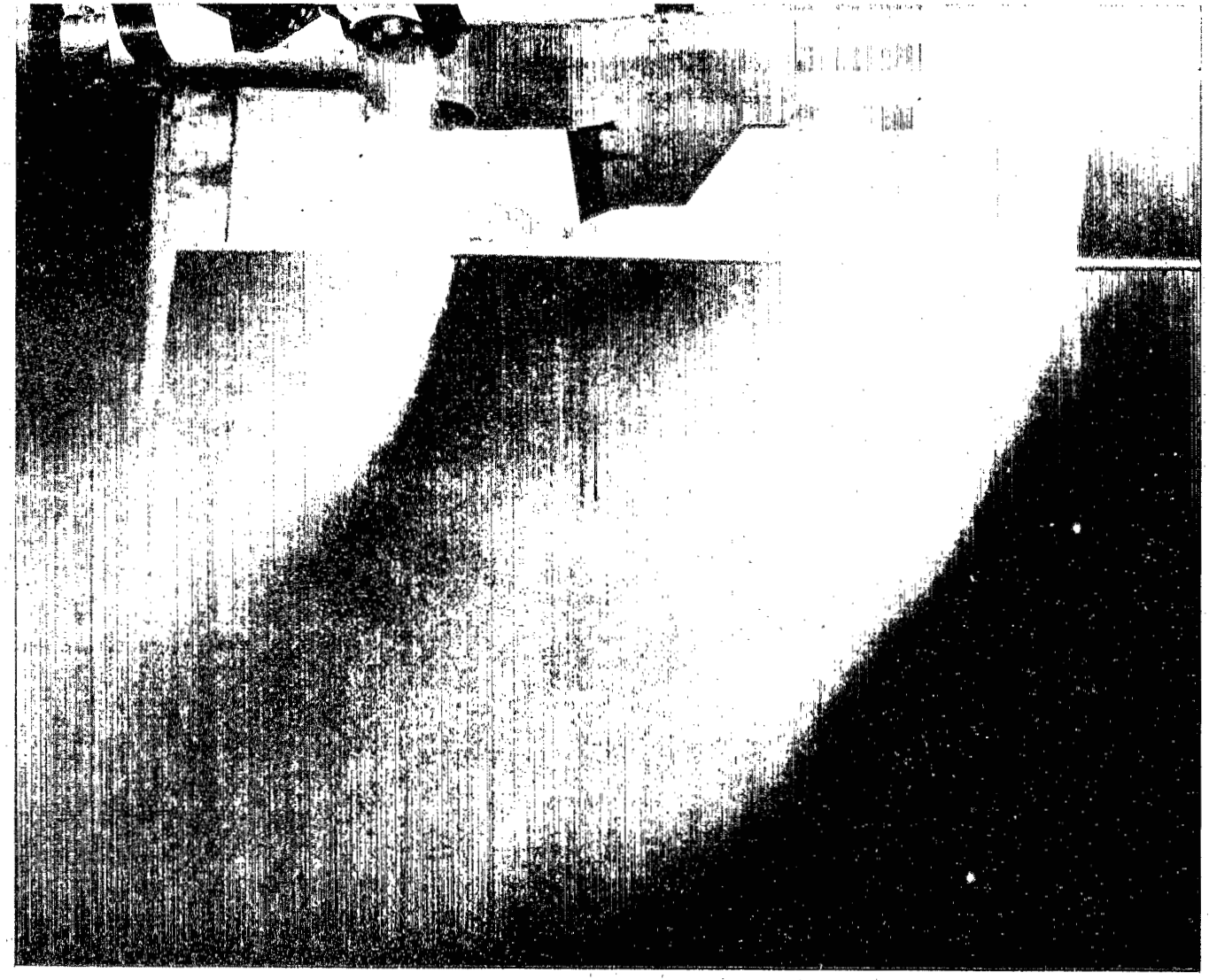

(d) $\delta_n = 90^0$; $\sqrt{\frac{\rho_\infty V_\infty^2}{\rho_j V_j^2}} \approx .0.23.$ L-68-5644

Figure 45.- Concluded.

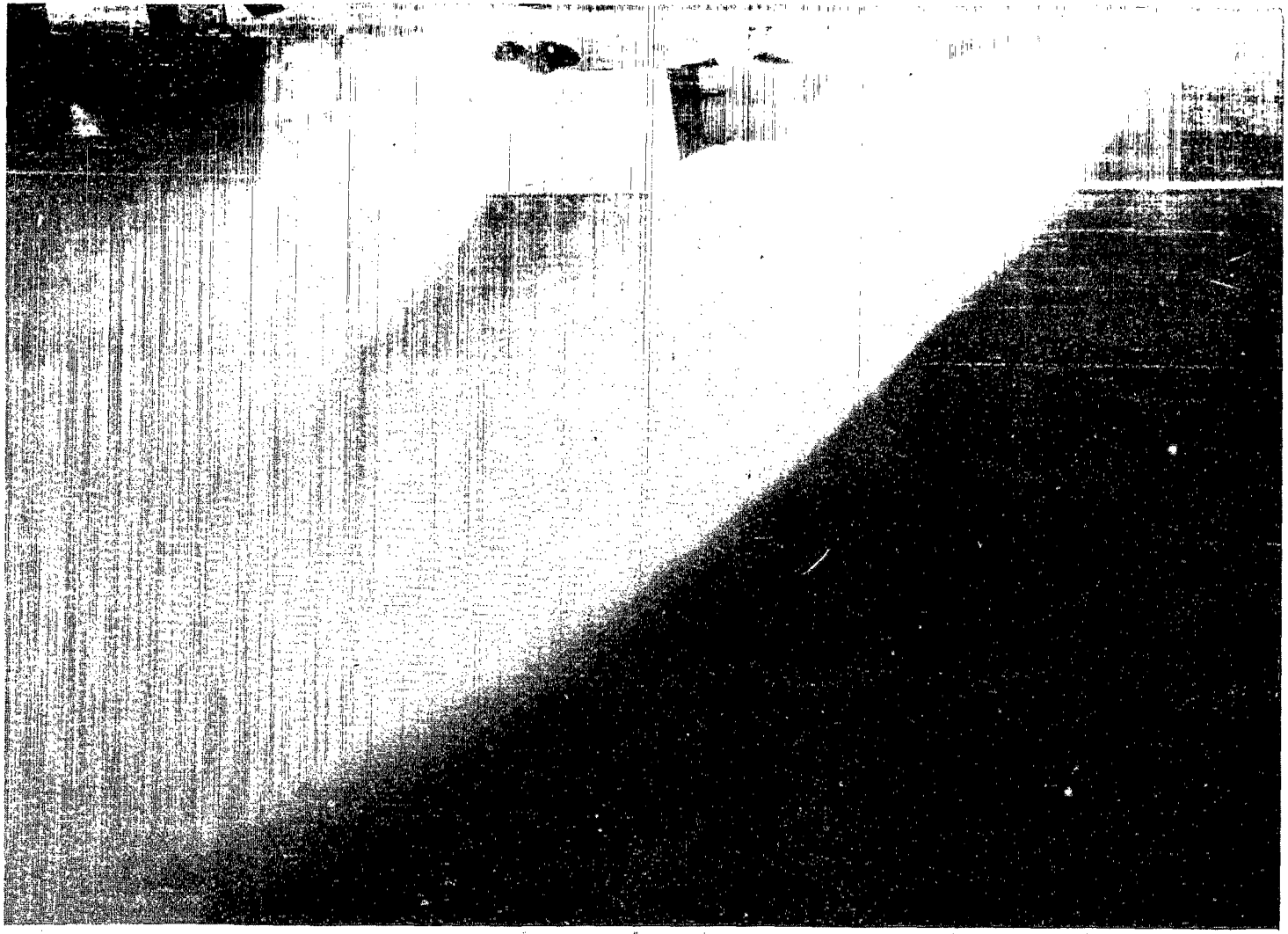

(c) $\delta_n = 60^o$; $\sqrt{\frac{\rho_\infty V_\infty^2}{\rho_j V_j^2}} \approx 0.23$. L-68-5643

Figure 45.- Continued.

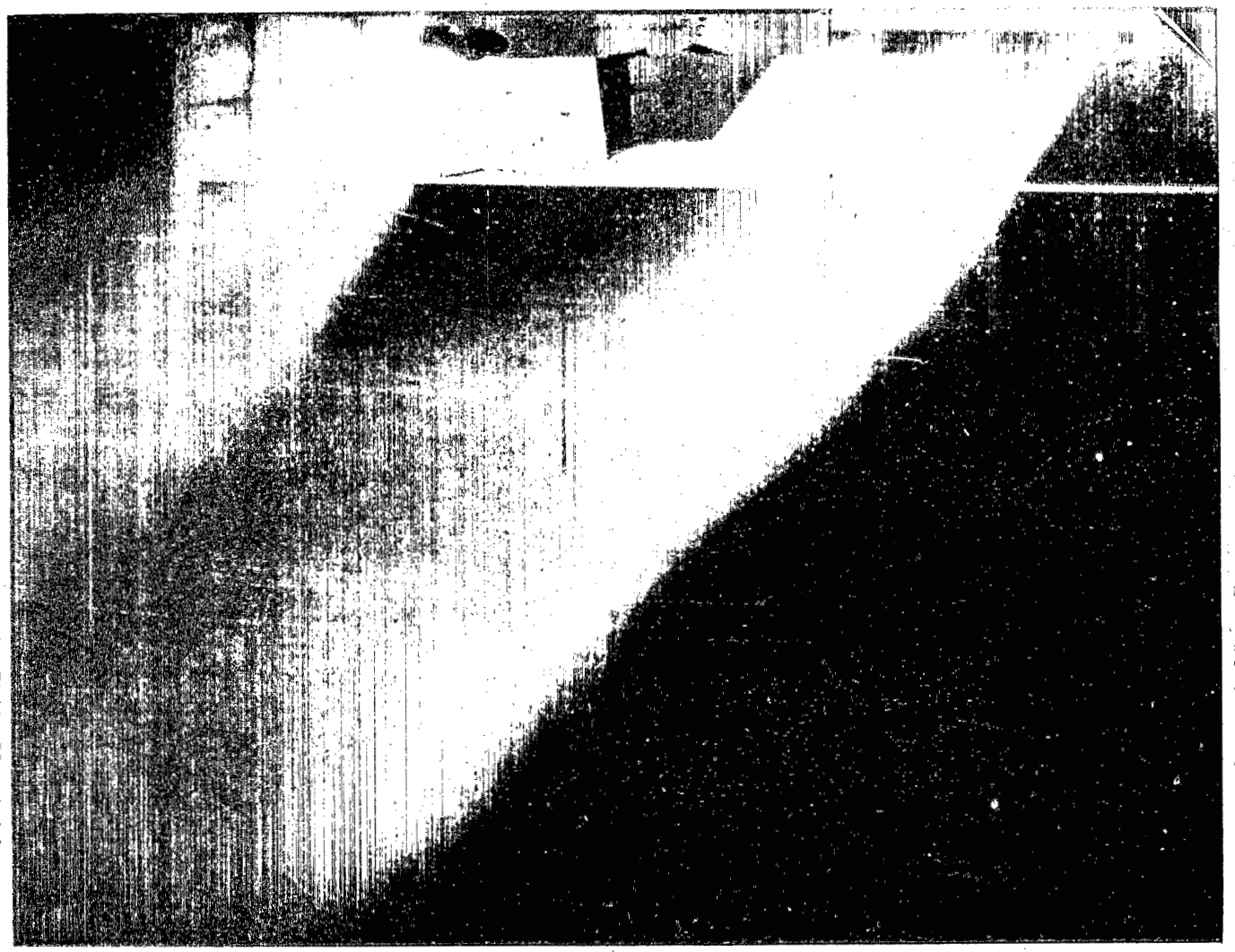

(b) $\delta_n = 60^0$; $\sqrt{\frac{\rho_\infty V_\infty^2}{\rho_j V_j^2}} \approx 0.16$. L-68-5642

Figure 45.- Continued.

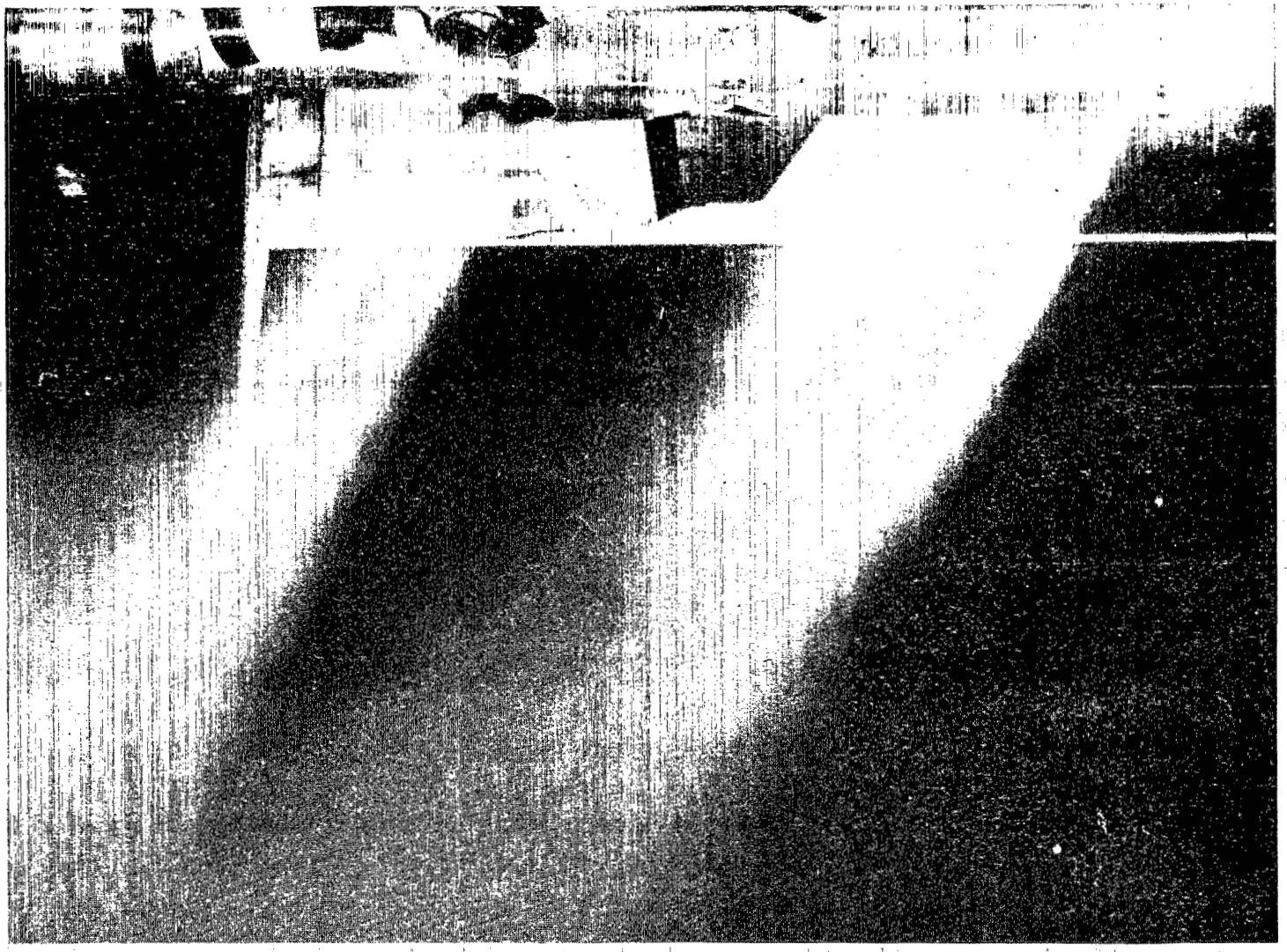

(a) $\delta_n = 60^0$; $\sqrt{\frac{\rho_\infty V_\infty^2}{\rho_j V_j^2}} = 0$.

L-68-5641

Figure 45.- Flow field caused by wakes from five jet-engine simulators used to power model. Configuration B ($\delta_f = 30^0$) with tail off.

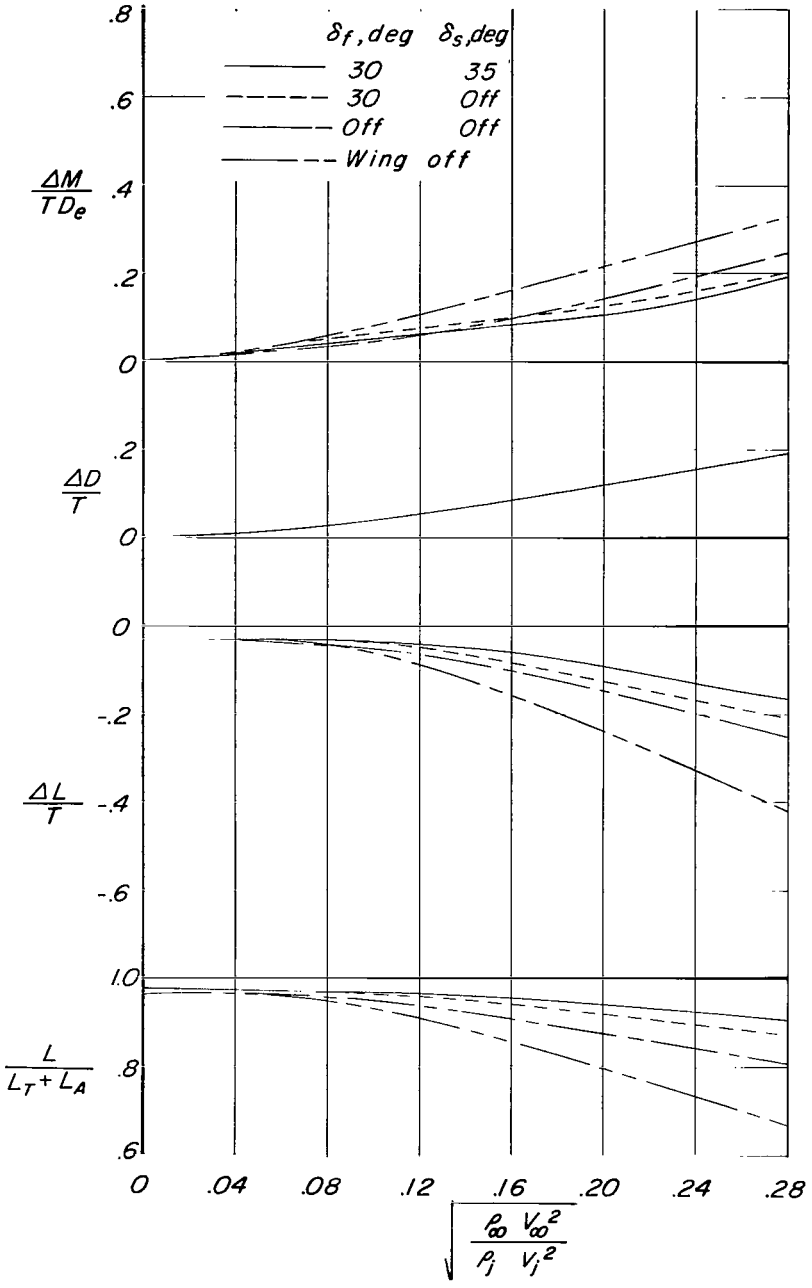

(a) $\alpha \approx 0.6^0$.

Figure 46.- Basic interference effects for configurations A ($\delta_f = 30^0$, $\delta_s = 35^0$, fixed forewing), B ($\delta_f = 30^0$), and C ($\delta_f = 0^0$) and for fuselage alone (model with wings off). Horizontal tail off.

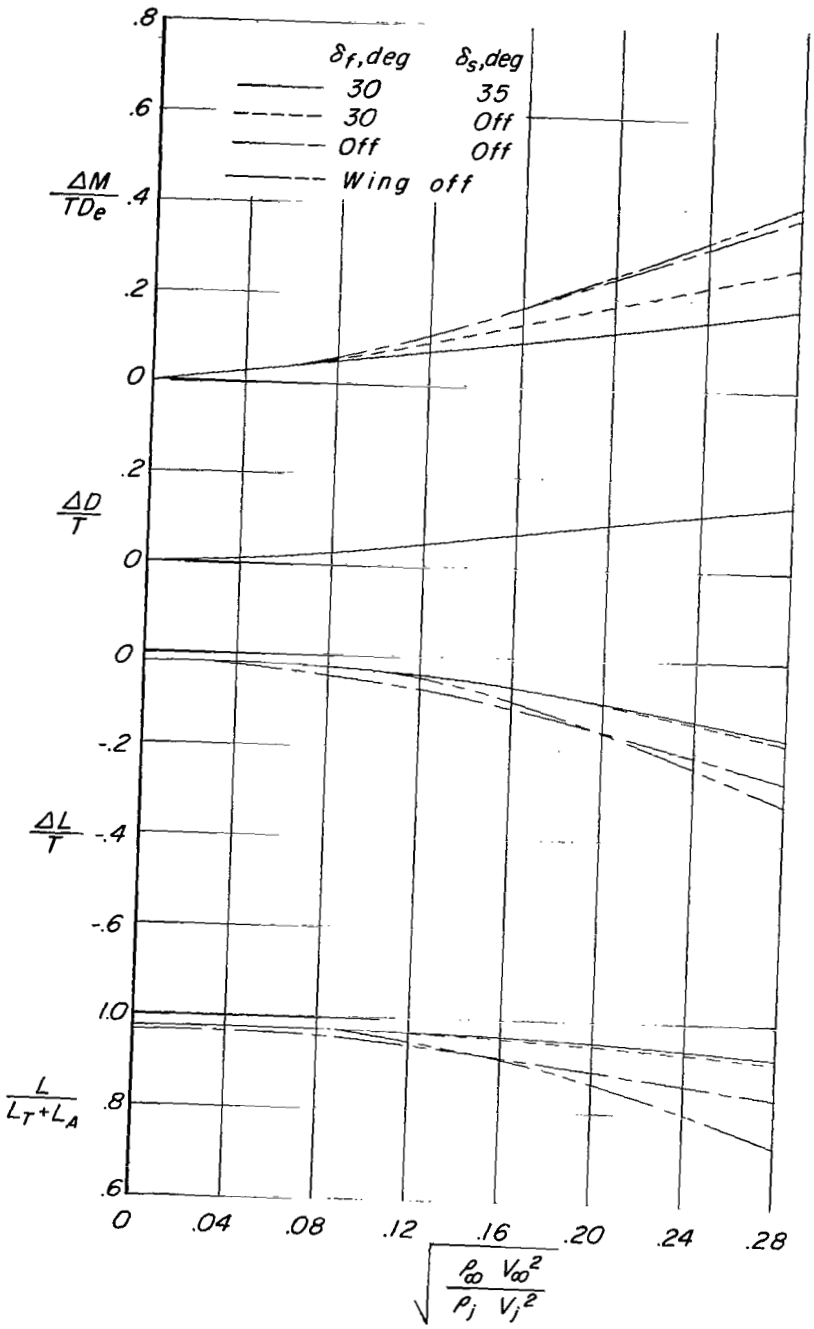

(b) $\alpha \approx 10.8^0$.

Figure 46.- Concluded.

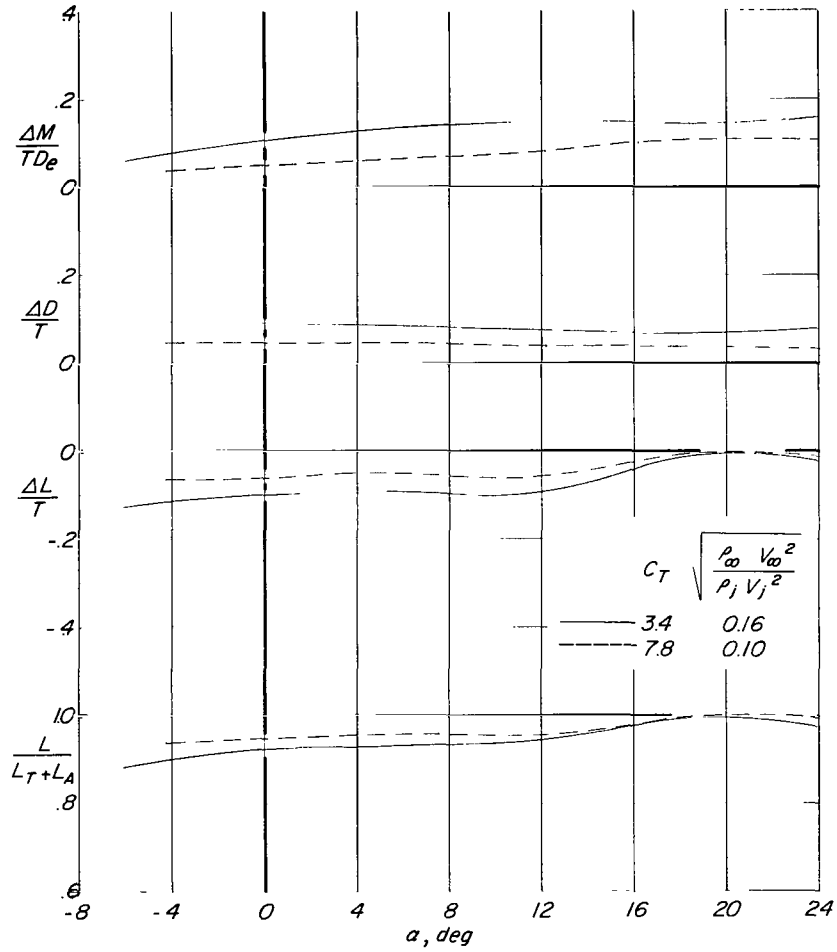

(a) Tail off.

Figure 47.- Effect of angle of attack on interference effects for configuration A ($\delta_f = 30^0$, $\delta_s = 35^0$, fixed forewing).

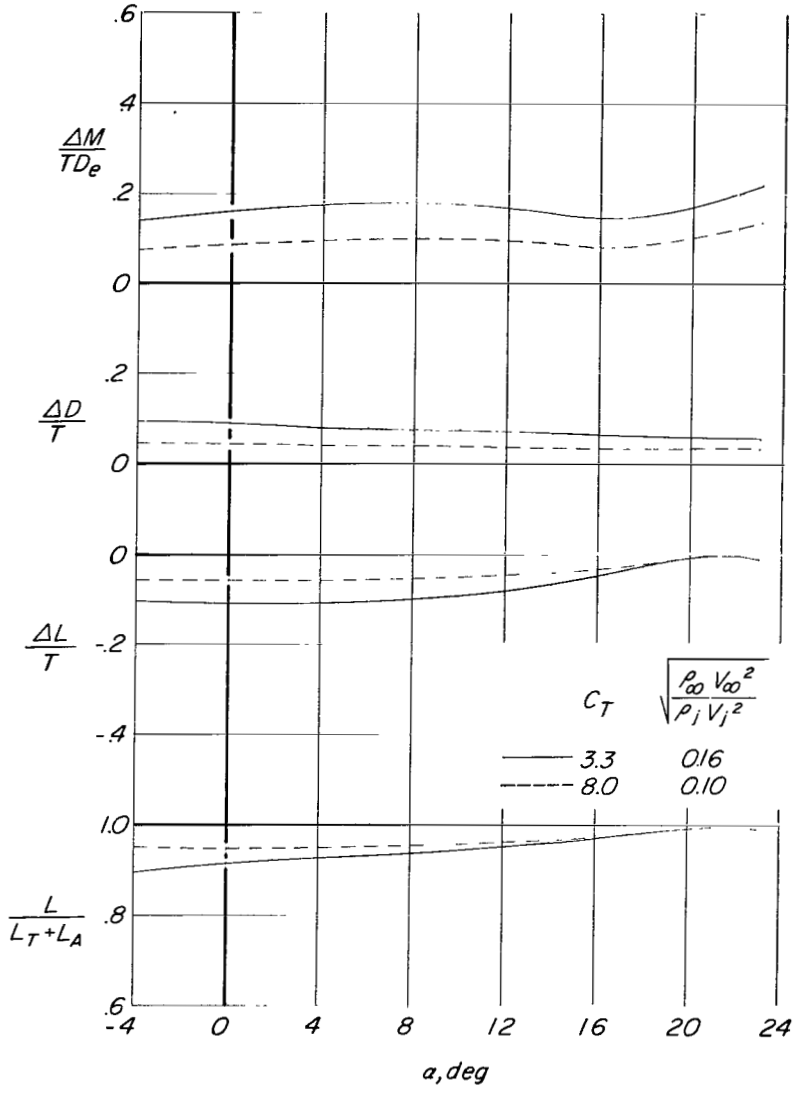

(b) High tail position.

Figure 47.- Continued.

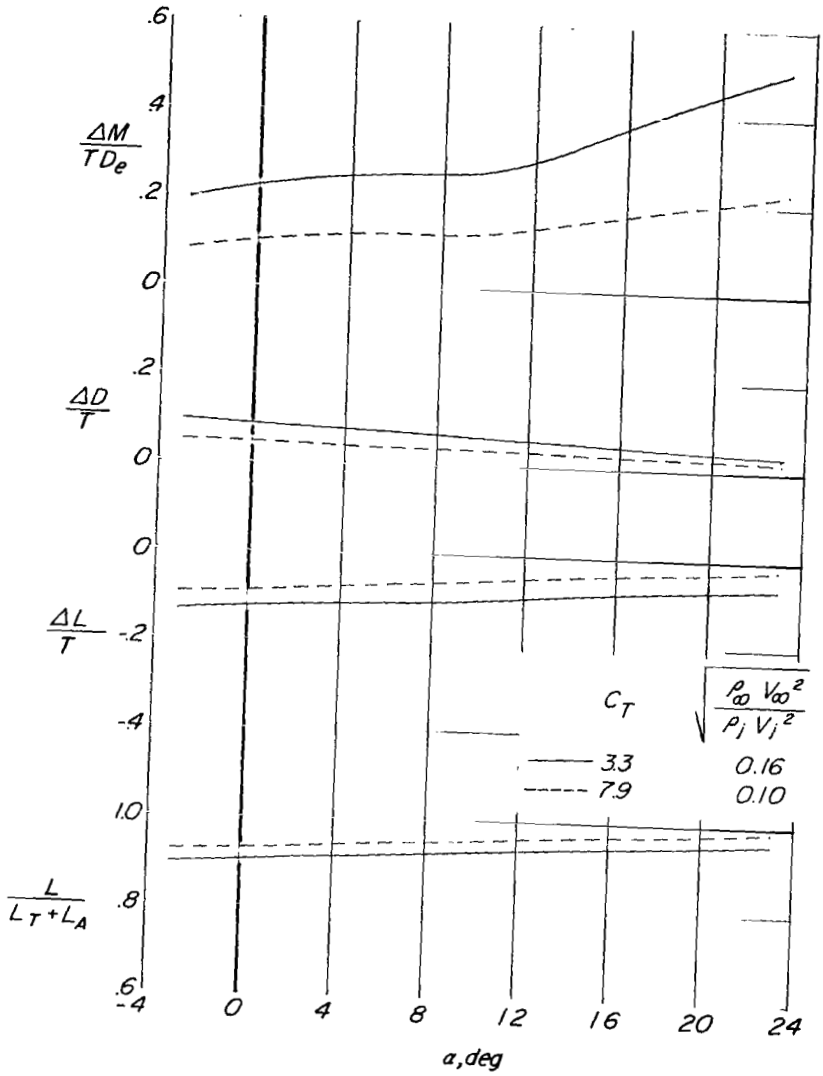

(c) Mid tail position.

Figure 47.- Continued.

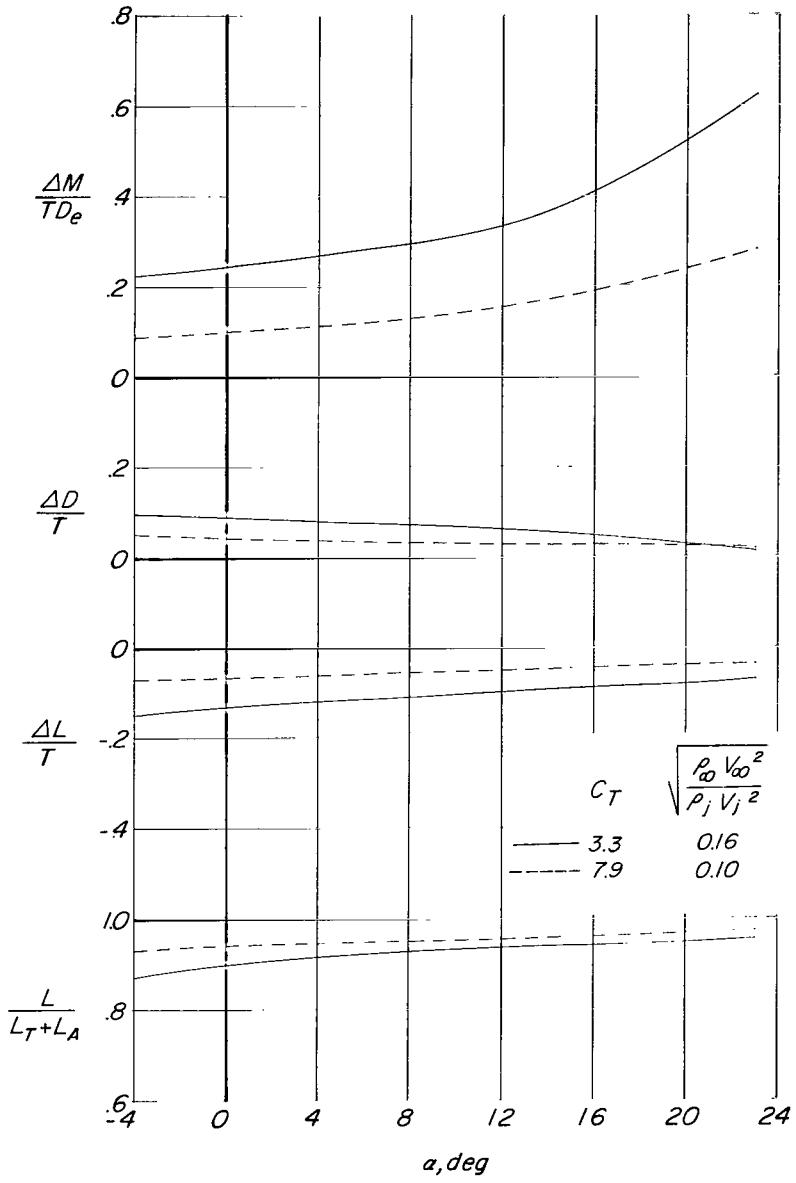

(d) Low tail position.

Figure 47.- Concluded.

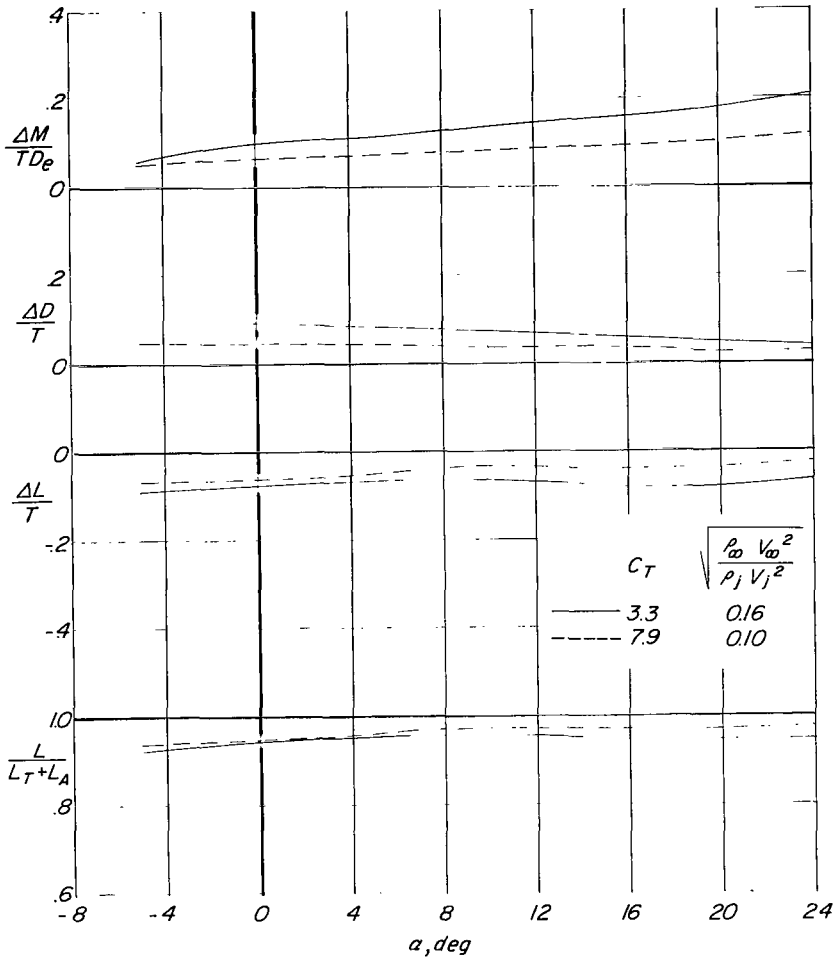

(a) Tail off.

Figure 48.- Effect of angle of attack on interference effects for configuration B ($\delta_f = 30^0$).

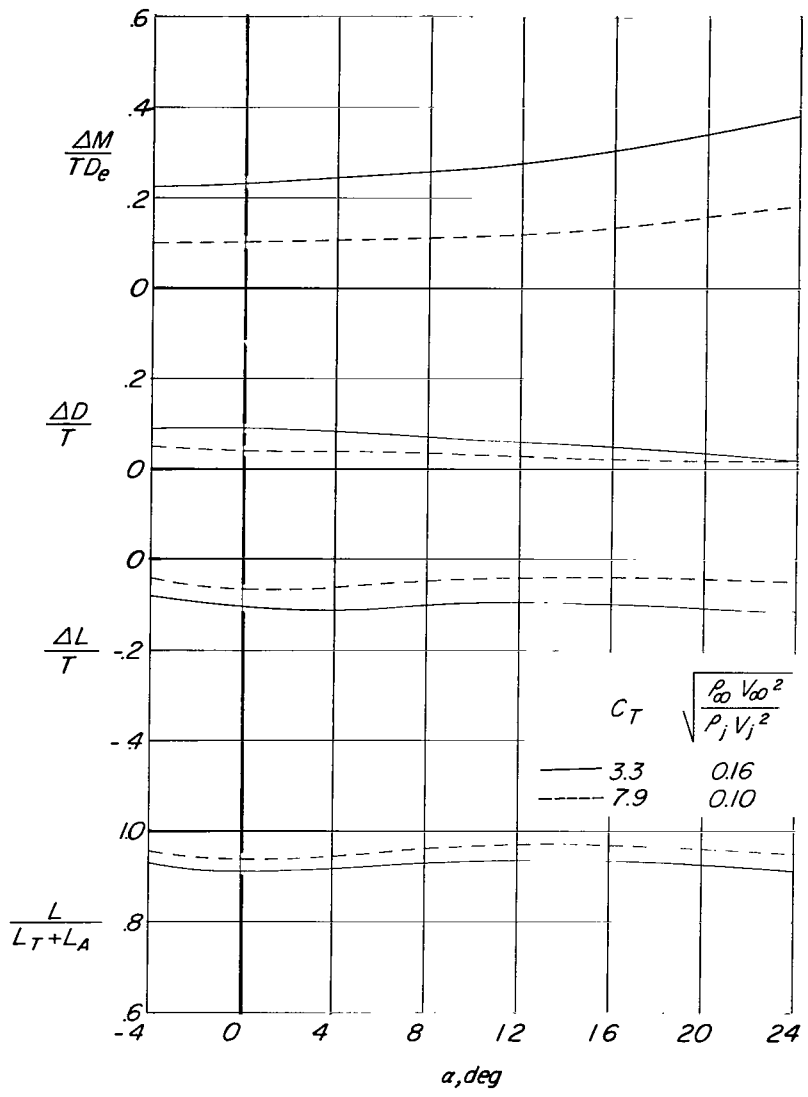

(b) Mid tail position.

Figure 48.- Continued.

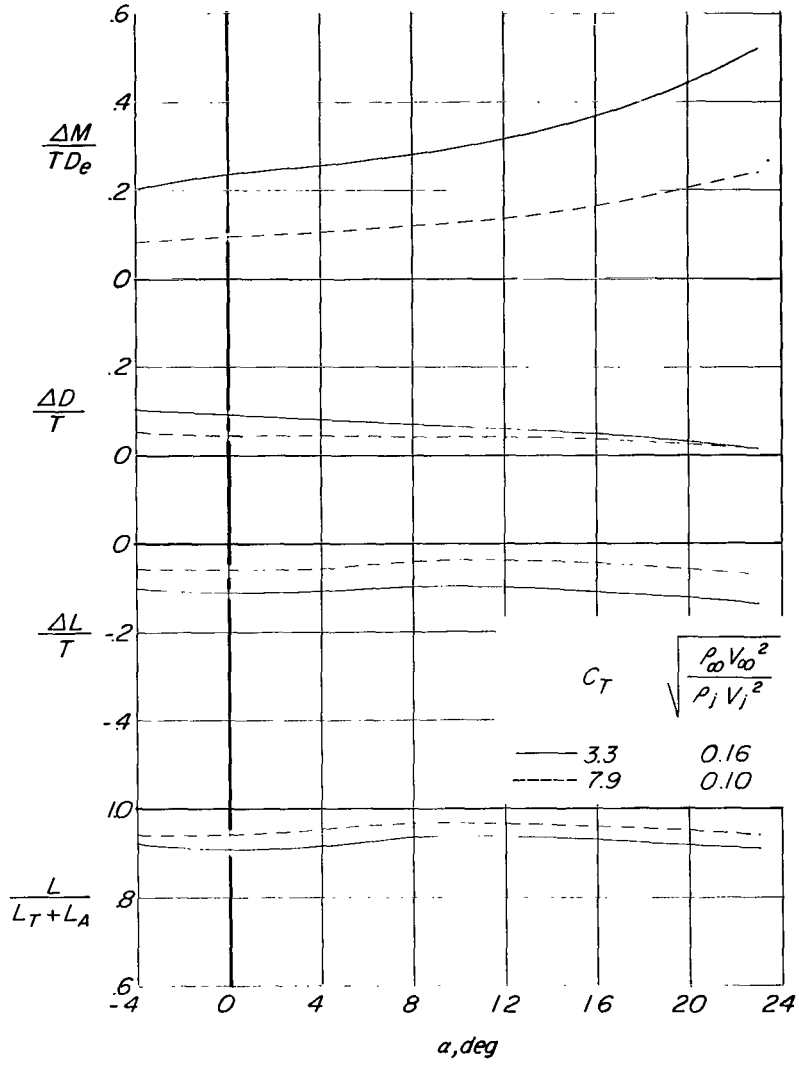

(c) Low tail position.

Figure 48.- Concluded.

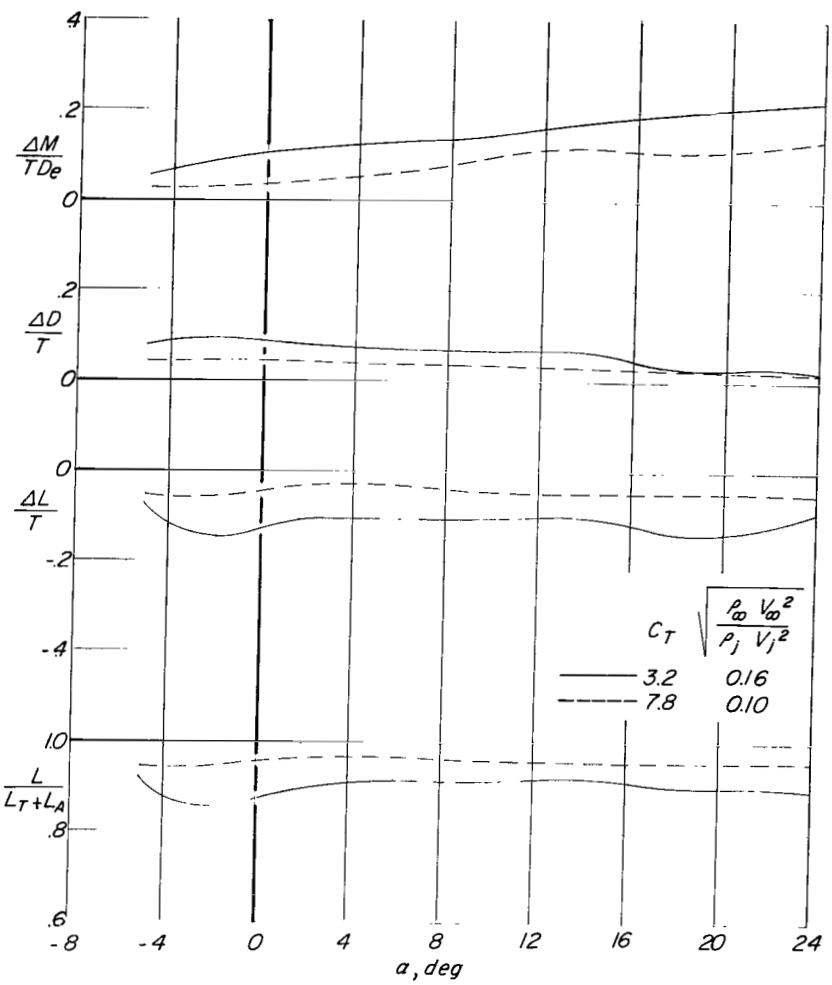

(a) Tail off.

Figure 49.- Effect of angle of attack on interference effects for configuration C ($\delta_f = 0^0$).

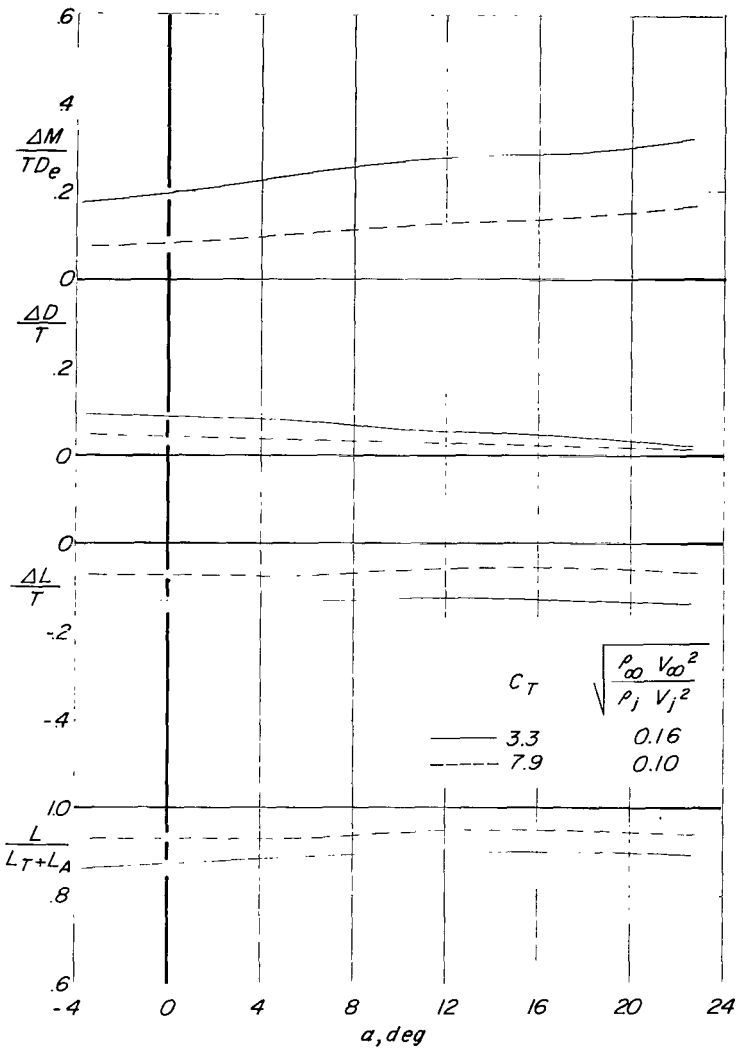

(b) Mid tail position.

Figure 49.- Continued.

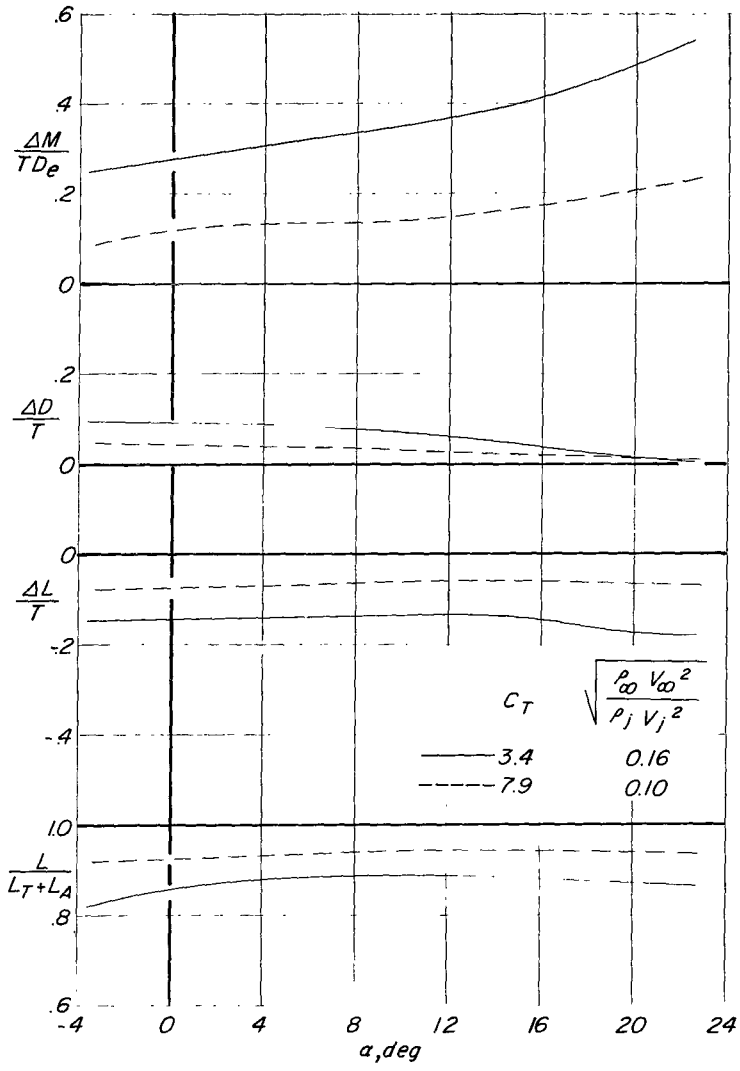

(c) Low tail position.

Figure 49.- Concluded.

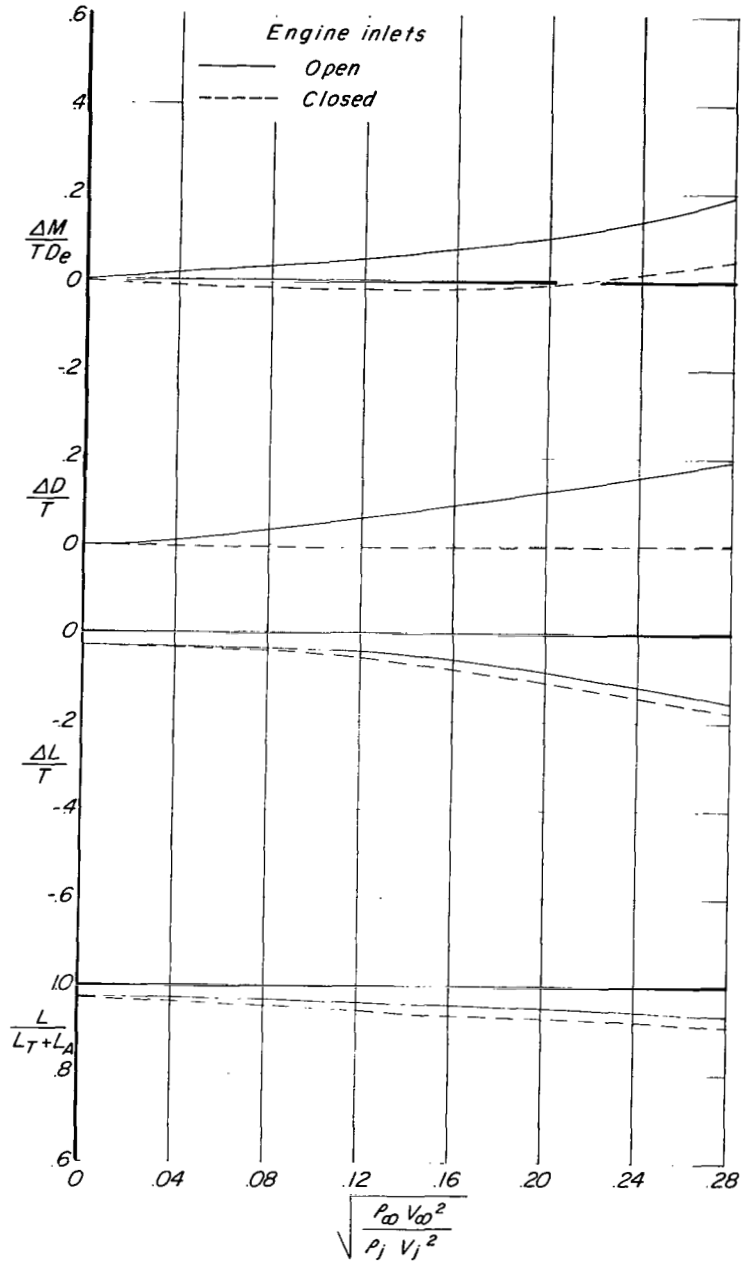

(a) $\alpha \approx 0.6^0$.

Figure 50.- Effect of inlet mass flow on interference for configuration A ($\delta_f = 30^0$, $\delta_s = 35^0$, fixed forewing) with horizontal tail off.

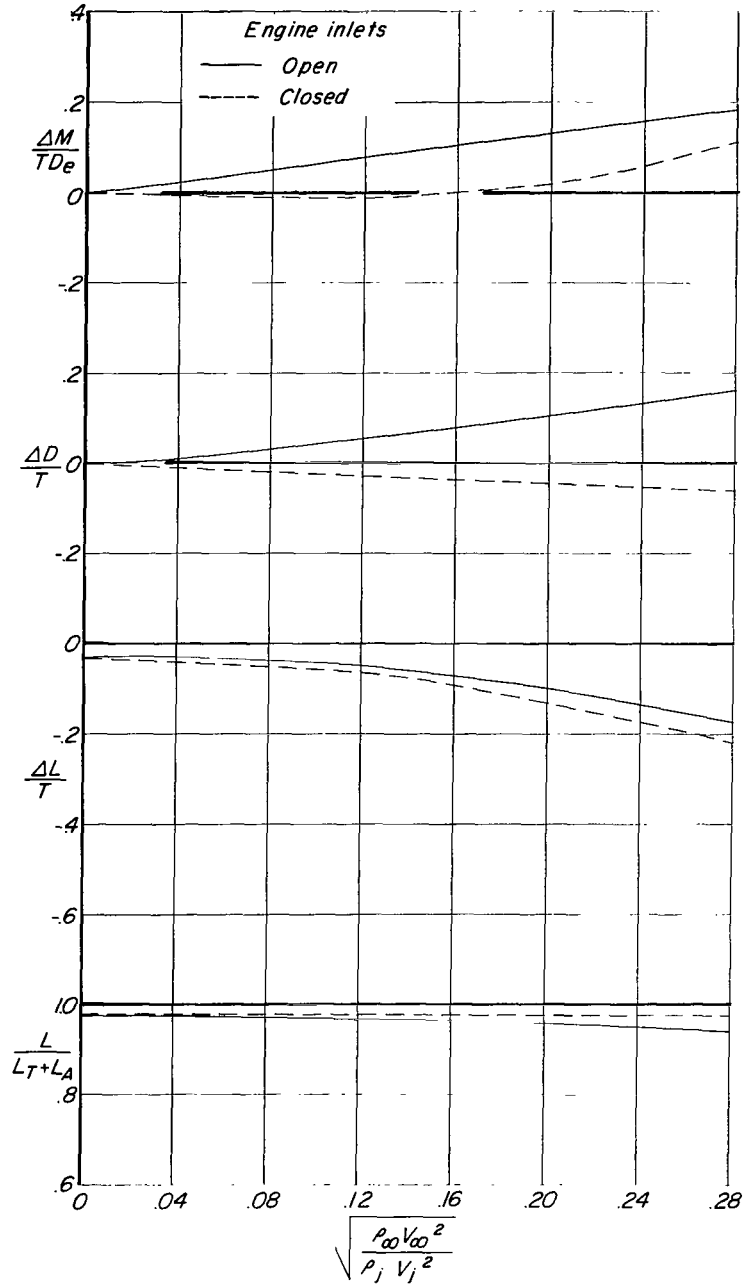

(b) $\alpha \approx 10.8^{0}$.

Figure 50.- Concluded.

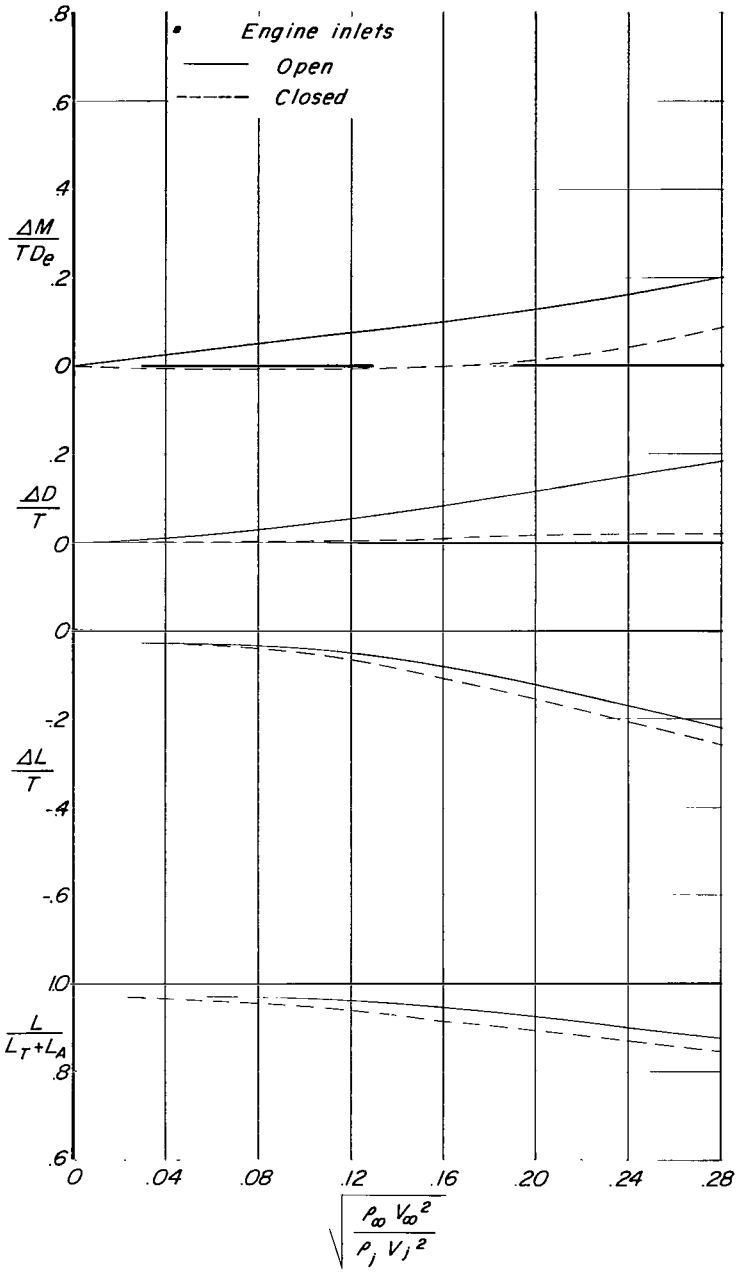

(a) $\alpha \approx 0.6^0$.

Figure 51.- Effect of inlet mass flow on interference for configuration B ($\delta_f = 30^0$) with horizontal tail off.

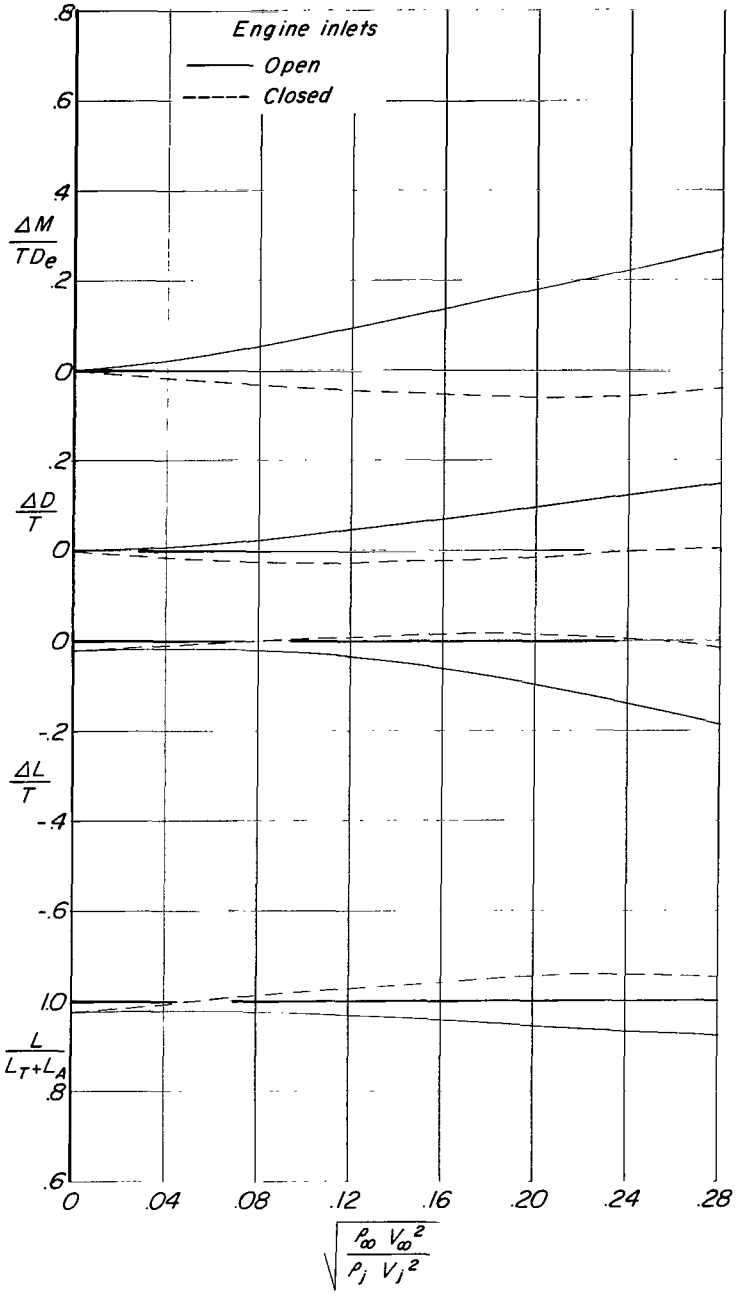

(b) $\alpha \approx 10.8^{0}$.

Figure 51.- Concluded.

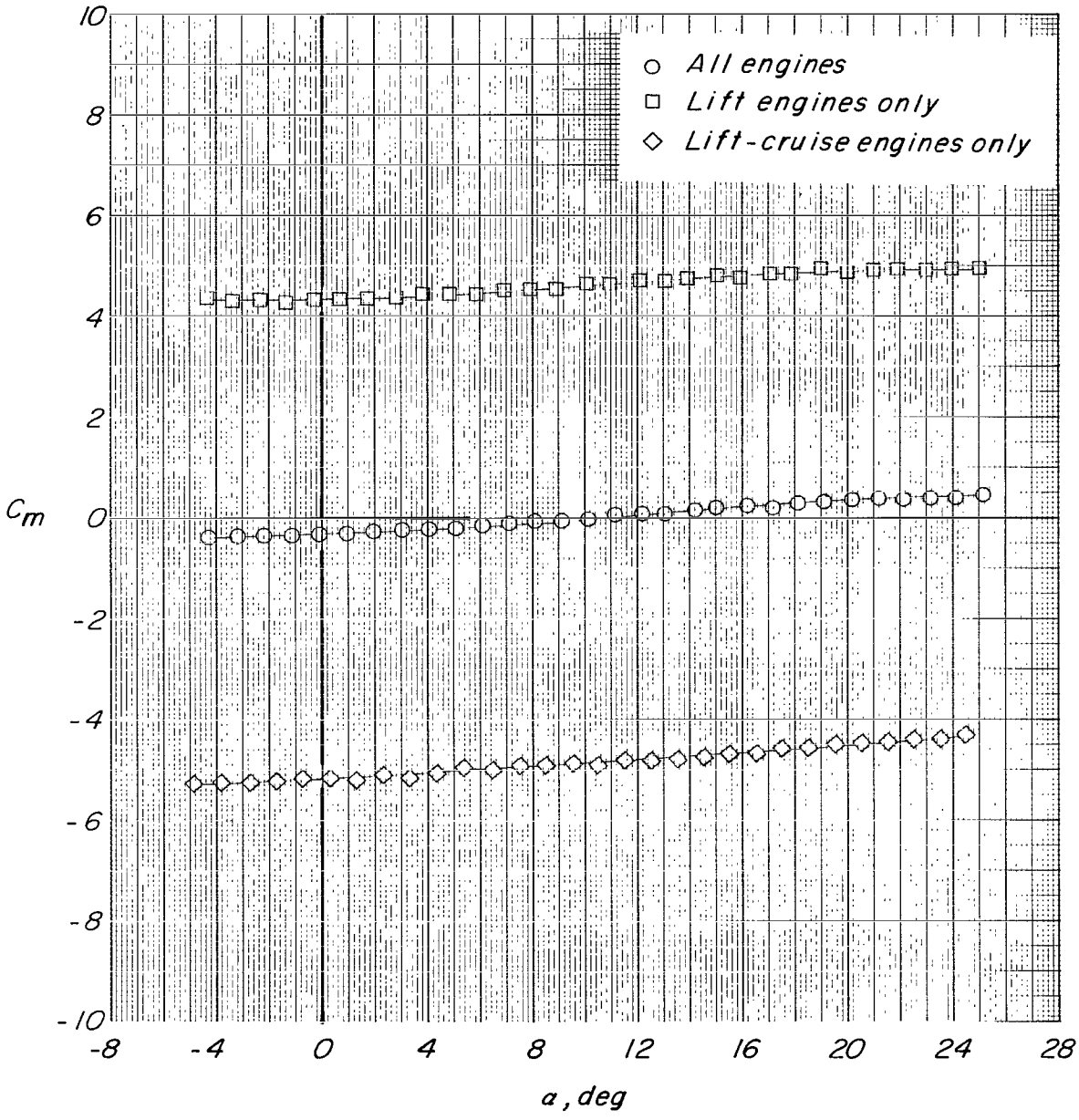

Figure 52.- Effect of engine location on variation of pitching-moment coefficient with angle of attack for configuration A ($\delta_f = 30^0$, $\delta_s = 35^0$, fixed forewing) with horizontal tail off.

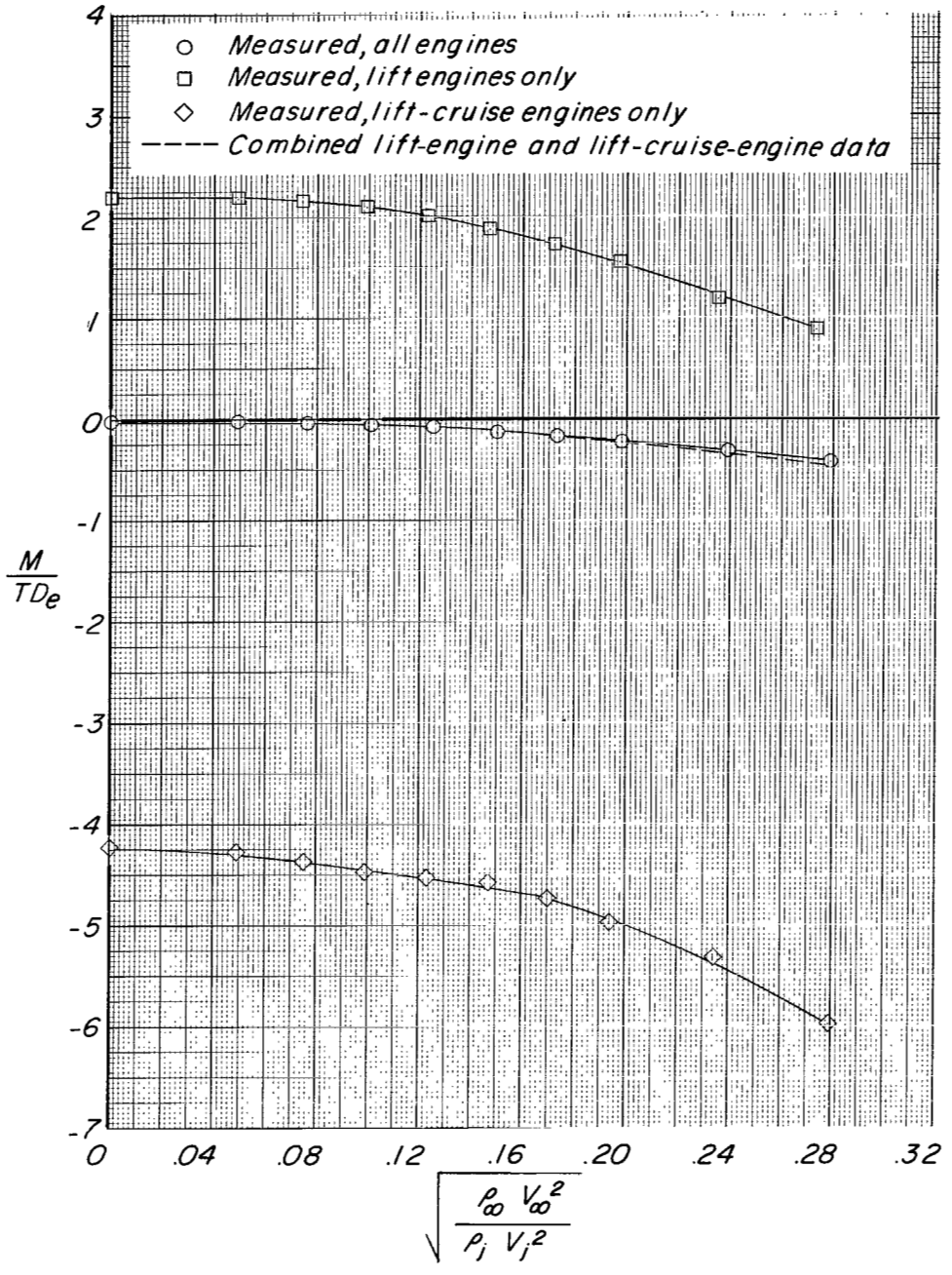

Figure 53.- Effect of engine location on mutual interference effects for configuration A ($\delta_f = 30^0$, $\delta_s = 35^0$, fixed forewing) with horizontal tail off. $\alpha \approx 0.6^0$.

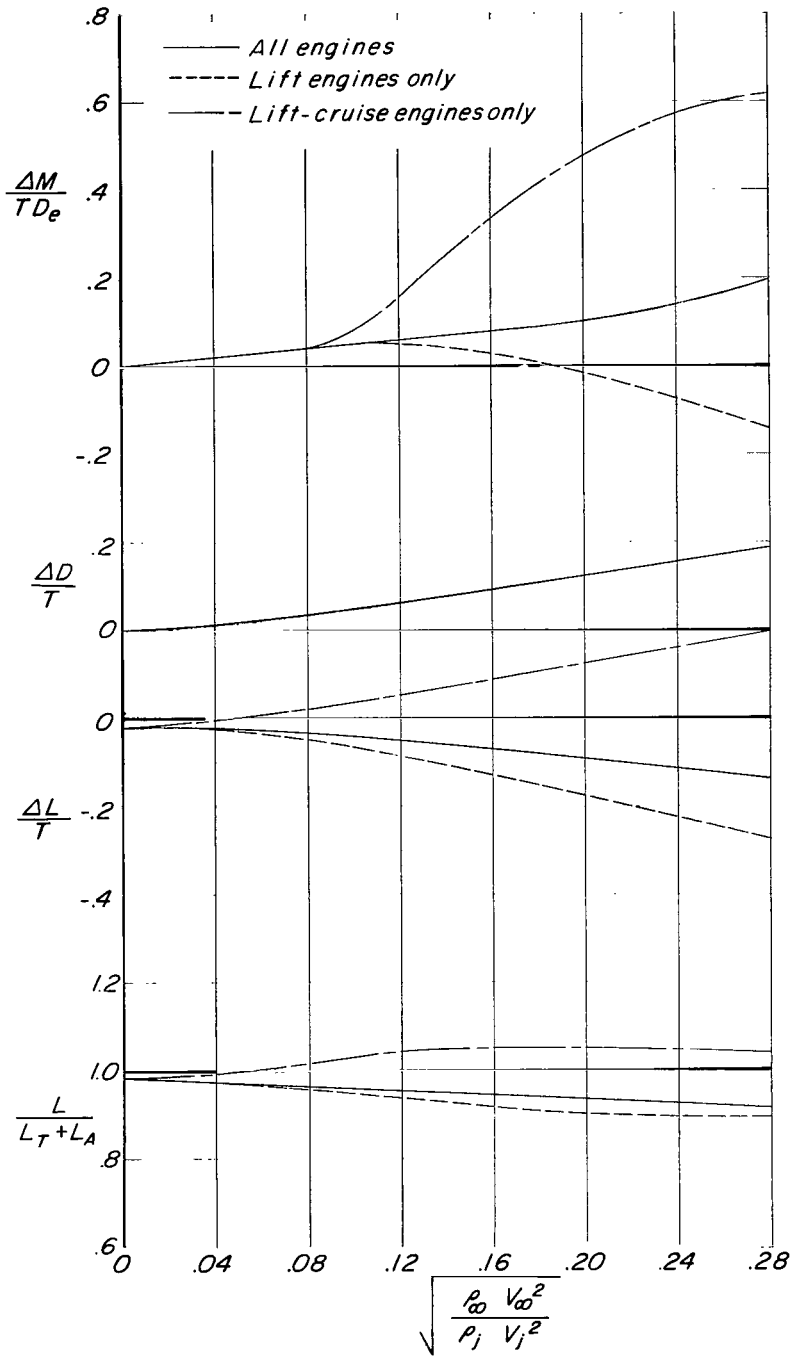

(a) Configuration A ($\delta_f = 30^0$, $\delta_s = 35^0$, fixed forewing).

Figure 54.- Effect of engine location on interference increments for three configurations tested with horizontal tail off. $\alpha \approx 0.6^0$.

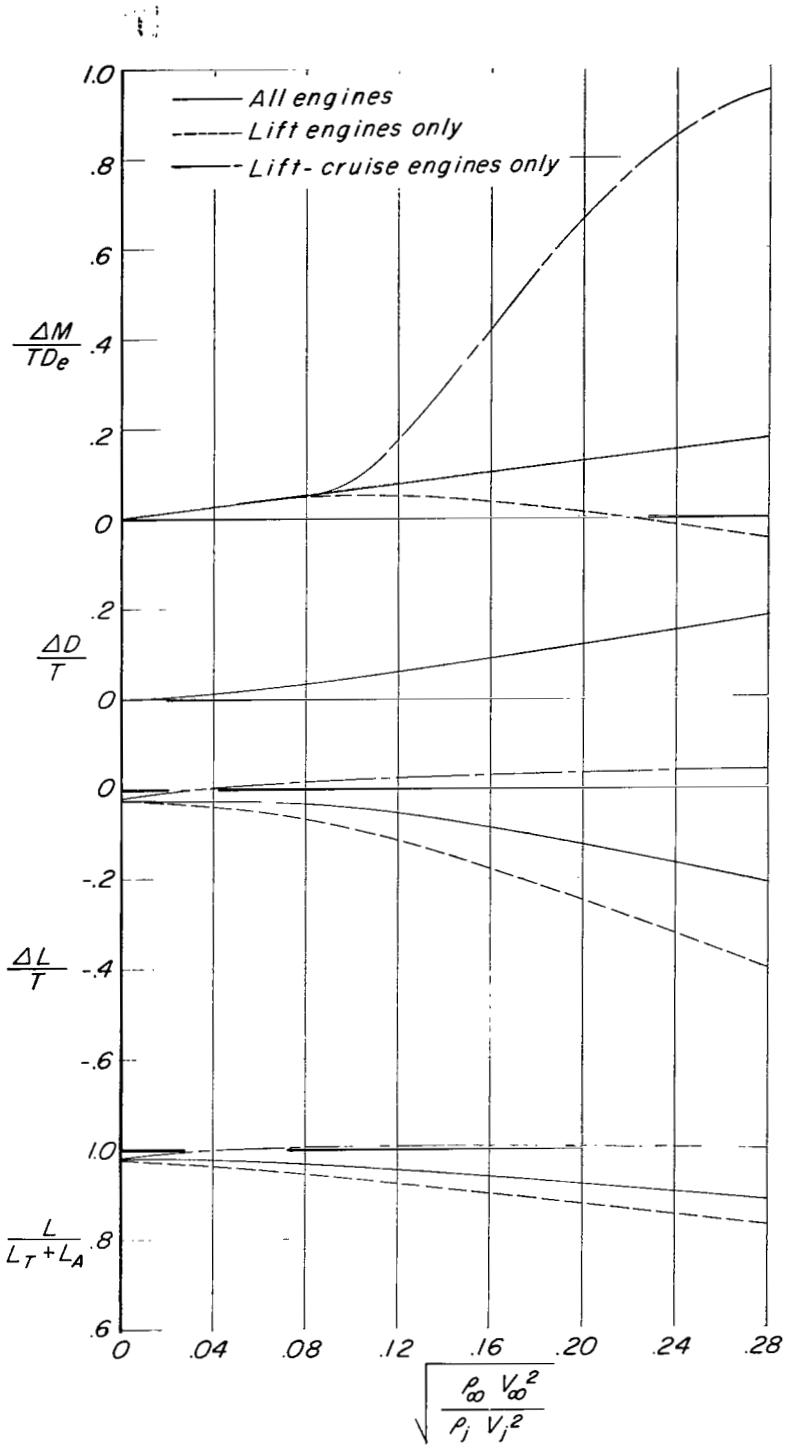

(b) Configuration B ($\delta_f = 30^0$).

Figure 54.- Continued.

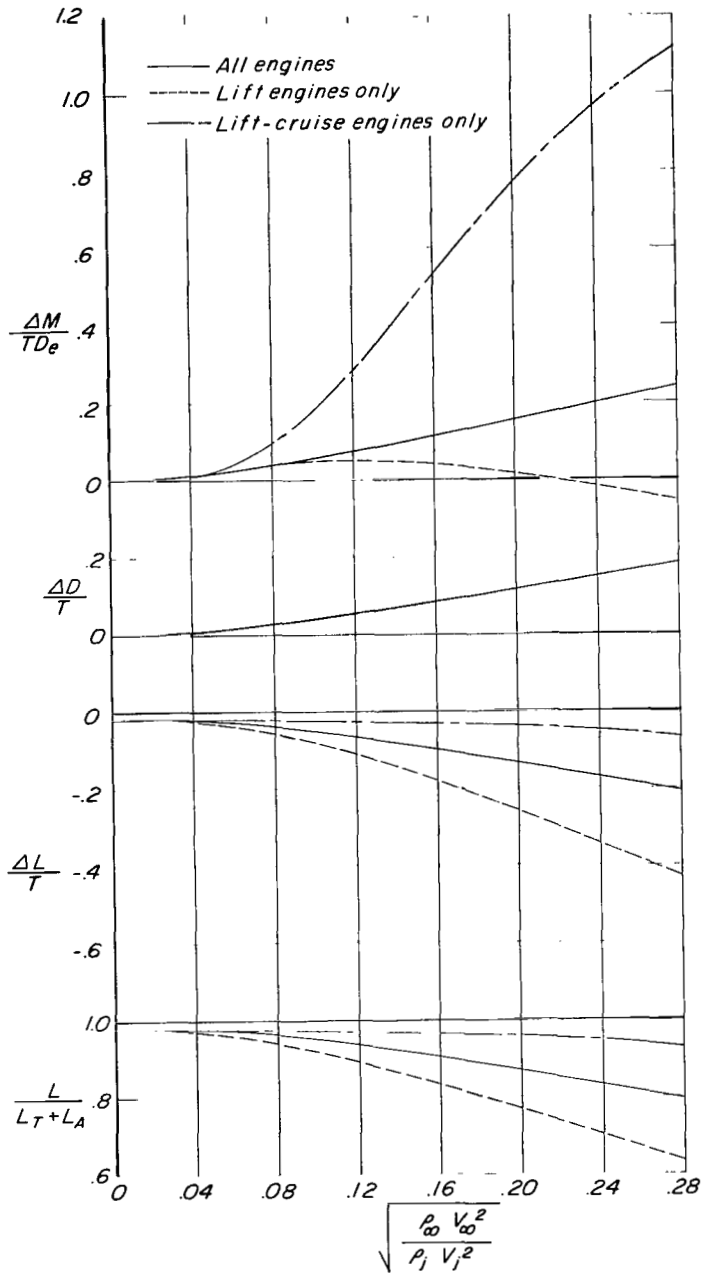

(c) Configuration C ($\delta_f = 0^0$).

Figure 54.- Concluded.

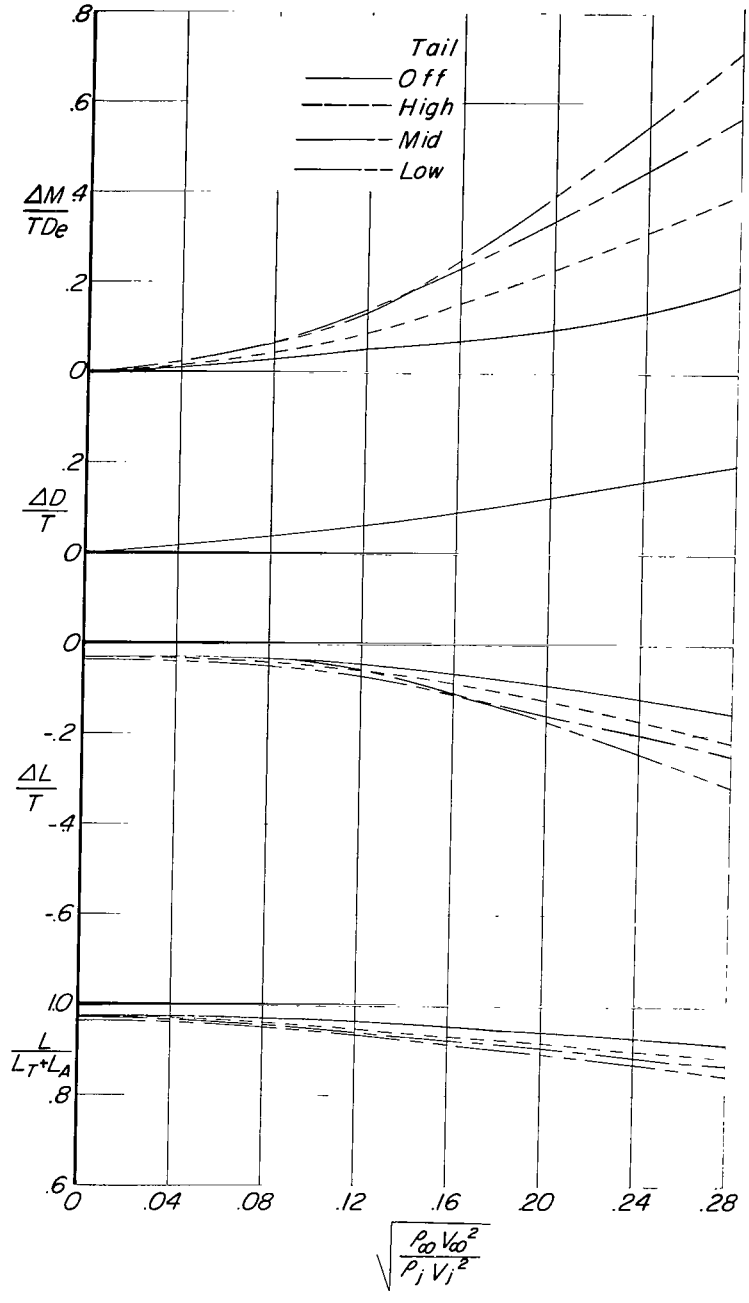

(a) $\alpha = 0.6^{0}$.

Figure 55.- Effect of horizontal-tail height on interference increments for configuration A ($\delta_f = 30^{0}$, $\delta_s = 35^{0}$, fixed forewing).

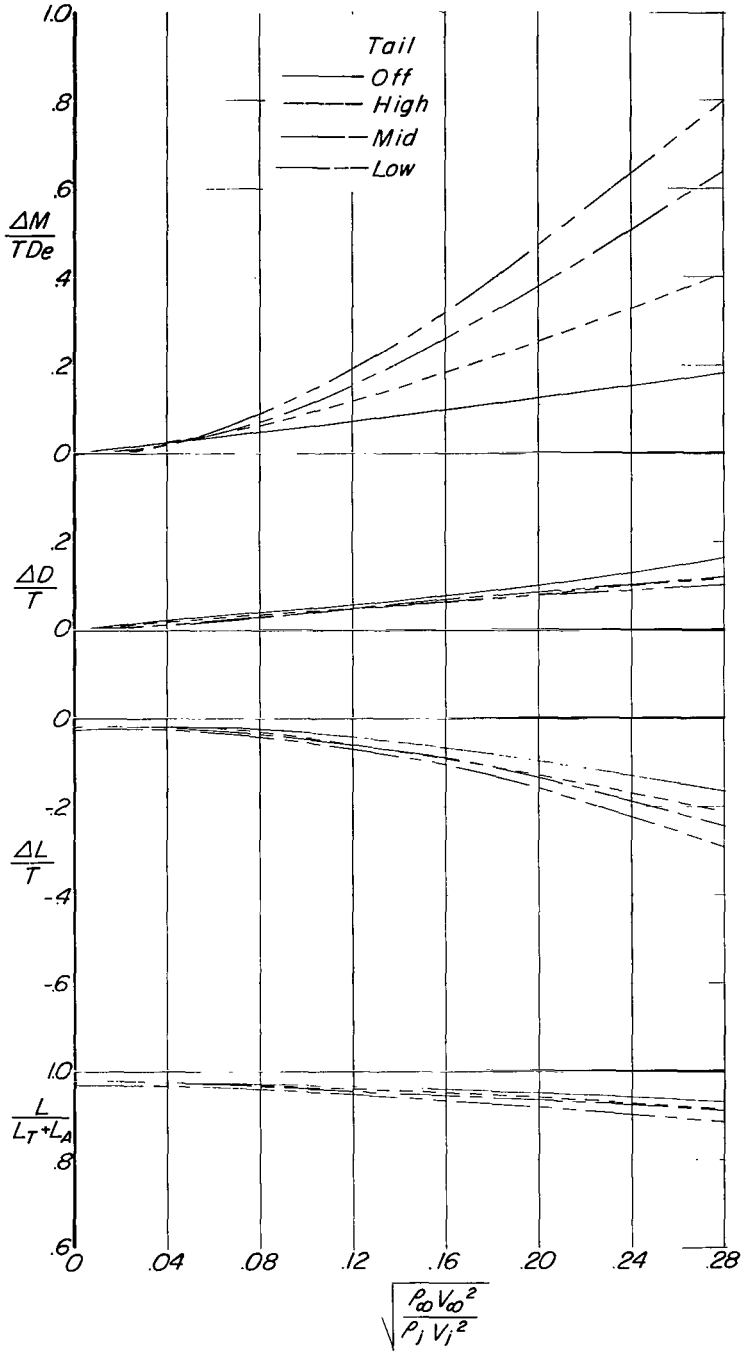

(b) $\alpha \approx 10.8^{0}$.

Figure 55.- Concluded.

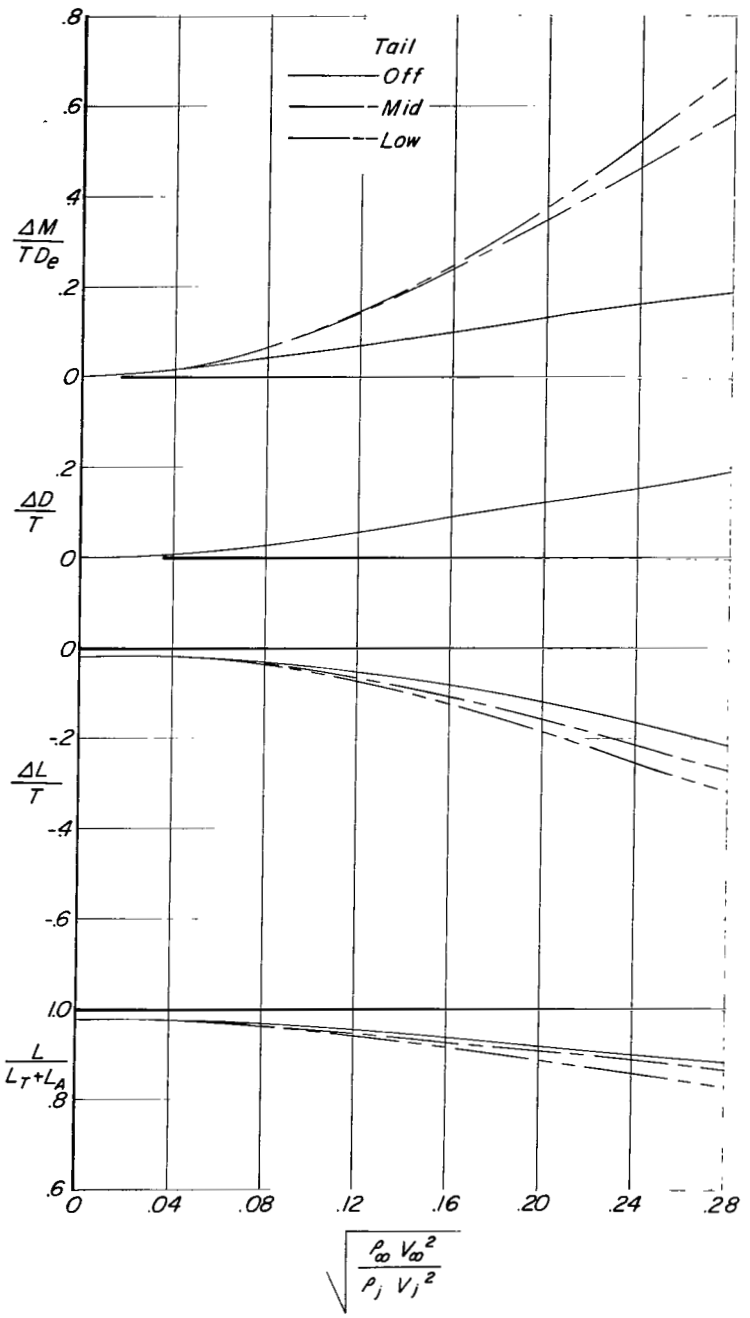

(a) $\alpha \approx 0.6^{0}$.

Figure 56.- Effect of horizontal-tail height on interference increments for configuration B ($\delta_f = 30^{0}$).

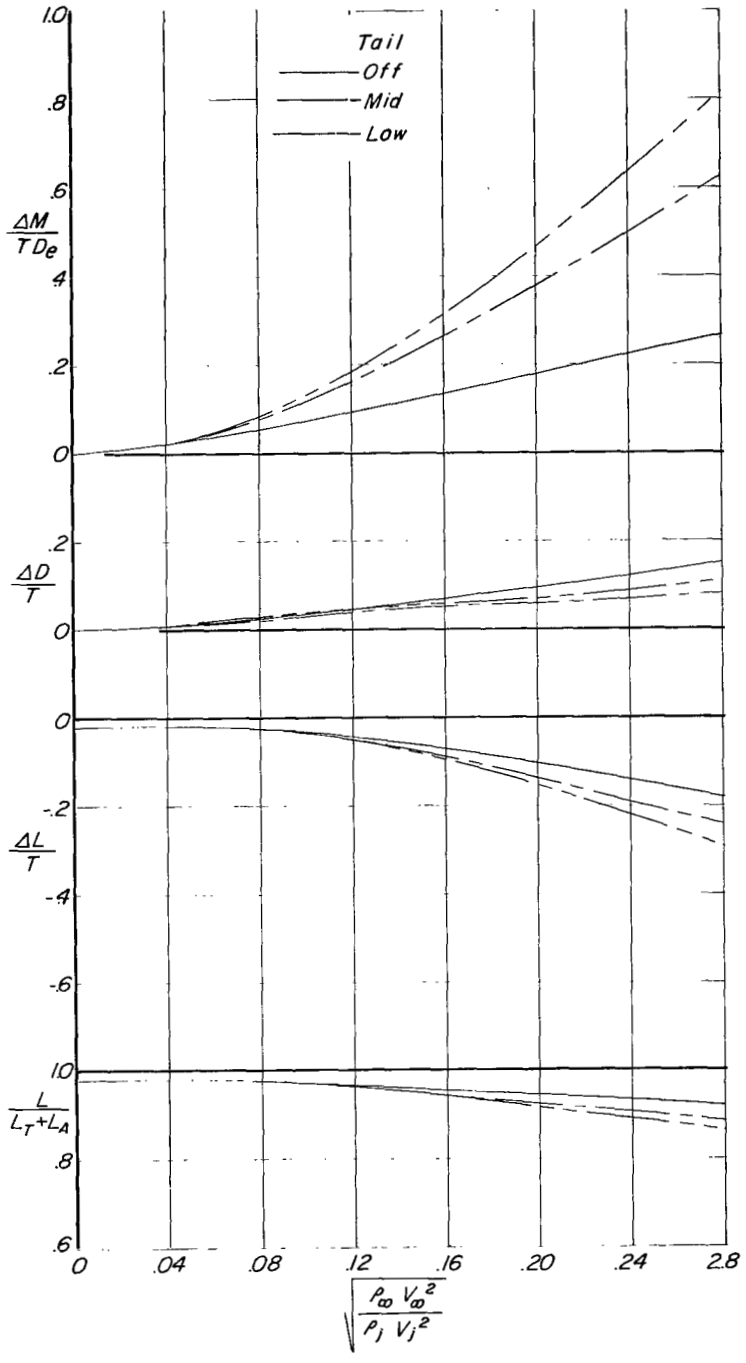

(b) $\alpha \approx 10.8^{0}$.

Figure 56.- Concluded.

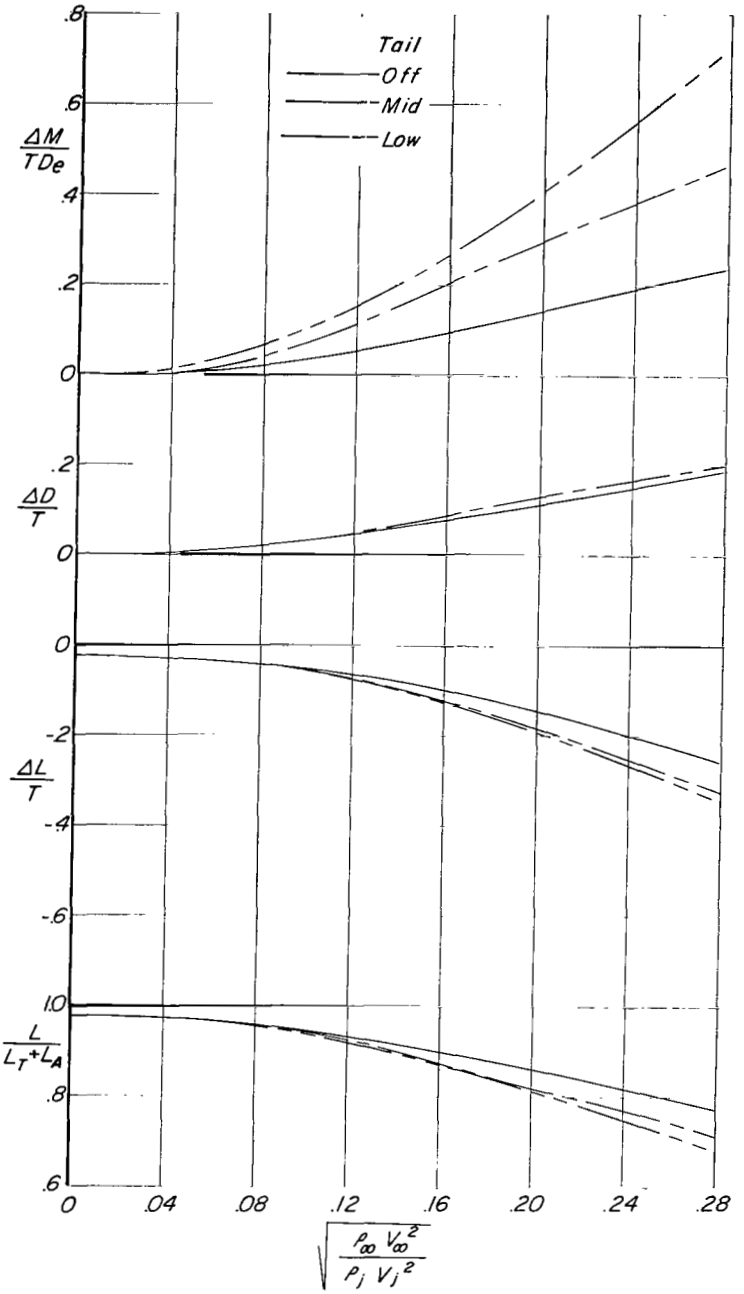

(a) $\alpha \approx 0.6^0$.

Figure 57.- Effect of horizontal-tail height on interference increments for configuration C ($\delta_f = 0^0$).

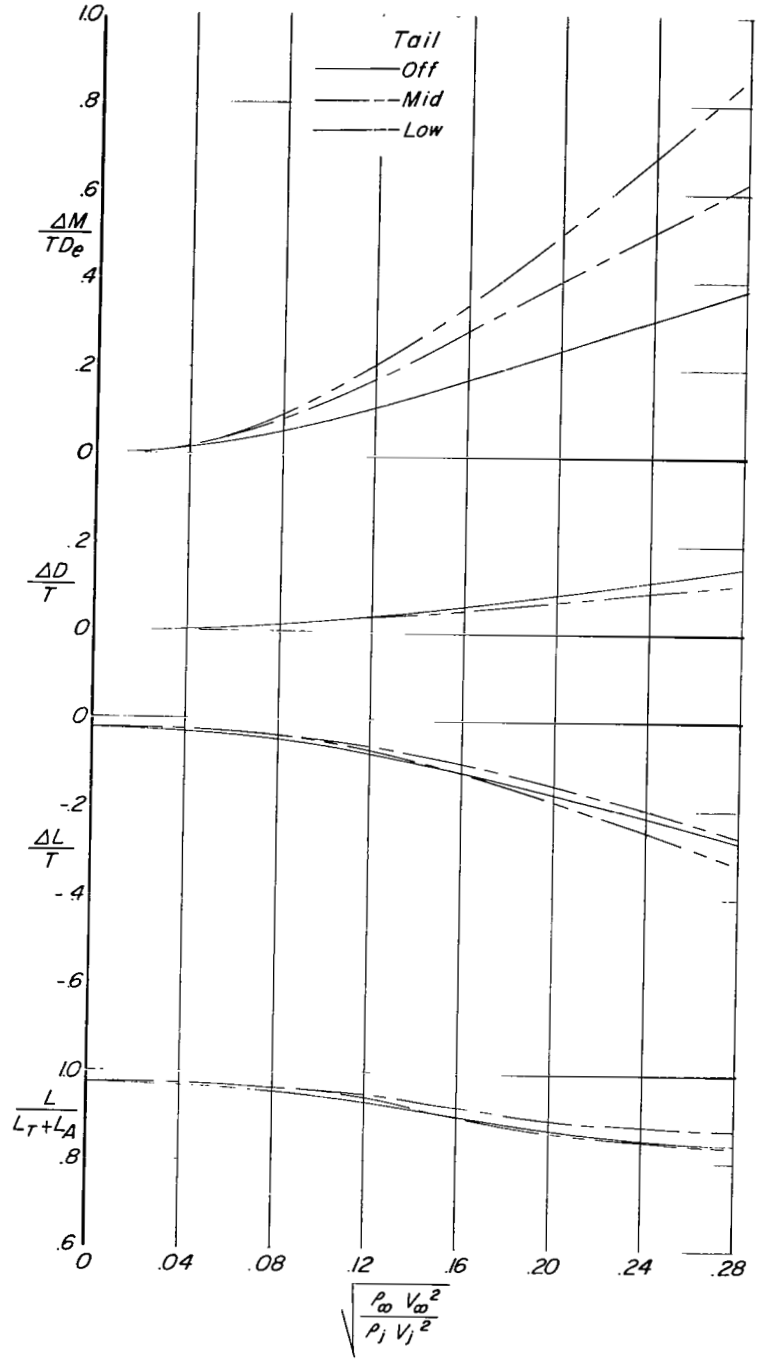

(b) $\alpha \approx 10.8^{0}$.

Figure 57.- Concluded.

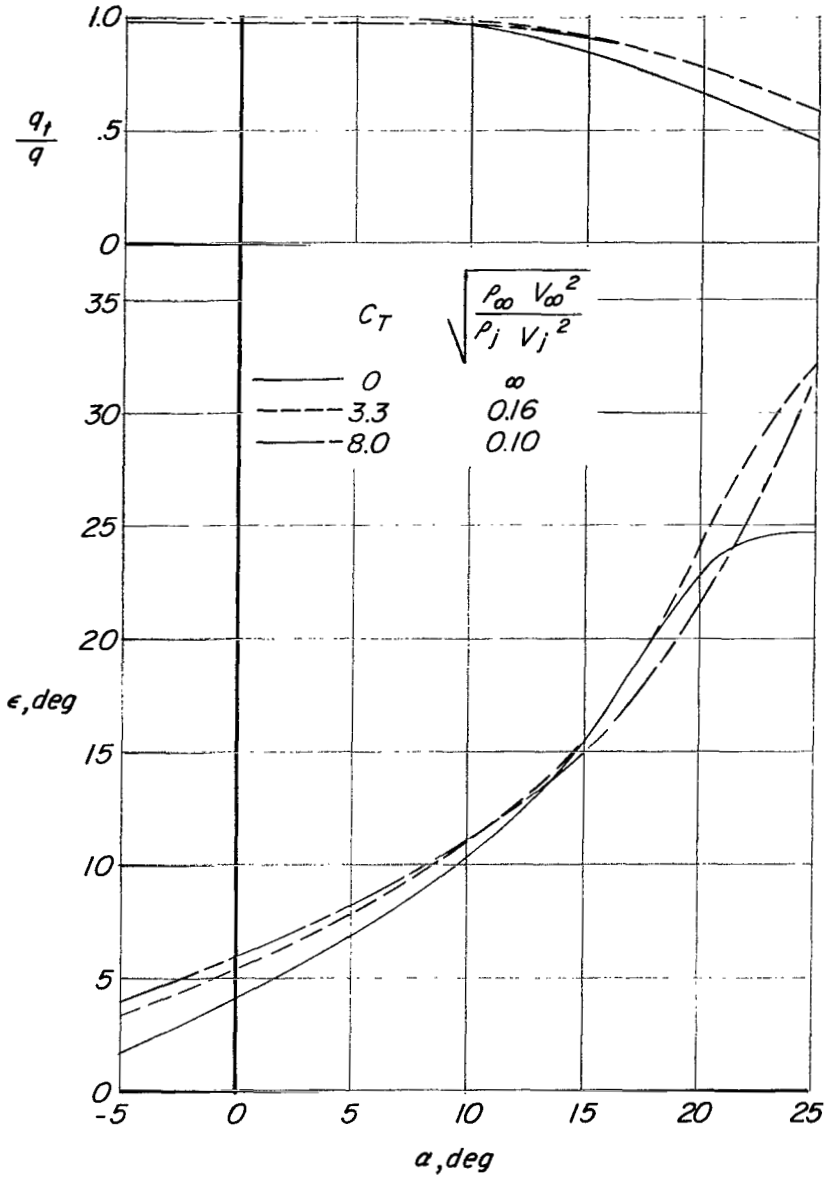

(a) High tail position.

Figure 58.- Downwash at horizontal tail for configuration A ($\delta_f = 30^0$, $\delta_s = 35^0$, fixed forewing).

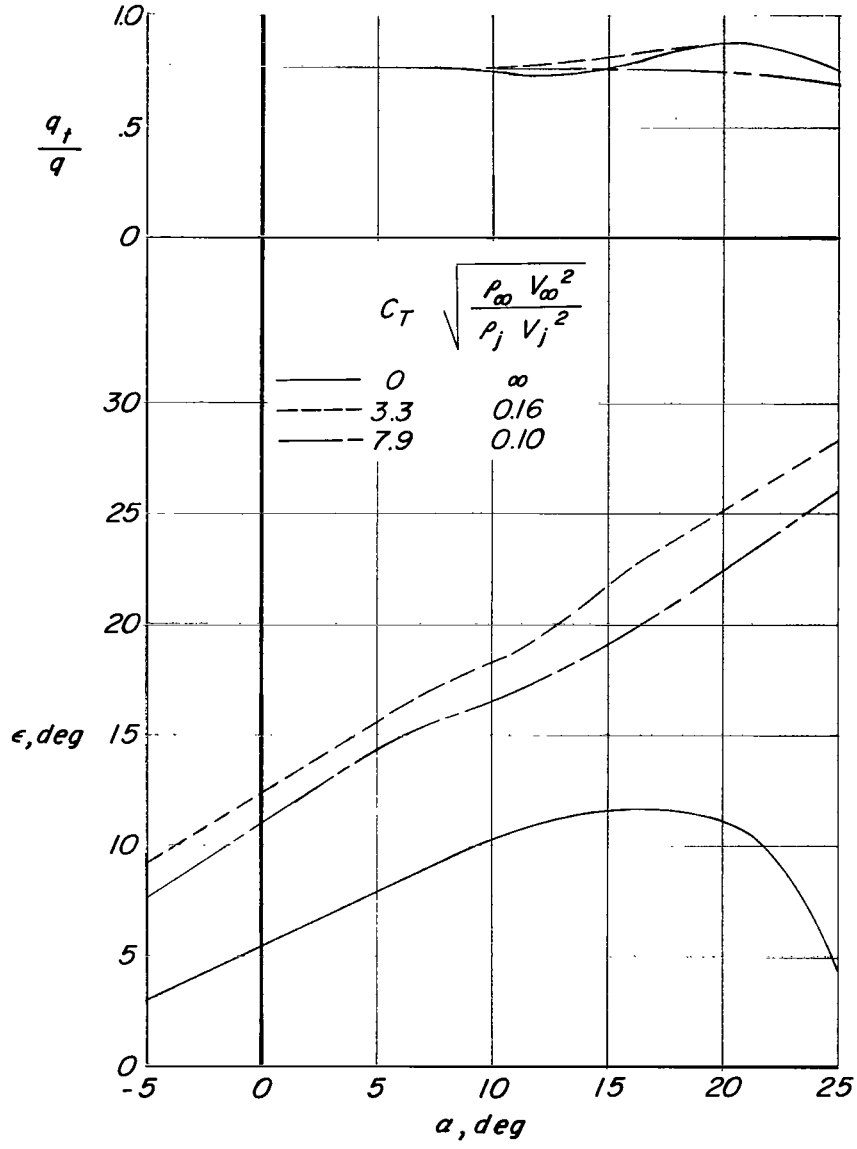

(b) Mid tail position.

Figure 58.- Continued.

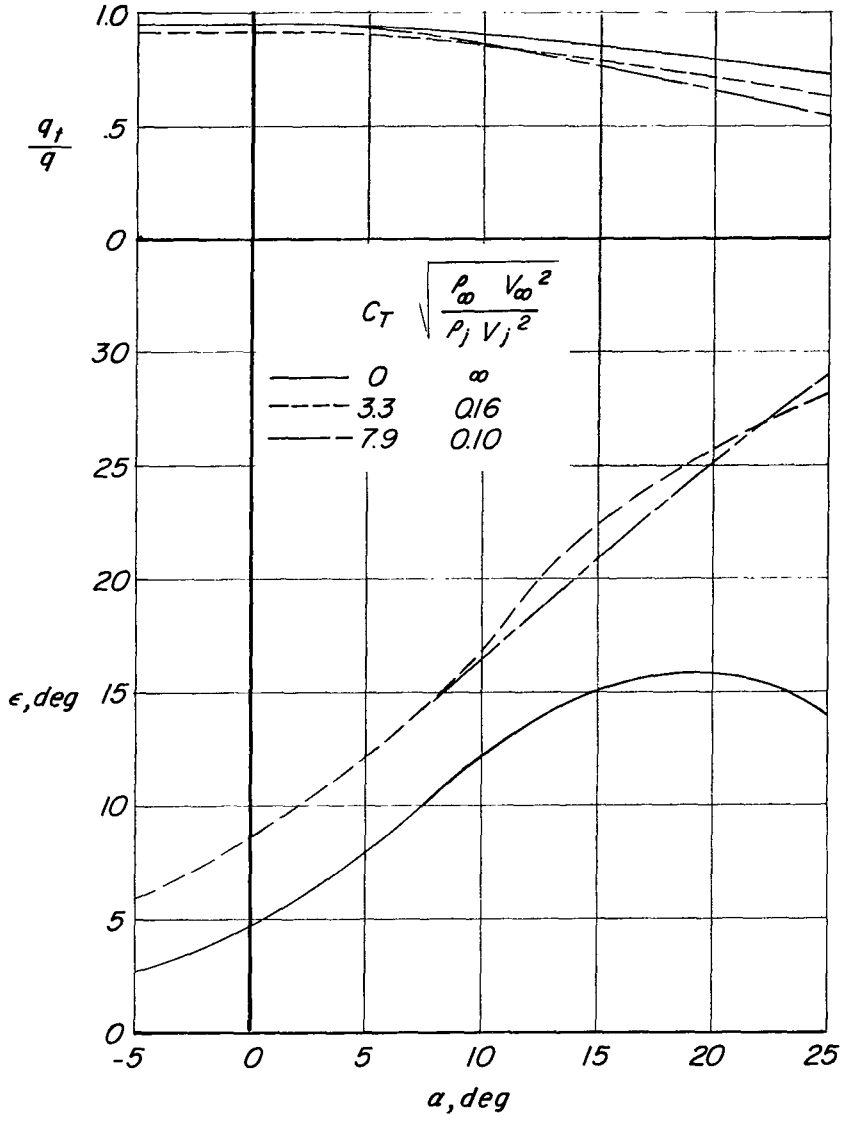

(c) Low tail position.

Figure 58.- Concluded.

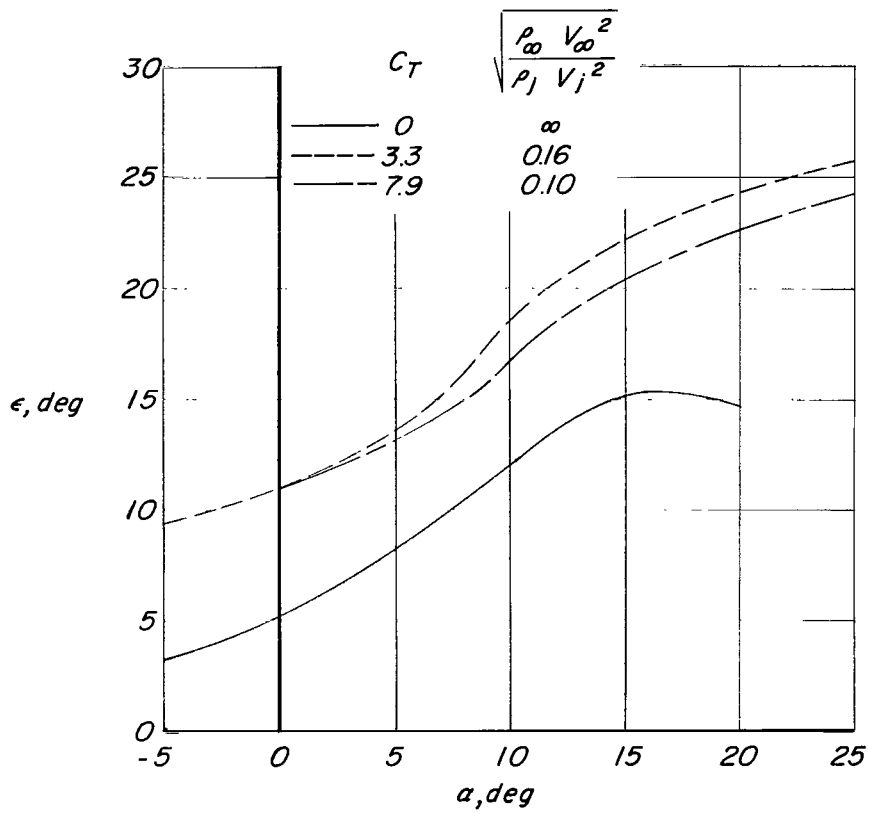

(a) Mid tail position.

Figure 59.- Downwash at horizontal tail for configuration B ($\delta_f = 30^0$).

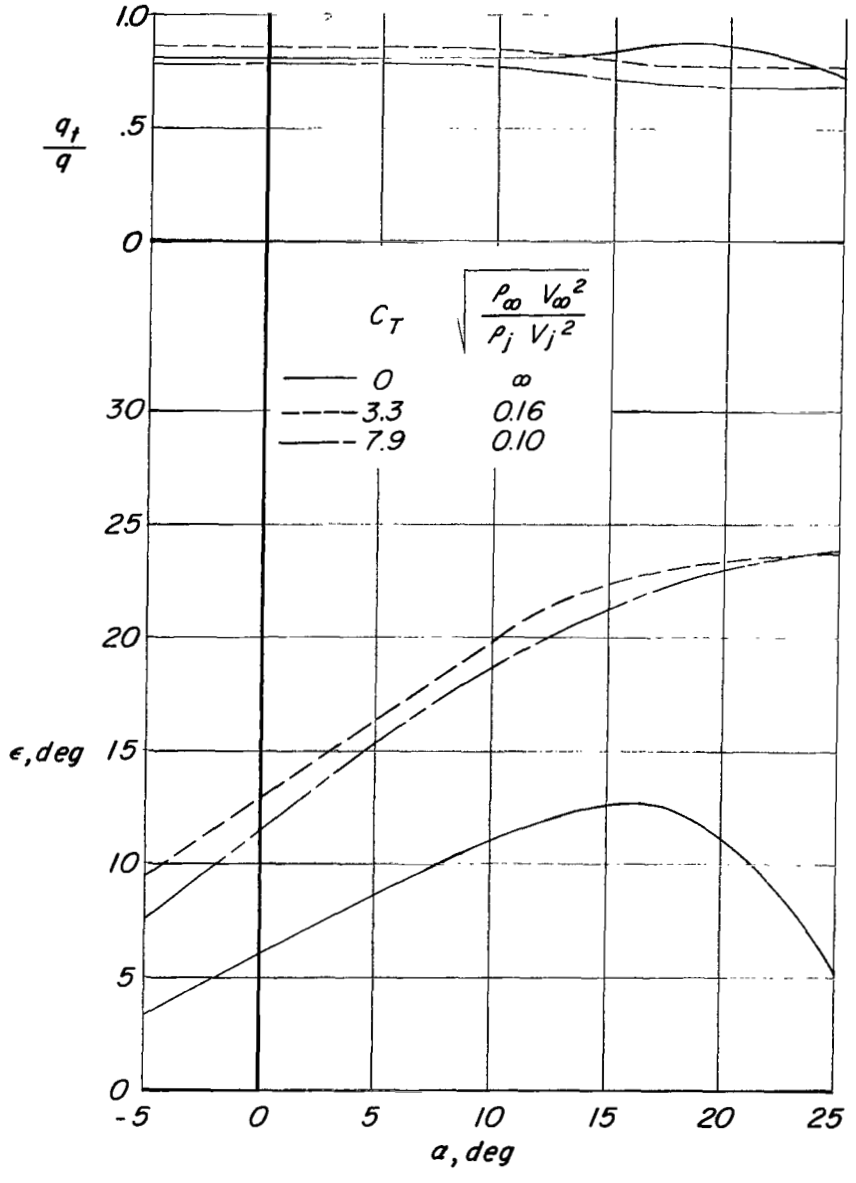

(b) Low tail position.

Figure 59.- Concluded.

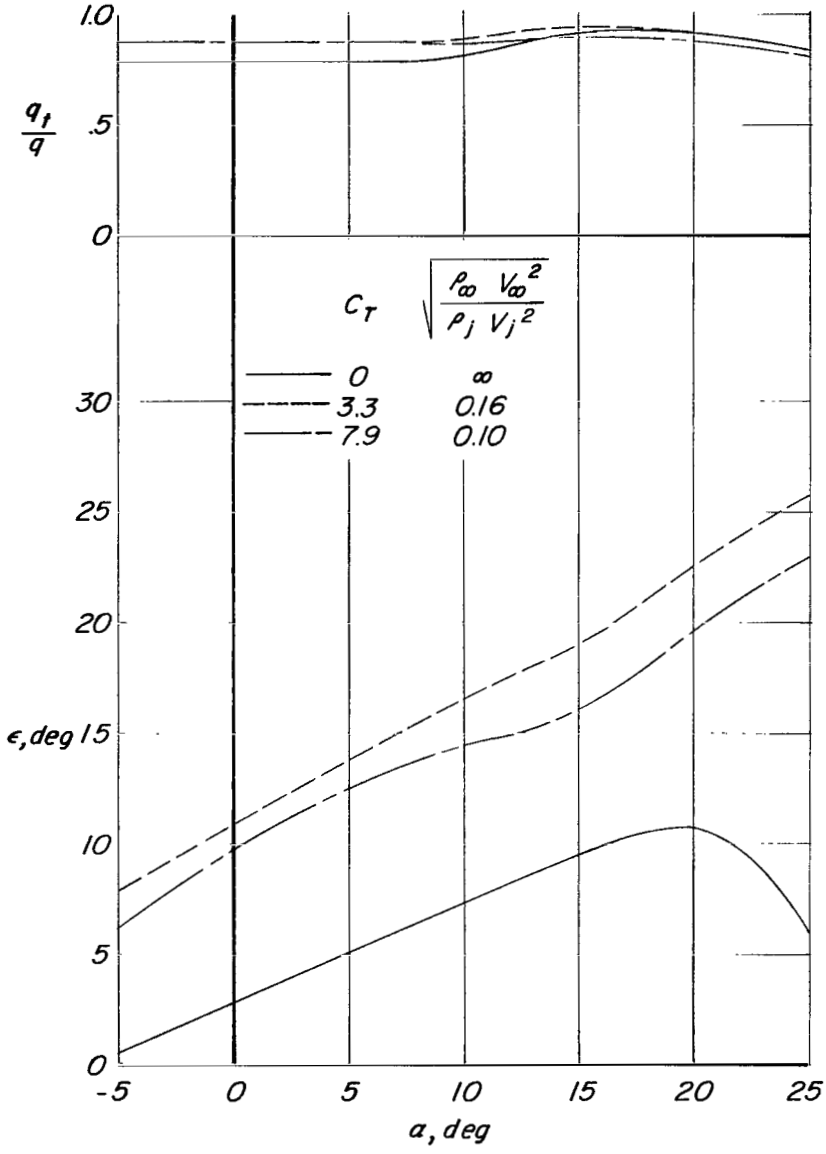

(a) Mid tail position.

Figure 60.- Downwash at horizontal tail for configuration C ($\delta_f = 0^0$).

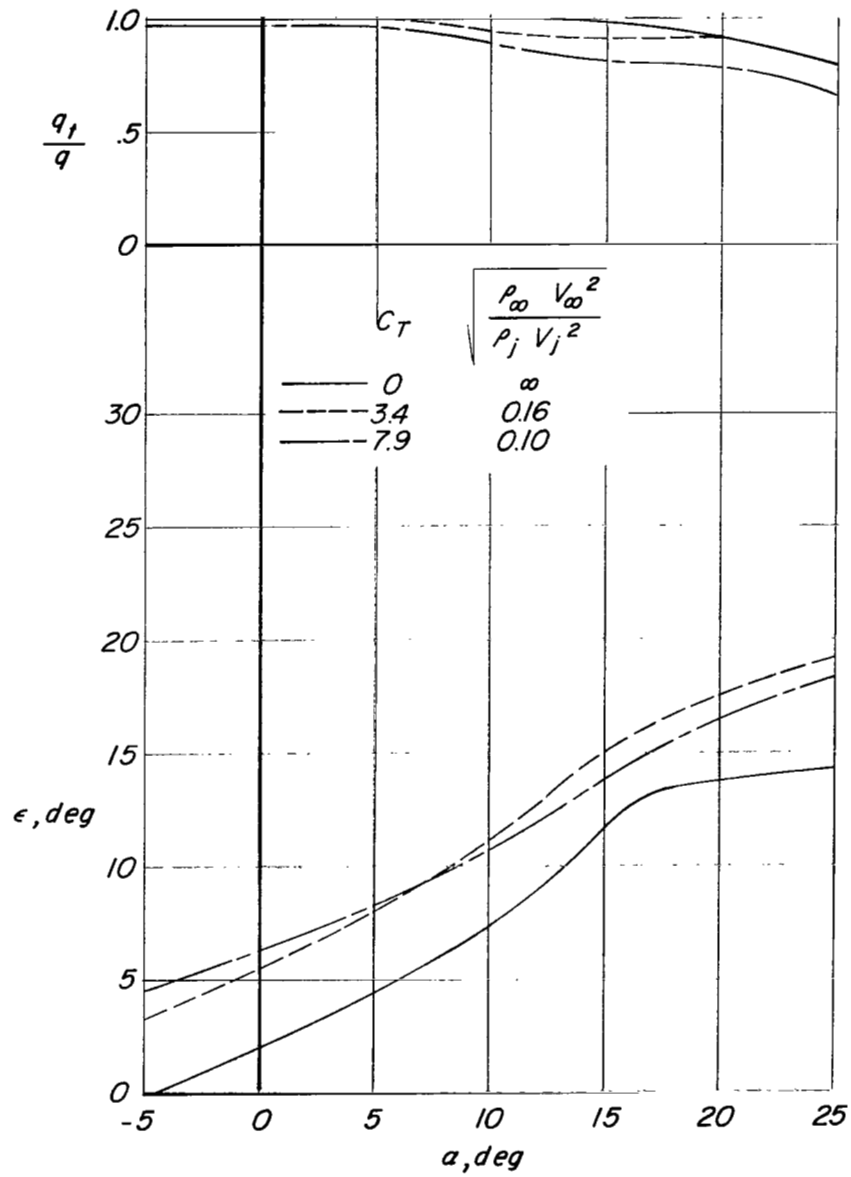

(b) Low tail position.

Figure 60.- Concluded.

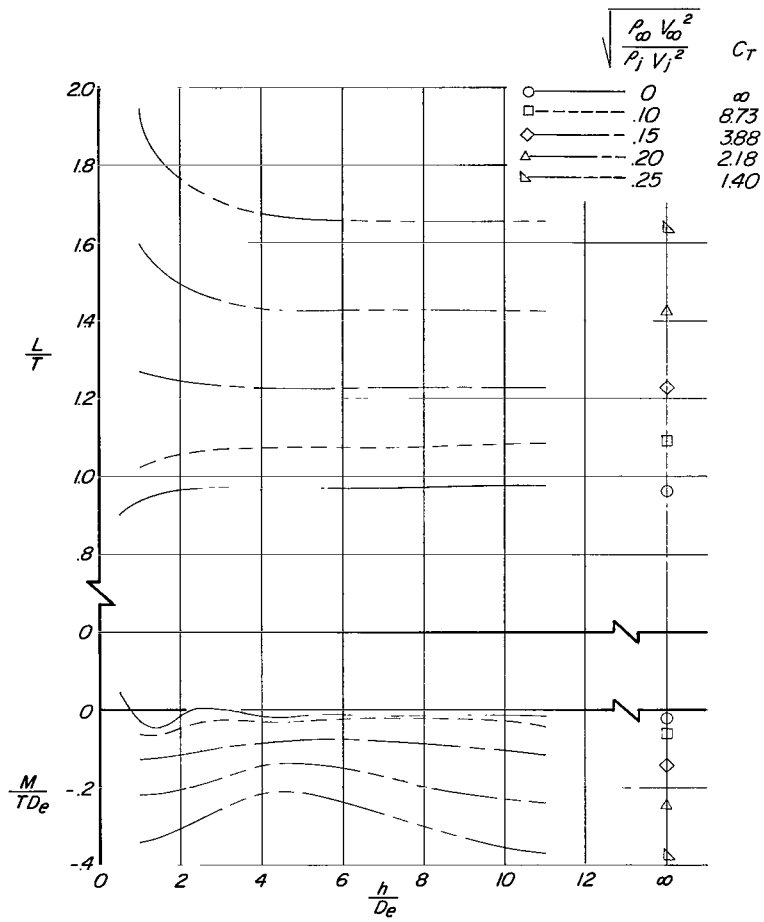

(a) $\alpha \approx 0.6^0$.

Figure 61.- Effect of height above ground on lift and pitching-moment parameters for configuration A ($\delta_f = 30^0$, $\delta_s = 35^0$, fixed forewing) with horizontal tail off for several thrust coefficients.

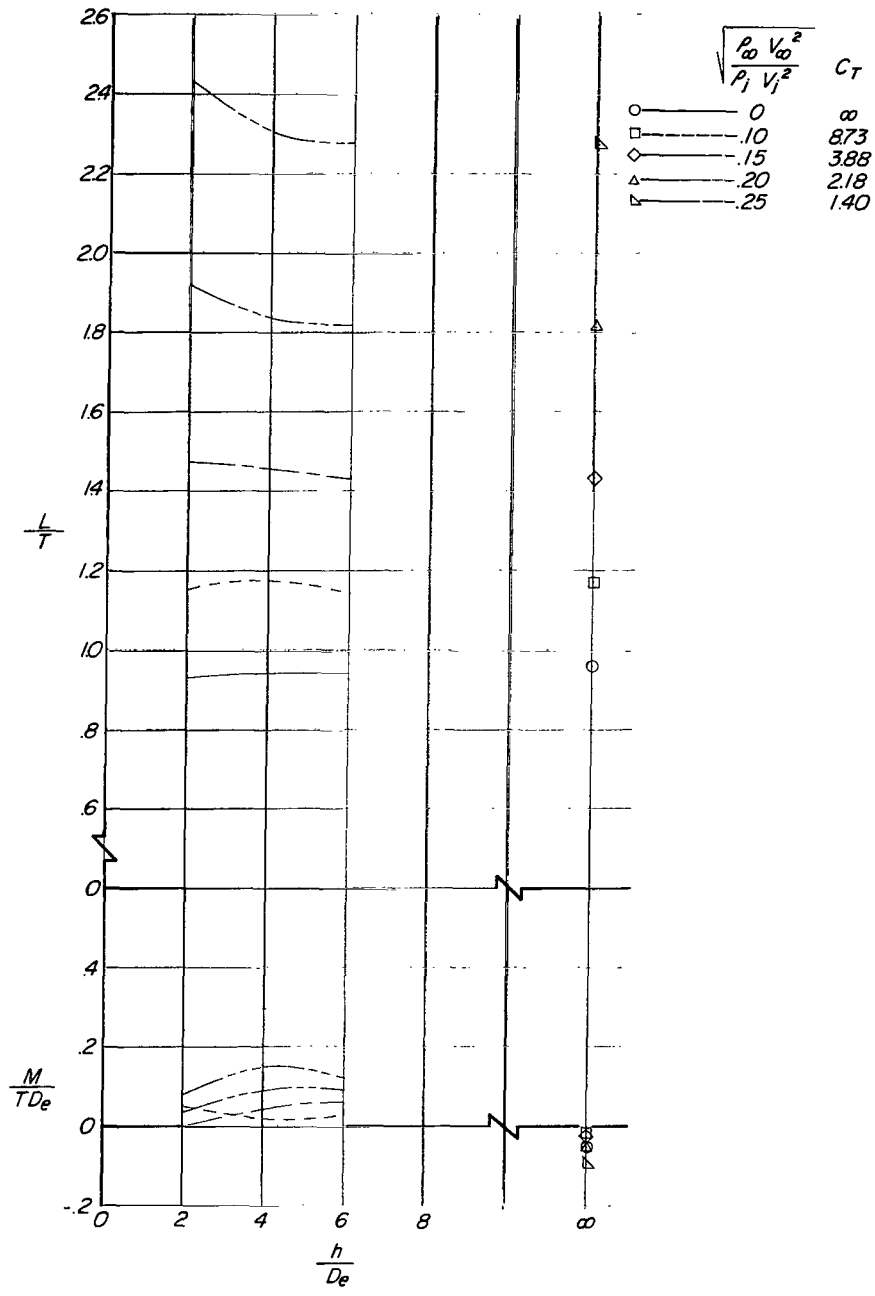

(b) $\alpha \approx 10.8^0$.

Figure 61.- Concluded.

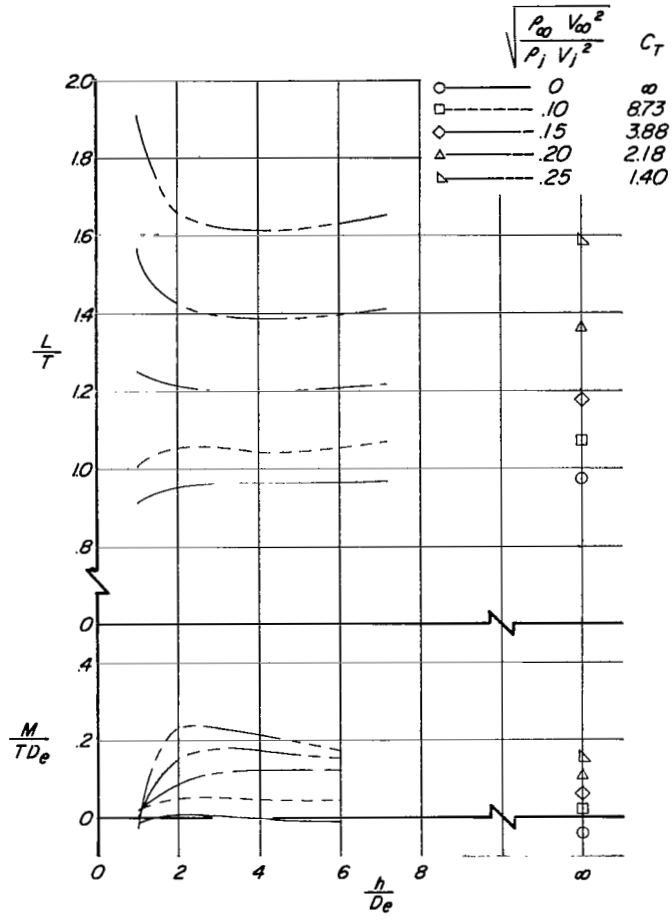

(a) $\alpha \approx 0.6^0$.

Figure 62.- Effect of height above ground on lift and pitching-moment parameters for configuration A ($\delta_f = 30^0$, $\delta_s = 35^0$, fixed forewing) with horizontal tail in high position ($i_t = 0^0$) for several thrust coefficients.

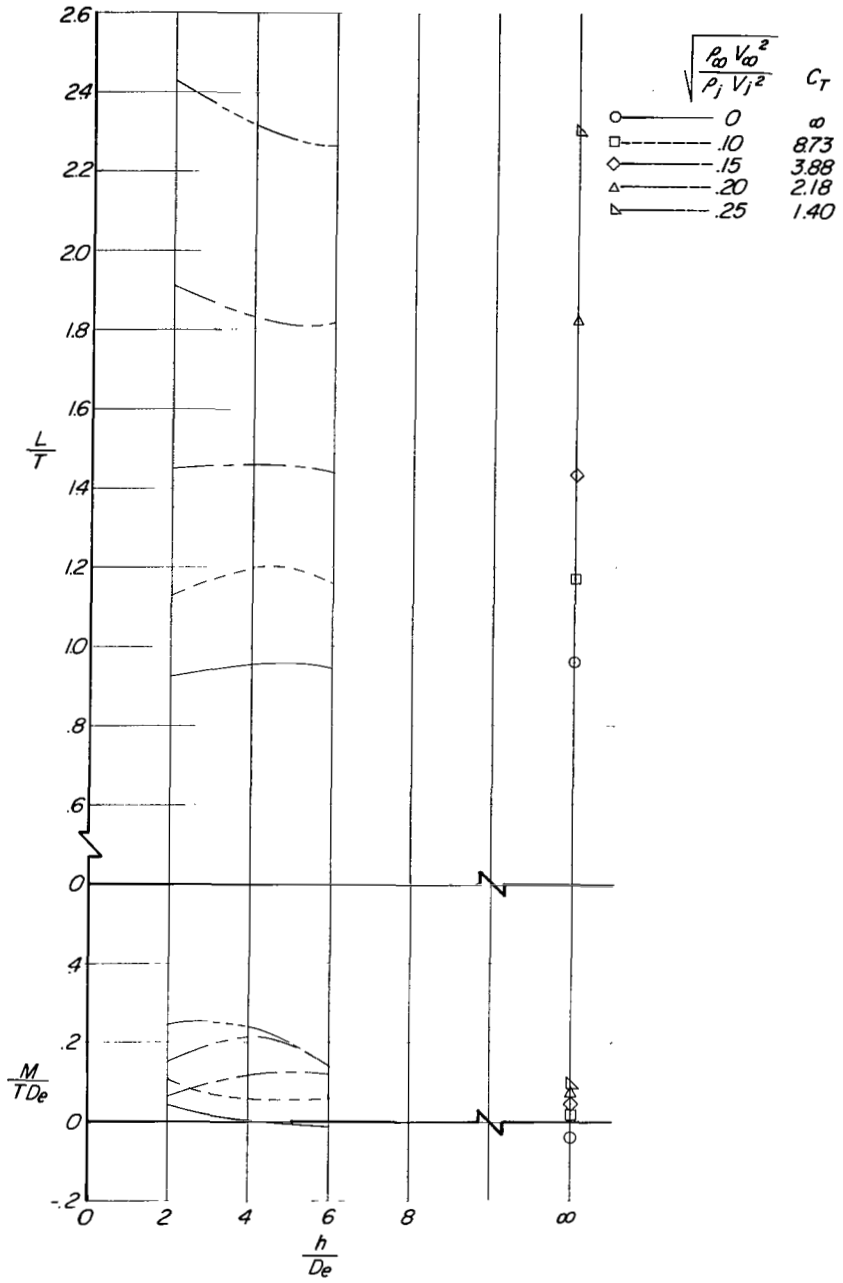

(b) $\alpha \approx 10.8^{\circ}$.

Figure 62.- Concluded.

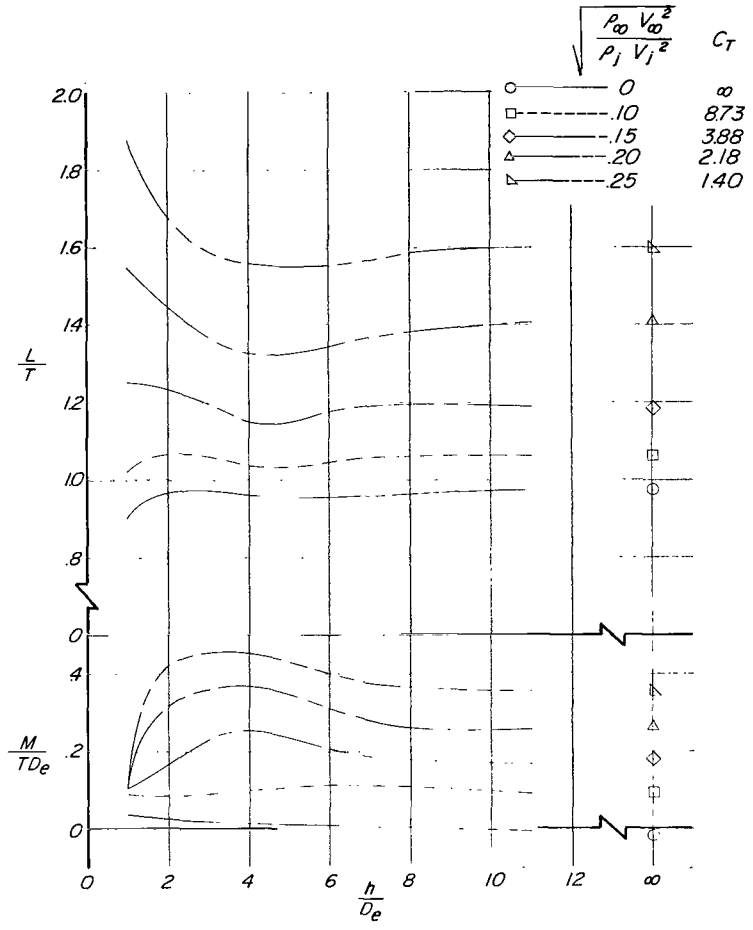

(a) $\alpha \approx 0.6^0$.

Figure 63.- Effect of height above ground on lift and pitching-moment parameters for configuration A ($\delta_f = 30^0$, $\delta_s = 35^0$, fixed forewing) with horizontal tail in mid position ($i_t = 0^0$) for several thrust coefficients.

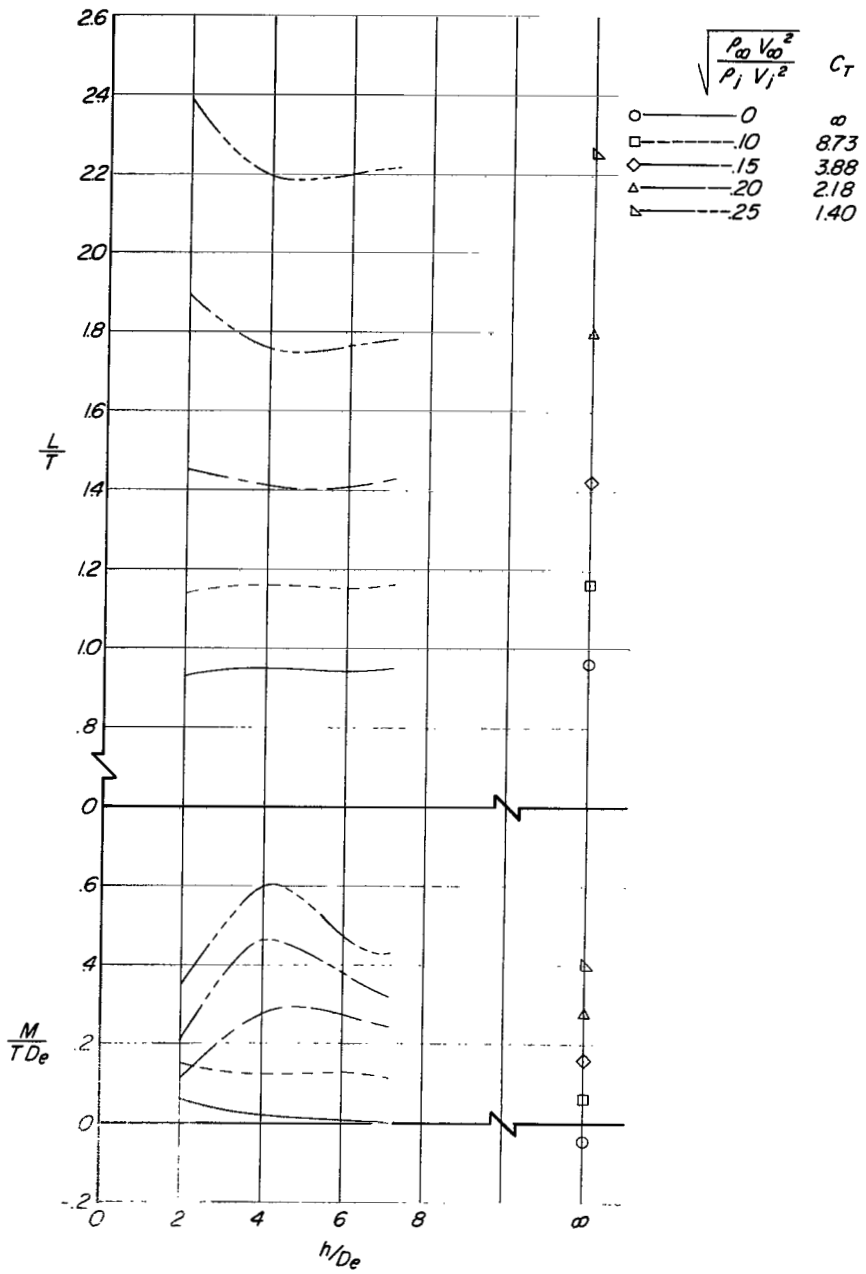

(b) $\alpha \approx 10.8^0$.

Figure 63.- Concluded.

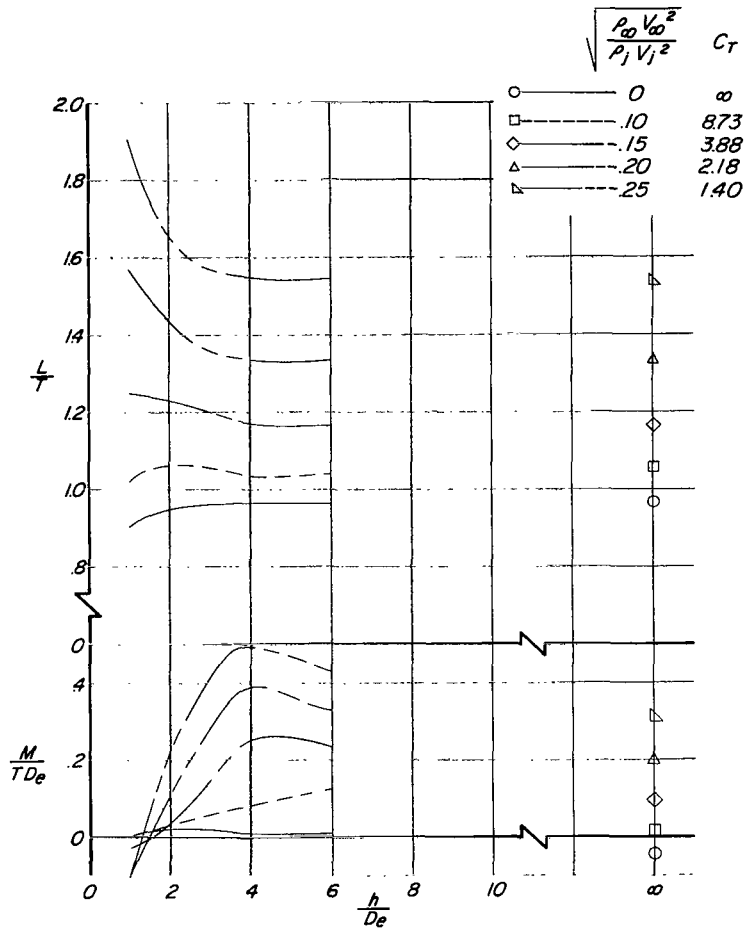

(a) $\alpha \approx 0.6^0$.

Figure 64.- Effect of height above ground on lift and pitching-moment parameters for configuration A ($\delta_f = 30^0$, $\delta_s = 35^0$, fixed forewing) with horizontal tail in low position ($i_t = 0^0$) for several thrust coefficients.

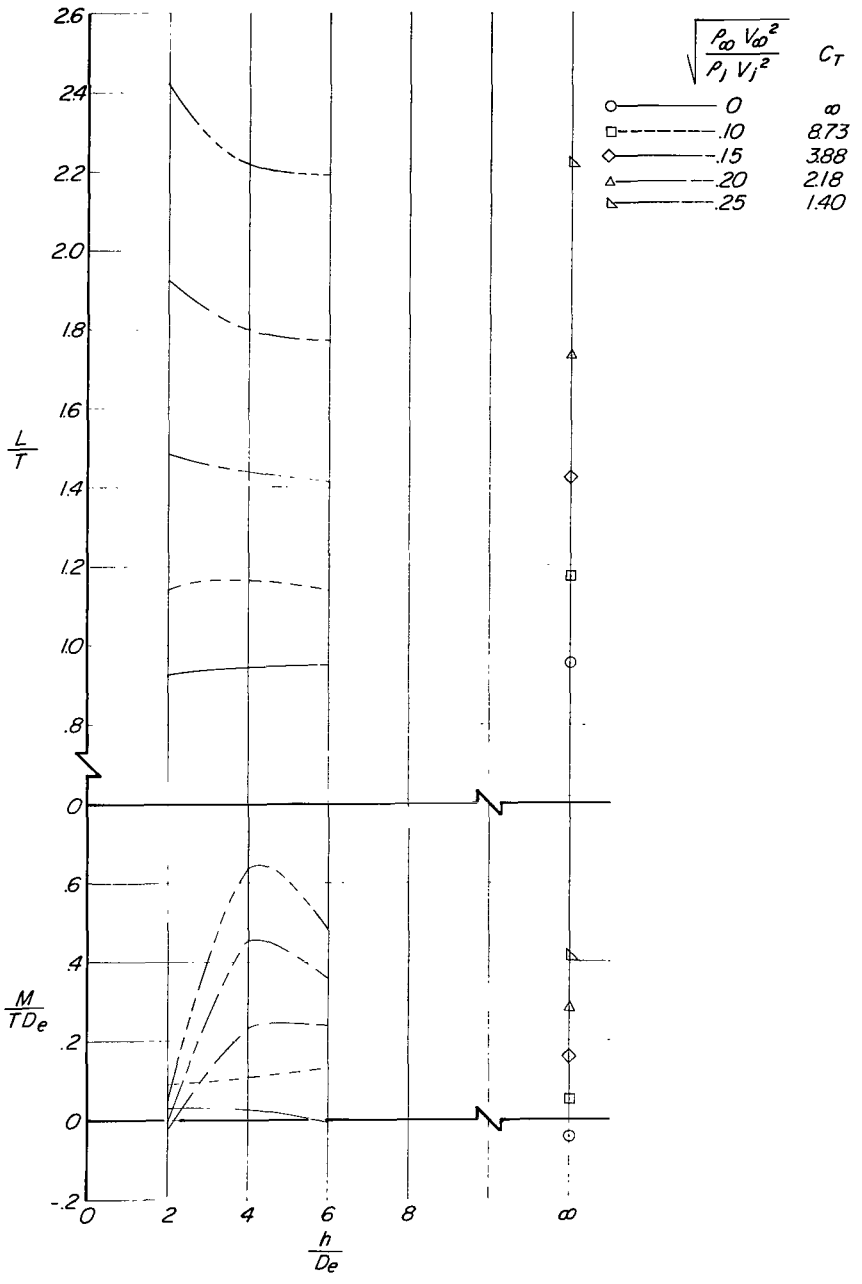

(b) $\alpha \approx 10.8^{\circ}$.

Figure 64.- Concluded.

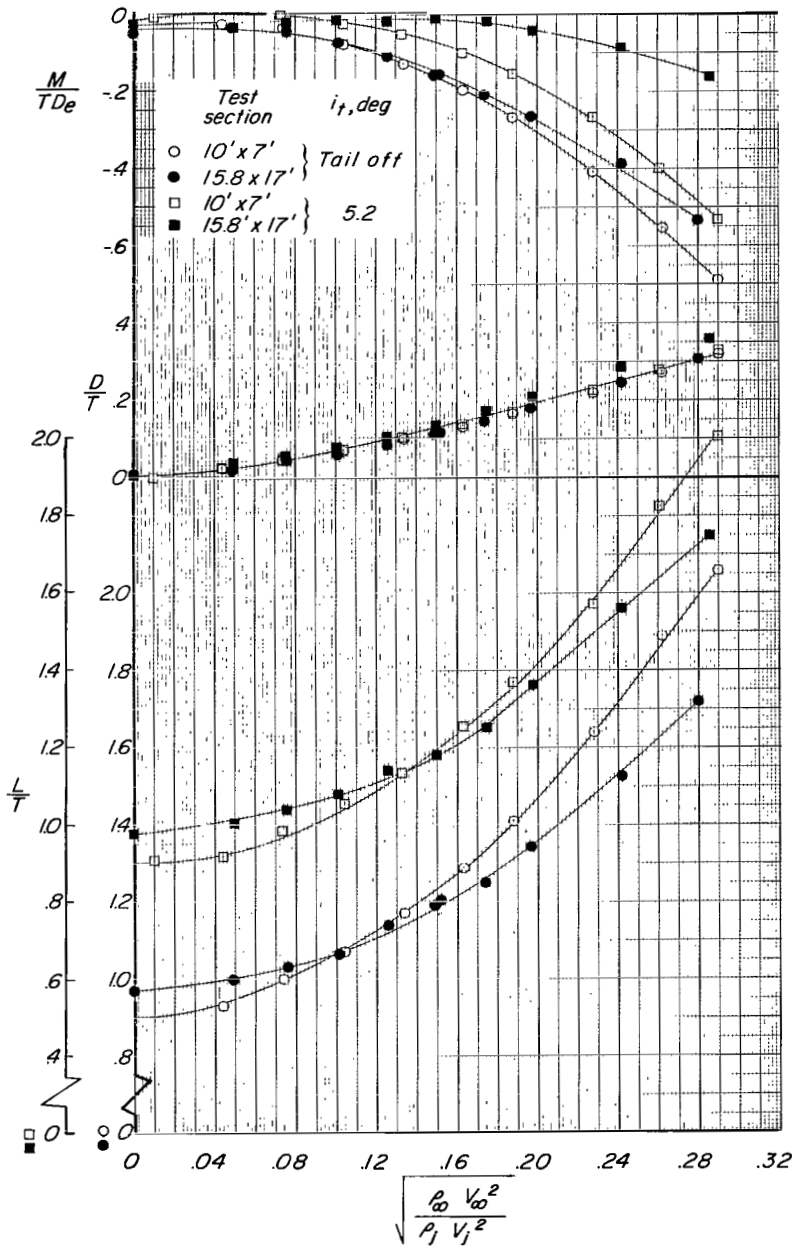

Figure 65.- Comparison of data from 10- by 7-foot (3.05- by 2.13-meter) test section and from the 15.8- by 17-foot (4.82- by 5.18-meter) test section of Langley 300-MPH 7- by 10-foot tunnel for configuration B ($\delta_f = 30^0$) through a range of effective velocity ratio. $\alpha \approx 0.6^0$.

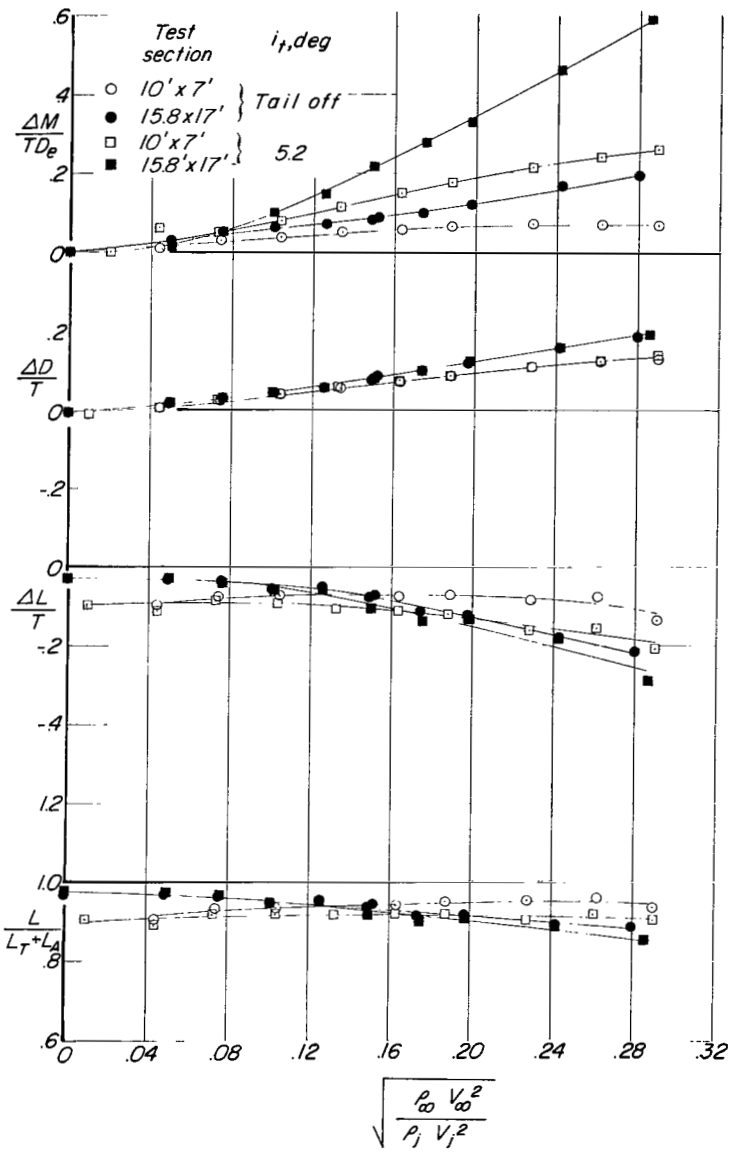

Figure 66.- Comparison of longitudinal interference effects from 10- by 7-foot (3.05- by 2.13-meter) test section and from 15.8- by 17-foot (4.82- by 5.18-meter) test section of Langley 300-MPH 7- by 10-foot tunnel for configuration B ($\delta_f = 30^0$) through a range of effective velocity ratios. $\alpha \approx 0.6^0$.

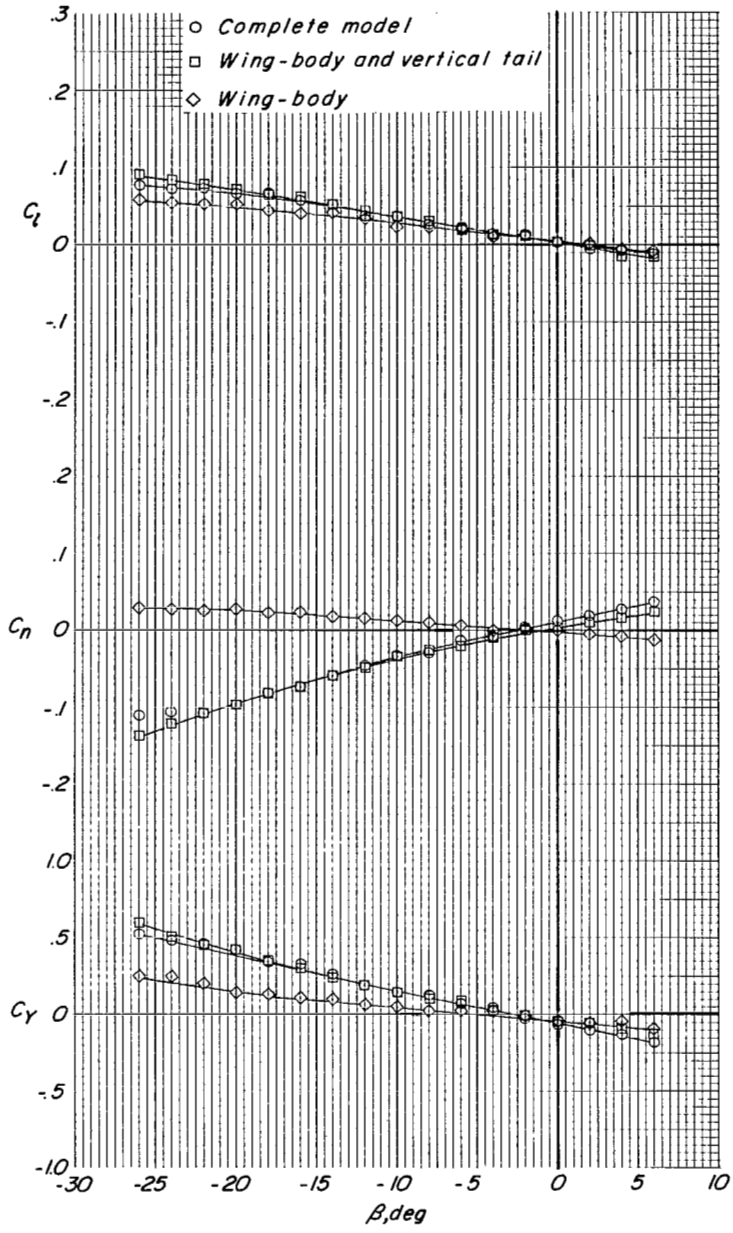

(a) Lateral-directional aerodynamic characteristics.

Figure 67.- Effect of sideslip angle on aerodynamic characteristics for configuration A ($\delta_f = 30^0$, $\delta_s = 35^0$, fixed forewing). $C_T = 0$; $\alpha \approx 0.6^0$.

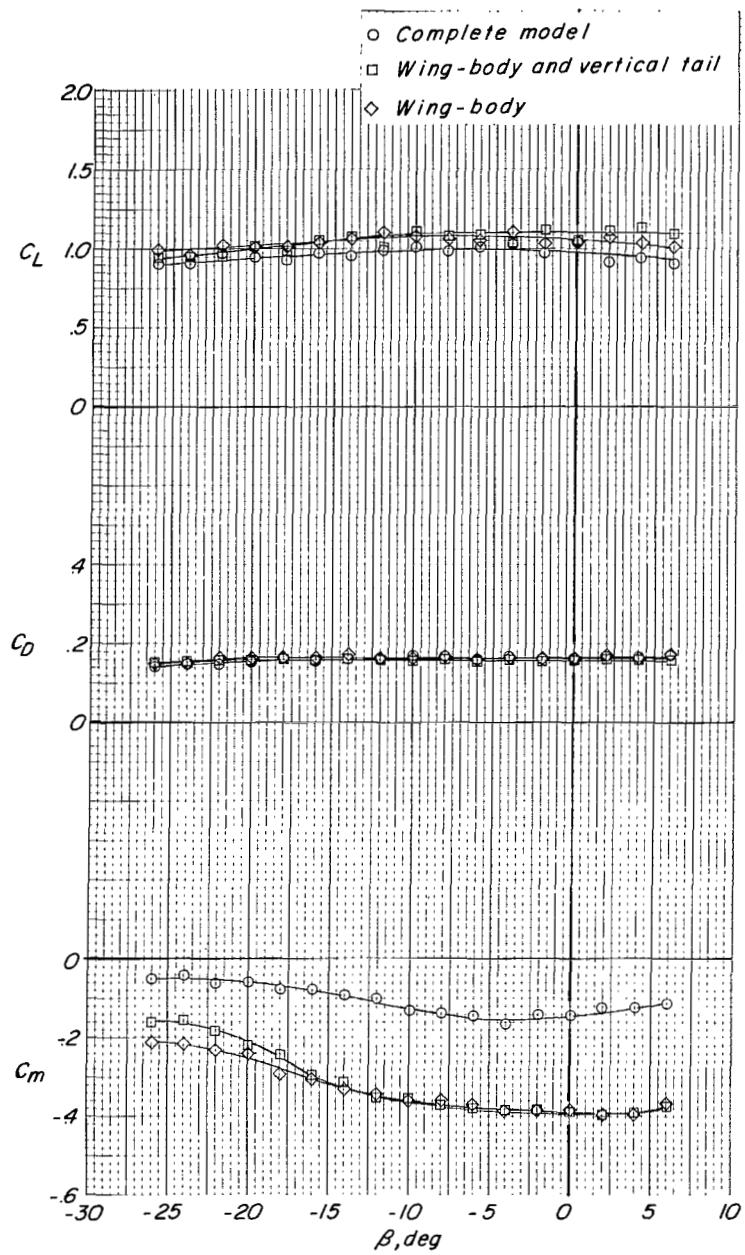

(b) Longitudinal aerodynamic characteristics.

Figure 67.- Concluded.

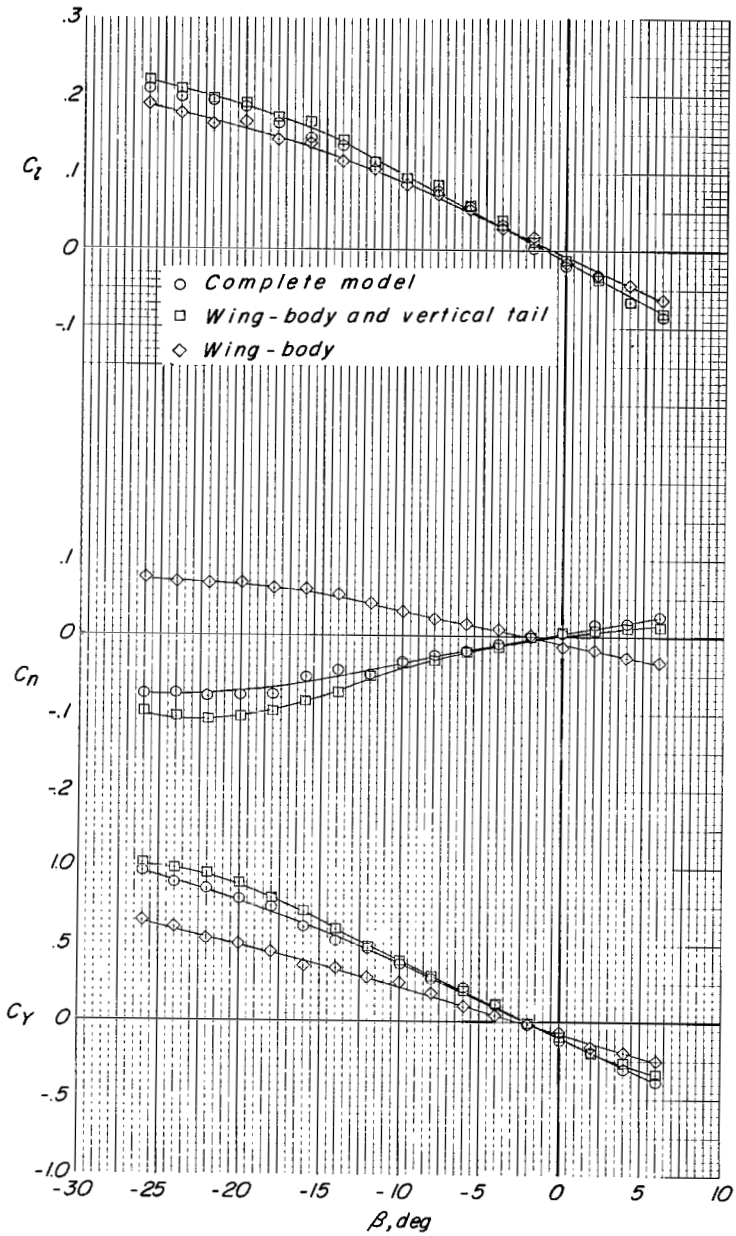

(a) Lateral-directional aerodynamic characteristics.

Figure 68.- Effect of sideslip angle on aerodynamic characteristics for configuration A ($\delta_f = 30^0$, $\delta_s = 35^0$, fixed forewing). $C_T \approx 3.4$; $\alpha \approx 0.6^0$.

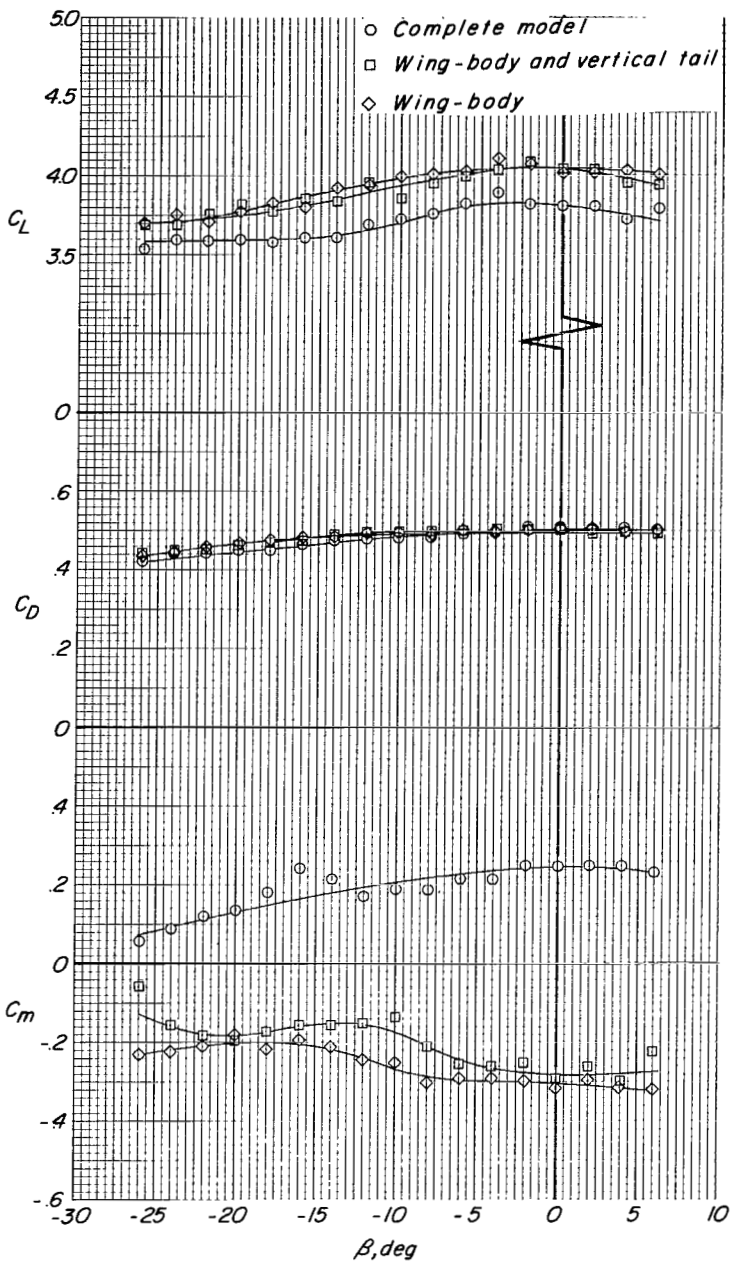

(b) Longitudinal aerodynamic characteristics.

Figure 68.- Concluded.

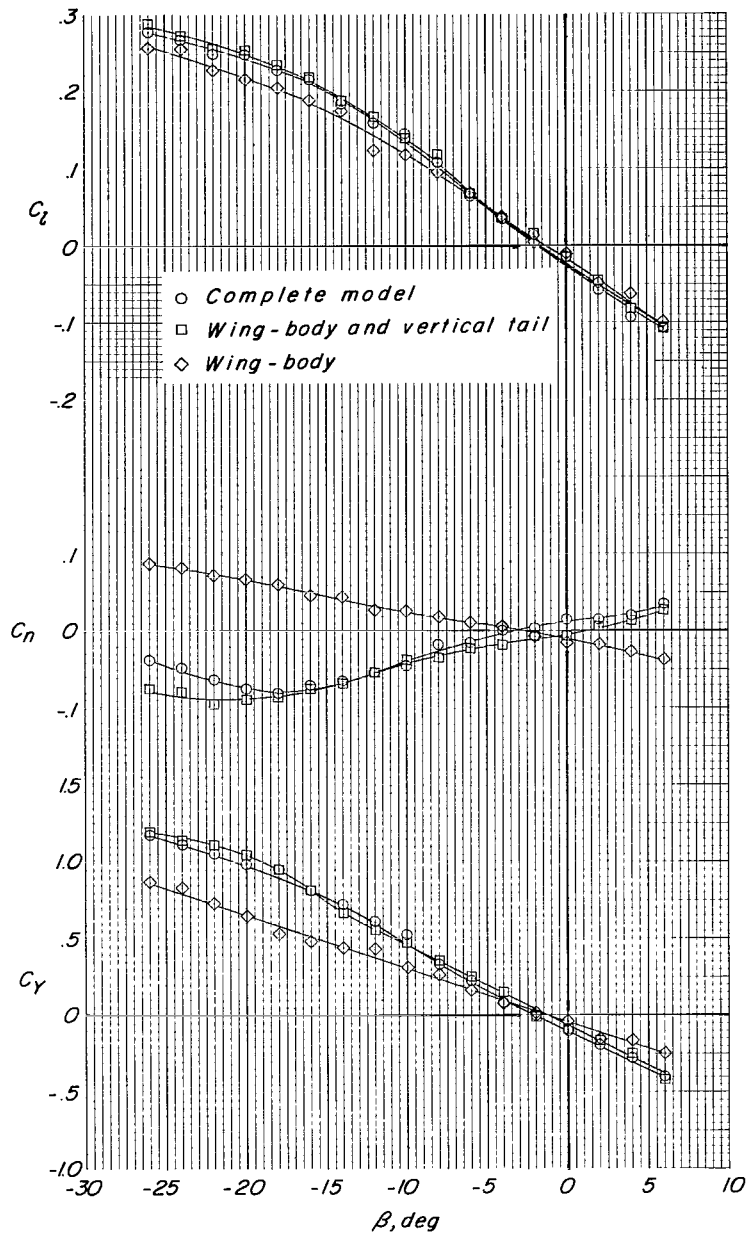

(a) Lateral-directional aerodynamic characteristics.

Figure 69.- Effect of sideslip angle on aerodynamic characteristics for configuration A ($\delta_f = 30^0$, $\delta_s = 35^0$, fixed forewing). $C_T \approx 7.9$; $\alpha \approx 0.6^0$.

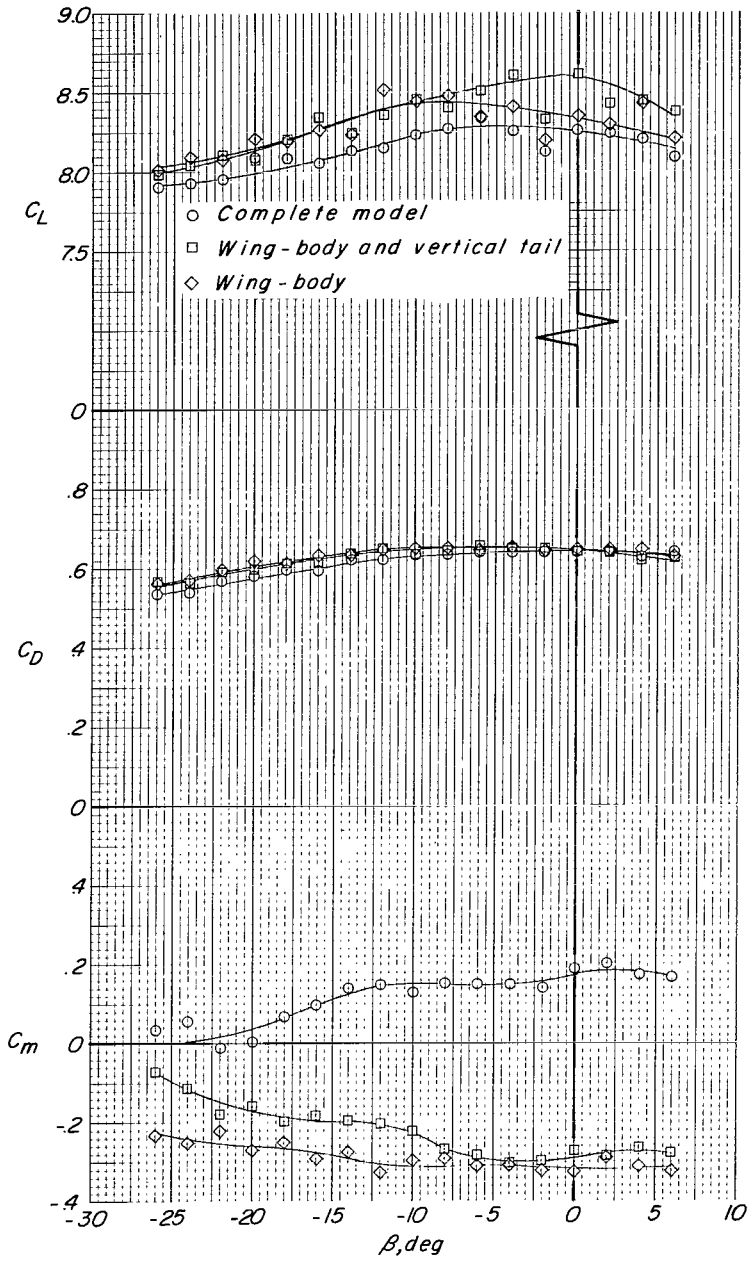

(b) Longitudinal aerodynamic characteristics.

Figure 69.- Concluded.

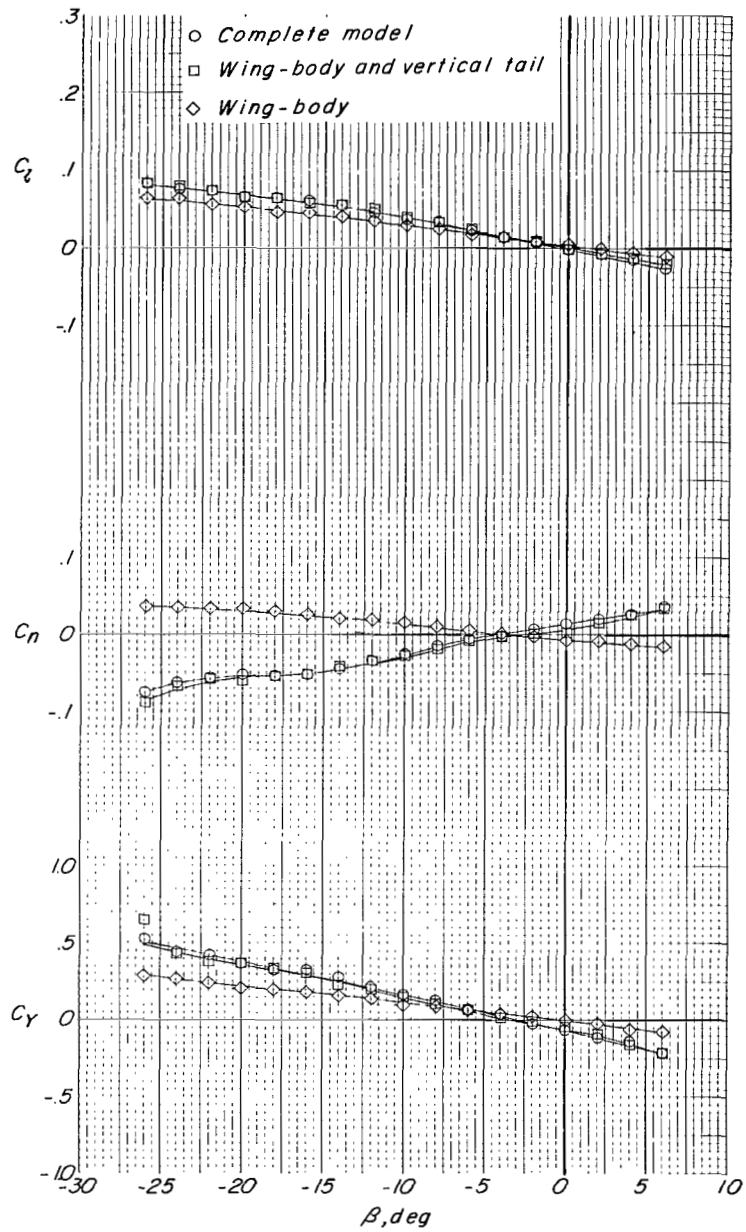

(a) Lateral-directional aerodynamic characteristics.

Figure 70.- Effect of sideslip angle on aerodynamic characteristics for configuration A ($\delta_f = 30^0$, $\delta_s = 35^0$, fixed forewing). $C_T = 0$; $\alpha \approx 11^0$.

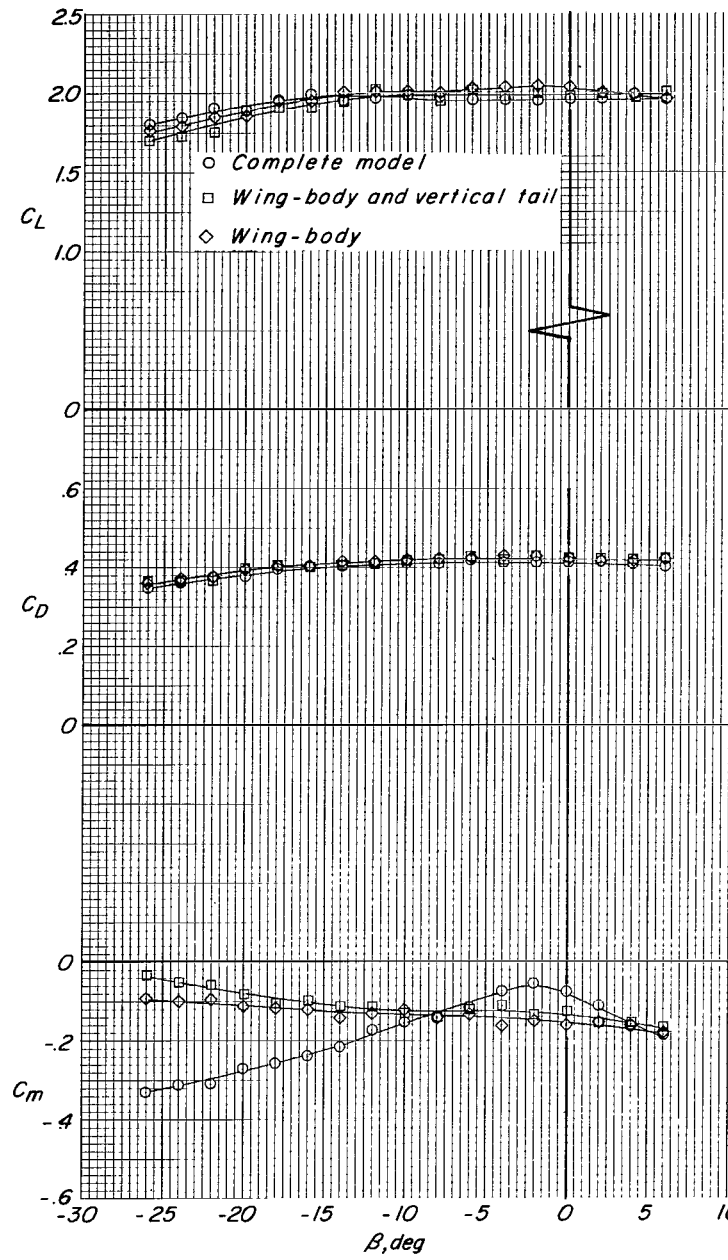

(b) Longitudinal aerodynamic characteristics.

Figure 70.- Concluded.

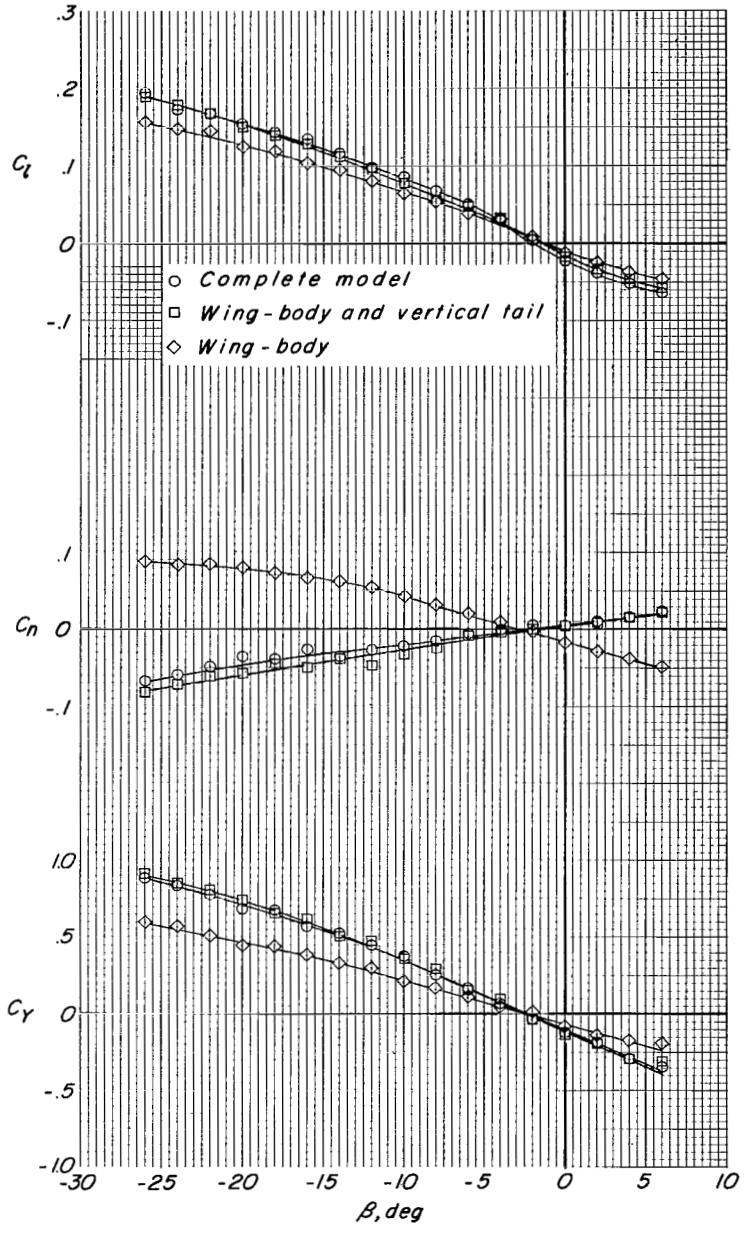

(a) Lateral-directional aerodynamic characteristics.

Figure 71.- Effect of sideslip angle on aerodynamic characteristics for configuration A ($\delta_f = 30^0$, $\delta_s = 35^0$, fixed forewing). $C_T \approx 3.3$; $\alpha \approx 11^0$.

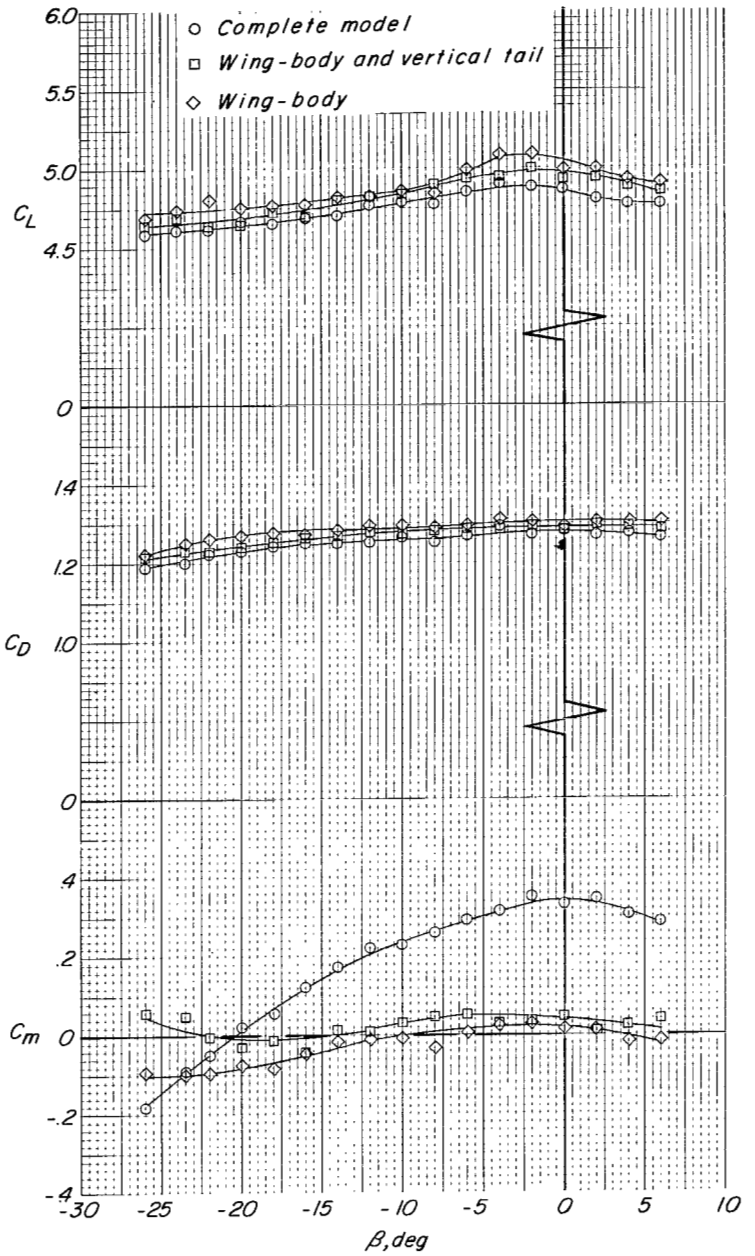

(b) Longitudinal aerodynamic characteristics.

Figure 71.- Concluded.

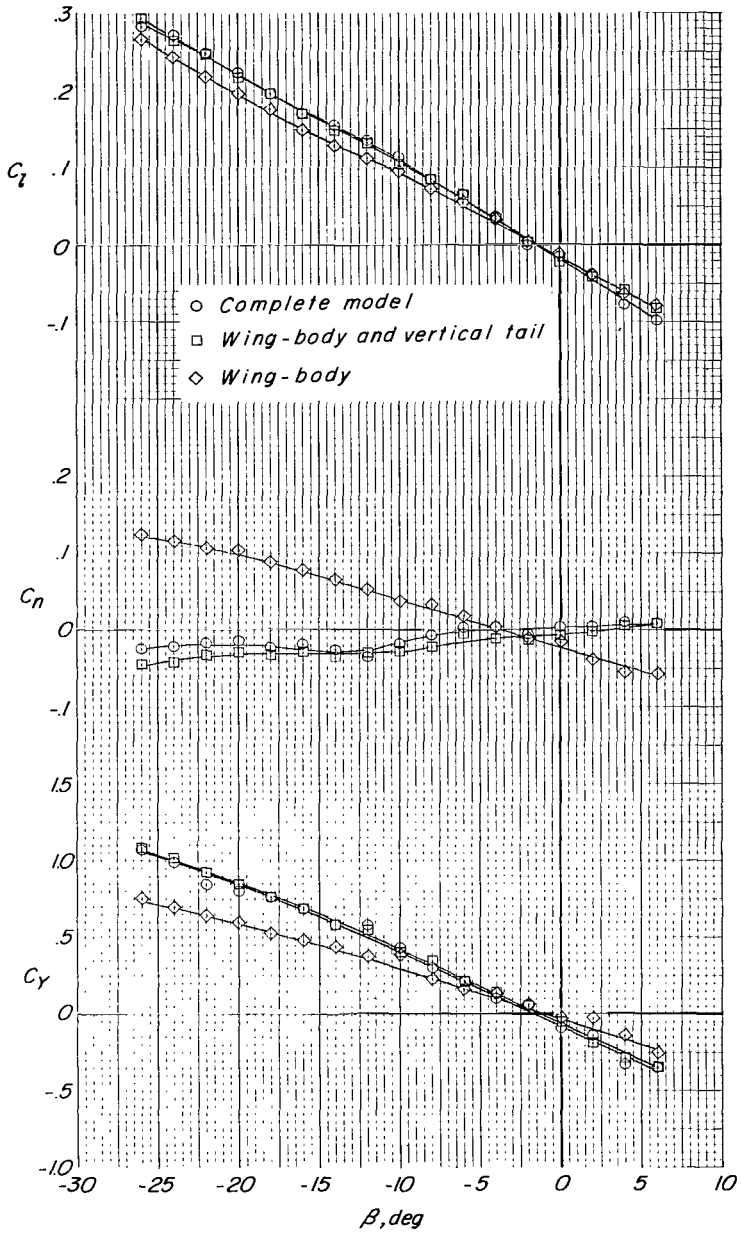

(a) Lateral-directional aerodynamic characteristics.

Figure 72.- Effect of sideslip angle on aerodynamic characteristics for configuration A ($\delta_f = 30^0$, $\delta_s = 35^0$, fixed forewing). $C_T \approx 8.0$; $\alpha \approx 11^0$.

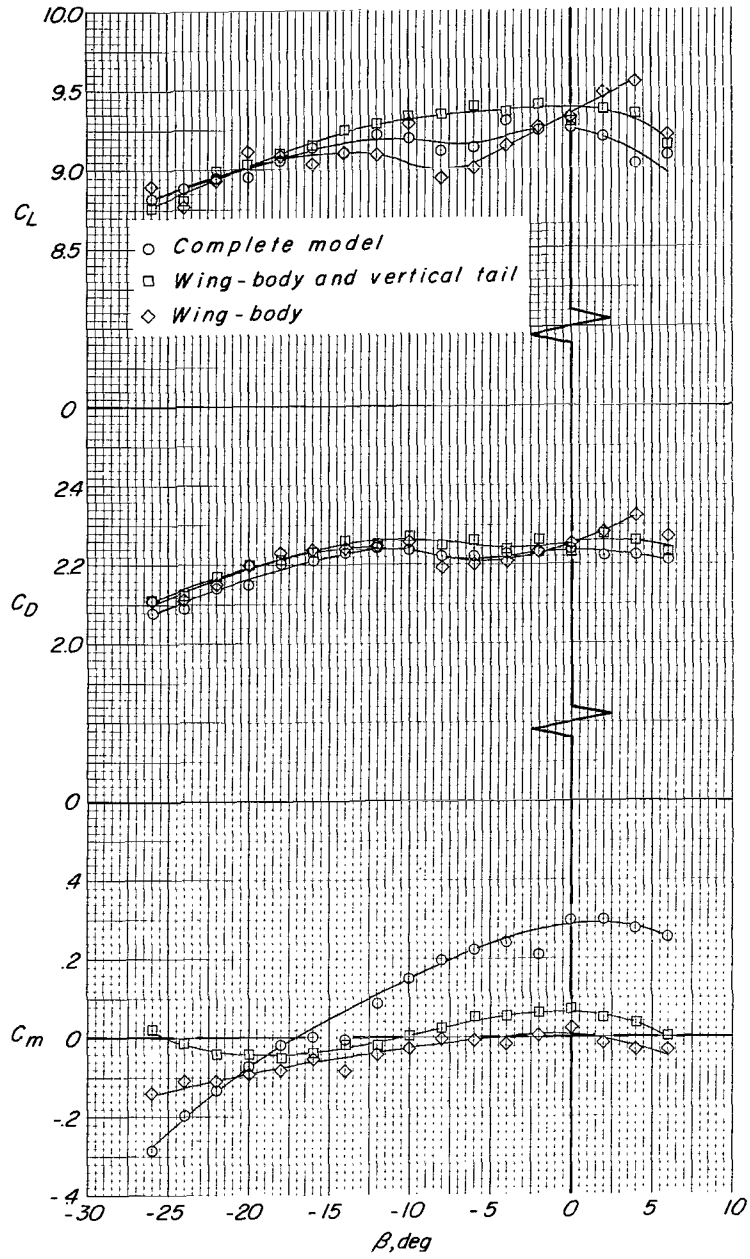

(b) Longitudinal aerodynamic characteristics.

Figure 72.- Concluded.

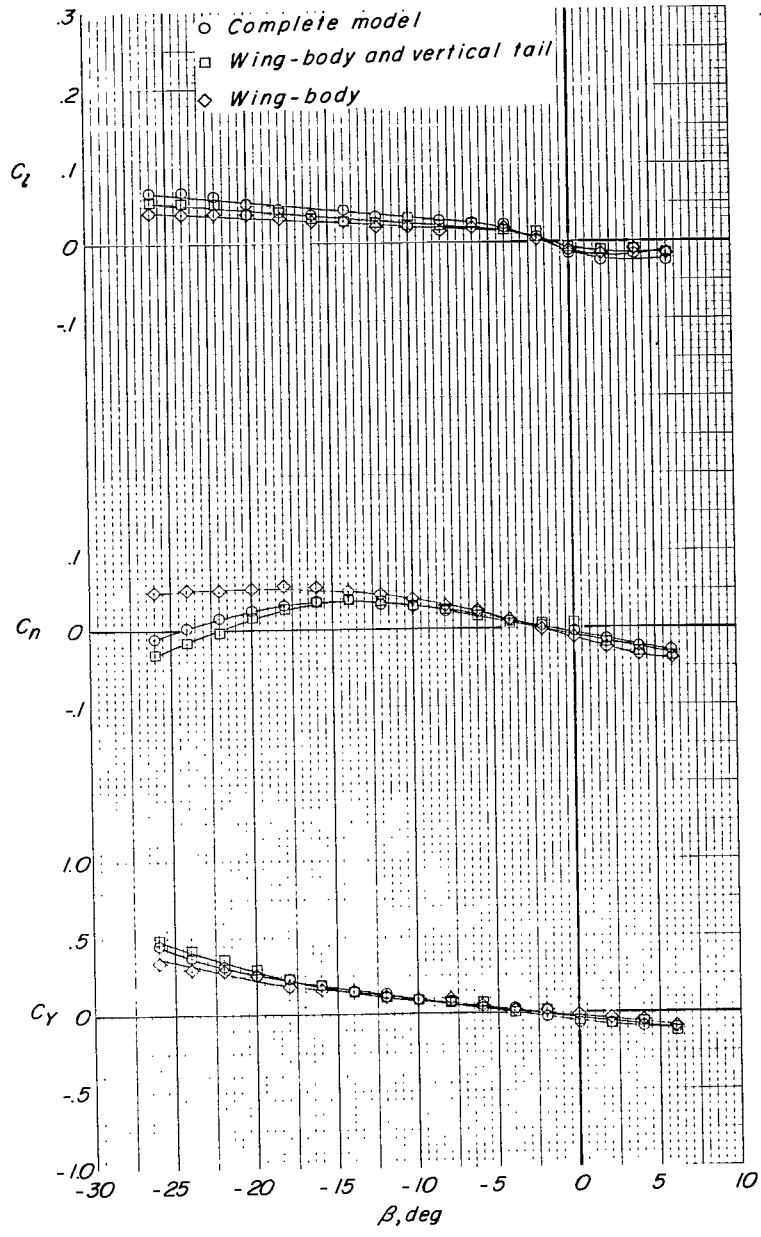

(a) Lateral-directional aerodynamic characteristics.

Figure 73.- Effect of sideslip angle on aerodynamic characteristics for configuration A ($\delta_f = 30^0$, $\delta_s = 35^0$, fixed forewing). $C_T = 0$; $\alpha \approx 21^0$.

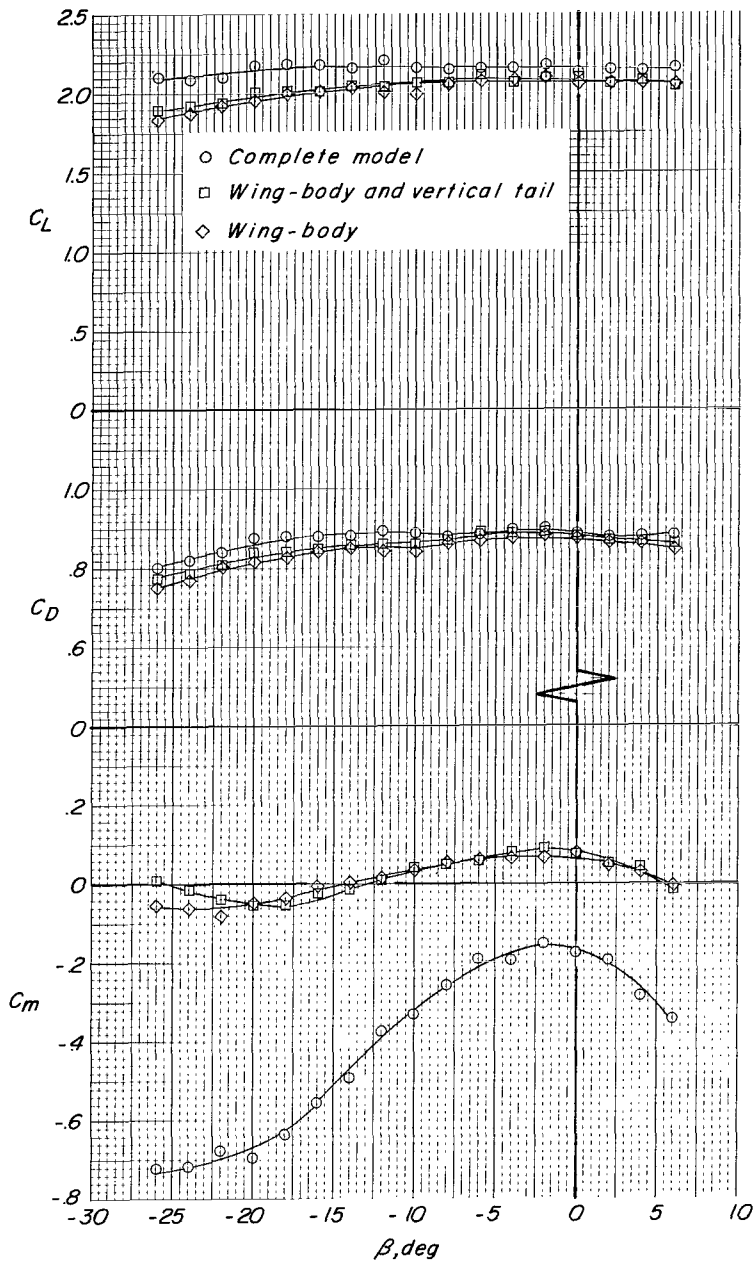

(b) Longitudinal aerodynamic characteristics.

Figure 73.- Concluded.

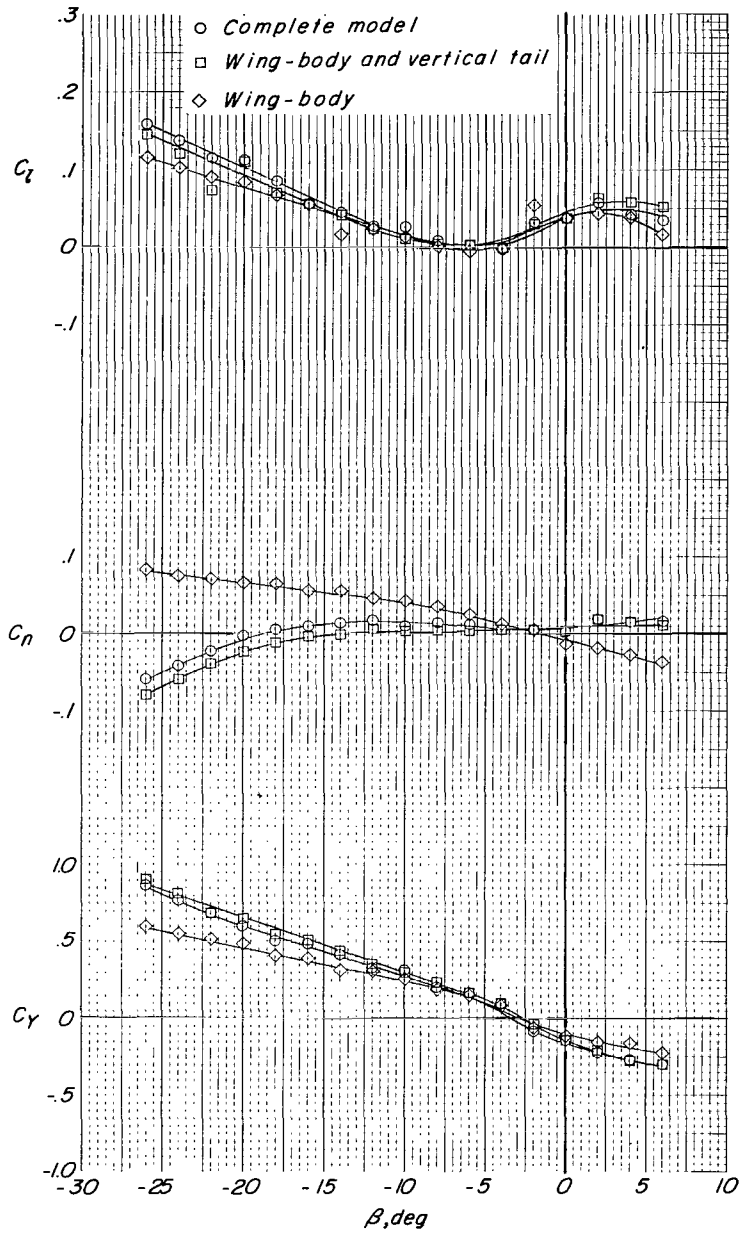

(a) Lateral-directional aerodynamic characteristics.

Figure 74.- Effect of sideslip angle on aerodynamic characteristics for configuration A ($\delta_f = 30^0$, $\delta_s = 35^0$, fixed forewing). $C_T \approx 3.3$; $\alpha \approx 21^0$.

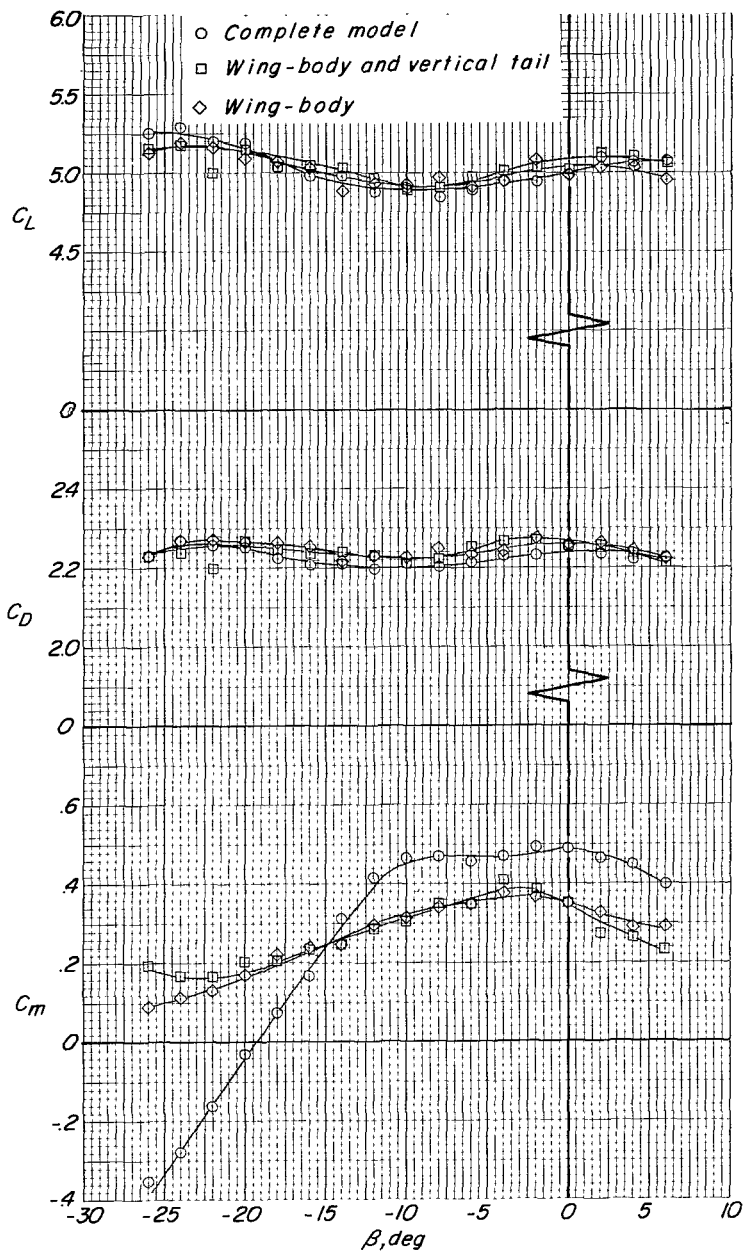

(b) Longitudinal aerodynamic characteristics.

Figure 74.- Concluded.

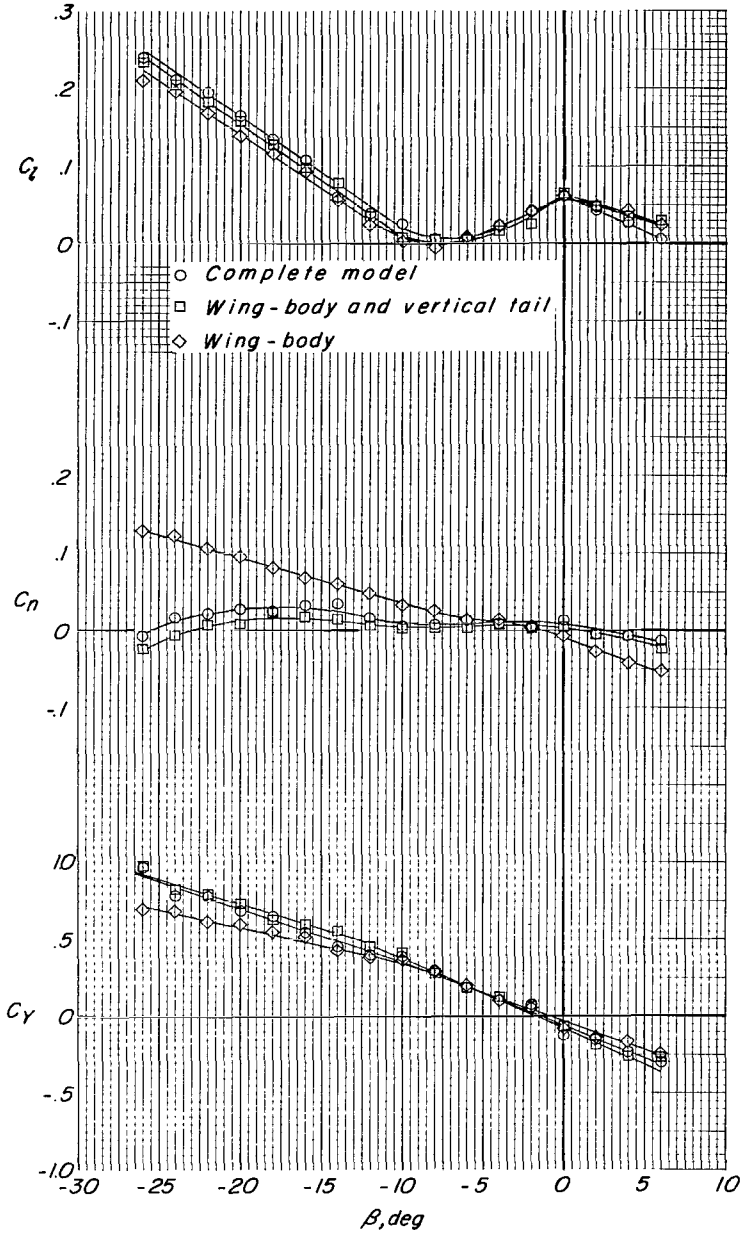

(a) Lateral-directional aerodynamic characteristics.

Figure 75.- Effect of sideslip angle on aerodynamic characteristics for configuration A ($\delta_f = 30^0$, $\delta_s = 35^0$, fixed forewing). $C_T \approx 7.9$; $\alpha \approx 21^0$.

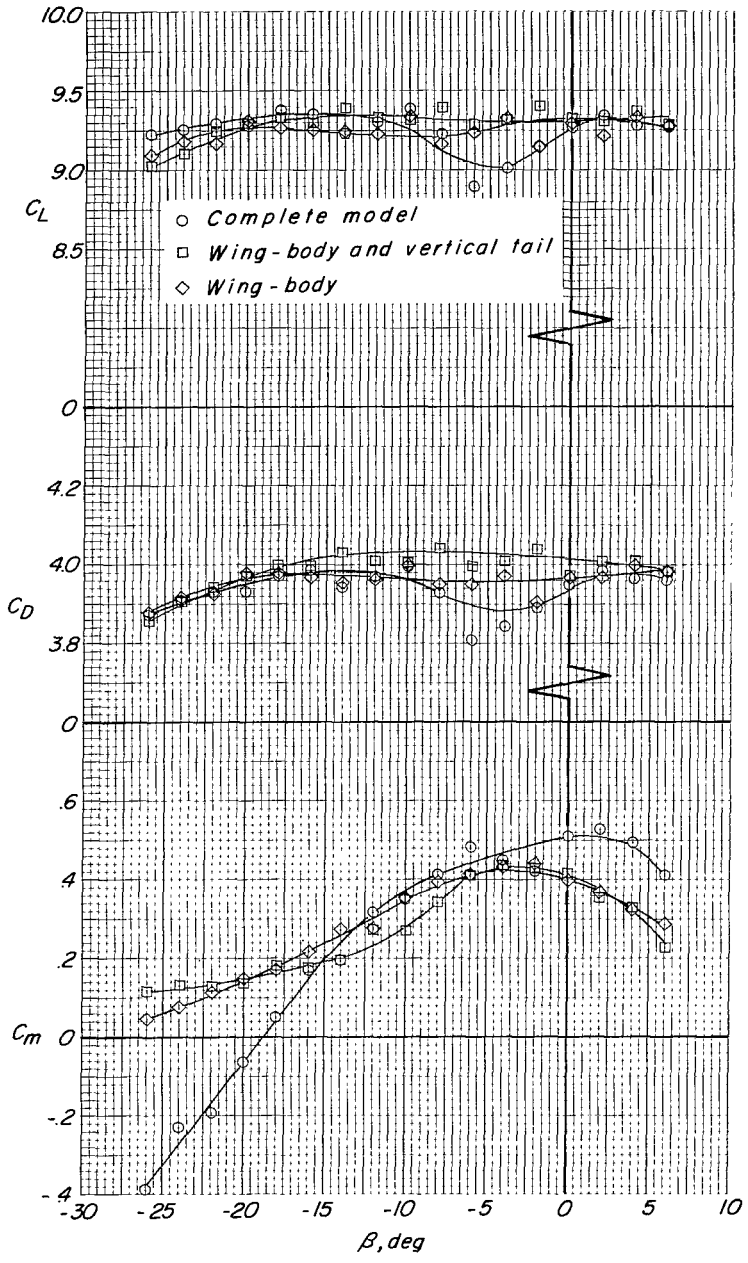

(b) Longitudinal aerodynamic characteristics.

Figure 75.- Concluded.

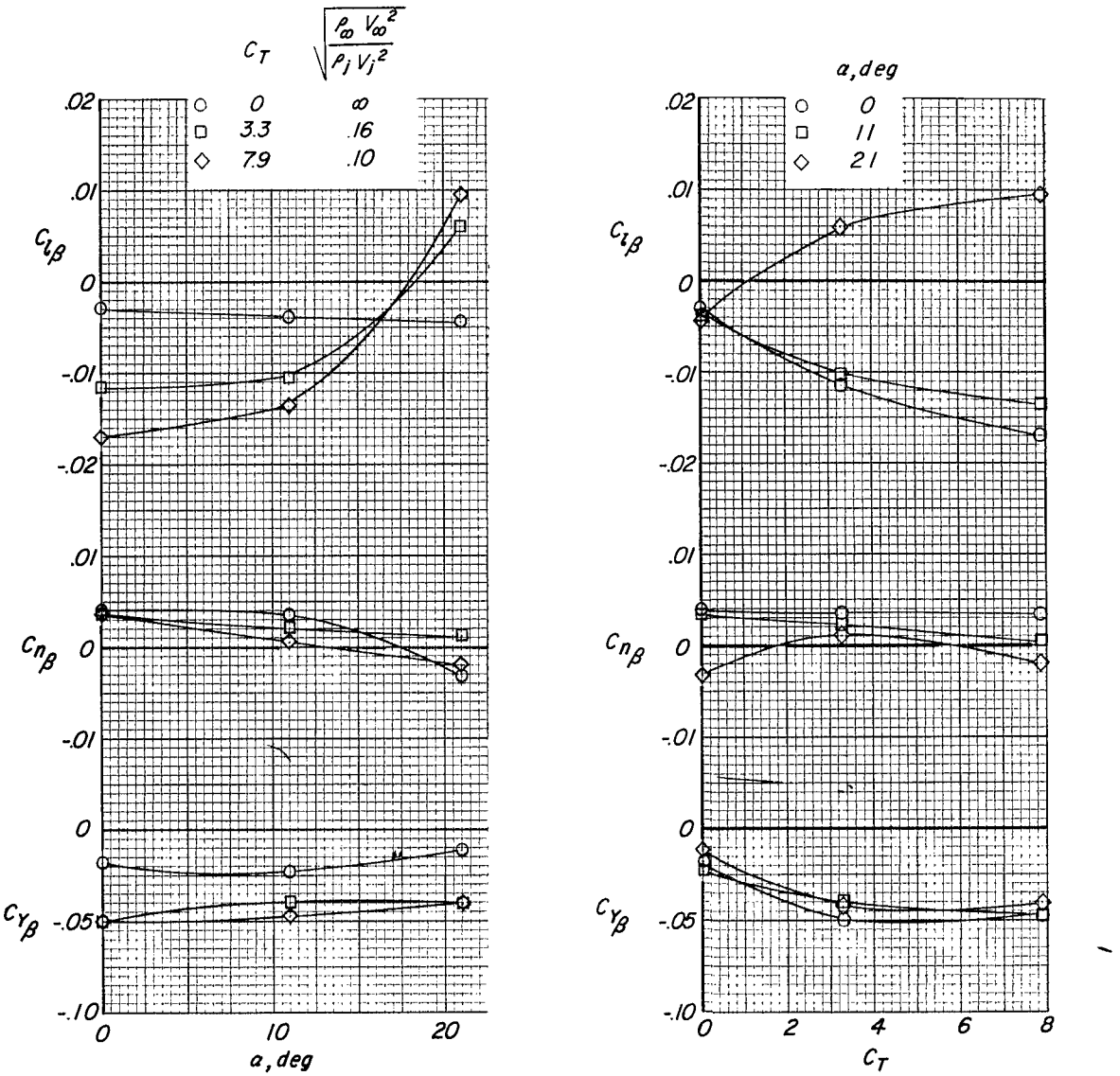

Figure 76.- Effect of angle of attack and thrust coefficient on lateral-directional stability derivatives for configuration A ($\delta_f = 30^0$, $\delta_s = 35^0$, fixed forewing) with complete empennage.

"The aeronautical and space activities of the United States shall be conducted so as to contribute . . . to the expansion of human knowledge of phenomena in the atmosphere and space. The Administration shall provide for the widest practicable and appropriate dissemination of information concerning its activities and the results thereof."

—NATIONAL AERONAUTICS AND SPACE ACT OF 1958

NASA SCIENTIFIC AND TECHNICAL PUBLICATIONS

TECHNICAL REPORTS: Scientific and technical information considered important, complete, and a lasting contribution to existing knowledge.

TECHNICAL NOTES: Information less broad in scope but nevertheless of importance as a contribution to existing knowledge.

TECHNICAL MEMORANDUMS: Information receiving limited distribution because of preliminary data, security classification, or other reasons.

CONTRACTOR REPORTS: Scientific and technical information generated under a NASA contract or grant and considered an important contribution to existing knowledge.

TECHNICAL TRANSLATIONS: Information published in a foreign language considered to merit NASA distribution in English.

SPECIAL PUBLICATIONS: Information derived from or of value to NASA activities. Publications include conference proceedings, monographs, data compilations, handbooks, sourcebooks, and special bibliographies.

TECHNOLOGY UTILIZATION PUBLICATIONS: Information on technology used by NASA that may be of particular interest in commercial and other non-aerospace applications. Publications include Tech Briefs, Technology Utilization Reports and Notes, and Technology Surveys.

Details on the availability of these publications may be obtained from:

SCIENTIFIC AND TECHNICAL INFORMATION DIVISION

NATIONAL AERONAUTICS AND SPACE ADMINISTRATION

Washington, D.C. 20546